

University of Trento
Doctoral School in Physics
XXIX cycle (2013-2016)



**Decoration of graphene sheets with metal and metal oxide nanostructures by
low-pressure plasma deposition**

PhD candidate: Hafeez Ullah

Supervisor: Dr. Nadhira Bensaada Laidani

Trento, Italy

April 2017

Acknowledgement

It gives me great pleasure and satisfaction to acknowledge the endowment of the creator of the universe, **Allah Almighty**, the most gracious, compassionate and beneficent to his creature, which enabled me to complete my work successfully.

I would like to express my sincere gratitude to my supervisor Dr. *Nadhira Bensaada Laidani* for providing me an opportunity to join in her research group. I also feel great honor to express the deepest sense of appreciation for her inspiring guidance, skillful suggestions, and keen interest during the whole period of my study. This dissertation would not have been possible without her motivation, encouragement, guidance and support. I am sure that her guidance will provide valuable source of inspiration throughout in my life.

I am very grateful to my colleagues Victor, Ruben and Gianni for their cooperation, help and unforgettable attitude during my research work. A special thanks to Giorgio Speranza for providing and teaching me a very useful, user-friendly RStudio tool for the XPS data elaborations and valuable discussion related to the XPS analysis during the lunch time. I am also grateful to Manoj, Eki, Gloria, and Firas and special thanks to Francesca Marchetti for her help regarding to the photocatalytic characterization. I am also very thankful to Prof .Giovanni Prodi, and Prof. Lorenzo Pavesi for their moral support and cooperation. I would also like to thank to Flavio Rossi and Gloria Ischia for their help in the Raman and TEM characterizations.

I am extremely thankful to my colleague and best friend Mian Kashif safeen, who completed his PhD last year for his cooperation. I would like to thank Dr. Georg Pucker for all his support and encouragement. I would also like to thank Cecilia Pederzoli and Christina Potrich for allowing me to use the Bio lab facilities during my research period. I would also like to thank the secretary, Micaela Paoli (Doctoral School of Physics, Unitn) and all staff of FBK for helping me

Tables of contents

in all the administrative procedures. I am sincerely grateful to all my friends including Maqsood, Saleem Khan, Waqar, and special thanks to Tahir for their help through various stages and friendly discussion. I am very thankful to Dr. Wei Liu and Guglielmo Mazzà for their encouragement at last stage of thesis writing.

Finally, I am most severely obliged to my family particularly my parent for their care and understanding have always been a great source of inspiration to me during my educational accomplishments. I am also extremely grateful to my lovely brother, Saif Ullah who provided me immense encouragement throughout my PhD. Program.

Hafeez Ullah

Trento, Italy

Tables of contents

CONTENTS

Introduction and aim of the thesis.....	4
Chapter # 1.....	7
Back ground and literature survey.....	7
1 Introduction.....	7
1.1 Graphene.....	7
1.2 Band structure of graphene.....	9
1.3 Physical properties of graphene.....	11
1.3.1 Electrical Conductivity of graphene.....	11
1.3.2 Thermal Conductivity.....	11
1.3.3 Optical properties of graphene.....	12
1.4 Overview method of preparation of graphene and metal oxide composites.....	12
1.4 .1 Solution based methods of graphene and metal oxide composites.....	13
1.4 .2 Graphene and metal oxide composites prepared by Sol–gel method.....	13
1.4 .3 Preparation of graphene and metal oxide by Hydrothermal/ solvothermal method.....	14
1.5 Decoration of graphene with metal oxide by Atomic layer deposition.....	15
1.6 Choice of the materials for the decoration of graphene sheets.	16
1.6.1 Properties of Nb ₂ O ₅	16
1.6.2 Characteristic of TiO ₂	17
1.6.3 Properties of Mg nanostructure.....	17
1.7 Review of the preparation study of transition metal oxide and graphene composite.....	18
1.8 Review of the preparation study of Mg and graphene based hybrid materials,.....	19
1.9 Review of the preparation TiO ₂ and graphene based hybrid materials.....	20
1.10 Defects in Graphene structure.....	22
1.11 Applications of graphene hybrid based materials.....	23
1.11.1 Graphene and TiO ₂ based photo catalytic application.....	23
1.11.2 Magnetic properties of graphene based hybrid materials.....	25
1.11.3 Hydrogen storage in graphene based material.....	27

Tables of contents

Chapter # 2	43
EXPERIMENTAL METHODS	43
2.1 Introduction.....	43
2.2 Samples preparation.....	43
2.3 Plasma material for synthesis and RF Sputtering	44
2.3.1 Decoration of graphene sheets with Metal and Metal oxide (Piezoelectric shaker).	48
2.3.2 Decoration of GNPs with Nb ₂ O ₅ nanoparticle.	51
2.3.3 The deposition of Mg nanoparticle onto graphene sheet.	51
2.3.4 Decoration of graphene powder with TiO ₂ nanoparticles	51
2.5 Thin Films Characterizations	52
2.5.1 Structural Properties: X-Ray Diffraction:	52
2.5.2 Raman Spectroscopy studies.....	54
2.5.3 X-Ray photoelectron spectroscopy (XPS)	55
2.5.4 Transmission Electron Microscopy	57
Chapter # 3	59
<i>The influence of Nb₂O₅ deposited by RF sputtering on the structural chemical and electronic properties of graphite nanoplatelets</i>	59
3.1 Introduction:.....	59
3.2 Experimental details:	59
3.3 The influence of Nb ₂ O ₅ concentration on the properties of graphite nanoplatelets	61
deposited by varying the RF power	61
3.3.1 XPS analysis of pristine GNPs and Nb ₂ O ₅ decorated GNPs at different RF powers	61
3.3.2 XRD analysis of pristine GNPs and Nb ₂ O ₅ decorated GNPs at different RF power values	65
3.3.3 TEM analysis of undoped and Nb ₂ O ₅ doped GNP at 100 W RF power value	71
3.3.4 Raman study of undoped GNPs and Nb ₂ O ₅ doped GNPs.....	72
3.4 The influence of Nb ₂ O ₅ concentration on the structural and chemical properties of graphite Nanoplatelets deposited by varying the process pressure	77
3.4.1 XPS analysis of undoped GNPs and Nb ₂ O ₅ doped GNPs at different process pressure values ..	78
3.4.2 XRD analysis of undoped GNPs and Nb ₂ O ₅ decorated GNPs at different working pressure values	81

Tables of contents

3.4.3 Raman study of undoped GNPs and Nb ₂ O ₅ doped GNPs at different process pressure values .	85
3.5 Effect of Nb ₂ O ₅ concentration on the structural and chemical properties of graphite nanoplatelets decorated by varying powder vibration frequencies	87
3.5.1 Chemical analysis of undoped GNPs and Nb ₂ O ₅ doped GNPs deposited at different powder vibration frequencies.....	88
3.5.2 Structural analysis of undoped GNPs and Nb ₂ O ₅ doped GNPs at different powder vibration frequencies	90
3.5.3 Raman study of undoped GNPs and Nb ₂ O ₅ doped GNPs at different powder vibration frequencies	94
3.6 Effect of Nb ₂ O ₅ concentration on the structural and chemical properties of graphite nanoplatelets decorated by varying deposition time	96
3.6.1 Chemical analysis of undoped GNPs and Nb ₂ O ₅ doped GNPs at different time of deposition .	97
3.6.2 XRD analysis of undoped GNPs and Nb ₂ O ₅ doped GNPs at different times of deposition.....	99
3.6.3 Raman study of undoped GNPs and Nb ₂ O ₅ doped GNPs with different times of deposition..	102
3.7 Concluding Remarks.....	105
Chapter # 4	108
<i>Effect of Nb₂O₅ concentration on the structural electronics and chemical properties of graphene powder</i>	<i>108</i>
4.1 Introduction:	108
4.2 Experimental details.....	109
4.3: The influence of the Nb ₂ O ₅ concentrations on the properties of graphene deposited by RF sputtering technique on static graphene powders:.....	110
4.3.1 XPS Analysis of undoped graphene and Nb ₂ O ₅ doped graphene:	110
4.3.2 XRD analysis of undoped Graphene and Nb ₂ O ₅ doped graphene.....	114
4.3.3 Raman analysis of undecorated graphene and decorated graphene with Nb ₂ O ₅ nanoparticles	116
4.3.4 TEM analysis of decorated graphene at 16 and 32 min.	120
4.4: The effect of the Nb ₂ O ₅ concentration on the structural and chemical properties graphene powder via given 10 Hz vibration to the graphene powder	122
4.4.1 XPS analysis of undoped graphene and Nb ₂ O ₅ doped graphene	122
4.4.2 XRD analysis of undecorated Graphene and Nb ₂ O ₅ doped graphene.....	125

Tables of contents

4.4.3 Raman Spectroscopy of Nb ₂ O ₅ decorated graphene via given vibration to graphene powder	127
4.5 Effect of Nb ₂ O ₅ nanoparticles on the structural and chemical properties of graphene powder deposited by varying the RF power values	130
4.5.1 Chemical analysis of undoped graphene and Nb ₂ O ₅ doped graphene at different RF power ..	131
4.5.2 XRD of undoped Graphene and Nb ₂ O ₅ decorated graphene at different RF power	134
4.5.3 Raman Spectroscopy of undoped graphene and Nb ₂ O ₅ doped graphene at different RF power values.	135
4.6 Conclusion Remarks:	139
Chapter # 5	142
<i>Effect of Mg crystalline nanoparticles and crystalline film on the structural and chemical properties of graphene powder</i>	<i>142</i>
5.1 Introduction:	142
5.2 Experimental details.....	143
5.3 The effect of crystalline Mg nanoparticles on the properties of graphene powder deposited at different RF power values.....	144
5.3.1 TEM analysis of graphene sheets decorated with Mg nanoparticles at 27 min of deposition.	145
5.3.2 XPS analysis of undoped graphene and Mg doped graphene at different RF power values....	146
5.3.3 XRD analysis of undoped graphene and Mg doped graphene at different RF power values ..	150
5.3.4 Raman study of undoped graphene and Mg doped graphene at different RF power values....	153
5.4 The effect of crystalline Mg nanoparticles on the properties of graphene powder decorated deposited at different times of deposition	156
5.4.1 XPS analysis of graphene and Mg deposited onto graphene at different times of deposition .	157
5.4.2 XRD analysis of undecorated graphene and Mg decorated graphene at different times of deposition	159
5.4.3 Raman study of undecorated graphene and Mg doped graphene at different times of deposition	161
5.5 The influence of Mg crystalline nanoparticles on the structure and chemical properties of graphene powder via given different vibration frequencies to graphene powders	164
5.5.1 TEM analysis of decorated graphene with Mg nanoparticles deposited at 0 Hz and 80 Hz....	165
5.5.2 XPS analysis of undoped graphene and Mg doped graphene at different powder vibration frequencies.	168

Tables of contents

5.5.3 XRD investigation of undoped graphene and Mg doped graphene decorated at different powder vibration frequencies.....	173
5.5.4 Raman study of undoped graphene and Mg doped graphene decorated at different powder vibration frequencies.....	Error! Bookmark not defined.
5.6 Concluding Remarks:	179
Chapter # 6	182
<i>The influence of TiO₂ concentration on the structural, chemical and electronic properties of graphene powder by plasma processing</i>	182
6.1 Introduction:	182
6.2 Experimental detail:	183
6.3 Effect of TiO ₂ nanoparticles on the structural, chemical and electronic properties of graphene powder deposited by varying RF power values	184
6.3.1 TEM analysis of decorated graphene with TiO ₂ nanoparticles deposited at 80 W	185
6.3.2 XPS analysis undoped graphene and TiO ₂ doped graphene deposited at different RF power values	186
6.3.3 XRD analysis undoped graphene and TiO ₂ doped graphene deposited at different RF powers.....	190
6.3.4 Raman analysis of undoped graphene and TiO ₂ doped graphene deposited at different RF power values	192
6.4 influence of TiO ₂ on the structural, chemical and electronic properties of graphene powder deposited by varying the deposition time.	195
6.4.1 XPS analysis undoped graphene and TiO ₂ doped graphene deposited with different times	196
6.4.2 Raman analysis of undoped graphene and TiO ₂ doped graphene deposited with different times.....	200
6.4.3 XRD analysis undoped graphene and TiO ₂ doped graphene at different times deposition	203
6.5 The influence of TiO ₂ nanoparticles on the structure and chemical properties of graphene powder via given different vibration frequencies	205
6.5.1 XPS analysis undoped graphene and TiO ₂ doped graphene deposited at different powder vibration frequencies	206
6.5.2 XRD analysis undoped graphene and TiO ₂ doped graphene deposited at different powder vibration frequencies.....	211
6.5.3 Raman analysis undoped graphene and TiO ₂ doped graphene deposited at different powder vibration frequencies	213
6.6 Concluding Remarks	216
Chapter # 7	218

Tables of contents

<i>Exploration of decorated graphene with metal and metal oxide nanostructures applications.</i>	218
7.1 Introduction.....	218
7.2 Magnetic properties of undecorated graphene and decorated graphene with Nb ₂ O ₅ nanoparticles	219
7.3 Photo catalytic activity of the TiO ₂ and graphene composite.	225
7.4 Hydrogen sorption capacity of the decorated graphene with Mg nanoparticles	227
7.5 Conclusions.....	231
Concluding Remarks.....	232

List of Figures

Fig 1. 1 Schematic diagram of the allotropic forms of carbon.....	8
Fig 1. 2 Schematic diagram for the band structure of graphene and band opening.....	10
Fig 1. 3 Schematic diagram of TiO ₂ and graphene based material for photocatalytic application.....	24
Fig 2. 1 Glove box and substrate holder used for the samples preparation.....	44
Fig 2. 2 Schematics of the sputtering process.....	47
Fig 2. 3 A schematic of the RF sputtering system	49
Fig 2. 4 Vibrating stage for the decoration of the sample.....	50
Fig 2. 5 Interaction of X-ray with crystalline materials according to the Bragg's law	52
Fig 2. 6 Energy level diagram for Raman scattering; Stokes and anti-Stokes Raman scattering.....	54
Fig 2. 7 Schematic of XPS and "Photoelectric Effect	56
Fig 2. 8 Schematic diagram for TEM analysis.....	58
Fig 3. 1 (a) XRD patterns Nb ₂ O ₅ doped GNPs (b) Variation of the 2θ angle of the (002) at different powder vibration frequencies peak with through varying powder vibration frequencies (RF power =40 W deposition time =15 min and process pressures =6 Pa)	91
Fig 4. 1 XPS spectra of graphene powder with incrementally increased Nb ₂ O ₅ contents by varying the deposition time (a) Shift in the C 1s core levels position upon Nb ₂ O ₅ deposition (b) Nb 3d core level spectra with positions of the Nb+5 peaks. [Process pressure = 6 Pa, Time= 8 to 32 min, Frequency = 0 Hz RF power= 40 W].....	112
Fig 4. 2 (a) De-convolution of the O 1s core level (b) variations of Nb/C and Stoichiometry with respect ..	113
Fig 4. 3 (a) XRD patterns of undoped and Nb ₂ O ₅ doped graphene at (b) Variation of the 2θ angle position of the (002) different time of depositions and d-spacing as function of Nb/C at.%	114
Fig 4. 4 Variation in the FWHM of the (002) peak and crystallite thickness as function of Nb/C sp ² atomic ratio	115
Fig 4. 5 (a) Raman spectra of undoped graphene and (b) positions of the G and FWHM (G) vs Nb to C (%) Nb ₂ O ₅ doped GNPs at different times of deposition.....	117
Fig 4. 6 Variation of Raman peak intensity ratios of I _D /I _G plotted against the Nb to C atomic ratio (%)	119
Fig 4. 7 TEM images (A-B) decorated graphene at 16 min of deposition and (C-D) Nb ₂ O ₅ decorated graphene at 32 min of deposition	121
Fig 4. 8 XPS spectra of graphene powder with incrementally increased Nb ₂ O ₅ contents by varying the deposition time (a) Shift in the C 1s core levels position upon Nb ₂ O ₅ deposition (b) Nb 3d core level spectra with positions of the Nb+5 peaks.	123
Fig 4. 9 (a) De-convolution of the O 1s core level (b) variations of Nb/C and Stoichiometry with respect to	125
Fig 4. 10 (a) XRD patterns of the undoped graphene (b) Variation of the 2θ angle of the (002) and FWHM (002) as a and Nb ₂ O ₅ doped graphene at different times of deposition function Nb/C atomic ratio (%)	126
Fig 4. 11 (a) Raman spectra of undoped GNPs and (b) positions of the G and FWHM (G) vs Nb to C (%) Nb ₂ O ₅ doped GNPs at different time of deposition	127
Fig 4. 12 Variation of Raman peak intensity ratios of I _D /I _G plotted against the Nb to C atomic ratio (%).	129

List of figures

Fig 4. 13 XPS spectra of graphene powder with incrementally increased Nb2O5 contents by varying the RF power values (a) Shift in the C 1s core levels position upon Nb2O5 deposition (b) Nb 3d core level spectra	132
Fig 4. 14 (a) De-convolution of the O 1s core level (b) variations of Nb/C and with respect to RF power values	134
Fig 4. 15 (a) XRD patterns of the undoped graphene (b) Variation of the 2θ angle of the (002) and Nb2O5 doped graphene at different RF Power FWHM (002) as a function of Nb/C atomic ratio (%)	135
Fig 4. 16 (a) Raman spectra of undoped GNPs and (b) positions of the G and FWHM (G) vs Nb to C (%) Nb2O5 doped GNPs at different RF powers.....	137
Fig 4. 17 Variation of Raman peak intensity ratios of I _D /I _G plotted against the Nb to C atomic ratio (%).	138
Fig 5. 1 TEM images (A-B) of Mg decorated onto graphene at 27 min of deposition	145
Fig 5. 2 (a) XPS spectra acquired on graphene powders with incrementally increased of Mg contents by varying the RF power values (a) C Shift in the C 1s core levels position upon Mg deposition. (b) Mg 2p core level spectra (RF power =30 to 75 W, Process pressure=6 Pa, Time= 18 min and powder vibration frequency= 10 Hz).....	146
Fig 5. 3 (a) O 1s core peak and its de-convolution (b) variations of Mg/C sp ² atomic ratio with RF Power values	148
Fig 5.4 (a) XRD patterns of decorated graphene with Mg (b) crystallite sizes of the decorated Mg nanoparticles at different RF power values nanoparticles as function of RF power	151
Fig 5. 5 Variation of the 2θ angle position of the (002) and d-spacing as function of Mg/C at. %.....	152
Fig 5. 6 (a) Raman spectra of undoped graphene and (b) positions of the G and FWHM (G) as a function of Mg/C (%) Mg doped graphene at different time of deposition	154
Fig 5. 7 Variation of Raman peak intensity ratios of I _D /I _G and I _a plotted against the Mg to C atomic ratio (%) .	156
Fig 5. 8 (a) XPS spectra of graphene powder with incrementally increased of Mg contents by varying the deposition time (a) C Shift in the C 1s core levels position upon Mg deposition. (b) Mg 2p core level spectra (RF power =40 W, Process pressure= 6 Pa, Time= (6 to 27 min and powder vibration frequency= 0 Hz.	158
Fig 5. 9 (a) O 1s core peak and its de-convolution (b) variations of Mg/C and atomic ratio with time	159
Fig 5. 10 Variation of the 2θ angle position of the (002) and d-spacing as function of Mg/C at. %.....	161
Fig 5. 11 (a) Raman spectra of undoped graphene and (b) positions of the G and FWHM (G) vs Mg to C (%) Mg doped graphene at different time of deposition.....	162
Fig 5. 12 Variation of Raman peak intensity ratios of I _D /I _G and I _a plotted against the Mg to C atomic ratio (%).	163
Fig 5. 13 TEM images (a-d) of deposited Mg nanoparticles without moving powder (0 Hz).....	166
Fig 5. 14 TEM images (a-d) of deposited Mg nanoparticles at high powder vibration frequency (80 Hz	167
Fig 5. 15 (a) XPS spectra of graphene powder with varying the powder vibration frequencies (a) C Shift in the C 1s core levels position upon Mg deposition. (b) Mg 2p core level spectra (RF power =40 W, Process pressure=6 Pa, Time= 27 min and powder vibration frequency= (0 to 100 Hz).	169
Fig 6. 1 TEM images (a-b) of deposited TiO ₂ nanoparticles onto graphene sheet at 80 W	185
Fig 6. 2 (a) XPS spectra for graphene powder and deposited TiO ₂ nanoparticles at different RF power values (a) Shift in the C 1s core levels position upon TiO ₂ deposition. (b) Ti 2p core level spectra. [Process pressure = 6 Pa, Time=40 min, Frequency = 20 Hz RF power= 30 to 80 W]	186
Fig 6. 3 (a) XPS O 1s core peak of decorated graphene (b) variations of Ti /C sp ² and OI/Ti atomic ratio as a function of RF power values	189

List of figures

6.4 (a) XRD patterns of undoped and TiO ₂ doped graphene powers values	(b) Variation of the 2θ angle of the (002) and d-spacing as function of Ti/C sp ² atomic ratio.	191
Fig 6. 5	Variation in the FWHM of the (002) peak and crystallite thickness as function of Ti/C atomic ratio	192
Fig 6. 6	Raman spectra of undoped graphene and TiO ₂ doped graphene at different RF power values	193
Fig 6. 7	Variation of Raman peak intensity ratios of ID/IG and in plane crystallites size (L _a) plotted against the Ti/C.a (%).....	195
Fig 6. 8 (a)	XPS spectra from graphene powder and deposited TiO ₂ nanoparticles at different times of deposition (a) Shift in the C 1s core levels position u upon TiO ₂ deposition (b) Ti 2p core level spectra. [Process pressure = 6 Pa, Time=40 min, Frequency = 20 Hz RF power= 30 to 80 W]	198
Fig 6. 9 (a)	O 1s core peak of decorated graphene (b) variations of Ti /C and OI/Ti atomic ratio as a with TiO ₂ nanoparticles at different time of deposition function of different time of deposition	199
6. 10 (a)	Raman spectra of undoped graphene and TiO ₂ doped graphene at different time of deposition (b) positions of the G and FWHM (G) as a function of Ti/C at. %	201
Fig 6. 11	Variation of G and D peak intensity ratio ID/IG and in plane crystallites size (L _a) plotted against the Ti/C atomic ratio.....	202
Fig 6. 12 (a)	XRD patterns of undoped and TiO ₂ doped graphene at the (002) different times of depositions (b) Variation of the 2θ angle position of and d-spacing as function of Ti/C at.%.....	204
Fig 6. 13	Variation in the FWHM of the (002) peak and crystallite thickness as function of Ti/C atomic ratio	205
Fig 7. 1 (a, b)	M-H curves for undoped graphene and with various Nb doping concentration measured at (a) 5 K and (b) 300 K	220
Fig 7. 2	Magnetization curves as a function of the applied temperature 5≤T<300K for each sample, for all Nb (%) concentration. (a) Magnetization curves for undoped graphene flakes (b) for doped graphene with 0.49 Nb (%) concentration. (c) For doped graphene with 0.62 Nb (%) concentrations. (d) For doped graphene with 0.75 Nb (%) concentrations.	223
Fig 7. 3 (a)	Coercive field as a function of temperature for different Nb (%) concentrations. (b) Coercive field as a function of Nb concentration for different temperatures.....	224

#Introduction

Introduction and aim of the thesis

Graphene has got exceptional attention in the field of science and technology, regarding its remarkable, mechanical, electrical and electronic properties. Graphene has prominent potential to be next conducting materials to substitute the electrode materials in optoelectronic devices. With the increased demand in energy resources and other kinds of applications, pronounced effort has been dedicated to achieve advanced energy conversion and storage systems. Graphene and its composite have much pronounced attention for the energy storage system, because it's unique properties such as chemical stability, superior thermal and electrical properties and large surface area. A wide range and different variety of graphene based materials were prepared for potential applications in sensing, catalysis, electronics, magnetic and energy storage. Graphene presents unique properties when modified by means of metal (M) and metal oxide (MO) nanostructures decoration. Recently different research activities were done for hydrogen storage in graphene based materials. It is well established that the decoration of graphene with well dispersed M nanostructures improved hydrogen uptake capacity at ambient conditions. More over graphene has been used as a burgeoning support to accommodate well-dispersed semiconductor MO nanostructures to enhance the photocatalytic and magnetic properties.

The main objective of the current work was to decorate graphene sheets with M and MO nanostructures for improvement of some properties of graphene. The main target of this work was related to decorating graphene sheets with M and MO nanostructures for hydrogen storage, photocatalytic activity and the study of the magnetic properties of the graphene and metal/metal oxide composite. It is well known that decoration of graphene sheets with M and MO nanostructures not only enhances graphene properties but also displays novel properties resulting from the interaction between M and MO nanostructures with the graphene sheets. However the

#Introduction

decoration method of metal and metal oxide nanostructures which are nontoxic, environmentally friendly and fast is very challenging and important. Because the size and the distribution of the M and MO nanostructures onto graphene sheets are affected the efficiency of the prepared composite, which are difficult to control. In this thesis, the decoration of graphene powder with three kinds of materials Nb_2O_5 , TiO_2 and Mg deposited by radio frequency sputtering techniques was studied. The low-pressure plasma deposition is a clean compatible, scalable and widely used technique in industry. Moreover using RF sputtering technique for the decoration with MO of graphene sheets can degrade the layers of graphene due to the interaction of the plasma species and high-energy sputtered atoms. These sputtered atoms and plasma species induce disorders and defects in the graphene layers which can degrade graphene. The interaction of the plasma species with graphene was not studied for hybrids material obtained by low-pressure plasma deposition till date. Based on the unique properties of the graphene effort will be made to decorate graphene sheets with TiO_2 nanostructures using low-pressure plasma deposition for the improvement of the photo-catalytic activity. Nb_2O_5 is an n-type semiconductor used widely as a catalyst, gas sensing, energy storage, and other applications. Magnesium based hybrid materials are promising candidates for the hydrogen storage, because Mg has high volumetric and gravimetric hydrogen storage capacities.. It is believed that graphene which has high surface area serves as an ideal support for anchoring well-dispersed Mg nanoparticles for the improvement of its catalytic action toward the hydrogen dissociation.

My dissertation is composed of seven chapters, which are organized as follows; the chapter #1 gives an overview of the interaction of M and MO with graphene sheet and the application of the decorated graphene with M and MO nanostructures will be discussed. The Chapter#2 describes the experimental details used for the decoration of graphene sheets with M and MO

#Introduction

nanostructures. The basic principles of the growth and characterization techniques along with the analytical conditions are presented in this chapter. The chapter #3 describes the effect of the Nb₂O₅ nanostructures on the structural, chemical and electronic properties of graphite nanoplatelets (GNPs). Chapter # 4 focuses on the study of Nb₂O₅ effect on the structural, magnetic and chemical properties of graphene powders. Chapter # 5 describes the effect of crystalline Mg nanoparticles and crystalline film on the structural and chemical properties of graphene powder. Chapter # 6 deals with the influence of TiO₂ effect on the structural, chemical properties of graphene powders. In Chapter # 7 an exploration of potential applications of the deposited M and MO nanostructures onto graphene sheets is reported. Concluding remarks and future prospective are presented at the end of the thesis.

Chapter #1 Back ground and literature survey

Chapter # 1

Back ground and literature survey

1 Introduction

This chapter presents the basics of graphene which include band structure and some physical properties of graphene. The preparation methods of graphene based composite with M and MO nanostructures and types of defects induced in the structure of graphene by the interaction of metal and metal oxide nanostructures will be presented. The applications graphene based composite with M and MO will be discussed at the end of this chapter.

1.1 Graphene

Graphene is a 2D one-atom-thick planar sheet of sp^2 carbon bonded, which is organized in a honeycomb lattice structure. Graphene is one of the thinnest materials in the world. The structure of single layer graphene is hexagonal [1]. Graphene and diamond is an allotropic form of carbon, even though both have different physical properties. When single layer graphene wrapped, it forms 0D fullerenes and rolled it form 1D nanotube. Graphene layers can be stacked together to form crystal lattice of graphite and the stacking order of layers of graphene can be found in the form of highly ordered pyrolytic graphite (HOPG) or even the core of a pencil [2] as shown in Fig 1.1. In single carbon atom consist of four electrons in the outer shell. The graphene structure contains three sigma σ bonds and one π bond. The sp^2 hybridization present in sigma σ bonds with a mixture of the orbitals (s px, py), these orbitals providing a strong bonding force to a neighbor carbon atom. The fourth electron of the carbon is called pz electron and it makes the π bond. This pz electron are responsible for the half-filled band that allows freeing moving electron, due to this free moving electrons graphene exhibit the metallic characteristic [3].

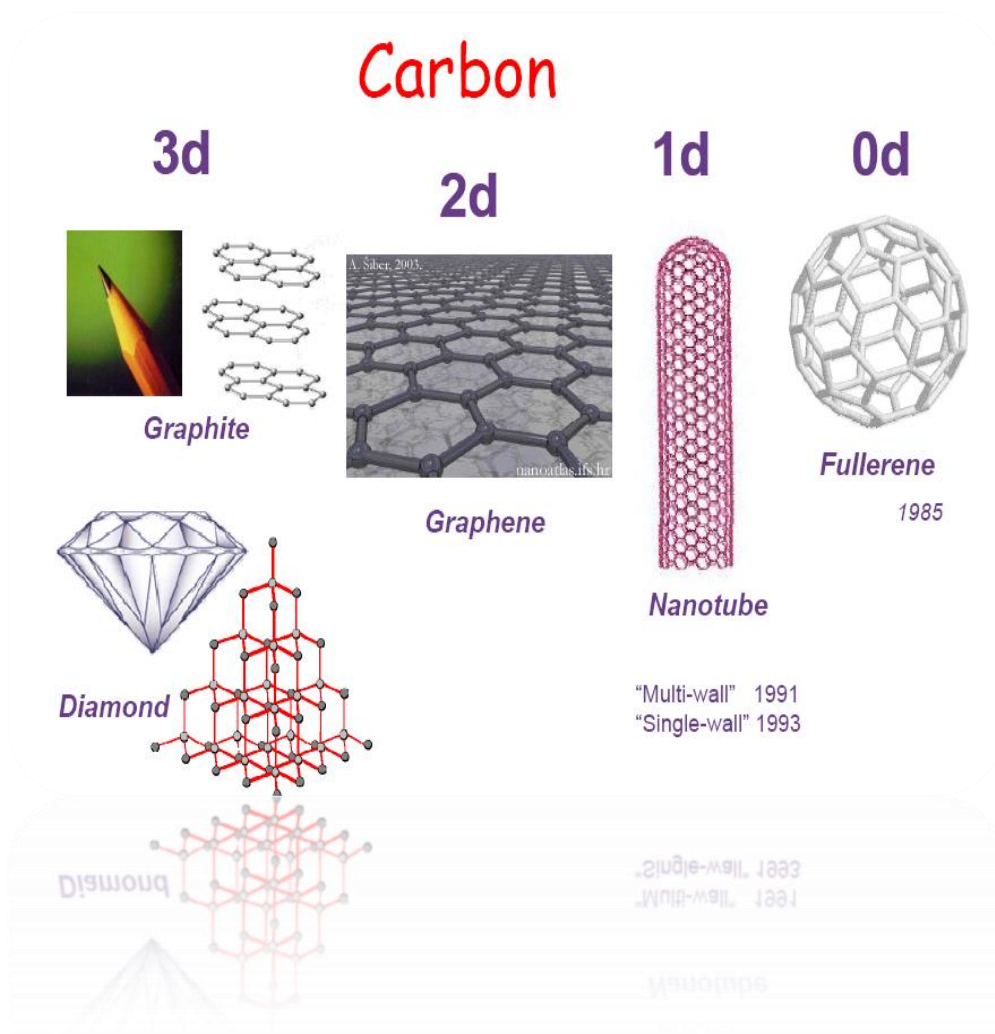


Fig 1. 1 Schematic diagram of the allotropic forms of carbon

Graphene surface can be modified with oxygen or hydrogen to form “graphane” or other carbonic materials respectively. Graphene displays astonishing properties. Graphene is more conductive than copper and stronger than diamond and having high flexibility than rubber. Due to the remarkable properties of graphene electrical, thermal and optical properties of graphene has attracted much attention in the field of science and technology [4,5,6,]. Graphene also presents the anomalous quantum phenomena [7] at room temperature, such as relativistic quantum Brownian motion, Klein tunneling [8-9] and the quantum Hall effect (QHE) [10]. For

Chapter #1 Back ground and literature survey

these phenomena graphene have also drawn much attention in the of field of quantum engineering [11, 12]

1.2 Band structure of graphene

Generally, for the semiconductor the electronic band is a parabolic shape with non-zero energy gap separated valance and conduction band [13, 14]. It is well understood that the band structure of the graphene cone like structure and there is no space between the valance and conduction band and this point is called Dirac point [15, 16]. Therefore, electrons can be excited from the valance band to the conduction band by means of small thermal fluctuation or with the application of small electric field [17]. The Fermi level of the graphene can increase or decrease with a variation of the applied electric field and due to this, the graphene displays metallic characteristics. More importantly, due to the zero band gap of graphene, there is the limited application of the graphene in semiconducting devices [18]. Consequently, the band gap opening of the graphene is the most significant assignment in making graphene transistor become a practical example. For this purpose, several approaches were made to create the gap in graphene in deformed structures of bi-layer graphene to work as a transistor channel [19, 20]. Moreover, recently it is well established that graphene oxide (GO) can provide a small band gap opening [21]. There are also so many other possibilities to open the band gap of graphene, it includes either physical strain or by bending of the graphene sheet and the schematic representation is illustrated in Fig 1.1. It is well established that, band gap property depends upon the width alignment of the graphene allotrope. The band gap of graphene can be opened by using chemical doping or either generate the defects in the structure of graphene as explained by Coletti et al. [22] and Terrones et al. [23]

Chapter #1 Back ground and literature survey

The sigma bond is one most strong bond, the addition of the M and MO is mostly placed onto the graphene sp^2 domains instead of replacing the carbon atom itself. Then dopant generates the defects and these defects can vary the electronic property of the graphene. Many dopants were used to modify the band structure of the graphene and the band structure can be controlled by means of dopant concentration. Some common dopants include gold, sulphur and many other metals.

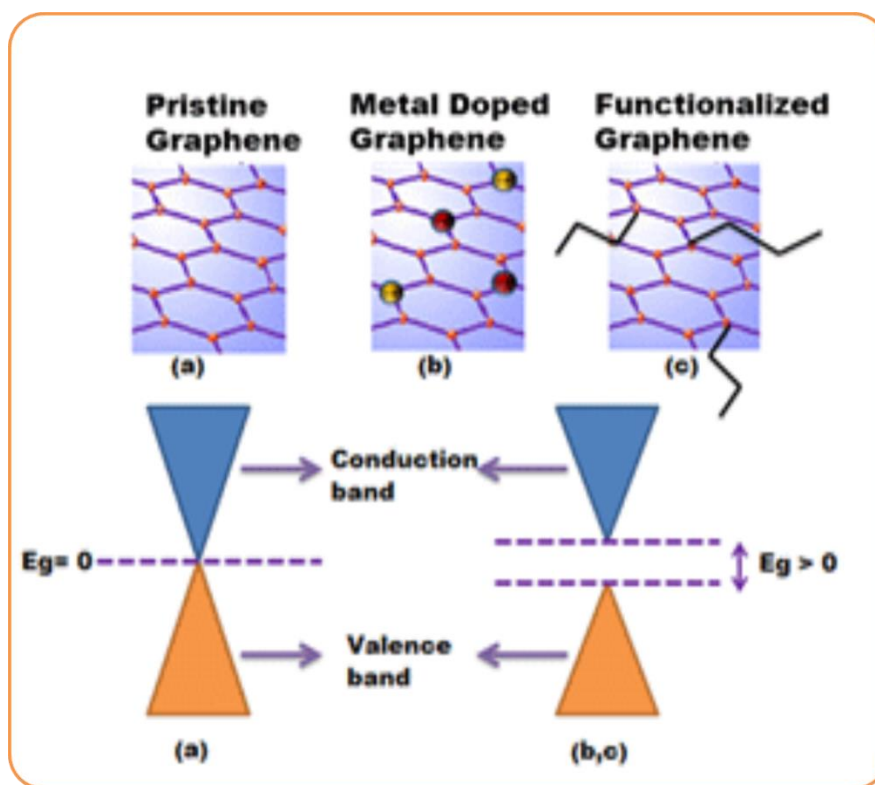


Fig 1. 2 Schematic diagram of the band structure of graphene and band opening

The mostly common and key compound for the band gap creation in graphene is Boron nitride (BN). Fet et al. have been described that, with random doping of BN onto graphene surface which is capable to modify the band structure and opening of the band gap [24]. The distribution of the surface charges (electron in π bond configuration) being modified with doping and subsequently a small gap is formed. Contrary the doping in graphene is sometimes not simple to

Chapter #1 Back ground and literature survey

control [25]. However, liu et al. reported a new route for the doping method, which is simpler and stable in term of opening the band gap [26].

1.3 Physical properties of graphene

1.3.1 Electrical Conductivity of graphene

The mobility of the graphene is depending on the interaction of the type material and interaction with substrate. It has been reported that mobility values after the annealing exfoliated graphene can reach upwards $200,000 \text{ cm}^2 \text{ V}^{-1} \text{ s}^{-1}$ in defects free structure of graphene [27, 28 29]. This measured valued of graphene is around double with respect to the value obtained for the conductance quantum wire [30]. This indicates that the charge carrier in graphene may execute long range (ballistic) transport without much scattering at all even at room temperature [31, 32]. Due to the strong resistance against the destruction and high elasticity of graphene, it is very useful material for the electronics application. For the graphene the Young's modulus value is around 1TPa. Graphene is one of the strongest material in the world, which is around 100 time stronger than steel [33]. More importantly the monolayer graphene can be stretched and bent rather easily.

1.3.2 Thermal Conductivity

Thermal conductivity of the material can be defined as the heat flux per unit area, (in W/m^2) to the temperature gradient, $Q'' = -\kappa \nabla T$. The thermal conductivity of suspended graphene is generally carried out by the ballistic phonons, it was found by using the high-resolution vacuum scanning thermal microscopy [34]. Accordingly, due to the number of scattering channels increase with substrate the thermal conductance of the graphene degrades significantly. It means that the heat may lose to the substrate. It is also well established that with increasing number of graphene layers the thermal conductance also decreased [35]. The value of thermal conductivity

Chapter #1 Back ground and literature survey

of graphene on the silicon dioxide substrate around $600 \text{ Wm}^{-1}\text{K}^{-1}$ is reported by Prasher et al [36], which much higher than copper. The in- plane thermal conductivity of the graphene is even higher values in order of $1,000 \text{ Wm}^{-1}\text{K}^{-1}$ [37, 38]. The dissipation of the heat flow between the graphene and the substrate can be influenced thermal of conductivity graphene. The acoustic phonon is responsible for the heat transport in plane of graphene. Though, the heat transport between the graphene and substrate interface in the cross plane direction is currently unidentified as described by Koh et al. [39].

1.3.3 Optical properties of graphene

Single layer graphene is almost transparent and absorbed only mere $\pi\alpha \approx 2.3\%$ of visible light (where $\alpha = 1/137$ is the fine structure constant [40]. This indicates that the graphene is highly transparent and the transparency of the single layer graphene is 97.7 %. The absorption of graphene is almost independent of wavelength range. Therefore, graphene is a suitable material for the photonic devices. Due to the high transparency of the graphene in the visible range, it can be used to make small screen devices. Additionally, for the same scenario the graphene has a true potential to use it in opto- electronics devices, which is explained by Nair et al. [41]. Moreover, the optical luminance property was also observed in graphene by Stoehr et al. [42]. They described that the luminescence property arises in graphene due to the electron-hole recombination when it is created in a broad energy range [43].

1.4 Overview method of preparation of graphene and metal oxide composites

The role of graphene in the graphene-based composite as a supporting material for the metal or metal oxide or acts as a functional component. The large surface areas and the conductive strong structure of graphene frequently enable the charge transfer, redox reaction, as well as strength the mechanical properties of resulting of the interaction of metal oxide graphene composites.

Chapter #1 Back ground and literature survey

Therefore, anchoring of metal and metal oxides nanostructures onto graphene sheet improve the various kinds of properties of graphene in terms of storage of energy, catalytic energy conversion, and magnetic properties etc.[^{44, 45, 46, 47, 48, 49}]. In this study, we mainly focus on recently developed methods for synthesis or decoration of high-quality graphene and metal oxide composite.

1.4 .1 Solution-based methods of graphene and metal oxide composites

The solution-based method is the efficient and direct method used for the preparation of the metal oxide and graphene composites. The solution-based method is a widely used method to prepare the graphene- metal oxide (MO) composite. Peak et al synthesized graphene and SnO₂ composite by solution mixing. They prepared the SnO₂ sol by hydrolysis of SnCl₄ with NaOH, and subsequently, the graphene was dispersed with SnO₂ sol in ethylene glycol to achieve the composite[⁵⁰]. The following strategy was also applied for the preparation of the Graphene–TiO₂ composites by Williams, et al. They mixed the commercialized TiO₂ nanoparticles with Nafion – coated graphene to assemble dye sensitized solar cell, the role of the Nafion as ‘glue’ to join the graphene and TiO₂ nanoparticle (P25) [⁵¹]. Likewise the TiO₂ nanoparticles were mixed using ultra sonication, then followed with ultraviolet-assisted photo catalytic reduction of GO to synthesized graphene–TiO₂ composites [⁵²].For the preparation of graphene–TiO₂ composite Akhavan et al. followed the same strategy [⁵³].

1.4 .2 Graphene and metal oxide composites prepared by Sol–gel method

Sol gel is one of the most efficient methods for the synthesis of metal oxide nanostructures and films. TiO₂ and Fe₂O₃ nanostructures were synthesized onto graphene sheet by sol gel method reported in the literature [^{54, 55, 56, 57, 58}]. The generally used precursor for the TiO₂ nanostructures are TiCl₄ , titanium butoxide [⁵⁹] and titanium isopropoxide [58], the result of these precursor

Chapter #1 Back ground and literature survey

comes in nanoparticles, nanorods, mesoporous nanostructures of the TiO_2 , which is highly depending on the different experimental conditions applied for the synthesis of TiO_2 nanostructures. Two step methods are used to obtain the TiO_2 nanocrystals onto graphene oxide sheet. In the first step of synthesis the amorphous TiO_2 nanostructures were decorated by hydrolysis and subsequently, the TiO_2 anatase nanocrystals were obtained by hydrothermal treatment. Due to the strong interaction of the graphene with TiO_2 nanostructure, the composite displays various applications, which includes photocatalysis and energy storage [60]. The graphene/mesoporous silica composite was established using the sol-gel approach to prepared 2D sandwich composite was reported by Mullen group [61]. Additionally, the mesoporous Co_3O_4 graphene composite was synthesized using the template of the mesoporous silica sheet by means of nano casting method. The key advantage of synthesis of graphene and MO composite by using the sol-gel method is that the graphene oxide or reduced graphene oxide offer reactive and anchoring sites for the nucleation and support the nanoparticles and as a result, the chemical bond between the graphene and metal oxide establish on the surface of GO/RGO.

1.4.3 Preparation of graphene and metal oxide by Hydrothermal/ solvothermal method

For the preparation of the organic nanocrystals structure material mostly Hydrothermal/solvothermal methods are used. The main advantage of the preparation of graphene and MO composite of the hydrothermal over the sol-gel is that the hydrothermal method is operated at evaluated temperature in a confined volume to produce large pressure. The one-pot hydrothermal/solvothermal route can give growth to nanostructures martial with high crystallinity without any calcination or post-synthetic annealing. Additionally, this method is also used to reduce graphene oxide. Many MO graphene composite prepared by using the hydrothermal or solvothermal method. Shen et al. prepared the graphene and TiO_2 composited

Chapter #1 Back ground and literature survey

by using the hydrothermal method. They used the reduced graphene oxide and TiO₂ composite in water and the graphene oxide used as a precursor for the reduced graphene oxide and the precursor used for the TiO₂ is tetra butyl titanate under hydrothermal condition [62]. More importantly the hydrothermal process is very simple and can be compatible for the industry applications. The crystal defects in the graphene- TiO₂ composite can be controlled by means of varying the experimental parameters such precursor concentration solution and time of reaction. The hydrothermal method can be used to synthesize the other metal oxide nanostructures onto graphene sheet such Fe₃O₄, Co₃O₄, and SnO₂ nanostructures. The porous and very thin nanostructure arrays of the Co₃O₄ onto graphene sheet have been developed by using the facile hydrothermal process [63]. More likely, the compositions, grain size and surface area of the graphene and MO composites can be tuned by controlling the hydrothermal treatment parameters or annealing processes. The prepared graphene and MO composite can be used in different kinds of application such as the lithium-ion batteries and energy conversion etc. Huang et al used a one-step solvothermal synthesis of graphene and SnO₂ composites [64]. They distributed the SnO₂ nanocrystals uniformly on the graphene sheet by means of the solvothermal method. Some authors also reported the MO graphene composite other than the mention of the method [65].

1.5 Decoration of graphene with metal oxide by Atomic layer deposition

The Atomic layers deposition (ALD) is one of the efficient and capable techniques used to deposit ultrathin layers or mostly MO, metal (M) and other coating materials onto the substrate surface. Due to the precise film thickness obtained by means of ALD technique has got much attention in many technological, academic researcher and industrial applications. For the most of the nanoelectronic devices very thin layers and controlled deposition of the uniform, layers are required. For this purpose, the ALD is the suitable technique to produce such kind of ultra-thin

Chapter #1 Back ground and literature survey

layers films. Several research group was used the ALD technique for the deposition of the metal oxide thin film onto graphene sheet. Meric et al deposited the HfO₂ layers onto graphene by using the ALD technique [66]. The deposition metal oxide film onto graphene sheet is not very easy because there are no dangling bonds on the graphene surface by using ALD process. Moon et al also deposited a very thin layer of Al₂O₃ onto graphene directly by ALD process and they used the obtained composite for the top gated device to present good performance [67]. Wang et al also used the ALD technique to deposit 2 nm thin layers of Al₂O₃ onto exfoliated graphene sheets and the exfoliated graphene sheets were cleaned in Argon atmosphere at 600 °C. They used the vapor of trimethylaluminum (TMA; Al(CH₃)₃) and water used as a precursor to obtained thin layer of Al₂O₃ on graphene at 100 °C [68]. A similar strategy was also applied to deposit the Al₂O₃ and HfO₂ thin layer onto the surface of Highly Ordered Pyrolytic Graphite (HOPG) by Xuan et al. They obtained large number of nanoribbons of Al₂O₃ more than 50 μm in length and with the dimensions of 5 - 200 nm in width [69].

1.6 Choice of the materials for the decoration of graphene sheets.

1.6.1 Properties of Nb₂O₅

Recently Nb₂O₅ has got much attention in scientific area of research due to its excellent chemical stability with respect to the other oxides [70]. Nb₂O₅ is a wide band gap semiconductor having band gap of 3.2 eV [71]. Therefore, Nb₂O₅ has much potential to replace other oxide semiconductor in the different kinds of application. In this scenario, Nb₂O₅ based materials have presented substantial concern in the field of gas sensing and catalysis [72, 73]. Nb₂O₅ is also one of the impotent material for its desirable properties, which includes high refractive (n = 2.4 at 550 nm), high transparency and low absorption in the UV-vis –NIR and for this Nb₂O₅ is a widely used material in solar cell and bright windows [74]. It is also used for improving the

Chapter #1 Back ground and literature survey

optical performance of optical devices such as waveguide based optics and optical filters [75, 76]. Beside these properties, Nb₂O₅ present good electrical and magnetic properties and these properties can be improved by the addition of foreign impurities [77, 78]. Recently it is reported that Nb₂O₅ used for the electrode material in electrochemical applications [79].

1.6.2 Characteristic of TiO₂

Due to the astonishing physical and chemical properties of the TiO₂, it is a widely used material in different kinds of application. TiO₂ is extensively studied material in many scientific fields, which includes photocatalysis, electrolysis and photovoltaic cells [80, 81], where the TiO₂ is taken as active part for the solar energy conversion. TiO₂ has a high refractive index and it makes it a suitable candidate for the transparent conducting oxide and other optical applications [82, 83]. TiO₂ has also many potential applications in the field of ceramics and medical application. In the medical perspective, the TiO₂ plays a vital role in the biocompatibility of bone implants [84]. Due to the chemical stability at high temperature, TiO₂ shows good sensing characteristics toward the CO [85], Hydrogen [86], methane and ethanol [87, 88]. TiO₂ nanostructures show good magnetic properties with some metal doping [89]. TiO₂ is also widely used as an anode material for the lithium ions batteries [90].

1.6.3 Properties of Mg nanostructure

A useful substitute for the safe and efficient source of energy carrier is much needed to use as fossil fuels. [91]. In this scenario, light metal hydrate, such as MgH₂ is one the most prominent candidates used for the hydrogen storage application, because of its high volumetric and gravimetric hydrogen storage capacity (7.6 wt % H₂ and 110 kg H₂/m³ for MgH₂) [92]. Though, due to the slow kinetics and operating at high temperature for hydrogen absorption/desorption the practical use of MgH₂ are limited. To solve this issue regarding of slow kinetic and improve

Chapter #1 Back ground and literature survey

the hydrogen sorption properties at minimum temperatures, the nanoscale sizes Mg nanoparticles will be prepared. Recently, the enhancement of the hydrogen storage capacity and more rapid kinetics have been reported for the prepared Mg nanoparticle and nanocomposites [93]. Moreover, the reaction between Mg and hydrogen is one of most extensively used reaction for the hydrogen storage.

1.7 Review of the preparation study of transition metal oxide and graphene composite.

As discussed in the above section, MO and graphene composite can be prepared by wet chemistry methods and physical vapor deposition techniques. It has been reported that transition MO have got much attention in the field of organic electronic devices, because of its high work function values when it is inserted between the anode and organic layers would decrease the interfacial hole injection barriers [94, 95, 96]. Mostly used transition metal oxides for the hole injection layers (HILs) in organic electronic devices are V_2O_5 , WO_3 , and MoO_3 [97, 98, 99, 1317]. Jens Meyer et al deposited the molybdenum trioxide (MoO_3) layers onto graphene sheet by thermal evaporation and used the graphene and (MoO_3) interface for Efficient Organic Light Emitting Diodes [100]. Qi-Hui Wu et al is also studied the graphene and (MoO_{3-x}) interface for the Efficient Organic Light Emitting Diodes [101]. Recently very few studies have been done for the preparation of the transition Nb_2O_5 and graphene composite for the numerous kind of application. Jussara F. Carneiro et al prepared the Nb_2O_5 and reduced graphene oxide by using the hydrothermal method for the H_2O_2 electro generation [102]. They prepared the graphene oxide from the graphite flakes by modified hummer's method, subsequently the graphene oxide reduction and the synthesis of Nb_2O_5 nanoparticles supported on the reduced graphene oxide by hydrothermal method. Mahmood Jamil et al also prepared graphene- Nb_2O_5 composite material by hydrothermal method for the dye sensitized solar cell (DSSCs) [103]. Similar method was also

Chapter #1 Back ground and literature survey

employed by the Paulraj Arunkumar et al for the graphene and Nb₂O₅ nanoparticles composite for the electrochemical storage. They synthesized Nb₂O₅ nanoparticles of size 50 nm and decorated onto graphene sheets homogenously. They used very low content of graphene sheets of (4.5 wt. %) with high conducting Nb₂O₅ composite prepared by hydrothermal method. They used the prepared composite for the electrochemical characterizations, which include cyclic voltammetry, electrochemical impedance spectroscopy and galvanostatic charge/discharge [¹⁰⁴]. Luyuan Paul Wang et al used the graphene and Nb₂O₅ composite for the High-performance hybrid electrochemical capacitor[¹⁰⁵]. Litao Yan, et al is also prepared graphene and Nb₂O₅ composite by using the hydrolysis method for the application of high performance sodium ion battery¹⁰⁶.

1.8 Review of the preparation study of Mg and graphene based hybrid materials,

As discussed in the above section that, Mg is one of vital element for the solid state hydrogen storage application. It is already discussed that, the graphene has high surface area and have potential to support metal nanostructures for the improvement of their catalytic activity. The majority reported data for the preparation of the M and carbon materials are via ball milling or chemical wet chemistry method or solidification [¹⁰⁷]. However, the preparation of the M and carbon based materials via ball milling process intrinsically produced unwanted morphological structures, chemical in-homogeneity in properties, which can reduce the performance of the composite. Therefore, new methods are required for the preparation of the metal and carbon based material for the improvement of the catalytic activities. Recently Eun Seon Cho et al synthesized the reduced graphene and Mg nanocomposites via a simple solution based co-reduction method. They used the Mg⁺² precursors dispersed onto graphene oxide sheets and subsequently reduced the graphene oxide by using the lithium naphthalenide. The synthesized

Chapter #1 Back ground and literature survey

composite were used for the hydrogen storage application and they found hydrogen storage capacity was 6.5 wt. % and 0.105 kg H₂ per liter in the total composite at 200 °C and 250 °C at 15 bar [¹⁰⁸]. Jun Zhang et al studied the hydrogen adsorption in Mg doped graphene oxide by using density functional theory calculation. They described that; hydroxyl group from the graphene oxide surface can be reduced by the addition of Mg. Theoretically; they found that eight H₂ molecules are adsorbed on each side of Mg-doped graphene oxide and obtained hydrogen storage capacity was 5.6 wt % at a temperature of 200 K [¹⁰⁹]. Recently Guanglin Xia et al used chemical method for the well dispersed MgH₂ nanoparticles onto reduced graphene oxide sheets. They discussed that, by reducing the particles size of Mg onto graphene sheets, the hydrogenation and dehydrogenation kinetics can be increased notably. They also found that by reducing the particles size of Mg nanoparticles, the kinetic of hydrogenation and dehydrogenation could achieve 85.5 % and 57.3 % of the theoretical value for the Mg nanoparticles [¹¹⁰]. Xiuyi Lin et al is also simultaneously dispersed Mg and Cl onto graphene oxide by using chemical route method for the improvement of the mechanical dielectric and electrical properties of the composite [¹¹¹].

1.9 Review of the preparation TiO₂ and graphene based hybrid materials

Recently the TiO₂ nanostructure and graphene sheet were extensively studied for the high performance of the photo catalytic of graphene TiO₂ composite and also to improve other properties of graphene. Different chemical and physical approaches were used to prepare the nano size TiO₂ structure onto graphene sheet. Md. Selim Arif Sher Shah et al used one step hydrothermal method for the composite of reduced graphene oxide and TiO₂ nanostructure without using reducing agent [¹¹²]. They measured the photo catalytic activities of the prepared composite for the degradation of rhodamine B dye. They also observed that composite can

Chapter #1 Back ground and literature survey

degrade colorless dye such as benzoic acid under visible light. Lanbing Gu, et al adopted the same method for the preparation of graphene and TiO₂ nanostructure composite, but followed some modification with facile glucosamine assisted hydrothermal strategy in alkaline conditions, the obtained results indicate that with addition of glucosamine, which play an important role for the dispersion of the TiO₂ nanoparticles onto graphene^[113]. They measured photo catalytic performances of the prepared composite for the degradation of three kinds of dyes, which include the rhodamine B (RhB), methylene blue (MB) and methyl orange (MO) under UV light irradiation. Wan-Sheng Wang et al used one step solvothermal method for the graphene and high quality anatase ultrathin TiO₂ nanosheets^[114]. They observed that the prepared composite of graphene and ultrathin TiO₂ nanoparticles present high photo catalytic activity with respect to pure TiO₂ and P25. Nguyen-Phan et al illustrates that the hydrogenated graphene and TiO_{2-x} nanocomposites used as photocatalyst for the production of H₂ and O₂ from water, without any assistance of noble metal co-catalyst ^[115]. The charge transfer phenomenon between the graphene and TiO₂ composite has been explained by Aijun Du, etal^[116]. They described by using the ab initio calculation and observed the charge being transferred from graphene to TiO₂ as the consequence of large work function difference, which lead to significant hole doping in graphene. Yaxin Zhang et al using the hydrothermal method for the preparation of the TiO₂ and graphene composite, this exhibits that, the prepared composite shows high photo catalytic activity for the degradation of the sodium pentachlorophenol ^[117]. Zahra Gohari Bajestani et al prepared graphene with different concentration levels of TiO₂ nanoparticles by simple chemical method. They used the prepared composite for the hydrogen storage application at room temperature and pressure upto 10 bars. The reported hydrogen capacity for the graphene and TiO₂ composite was measured upto 0.39 wt% at room temperature ^[118]. Surajit Kumar Hazr et al

Chapter #1 Back ground and literature survey

used the TiO₂ and graphene composite for the chemical sensor [119]. Ying-Na Changa et al adopted a simple chemical method for the preparation of the TiO₂ and graphene composite for the magnetic and antibacterial properties under solar irradiation. They reported that magnetic graphene oxide and TiO₂ composite displayed a high antibacterial activity against Escherichia coli[120].

1.10 Defects in Graphene structure

Generally, defects in materials are measured to be unfavorable to the properties of materials and device based on such materials. However, defects in materials can also be useful in providing the dopant control both their carrier concentration and whether the carriers are n-type or p-type [121, 122]. Commonly one can refer to that defect in graphene that breaks the symmetry of the sp² bonded carbon atom in honeycomb lattice. The symmetry of graphene plane structure can break with the defects induced in the plane of graphene, which includes point defects, such as vacancies [123, 124, 125] substitutionally impurities, [126, 127] interstitial impurities^{128, 129} and the impurity can be a chemical impurity or an isotopic impurity [130, 131]. Mostly grain boundary defects were observed in graphene by using the chemical vapor deposition method for its preparation and the grain boundary defects also occur, when the graphene was mechanically, exfoliated but there are some differences found by comparing the two of graphene¹³². The grain boundaries of the graphene or edge defects also break the symmetry of graphene and these boundaries serve as scattering centers for electron and phonons.[133, 134]. Accordingly, also some defects present in the interlayer spacing when the graphene sheets were synthesized for the specific application, such as stacking faults within interlayer stacking, different chemical arrangement and the arrangement of the isotopic interplaner. Various kind of experimental techniques are used to understand the influence of the different defects in the graphene system,

Chapter #1 Back ground and literature survey

for the information driven from the atomic level structural of graphene characterized by high-resolution transmission electron microscopy^[135], spectroscopic information derived from Raman and scanning tunneling spectroscopies ^[136]. It is well known that, the structural defects are associated with both naturally occurring imperfections and growth induced defects. The structural defects which induced in the structural of graphene include cluster defects ^[137], boundaries or edges and point defects and these defects lowering the symmetry of the graphene crystal. The point defects occur in the plane of graphene in the form lattice vacancies and impurity atoms. These impurities onto graphene plane can be either in interstitial or substitutional and these impurities can be in the form of isotopic impurities ^[131, 138] These impurities normally perturb the phonon spectra. Impurities, which are in the form of foreign dopant (species), tend to generate strain and local electric fields, because of the small size of the carbon atoms in graphene planes relatively to all other dopant species. The size of boron atom is smaller than the size of carbon, which is spherical impurity atom that establishes a normal p-type dopant for graphene. Interestingly, Fluorine or hydrogen mostly either to physisorb onto graphene sheets in the defects site ^[139] and when fluorine is added to graphene in high concentration its forms covalent bond with graphene. Additionally, the defects can strongly influence the properties of graphene and defects can vary with the preparation and production methods. ,.

1.11 Applications of graphene hybrid based materials

1.11.1 Graphene and TiO₂ based photo catalytic application

In the above section, we discussed different approaches for the preparation of graphene and TiO₂ nanocomposites for the enhancement of the photo catalytic properties. The access of the purifying water for the human and other domestic uses has become a current issue around the

Chapter #1 Back ground and literature survey

world. Huge amount of the organic pollutants are introduced by various commercial and agricultural activities, which are regularly unrestricted into the eco-system. These organic pollutants are commonly toxic and can cause seriously health and environmental problems. In the past, much research has been done on these issues to remove these organic pollutants from the wastewater, which include biological treatment, coagulation, ultrafiltration and ion exchange. These approaches have some advantages, but these methods are not very efficient for a number of applications. Semiconductor photocatalysts have been got much attention toward the enhancement of the photocatalytic activity.

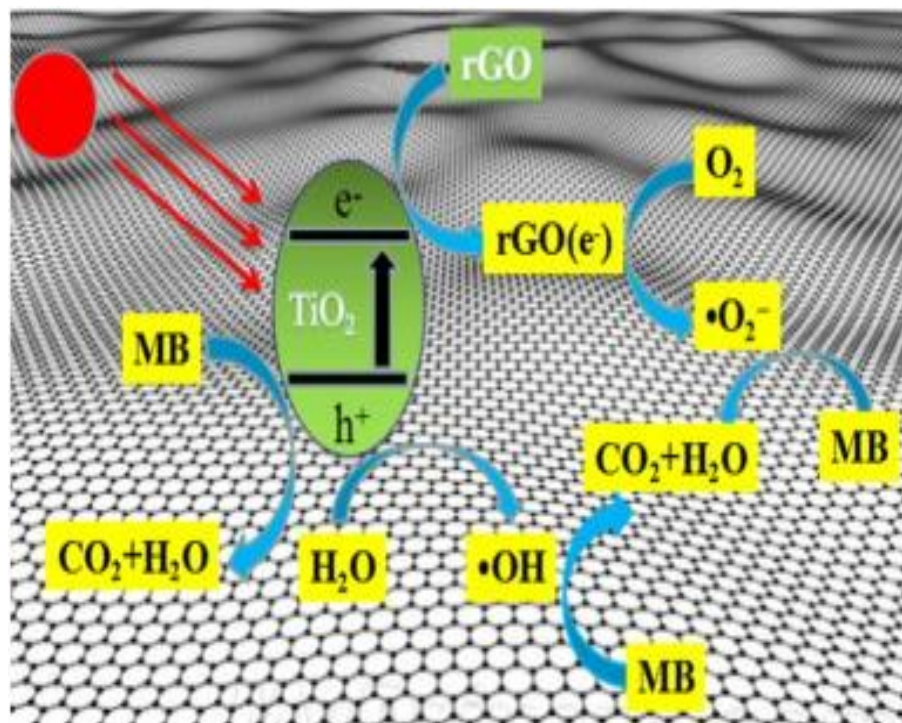


Fig1.3 Schematic diagram of TiO₂ and graphene based material for photocatalytic application

Titanium dioxide (TiO₂) is a very important and suitable semiconductor, which has been an extensively, used materials for the improvement of the photocatalytic properties due to its

Chapter #1 Back ground and literature survey

nontoxicity, low cost and high chemical stability. However the large band gap of the anatase TiO_2 (3.2 eV) restricts its photocatalytic properties to the limit range of the ultraviolet (only about 3– 5% of total sunlight). In this situation the electrons and holes can easily recombine before emigrates to the photocatalyst surface, which considerably reduced the photocatalytic efficiency. Recently, it has been well established that, graphene has high potential for the improvement of the photocatalytic activity due to its unique properties, such as high surface area, high transparency, huge electrical conductivity and good interfacial contact with adsorbents [140, 141]. Due to this large surface area of graphene can modify the surface properties of graphene, and then graphene is an anticipated material for the heterogeneous growth for the guest material. It is also a well interesting fact that, the surface function groups onto graphene sheets such as hydroxyl group act as favorable nucleation sites for the guest materials. The viable growth of nucleated clusters onto graphene sheets may modify the size and the structure of the final nanoclusters. More importantly, the well dispersed growth of the anatase TiO_2 nanoparticles onto graphene sheets is also a big challenge, however in some cases of nucleating nanoparticle or nanocrystals onto graphene sheets has been described [140, 142]. Furthermore, due to the high electrical conductivity of the graphene is one most suitable material in promoting electron transfer in photocatalytic reactions and electrochemical process. Therefore, the well dispersed nanosized mesoporous anatase TiO_2 nanoparticles onto graphene sheets are well appropriate composite for the improvement of the photocatalytic activity and application and the result is presented in Fig 1.3 [143].

1.11.2 Magnetic properties of graphene based hybrid materials

In the above section, we discussed that graphene has numerous exceptional properties in wide range of field, which includes microelectronics, sensor and superconductor energy storage and

Chapter #1 Back ground and literature survey

other so many. Several observations have been reported about the existence of ferromagnetic in long range of ordering in carbon based materials [¹⁴⁴,¹⁴⁵,¹⁴⁶,¹⁴⁷]. Induced ferromagnetic behavior in highly oriented graphite is related to the lattice imperfection, as reveal that graphite has shown the ferromagnetic behavior by proton irradiated and also the ferromagnetic signal enhanced in prepared pyrolytic graphite, which contained high defects concentration. In addition ferromagnetic behavior has been also observed in other carbon based materials, which includes carbon nanofoams ¹⁴⁸, proton-irradiated thin carbon films ¹⁴⁹ and carbon-ion-implanted nanodiamond ¹⁵⁰. All these observations indicate that, the carbon based materials possess ferromagnetic behavior [¹⁵¹]. Recently, it is well established that magnetism was observed in doped or defective graphene and graphene oxide [¹⁵²,¹⁵³,¹⁵⁴]. It was observed by Wang, Y. et al. that graphene shows a ferromagnetic behavior at room temperature. They explained that the very few contaminations such as (Fe, Ni) are responsible for the ferromagnetic behavior of the graphene at room temperature [¹⁵⁴]. Generally, different types of defects are responsible for the magnetic properties in the carbon based materials. However, the magnetic behavior details can be varied for different structures such as (graphene nanotubes, fullerenes and graphite based composite). Commonly, structural defects, which occurred in graphene based materials, are vacancy, atom at the edges, and adatoms. These structural defects induced the magnetic behavior in the graphene sheets. Moreover, the structural defects give rise to localized electronic states, a net magnetic moment, and an increase in the density of states at the Fermi level, and eventually to the development of magnetic order. Largely, the d and f elements are mostly used magnetic materials in the present technological applications. Additionally, the magnetic nanoparticle has got much attention in various sectors of applications, such as data storage [¹⁵⁵], catalysis [¹⁵⁶] and magnetic resonance imaging [¹⁵⁷]

Chapter #1 Back ground and literature survey

etc. In current scenario, the good dispersion of magnetic nanoparticles onto reduced graphene oxide sheets potentially provides a new path to develop unique catalytic, electrode and magnetic materials [158]. For the nanoscience and nanotechnology, the magnetic nanomaterials are the most forefronts and fast emerging fields in many fields of applications. Besides, it is also reported theoretically, that the atomic scale defects induced in graphene based material by foreign impurities and vacancies in the graphene can generate the magnetic moment of about one Bohr magneton, μ_B [156,159]. Additionally, the prospect of the long range magnetic ordering of graphene based material is established by the randomly dispersed grain boundaries and point defects [160, 161], and the ferromagnetism of the bi layer graphene was proposed by the spontaneous many-body system [162].

1.11.3 Hydrogen storage in graphene based material

For the renewable energy storage, hydrogen is one of the environmentally friendly energy sources and has pronounced potential to substitute the non-renewable other hydrocarbons for the energy carrier and transport application. For the replacement of the hydrocarbons, hydrogen is one of the best 'green' fuels, due to its light weight, very simple structure, nontoxic and one of abundant elements in the world. Hydrogen is a clean energy source and the high energy density with no emission of CO_2 gas. Compared to the other commonly used fuels, hydrogen has highest energy density by mass. The heating value of hydrogen is 140 MJ.kg^{-1} , which is three times greater than that of the gasoline. [163]. However, two simple steps are required to employ the molecular hydrogen as energy carrier, so called hydrogen storage and hydrogen production. First to describe the hydrogen production, in the universe less than (1 %) isolated hydrogen H_2 exists. H_2O is the main source for the production of hydrogen and also found some other compounds such as ammonia (NH_3), or hydrocarbons. Now secondly, appropriate material or surfaces are

Chapter #1 Back ground and literature survey

still needed for the reversible hydrogen storage and also become economically feasible for all intended applications. Carbon based materials such as carbon nanotubes, metal organic frameworks graphite nanofibers are the most favorable candidates for the hydrogen storage application, because of its many remarkable properties such as high specific area, stability for the large scale production, fast kinetics, which can tune the pore structure, low density and these material are mostly studied for hydrogen storage application. Big challenge for the hydrogen storage media in carbon based material is to find a structure, whereas the structures can tunable porosity and having high surface area and also provide a feasible surface for the absorption of hydrogen, which is thermodynamically stable and not too strongly so that reversible fast kinetics are possible [164]. Recently, graphene got much attention for the hydrogen storage application due to its remarkably properties such as unique 2D structure, high surface area which is theoretically measured about to 2630 m²/g a much higher surface area with respect to the other carbon based structures.. More importantly, in order to improve the hydrogen storage capacity at feasible condition, different approaches were studied theoretically for the functionalization of graphene. The most appropriate effort has been devoted to examine the role of the functionalized elements to improve the hydrogen storage capacity at viable pressure condition and room temperature. Several other theoretically methods were studied to improve both binding and gravimetric/volumetric storage capacity, because there is weak interaction between the graphene and molecular hydrogen. One approach for the enhancing of the hydrogen storage capacity is the chemical decoration of the alkali metals onto graphene sheets, such as Li, Na and K. It was found that decoration of graphene with Li nanostructure, which can adsorb four hydrogen molecules and reached the gravimetric hydrogen storage density above 10 wt% [165]. Moreover, a remarkable experimental result was achieved by the reduction of graphene oxide with decorated

Chapter #1 Back ground and literature survey

palladium atom. An enhancement of the gravimetric density at room temperature from 0.6% to 2.5% at 30 bars was obtained and the hydrogen molecules were dissociated to a spillover mechanism through Pd atoms followed by H passage onto the graphene sheet [¹⁶⁶].

1.12 References

- 1 Wallace, P. R. The band theory of graphite. *Physical Review* **71**, 622 (1947).
- 2 Savage, N. Materials science: Super carbon. *Nature* **483**, S30-S31 (2012).
- 3 Heyrovská, R. Atomic structures of graphene, benzene and methane with bond lengths as sums of the single, double and resonance bond radii of carbon. *arXiv preprint arXiv:0804.4086* (2008).
- 4 Fan, Y. *et al.* Preparation and electrical properties of graphene nanosheet/Al₂O₃ composites. *Carbon* **48**, 1743-1749 (2010).
- 5 Balandin, A. A. Thermal properties of graphene and nanostructured carbon materials. *Nature materials* **10**, 569-581 (2011).
- 6 Falkovsky, L. in *Journal of Physics: Conference Series*. 012004 (IOP Publishing).
- 7 Novoselov, K. S. *et al.* Room-temperature quantum Hall effect in graphene. *Science* **315**, 1379-1379 (2007).
- 8 Pototsky, A., Marchesoni, F., Kusmartsev, F. V., Hänggi, P. & Savel'ev, S. E. Relativistic Brownian motion on a graphene chip. *The European Physical Journal B-Condensed Matter and Complex Systems* **85**, 1-8 (2012).
- 9 Beenakker, C. Colloquium: Andreev reflection and Klein tunneling in graphene. *Reviews of Modern Physics* **80**, 1337 (2008).
- 10 Zhang, Y., Tan, Y.-W., Stormer, H. L. & Kim, P. Experimental observation of the quantum Hall effect and Berry's phase in graphene. *Nature* **438**, 201-204 (2005).
- 11 Guinea, F., Katsnelson, M. & Geim, A. Energy gaps and a zero-field quantum Hall effect in graphene by strain engineering. *Nature Physics* **6**, 30-33 (2010).
- 12 Gui, G., Li, J. & Zhong, J. Band structure engineering of graphene by strain: First-principles calculations. *Physical Review B* **78**, 075435 (2008).
- 13 Iyechika, Y. Application of graphene to high-speed transistors: expectations and challenges. *Sci. Technol. Trends* **37**, 76-92 (2010).
- 14 Schwierz, F. Graphene transistors. *Nature nanotechnology* **5**, 487-496 (2010).
- 15 Novoselov, K. S. *et al.* Electric field effect in atomically thin carbon films. *Science* **306**, 666-669 (2004).

Chapter #1 Back ground and literature survey

- 16 Geim, A. K. & Novoselov, K. S. The rise of graphene. *Nature materials* **6**, 183-191 (2007).
- 17 Avouris, P., Chen, Z. & Perebeinos, V. Carbon-based electronics. *Nature nanotechnology* **2**, 605-615 (2007).
- 18 Gilje, S., Han, S., Wang, M., Wang, K. L. & Kaner, R. B. A chemical route to graphene for device applications. *Nano letters* **7**, 3394-3398 (2007).
- 19 Xia, F., Farmer, D. B., Lin, Y.-m. & Avouris, P. Graphene field-effect transistors with high on/off current ratio and large transport band gap at room temperature. *Nano letters* **10**, 715-718 (2010).
- 20 O'hare, A., Kusmartsev, F. & Kugel, K. A Stable "Flat "Form of Two-Dimensional Crystals: Could Graphene, Silicene, Germanene Be Minigap Semiconductors? *Nano letters* **12**, 1045-1052 (2012).
- 21 Dreyer, D. R., Ruoff, R. S. & Bielawski, C. W. From conception to realization: an historical account of graphene and some perspectives for its future. *Angewandte Chemie International Edition* **49**, 9336-9344 (2010).
- 22 Coletti, C. *et al.* Charge neutrality and band-gap tuning of epitaxial graphene on SiC by molecular doping. *Physical Review B* **81**, 235401 (2010).
- 23 Terrones, H., Lv, R., Terrones, M. & Dresselhaus, M. S. The role of defects and doping in 2D graphene sheets and 1D nanoribbons. *Reports on Progress in Physics* **75**, 062501 (2012).
- 24 Ozyilmaz, B., Ahn, J.-H., Hong, B. H. & Iijima, S. Roll-to-roll production of 30-inch graphene films for transparent electrodes. (2010).
- 25 Geim, A. K. Graphene: status and prospects. *Science* **324**, 1530-1534 (2009).
- 26 Liu, H., Liu, Y. & Zhu, D. Chemical doping of graphene. *Journal of Materials Chemistry* **21**, 3335-3345 (2011).
- 27 Sarma, S. D., Adam, S., Hwang, E. & Rossi, E. Electronic transport in two-dimensional graphene. *Reviews of Modern Physics* **83**, 407 (2011).
- 28 Morozov, S. *et al.* Giant intrinsic carrier mobilities in graphene and its bilayer. *Physical review letters* **100**, 016602 (2008).
- 29 Kusmartsev, F. & Tselik, A. Semimetallic properties of a heterojunction. *JETP lett* **42** (1985).

Chapter #1 Back ground and literature survey

- 30 Datta, S. *Electronic transport in mesoscopic systems*. (Cambridge university press, 1997).
- 31 Du, X., Skachko, I., Barker, A. & Andrei, E. Y. Approaching ballistic transport in suspended graphene. *Nature nanotechnology* **3**, 491-495 (2008).
- 32 Bolotin, K. I. *et al.* Ultrahigh electron mobility in suspended graphene. *Solid State Communications* **146**, 351-355 (2008).
- 33 Cao, A. *et al.* A Facile One-step Method to Produce Graphene–CdS Quantum Dot Nanocomposites as Promising Optoelectronic Materials. *Advanced materials* **22**, 103-106 (2010).
- 34 Hinz, M., Marti, O., Gotsmann, B., Lantz, M. & Dürig, U. High resolution vacuum scanning thermal microscopy of Hf O 2 and Si O 2. *Applied Physics Letters* **92**, 043122 (2008).
- 35 Shahil, K. M. & Balandin, A. A. Graphene–multilayer graphene nanocomposites as highly efficient thermal interface materials. *Nano letters* **12**, 861-867 (2012).
- 36 Prasher, R. Graphene spreads the heat. *Science* **328**, 185-186 (2010).
- 37 Balandin, A. A. *et al.* Superior thermal conductivity of single-layer graphene. *Nano letters* **8**, 902-907 (2008).
- 38 Seol, J. H. *et al.* Two-dimensional phonon transport in supported graphene. *Science* **328**, 213-216 (2010).
- 39 Koh, Y. K., Bae, M.-H., Cahill, D. G. & Pop, E. Heat conduction across monolayer and few-layer graphenes. *Nano letters* **10**, 4363-4368 (2010).
- 40 Piper, J. R. & Fan, S. Total absorption in a graphene monolayer in the optical regime by critical coupling with a photonic crystal guided resonance. *ACS Photonics* **1**, 347-353 (2014).
- 41 Nair, R. R. *et al.* Fine structure constant defines visual transparency of graphene. *Science* **320**, 1308-1308 (2008).
- 42 Stöhr, R. J., Kolesov, R., Pflaum, J. & Wrachtrup, J. Fluorescence of laser-created electron-hole plasma in graphene. *Physical Review B* **82**, 121408 (2010).
- 43 Bonaccorso, F., Sun, Z., Hasan, T. & Ferrari, A. Graphene photonics and optoelectronics. *Nature photonics* **4**, 611-622 (2010).

Chapter #1 Back ground and literature survey

- 44 Wu, Q., Xu, Y., Yao, Z., Liu, A. & Shi, G. Supercapacitors based on flexible graphene/polyaniline nanofiber composite films. *ACS nano* **4**, 1963-1970 (2010).
- 45 Hong, W., Xu, Y., Lu, G., Li, C. & Shi, G. Transparent graphene/PEDOT-PSS composite films as counter electrodes of dye-sensitized solar cells. *Electrochemistry Communications* **10**, 1555-1558 (2008).
- 46 Ng, Y. H., Iwase, A., Kudo, A. & Amal, R. Reducing graphene oxide on a visible-light BiVO₄ photocatalyst for an enhanced photoelectrochemical water splitting. *The Journal of Physical Chemistry Letters* **1**, 2607-2612 (2010).
- 47 Yang, S., Feng, X., Ivanovici, S. & Müllen, K. Fabrication of graphene-encapsulated oxide nanoparticles: towards high-performance anode materials for lithium storage. *Angewandte Chemie* **122**, 8586-8589 (2010).
- 48 Yang, N., Zhai, J., Wang, D., Chen, Y. & Jiang, L. Two-dimensional graphene bridges enhanced photoinduced charge transport in dye-sensitized solar cells. *ACS nano* **4**, 887-894 (2010).
- 49 Sun, Y. *et al.* Chemically converted graphene as substrate for immobilizing and enhancing the activity of a polymeric catalyst. *Chemical Communications* **46**, 4740-4742 (2010).
- 50 Paek, S.-M., Yoo, E. & Honma, I. Enhanced cyclic performance and lithium storage capacity of SnO₂/graphene nanoporous electrodes with three-dimensionally delaminated flexible structure. *Nano letters* **9**, 72-75 (2008).
- 51 Williams, G., Seger, B. & Kamat, P. V. TiO₂-graphene nanocomposites. UV-assisted photocatalytic reduction of graphene oxide. *ACS nano* **2**, 1487-1491 (2008).
- 52 孙盛睿 & 刘阳桥. Enhanced dye-sensitized solar cell using graphene-TiO₂ photoanode prepared by heterogeneous coagulation. (2010).
- 53 Akhavan, O. & Ghaderi, E. Photocatalytic reduction of graphene oxide nanosheets on TiO₂ thin film for photoinactivation of bacteria in solar light irradiation. *The Journal of Physical Chemistry C* **113**, 20214-20220 (2009).
- 54 Zhang, X.-Y., Li, H.-P., Cui, X.-L. & Lin, Y. Graphene/TiO₂ nanocomposites: synthesis, characterization and application in hydrogen evolution from water photocatalytic splitting. *Journal of materials chemistry* **20**, 2801-2806 (2010).

Chapter #1 Back ground and literature survey

- 55 Du, J. *et al.* Hierarchically ordered macro– mesoporous TiO₂– graphene composite films: improved mass transfer, reduced charge recombination, and their enhanced photocatalytic activities. *ACS nano* **5**, 590-596 (2010).
- 56 Wang, D. *et al.* Self-assembled TiO₂–graphene hybrid nanostructures for enhanced Li-ion insertion. *ACS nano* **3**, 907-914 (2009).
- 57 Li, B. *et al.* All-Carbon Electronic Devices Fabricated by Directly Grown Single-Walled Carbon Nanotubes on Reduced Graphene Oxide Electrodes. *Advanced materials* **22**, 3058-3061 (2010).
- 58 Zhou, G. *et al.* Graphene-wrapped Fe₃O₄ anode material with improved reversible capacity and cyclic stability for lithium ion batteries. *Chemistry of Materials* **22**, 5306-5313 (2010).
- 59 Tang, Y.-B. *et al.* Incorporation of graphenes in nanostructured TiO₂ films via molecular grafting for dye-sensitized solar cell application. *ACS nano* **4**, 3482-3488 (2010).
- 60 Liang, Y., Wang, H., Casalongue, H. S., Chen, Z. & Dai, H. TiO₂ nanocrystals grown on graphene as advanced photocatalytic hybrid materials. *Nano Research* **3**, 701-705 (2010).
- 61 Yang, S. *et al.* Graphene-Based Nanosheets with a Sandwich Structure. *Angewandte Chemie International Edition* **49**, 4795-4799 (2010).
- 62 Shen, J. *et al.* One step hydrothermal synthesis of TiO₂-reduced graphene oxide sheets. *Journal of Materials Chemistry* **21**, 3415-3421 (2011).
- 63 Zhu, J. *et al.* Cobalt oxide nanowall arrays on reduced graphene oxide sheets with controlled phase, grain size, and porosity for Li-ion battery electrodes. *The Journal of Physical Chemistry C* **115**, 8400-8406 (2011).
- 64 Wang, Z. *et al.* Crystal facets controlled synthesis of graphene@ TiO₂ nanocomposites by a one-pot hydrothermal process. *CrystEngComm* **14**, 1687-1692 (2012).
- 65 Qu, D. *et al.* Highly luminescent S, N co-doped graphene quantum dots with broad visible absorption bands for visible light photocatalysts. *Nanoscale* **5**, 12272-12277 (2013).
- 66 Meric, I. *et al.* Current saturation in zero-bandgap, top-gated graphene field-effect transistors. *Nature nanotechnology* **3**, 654-659 (2008).
- 67 Moon, J. *et al.* in *2009 Device Research Conference*.

Chapter #1 Back ground and literature survey

- 68 Wang, X., Tabakman, S. M. & Dai, H. Atomic layer deposition of metal oxides on pristine and functionalized graphene. *Journal of the American Chemical Society* **130**, 8152-8153 (2008).
- 69 Xuan, Y. *et al.* Atomic-layer-deposited nanostructures for graphene-based nanoelectronics. *Applied Physics Letters* **92**, 013101 (2008).
- 70 Yan, C. & Xue, D. Formation of Nb₂O₅ nanotube arrays through phase transformation. *Advanced materials* **20**, 1055-1058 (2008).
- 71 Le Viet, A., Jose, R., Reddy, M., Chowdari, B. & Ramakrishna, S. Nb₂O₅ photoelectrodes for dye-sensitized solar cells: choice of the polymorph. *The Journal of Physical Chemistry C* **114**, 21795-21800 (2010).
- 72 Wang, Y.-D., Yang, L.-F., Zhou, Z.-L., Li, Y.-F. & Wu, X.-H. Effects of calcining temperature on lattice constants and gas-sensing properties of Nb₂O₅. *Materials Letters* **49**, 277-281 (2001).
- 73 Braga, V. S., Dias, J. A., Dias, S. C. & de Macedo, J. L. Catalyst materials based on Nb₂O₅ supported on SiO₂-Al₂O₃: preparation and structural characterization. *Chemistry of Materials* **17**, 690-695 (2005).
- 74 Lin, H. *et al.* Er³⁺ doped Na₂O-Nb₂O₅-TeO₂ glasses for optical waveguide laser and amplifier. *Journal of Physics D: Applied Physics* **36**, 812 (2003).
- 75 Nishihara, H., Haruna, M. & Suhara, T. Optical integrated circuits. *New York*, 7-8 (1989).
- 76 Xiao, X. *et al.* Structure and optical properties of Nb₂O₅ sculptured thin films by glancing angle deposition. *Applied Surface Science* **255**, 2192-2195 (2008).
- 77 Wang, X. *et al.* High-Performance Supercapacitors Based on Nanocomposites of Nb₂O₅ Nanocrystals and Carbon Nanotubes. *Advanced Energy Materials* **1**, 1089-1093 (2011).
- 78 Sun, K., Lan, Z., Yu, Z., Li, L. & Huang, J. Grain growth and magnetic properties of Nb₂O₅-doped NiZn ferrites. *Japanese Journal of Applied Physics* **47**, 7871 (2008).
- 79 Özer, N., Chen, D.-G. & Lampert, C. M. Preparation and properties of spin-coated Nb₂O₅ films by the sol-gel process for electrochromic applications. *Thin Solid Films* **277**, 162-168 (1996).
- 80 Jagadale, T. C. *et al.* N-doped TiO₂ nanoparticle based visible light photocatalyst by modified peroxide sol-gel method. *The Journal of Physical Chemistry C* **112**, 14595-14602 (2008).

Chapter #1 Back ground and literature survey

- 81 Arango, A., Carter, S. & Brock, P. Charge transfer in photovoltaics consisting of interpenetrating networks of conjugated polymer and TiO₂ nanoparticles. *Applied Physics Letters* **74**, 1698-1700 (1999).
- 82 Liu, B. & Aydil, E. S. Growth of oriented single-crystalline rutile TiO₂ nanorods on transparent conducting substrates for dye-sensitized solar cells. *Journal of the American Chemical Society* **131**, 3985-3990 (2009).
- 83 Tian, Y. & Tatsuma, T. Mechanisms and applications of plasmon-induced charge separation at TiO₂ films loaded with gold nanoparticles. *Journal of the American Chemical Society* **127**, 7632-7637 (2005).
- 84 Kay, S., Thapa, A., Haberstroh, K. M. & Webster, T. J. Nanostructured polymer/nanophase ceramic composites enhance osteoblast and chondrocyte adhesion. *Tissue engineering* **8**, 753-761 (2002).
- 85 Buso, D., Post, M., Cantalini, C. & Mulvaney, P. Gold Nanoparticle-Doped TiO₂ Semiconductor Thin Films: Gas Sensing Properties. *Advanced Functional Materials* **18**, 3843-3849 (2008).
- 86 Tang, H., Prasad, K., Sanjines, R. & Levy, F. TiO₂ anatase thin films as gas sensors. *Sensors and Actuators B: Chemical* **26**, 71-75 (1995).
- 87 Lu, C. & Chen, Z. High-temperature resistive hydrogen sensor based on thin nanoporous rutile TiO₂ film on anodic aluminum oxide. *Sensors and Actuators B: Chemical* **140**, 109-115 (2009).
- 88 Garzella, C., Comini, E., Tempesti, E., Frigeri, C. & Sberveglieri, G. TiO₂ thin films by a novel sol-gel processing for gas sensor applications. *Sensors and Actuators B: Chemical* **68**, 189-196 (2000).
- 89 Matsumoto, Y. *et al.* Ferromagnetism in Co-doped TiO₂ rutile thin films grown by laser molecular beam epitaxy. *Japanese Journal of Applied Physics* **40**, L1204 (2001).
- 90 Ortiz, G. F. *et al.* Alternative Li-ion battery electrode based on self-organized titania nanotubes. *Chemistry of Materials* **21**, 63-67 (2008).
- 91 Turner, J. A. A realizable renewable energy future. *Science* **285**, 687-689 (1999).
- 92 Jain, I., Lal, C. & Jain, A. Hydrogen storage in Mg: a most promising material. *International Journal of Hydrogen Energy* **35**, 5133-5144 (2010).

Chapter #1 Back ground and literature survey

- 93 Sakintuna, B., Lamari-Darkrim, F. & Hirscher, M. Metal hydride materials for solid hydrogen storage: a review. *International Journal of Hydrogen Energy* **32**, 1121-1140 (2007).
- 94 Wang, Y., Chen, X., Zhong, Y., Zhu, F. & Loh, K. P. Large area, continuous, few-layered graphene as anodes in organic photovoltaic devices. *Applied Physics Letters* **95**, 209 (2009).
- 95 Sun, T. *et al.* Multilayered graphene used as anode of organic light emitting devices. *Applied Physics Letters* **96**, 55 (2010).
- 96 Wu, J. *et al.* Organic light-emitting diodes on solution-processed graphene transparent electrodes. *ACS nano* **4**, 43-48 (2009).
- 97 Zilberberg, K., Trost, S., Schmidt, H. & Riedl, T. Solution processed vanadium pentoxide as charge extraction layer for organic solar cells. *Advanced Energy Materials* **1**, 377-381 (2011).
- 98 Stubhan, T. *et al.* High fill factor polymer solar cells incorporating a low temperature solution processed WO₃ hole extraction layer. *Advanced Energy Materials* **2**, 1433-1438 (2012).
- 99 Giroto, C., Voroshazi, E., Cheyins, D., Heremans, P. & Rand, B. P. Solution-processed MoO₃ thin films as a hole-injection layer for organic solar cells. *ACS applied materials & interfaces* **3**, 3244-3247 (2011).
- 100 Meyer, J. *et al.* Metal oxide induced charge transfer doping and band alignment of graphene electrodes for efficient organic light emitting diodes. *Scientific reports* **4**, 5380 (2014).
- 101 Wu, Q.-H. *et al.* Electronic structure of MoO₃/graphene interface. *Carbon* **65**, 46-52 (2013).
- 102 Carneiro, J. F., Paulo, M. J., Siaj, M., Tavares, A. C. & Lanza, M. R. Nb₂O₅ nanoparticles supported on reduced graphene oxide sheets as electrocatalyst for the H₂O₂ electrogeneration. *Journal of Catalysis* **332**, 51-61 (2015).
- 103 Jamil, M., Khan, Z. S., Ali, A. & Iqbal, N. Studies on solution processed Graphene-Nb₂O₅ nanocomposite based photoanode for dye-sensitized solar cells. *Journal of Alloys and Compounds* **694**, 401-407 (2017).

Chapter #1 Back ground and literature survey

- 104 Arunkumar, P. *et al.* Nb₂O₅/graphene nanocomposites for electrochemical energy storage. *RSC Advances* **5**, 59997-60004 (2015).
- 105 Wang, L. P. *et al.* High-performance hybrid electrochemical capacitor with binder-free Nb₂O₅@ graphene. *RSC Advances* **4**, 37389-37394 (2014).
- 106 Yan, L. *et al.* Ultrafine Nb₂O₅ Nanocrystal Coating on Reduced Graphene Oxide as Anode Material for High Performance Sodium Ion Battery. *ACS applied materials & interfaces* **8**, 22213-22219 (2016).
- 107 Jeon, I.-Y. *et al.* Edge-carboxylated graphene nanosheets via ball milling. *Proceedings of the National Academy of Sciences* **109**, 5588-5593 (2012).
- 108 Cho, E. S. *et al.* Graphene oxide/metal nanocrystal multilaminates as the atomic limit for safe and selective hydrogen storage. *Nature communications* **7** (2016).
- 109 Chen, C., Zhang, J., Zhang, B. & Ming Duan, H. Hydrogen adsorption of Mg-doped graphene oxide: a first-principles study. *The Journal of Physical Chemistry C* **117**, 4337-4344 (2013).
- 110 Xia, G. *et al.* Monodisperse Magnesium Hydride Nanoparticles Uniformly Self-Assembled on Graphene. *Advanced Materials* **27**, 5981-5988 (2015).
- 111 Lin, X. *et al.* Graphene Oxide Papers Simultaneously Doped with Mg²⁺ and Cl⁻ for Exceptional Mechanical, Electrical, and Dielectric Properties. *ACS applied materials & interfaces* **8**, 2360-2371 (2016).
- 112 Sher Shah, M. S. A., Park, A. R., Zhang, K., Park, J. H. & Yoo, P. J. Green synthesis of biphasic TiO₂-reduced graphene oxide nanocomposites with highly enhanced photocatalytic activity. *ACS applied materials & interfaces* **4**, 3893-3901 (2012).
- 113 Gu, L. *et al.* Glucosamine-induced growth of highly distributed TiO₂ nanoparticles on graphene nanosheets as high-performance photocatalysts. *RSC Advances* **6**, 67039-67048 (2016).
- 114 Wang, W.-S., Wang, D.-H., Qu, W.-G., Lu, L.-Q. & Xu, A.-W. Large ultrathin anatase TiO₂ nanosheets with exposed {001} facets on graphene for enhanced visible light photocatalytic activity. *The Journal of Physical Chemistry C* **116**, 19893-19901 (2012).
- 115 Nguyen-Phan, T.-D. *et al.* Striving Toward Noble-Metal-Free Photocatalytic Water Splitting: The Hydrogenated-Graphene-TiO₂ Prototype. *Chemistry of Materials* **27**, 6282-6296 (2015).

Chapter #1 Back ground and literature survey

- 116 Du, A. *et al.* Hybrid graphene/titania nanocomposite: interface charge transfer, hole doping, and sensitization for visible light response. *The journal of physical chemistry letters* **2**, 894-899 (2011).
- 117 Zhang, H., Lv, X., Li, Y., Wang, Y. & Li, J. P25-graphene composite as a high performance photocatalyst. *ACS nano* **4**, 380-386 (2009).
- 118 Bajestani, Z. G., Yürüm, A. & Yürüm, Y. Significant improvement in the hydrogen storage capacity of a reduced graphene oxide/TiO₂ nanocomposite by chemical bonding of Ti–O–C. *RSC Advances* **6**, 32831-32838 (2016).
- 119 Hazra, S. K. & Basu, S. Graphene-Oxide Nano Composites for Chemical Sensor Applications. *C* **2**, 12 (2016).
- 120 Chang, Y.-N. *et al.* Synthesis of magnetic graphene oxide–TiO₂ and their antibacterial properties under solar irradiation. *Applied Surface Science* **343**, 1-10 (2015).
- 121 Panchakarla, L. *et al.* Synthesis, structure and properties of boron and nitrogen doped graphene. *arXiv preprint arXiv:0902.3077* (2009).
- 122 Terrones, M., Souza Filho, A. G. & Rao, A. M. in *Carbon nanotubes* 531-566 (Springer, 2007).
- 123 Kotakoski, J., Krasheninnikov, A. & Nordlund, K. Energetics, structure, and long-range interaction of vacancy-type defects in carbon nanotubes: Atomistic simulations. *Physical Review B* **74**, 245420 (2006).
- 124 Lucchese, M. M. *et al.* Quantifying ion-induced defects and Raman relaxation length in graphene. *Carbon* **48**, 1592-1597 (2010).
- 125 Meyer, J. C. *et al.* Experimental analysis of charge redistribution due to chemical bonding by high-resolution transmission electron microscopy. *Nature materials* **10**, 209-215 (2011).
- 126 Terrones, M., Hsu, W., Ramos, S., Castillo, R. & Terrenes, H. The role of boron nitride in graphite plasma arcs. *Fullerene science and technology* **6**, 787-800 (1998).
- 127 Yin, L. W. *et al.* Single-Crystalline AlN Nanotubes with Carbon-Layer Coatings on the Outer and Inner Surfaces via a Multiwalled-Carbon-Nanotube-Template-Induced Route. *Advanced materials* **17**, 213-217 (2005).
- 128 Villalpando-Paez, F. *et al.* Synthesis and characterization of long strands of nitrogen-doped single-walled carbon nanotubes. *Chemical Physics Letters* **424**, 345-352 (2006).

Chapter #1 Back ground and literature survey

- 129 Subrahmanyam, K., Panchakarla, L., Govindaraj, A. & Rao, C. Simple method of preparing graphene flakes by an arc-discharge method. *The Journal of Physical Chemistry C* **113**, 4257-4259 (2009).
- 130 Stürzl, N., Lebedkin, S., Malik, S. & Kappes, M. M. Preparation of ¹³C single-walled carbon nanotubes by pulsed laser vaporization. *physica status solidi (b)* **246**, 2465-2468 (2009).
- 131 Xiang, R. *et al.* Vertically aligned ¹³C single-walled carbon nanotubes synthesized by no-flow alcohol chemical vapor deposition and their root growth mechanism. *Japanese Journal of Applied Physics* **47**, 1971 (2008).
- 132 Yang, L., Park, C.-H., Son, Y.-W., Cohen, M. L. & Louie, S. G. Quasiparticle energies and band gaps in graphene nanoribbons. *Physical review letters* **99**, 186801 (2007).
- 133 Jia, X. *et al.* Controlled formation of sharp zigzag and armchair edges in graphitic nanoribbons. *Science* **323**, 1701-1705 (2009).
- 134 Cançado, L. *et al.* Anisotropy of the Raman spectra of nanographite ribbons. *Physical review letters* **93**, 047403 (2004).
- 135 Dresselhaus, M. S., Jorio, A., Hofmann, M., Dresselhaus, G. & Saito, R. Perspectives on carbon nanotubes and graphene Raman spectroscopy. *Nano letters* **10**, 751-758 (2010).
- 136 Cançado, L. G. *et al.* Quantifying defects in graphene via Raman spectroscopy at different excitation energies. *Nano letters* **11**, 3190-3196 (2011).
- 137 Bhowmick, S. & Waghmare, U. V. Anisotropy of the Stone-Wales defect and warping of graphene nanoribbons: A first-principles analysis. *Physical Review B* **81**, 155416 (2010).
- 138 Neto, A. C., Guinea, F., Peres, N. M., Novoselov, K. S. & Geim, A. K. The electronic properties of graphene. *Reviews of Modern Physics* **81**, 109 (2009).
- 139 Elias, D. C. *et al.* Control of graphene's properties by reversible hydrogenation: evidence for graphane. *Science* **323**, 610-613 (2009).
- 140 Park, S. *et al.* Graphene oxide papers modified by divalent ions—enhancing mechanical properties via chemical cross-linking. *ACS nano* **2**, 572-578 (2008).
- 141 Kim, H.-i., Moon, G.-h., Monllor-Satoca, D., Park, Y. & Choi, W. Solar photoconversion using graphene/TiO₂ composites: nanographene shell on TiO₂ core versus TiO₂ nanoparticles on graphene sheet. *The Journal of Physical Chemistry C* **116**, 1535-1543 (2011).

Chapter #1 Back ground and literature survey

- 142 Li, B. *et al.* Photo-assisted preparation and patterning of large-area reduced graphene oxide–TiO₂ conductive thin film. *Chemical Communications* **46**, 3499-3501 (2010).
- 143 Tian, H., Shen, K., Hu, X., Qiao, L. & Zheng, W. N, S co-doped graphene quantum dots-graphene-TiO₂ nanotubes composite with enhanced photocatalytic activity. *Journal of Alloys and Compounds* **691**, 369-377 (2017).
- 144 Červenka, J., Katsnelson, M. & Flipse, C. Room-temperature ferromagnetism in graphite driven by two-dimensional networks of point defects. *Nature Physics* **5**, 840-844 (2009).
- 145 Esquinazi, P. *et al.* Induced magnetic ordering by proton irradiation in graphite. *Physical review letters* **91**, 227201 (2003).
- 146 Esquinazi, P. *et al.* Ferromagnetism in oriented graphite samples. *Physical Review B* **66**, 024429 (2002).
- 147 Esquinazi, P. & Höhne, R. Magnetism in carbon structures. *Journal of magnetism and magnetic materials* **290**, 20-27 (2005).
- 148 Kopelevich, Y., Esquinazi, P., Torres, J. & Moehlecke, S. Ferromagnetic-and superconducting-like behavior of graphite. *Journal of Low Temperature Physics* **119**, 691-702 (2000).
- 149 Kumar, A., Avasthi, D., Pivin, J., Tripathi, A. & Singh, F. Ferromagnetism induced by heavy-ion irradiation in fullerene films. *Physical Review B* **74**, 153409 (2006).
- 150 Park, N. *et al.* Magnetism in all-carbon nanostructures with negative Gaussian curvature. *Physical review letters* **91**, 237204 (2003).
- 151 Wehling, T. *et al.* Local electronic signatures of impurity states in graphene. *Physical Review B* **75**, 125425 (2007).
- 152 Li, J. *et al.* Searching for magnetism in pyrrolic N-doped graphene synthesized via hydrothermal reaction. *Carbon* **84**, 460-468 (2015).
- 153 Raj, K. G. & Joy, P. Ferromagnetism at room temperature in activated graphene oxide. *Chemical Physics Letters* **605**, 89-92 (2014).
- 154 Yang, Z. *et al.* Magnetic nanomaterial derived from graphene oxide/layered double hydroxide hybrid for efficient removal of methyl orange from aqueous solution. *Journal of colloid and interface science* **408**, 25-32 (2013).
- 155 Chiba, D. *et al.* Magnetization vector manipulation by electric fields. *Nature* **455**, 515-518 (2008).

Chapter #1 Back ground and literature survey

- 156 Ji, Z., Shen, X., Zhu, G., Zhou, H. & Yuan, A. Reduced graphene oxide/nickel nanocomposites: facile synthesis, magnetic and catalytic properties. *Journal of materials chemistry* **22**, 3471-3477 (2012).
- 157 Mornet, S. *et al.* Magnetic nanoparticle design for medical applications. *Progress in Solid State Chemistry* **34**, 237-247 (2006).
- 158 Tsang, S. C., Caps, V., Paraskevas, I., Chadwick, D. & Thompsett, D. Magnetically Separable, Carbon-Supported Nanocatalysts for the Manufacture of Fine Chemicals. *Angewandte Chemie* **116**, 5763-5767 (2004).
- 159 Černák, J. *et al.* Magnetic properties of graphene nanodisk and nanocone powders at low temperatures. *Physical Review B* **92**, 155429 (2015).
- 160 Dai, Q., Zhu, Y. & Jiang, Q. Electronic and magnetic properties of armchair graphene nanoribbons with 558 grain boundary. *Physical Chemistry Chemical Physics* **16**, 10607-10613 (2014).
- 161 Nair, R. *et al.* Spin-half paramagnetism in graphene induced by point defects. *Nature Physics* **8**, 199-202 (2012).
- 162 Veligura, A. *et al.* Transport gap in suspended bilayer graphene at zero magnetic field. *Physical Review B* **85**, 155412 (2012).
- 163 Gupta, R. B. *Hydrogen fuel: production, transport, and storage*. (Crc Press, 2008).
- 164 Spyrou, K., Gournis, D. & Rudolf, P. Hydrogen storage in graphene-based materials: efforts towards enhanced hydrogen absorption. *ECS Journal of Solid State Science and Technology* **2**, M3160-M3169 (2013).
- 165 Huang, S.-h. *et al.* Lithium-decorated oxidized porous graphene for hydrogen storage by first principles study. *Journal of Applied Physics* **112**, 124312 (2012).
- 166 Huang, C.-C. *et al.* Hydrogen storage in graphene decorated with Pd and Pt nanoparticles using an electroless deposition technique. *Separation and purification technology* **82**, 210-215 (2011).

Chapter # 2

EXPERIMENTAL METHODS

2.1 Introduction

The main goal of this chapter is to describe the characterization techniques, tools and the sample preparation methods used to deposit the metal and metal oxide nanostructure onto graphene sheets. In the first section of this chapter will be described the method of the preparation of the samples. The first section also following to cover the RF sputtering technique and deposition parameters were used for the deposition of the metal and metal oxide nanostructure onto graphene sheet. In the second section of the thesis will describe, different characterization techniques used to understand the fundamental structural, chemical, electronic and the interface properties of the decorated graphene with metal and metal oxide nanostructures. The techniques used for the characterization of the graphene composite include, X-ray diffraction (XRD), Raman, X-ray photoelectron spectroscopy (XPS), synchrotron x-ray photoelectron spectroscopy transmission electron microscopy (TEM), Magnetometer and photo catalytic activity. The following properties; crystal structure, grain size, surface morphology, chemical bonding position and the stoichiometry of deposited oxide nanostructures onto graphene sheet were measured by using the above stated techniques.

2.2 Samples preparation

The graphene powder samples for the deposition were prepared in the glove box. The graphene powder and deposited M and MO onto graphene was protected from the moisture in the glove box and the other kind of the contaminations. Especially in case of metal deposition onto graphene sheet, subsequently oxidized, when it was exposed to the air moisture. A special kind of sample holder was designed to protect the graphene powder from the air exposure and other kind contaminations. Moreover the atmosphere inside the glove box contains an inert gas

Chapter #2 Experimental methods

(Argon). There are two analyzers in the glove box one is the O₂ analyzer and the other H₂O analyzer, which are used to measure the amount of oxygen and water molecules inside the glove box. The powder samples were prepared in the glove box and subsequently the graphene powders are protected from the air by using the special kind substrate holder as shown in Fig. 2.1.

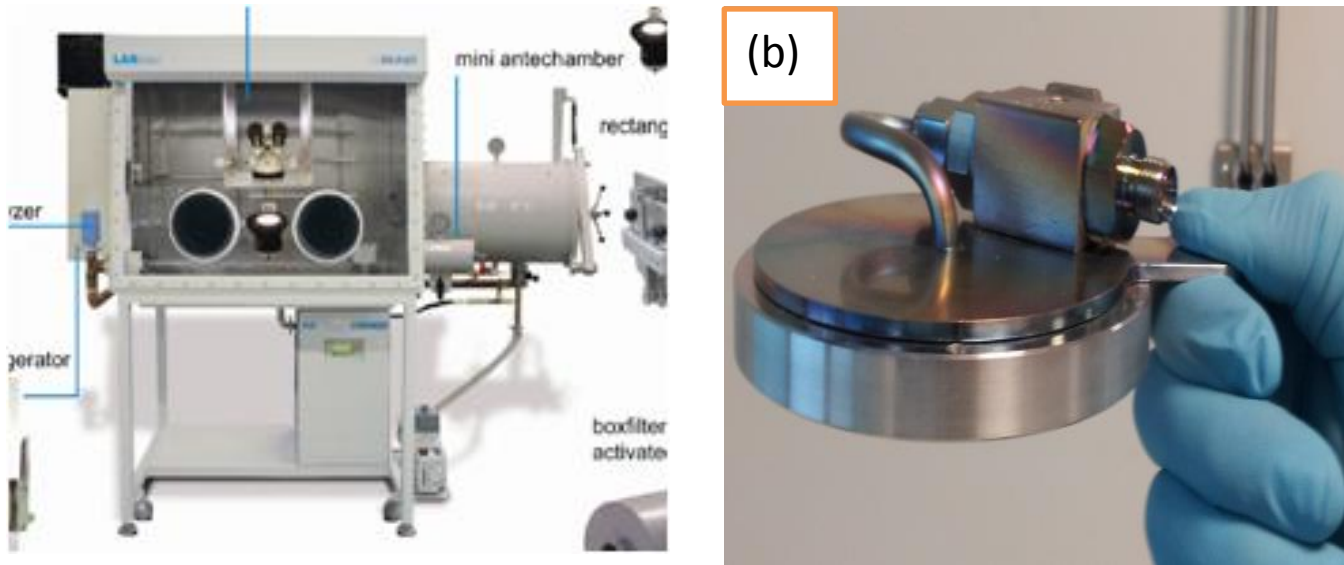


Fig 2. 1 Glove box and substrate holder used for the samples preparation

2.3 Plasma for material synthesis and RF Sputtering technique

The electrical discharge of an inert gas is mostly used for the generation of plasma for material synthesis by PVD. This process is performed by the introduction of inert gas (like Ar) into the process chamber, while maintaining a specific base pressure (In our work, the base pressure is maintained below 10^{-5} Pa). The process chamber comprises an electrode pair, one each for cathode and anode. The target serves as a cathode and is usually connected with negative potential whereas the sample holder acts as anode. The acceleration of charged particles achieved by the potential difference of cathode and anode is vital for the transfer from neutral gas to the plasma. The (inelastic) collision of free electrons and neutral gas atom is initiated. The free

Chapter #2 Experimental methods

electrons are accelerated to an energy level greater than the ionization energy of the neutral gas. The process of inelastic collisions results in ionization and excitation of gas atoms [34].



Every ionization collision results in two free electrons and in case of sufficient kinetic energy also induce the ionization of gas atoms and these ionized gas species accelerating towards the cathode. As a consequence, the sputtering process ejects the target atoms and also the secondary electrons from target surface. The process eventually leads with the cascade of free electrons and ions. The resultant plasma discharge is self-sustained and occurs due to the continuous supply of secondary electrons, which ensures regeneration of enough secondary electrons during the sputtering process due to production of enough Ar^+ ions. The process also includes diffusion to the wall in order to compensate the loss of charged particles. On the basis of the applied potential and the obtained discharge current density, a plasma discharge occurred into numerous regimes [3]. This thesis is related about the deposition of the metal (M) and metal oxide (Mo) onto graphene by low pressure plasma. In the plasma deposition, the discharge potential and current density rising with increasing RF power values, until the surface of the target completely cover by the ionized gas species. Furthermore, by raising RF power values leads to the arc discharge regime, which is categorized by an exceptionally high current density at the target surface, in this case the plasma density reached at a value of 10^{21} m^{-3} [3].

It is well established that plasma is supposed to be quasi-neutral, therefore this characteristic is essentially related to the bulk plasma. Some nonconformity, such as charge disparity can occur at the wall of the chamber or at the plasma boundaries where the plasma species interrelates with other kinds of particles or may be wall of the chamber. The main reason of this case is due to the fact that mobile ions are heavier than electrons and diffuse very fast to the wall of the chamber,

Chapter #2 Experimental methods

subsequently they leave the bulk plasma at a potential (which is called plasma potential) higher as compared to the grounded chamber wall. Usually the plasma potential is in the range of couple volts [2]. Furthermore, any other isolated electrode working in the plasma process will be at slightly negative potential (floating potential) as compared to the ground potential, which is also an effect of the faster electrons. Generally, the region where the interaction takes place by the plasma species with other surface, in these region ions will outnumber the electrons. This space or region is known as plasma sheath [167]. The plasma sheath is a non-neutral region in contrast to the bulk of the plasma. The following is the expression for the sheath thickness and the Debye length, λ_D , and which is given as [167],

$$\lambda_D = \left(\frac{\epsilon_0 T_e}{en_0} \right)^{1/2} \dots\dots\dots(1)$$

In the above equation ϵ_0 is the constant of electric permittivity, T_e is represented the electronic temperature, e is related to the fundamental charge and where n_0 represent to the density of the plasma under the equilibrium condition ($n_i = n_e = n_0$). The Debye length is related to the length of the scale in which a substantial leaving from charge neutrality can be sustained [24].

Sputtering is a physical phenomenon, in which the atoms are ejected from the source material called target by means of incident energy and transfer of momentum [34]. When the vacuum chamber is evacuated to an anticipated level, a sputtering gas is introduced in the chamber. Generally inert gas is frequently used in the deposition process. Mostly the argon gas is used for the sputtering process. The sputtering gas is usually in the Pa range. A suitable negative potential is applied to cathode (Target) and the anode (substrate) is coupled to the chamber walls and to the ground or itself at fixed potential. The electrons are ejected from the target surface and

Chapter #2 Experimental methods

accelerating through the potential difference having high kinetic energy. The ejected electrons are colliding with gas molecules and ionized the gas molecules. Then plasma is generated by means of electric discharge of an inert gas. Plasma contains of electrons, gas species, ions and neutral atoms.

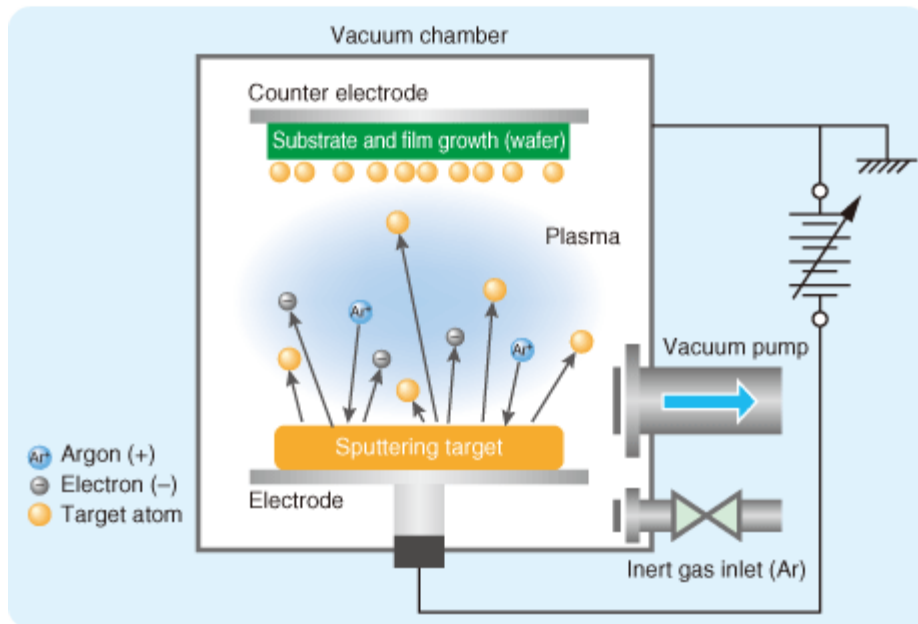


Fig 2. 2 Schematics of the sputtering process

The positive ions from the plasma reach to the target surface due to the large negative potential of the target and the electric fields are generated between the target and anode (substrate) by the influence of large negative potential of the target. The positive ions hitting the target surface part of energy of the positive ions is transferred to heating and remaining part of energy is transferred to the other particles. These particles eventually get enough energy and leave the target surface and reach the substrate. Different types of the particles are emitted from the surface of targets, which include negative ions, photon, and neutral atoms and the secondary electrons and the sputtered species will reach onto substrate and start growth of the film. These secondary electrons further ionize the gas molecules and the positive ion interacted with target and so on.

Chapter #2 Experimental methods

For the maintained the plasma inside the chamber the high yield of secondary electrons are needed. Different ion-solid surface interaction arises by the impact of the ion interaction on the target surface. Based on the incident energy of the ions, the sputtering process is occurred into three regimes, the first regime is related to the low energy regime ($< 1\text{keV}$) called single knock on, second regime is named linear cascade (moderate energy regime, $1\text{-}50\text{ keV}$) and the third regime called spike ((high energy regime, $>50\text{ keV}$).

The DC and RF sputtering are most commonly used sputtering techniques for the industry purposes. But RF sputtering is more useful sputtering technique over the DC sputtering, because of limitation of the DC sputtering technique. In the RF sputtering process, the potential of the target is changed continuously according to the voltage frequency. The electrons of the plasma travel to the electrode when target voltage is turn positive and argon ions accelerates towards the target surface when it turns negative. It indicates that, for each part of the cycle, the target acts as a cathode and anode. Due to the differences of masses of the electrons and the ions, electrons reach the surface of the target much faster than the ions, therefore the duration of the target as the anode is much shorter than the time when it is negative (the cathode) ¹⁶⁸. The negative self-bias (DC voltage) is developed at the surface of the target during the deposition process and the argon ions have accelerated the target and the extract the atoms from the surface of the target. Generally, 13.56 M Hz frequencies are used for the industrial purpose. The extracted atoms are settled on the substrate and build the film.

2.3.1 Decoration of graphene sheets with Metal and Metal oxide (Piezoelectric shaker).

Chapter #2 Experimental methods

In the present study, the radio frequency (13.56 MHz) sputtering was used to deposit the metal and metal oxide nanostructures onto the graphene sheets. The deposition chamber for the decoration of graphene with metal and metal oxide nanostructures is shown in schematic diagram in Fig 2.3. Our deposition chamber consists of vacuum gauges, wave generator (piezoelectric shakers), cathode rays oscilloscope, gas flow controller, power supply, substrate holder and target.

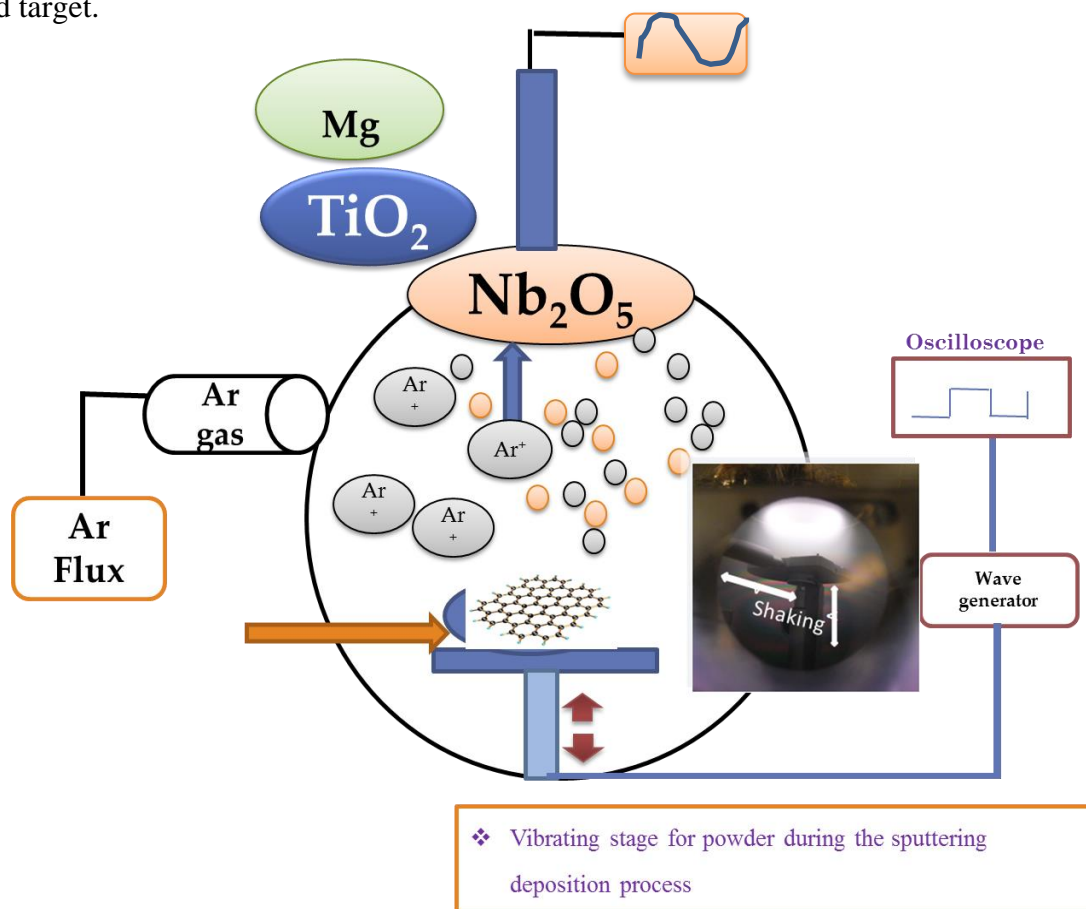


Fig 2. 3 A schematic of the RF sputtering system

Three different targets (TiO_2 , Mg and Nb_2O_5) with diameters of 5 and 10 cm were used for the deposition. The high vacuum inside the deposition chamber was introduced by means of the rotary pump and turbo molecular pump. The flow of gas and deposition pressures was tuned by means of mas flow controller. A special setup was designed for the powder shaking during the

Chapter #2 Experimental methods

deposition process. The setup consists of special kind of prepared sample holder contained the graphene powder and piezoelectric shaker. In the present study, this piezoelectric shaker is playing an important role in our deposition process. The input signal (voltage) will transform to the piezoelectric shaker, and the piezoelectric shaker starts the vibrating motion with desired amplitude. Three parameters, vibration amplitude, frequency and input voltage can be changed for the piezoelectric shaker during the deposition process. The schematic diagram of the piezoelectric shaker is used during the deposition process is illustrated in Fig 2.4.

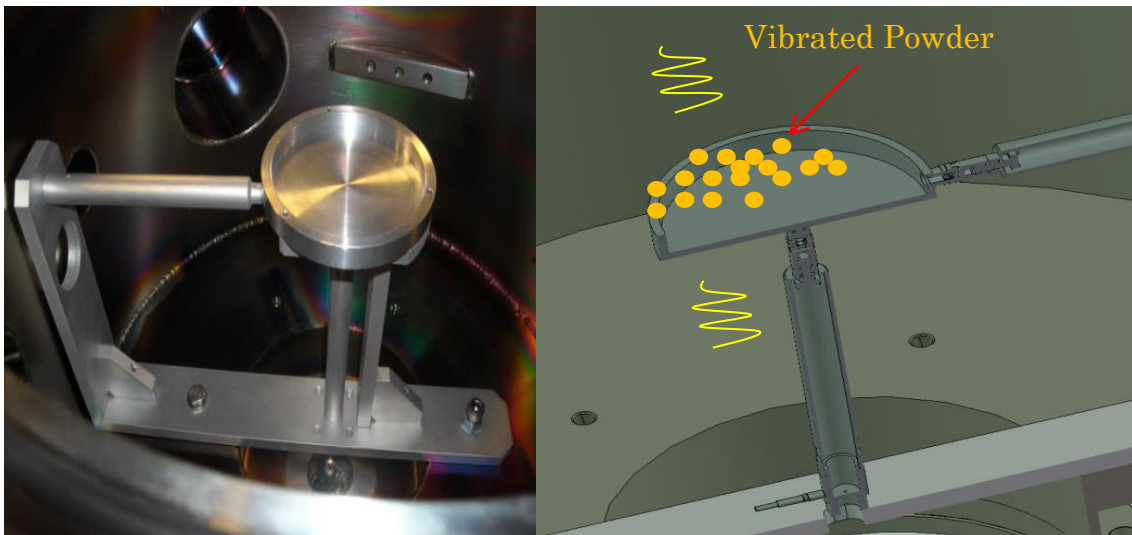


Fig 2. 4 Vibrating stage for the decoration of the sample

The wave generator was used to give the vibration to the piezoelectric shaker, the square waveform is generated into the shaker and this waveform can be tune according to their frequency, amplitude and shape. The oscilloscope is used for the measurement of the amplitude of the square shape waveform. The powder vibration frequency can play a significant role in the uniform decoration of metal and metal oxide nanostructures on the surface of graphene sheet compared to without powder vibration frequency. The metal and metal oxide nanostructures

were deposited onto moving graphene powder during the deposition process and the deposition process are described below.

2.3.2 Decoration of GNPs with Nb₂O₅ nanoparticle.

Nb₂O₅ nanoparticles were deposited onto graphite nanoplatelets by using RF sputtering (13.56 MHz) technique. A high purity (99.99%) and commercially available Nb₂O₅ with 10 cm diameter was used as sputtering target. Four different deposition process, RF power, process pressure, powder vibration frequency and deposition time parameters were varied for the deposition of Nb₂O₅ nanoparticles onto GNPs. The experimental detailed will be explained in their corresponding chapter.

2.3.3 The deposition of Mg nanoparticle onto graphene sheet.

Mg nanoparticles were deposited onto graphene by employing the RF sputtering (13.56 MHz) technique. Mg target which has high purity (99.99 with 5 cm diameter was used a sputtering target. Different amount of Mg nanoparticles were deposited by using three deposition process parameters variation. The base pressure was kept constant at 3×10^{-5} Pa foe each deposition and the deposition of Mg nanoparticles onto graphene sheet was carried out 6 Pa process pressure with constant flow rate at 21 sccm.

2.3.4 Decoration of graphene powder with TiO₂ nanoparticles

The graphene powder was decorated with TiO₂ nanoparticles by using RF sputtering technique. TiO₂ target (99.99 % high purity) with 5 cm diameter (Good fellow) was used as a sputtering target. The different level of anatase nanoparticles were obtained by employing three deposition process parameters. The RF power, deposition time and powder vibration frequency parameters were used to deposit the TiO₂ nanoparticles.

2.5 Thin Films Characterizations

2.5.1 Structural Properties: X-Ray Diffraction:

X-ray diffraction (XRD) is a non-destructive and useful technique used to investigate the structural properties of the crystalline solid materials. The crystalline and semi crystalline structures produce the diffraction patterns upon the interaction of the X-ray. Different features such crystalline size, graphite basal planes; interplaner distance can be measured from the X-ray diffraction patterns of the crystalline materials.

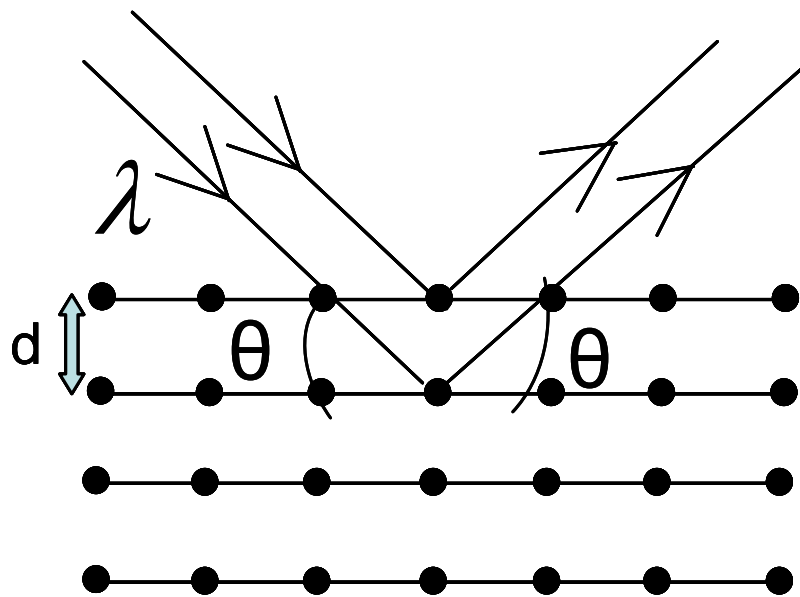


Fig 2. 5 Interaction of X-ray with crystalline materials according to the Bragg's law

The mono or multiphase crystalline sutures can be identified from the diffraction patterns of the crystalline materials. It is well known that in the crystalline materials the arrangement of the atoms are in periodic order and the atoms are spaced by atomic distance d . The diffraction patterns will be occurred by the incident of X-ray on the crystalline material, if it is fulfill the condition of the following equation.

$$2d \sin \theta = n\lambda \dots \dots \dots (2.1)$$

Chapter #2 Experimental methods

The equation 2.1 is known Bragg equation, where d is the distance between the lattice planes, n is an integer, λ is wavelength and θ is the incident glancing angle. The equation 2.1 exhibits that the diffraction pattern will be occurred from the planes of the crystalline material, if the path difference from the atomic planes is equals to the integral multiple of λ . In this case the coherent diffraction peak will be appeared on the spectrum from the reflection of the atomic planes. However no diffraction peak will be appeared in the spectrum if the Bragg condition is not fulfilling. Generally two conventional configuration are used for the acquiring the X-ray diffraction patterns. One is called the Bragg-Brentano and other one is grazing angle configuration. For the Bulk material the Bragg-Brentano configuration is extensively used. But Bragg-Brentano geometry is not useful for the very thin film due to the poor signal and the existence of inquisitive effect of the substrate. However the grazing angle configuration is used for the very thin films without penetration depth of x-ray incidence. In present work the influence of the metal and metal oxide nanostructures on the structural properties of the graphene sheets were investigated using a Seeman–Bohlin (Bragg Brentano) X-ray diffractometer. The measurements were carried out by using $\text{CuK}\alpha$ radiation ($\lambda=0.1541\text{nm}$) in steps of 0.02 operated at 40 kV and 30 mA. The effect of the Nb_2O_5 concentration onto graphite nanoplatelets were studied by using XRD analysis and measured the average crystalline thickness of the GNPs, interlayer spacing of graphene, degree of graphitization from the diffraction peak of GNPs and in the last strain induced in the planes of the GNPs by the interaction of the sputtered and plasma species. The Williamson hall plot was used for the determination of the crystalline thickness of the graphite nanoplatelets. Additionally the crystalline size of the decorated graphene with Mg nanoparticles were calculated using the using the Scherrer's formula. The silicon powder x-rays diffraction was use as standard for the instrumental broadening correction and the expression

$B = \sqrt{B_F^2 - B_S^2}$ where B_F and B_S are the FWHM of the lines from the film and the standard, respectively.

2.5.2 Raman Spectroscopy studies

Raman spectroscopy is a non-destructive and spectroscopic technique used to measure the inelastic scattering of the monochromatic light, usually from a laser source. The Raman spectroscopy is based on the inelastic scattering. The frequency of laser light is changed with the interaction of the sample. The schematized illustration of the Raman frequency shift is presented in Fig 2.6

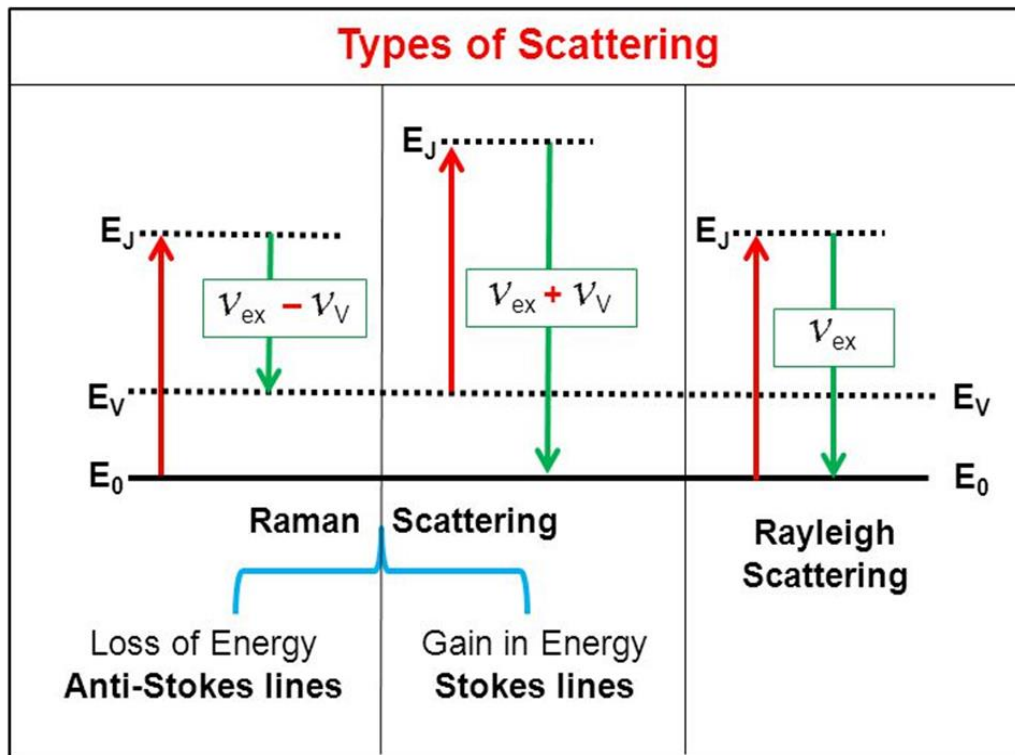


Fig 2.6 Energy level diagram for Raman scattering; Stokes and anti-Stokes Raman scattering

Chapter #2 Experimental methods

When the monochromatic light is interacted with molecule or crystal, mostly photon is scattered with same frequencies as the time of incident means that photon are the elastically scattered, this process is called Rayleigh scattering. However, small fraction of monochromatic light (approximately 1 in 10^7 photons) is scattered in-elastically and having different frequency than the incident photon, generally photon is shifted up or down in of the incident photon frequency. This phenomenon is called the Raman scattering and this Raman shift can change the vibrational, rotational or electronic energy states of the molecule. Then the Raman shift gives the information about the vibrational, rotational and other low vibration modes of the molecules. The Raman scattering phenomenon was discovered by Indian scientist named V. C. Raman in 1928. Raman spectroscopy is also used for the identification of the molecule and minerals.

In present study, Raman spectroscopy was used for the decorated graphene with M and MO nanostructures. It can be used to identify the disorderness and for measuring strain, electronic properties of multilayer graphene and single layer graphene. The Raman spectrum was taken at room temperature with a Labram Aramis micro spectrometer. To avoid the heating effect a low power at 10 mW was used to characterize the decorated graphene sheets with M and MO. The laser spot measured the area less than $2 \mu\text{m}^2$ and the spectral resolution was better than 1 cm^{-1} .

2.5.3 X-Ray photoelectron spectroscopy (XPS)

X-ray photoelectron spectroscopy is widely and useful surface analysis technique to evaluate the elemental composition and the chemical state of the material. The working principle of XPS is based on the photoelectric effect phenomenon. The electrons from the atomic shell is ejected by the interaction of the X-ray photon. The emitted electrons from sample are called photoelectrons

Chapter #2 Experimental methods

The emissions of these photoelectrons escape from atomic orbital of the samples to the vacuum level. The kinetic energy of the emitted photoelectrons and binding energy core level with respect to Fermi level of the material can be measured by using the following expression.

$$K.E = h\nu - B.E - \Phi_s \text{ ----- (2.4)}$$

In the above equation the $h\nu$ is the characteristic X-ray energy, B.E is the binding energy of the sample and Φ_s is the represent the work function of the sample.

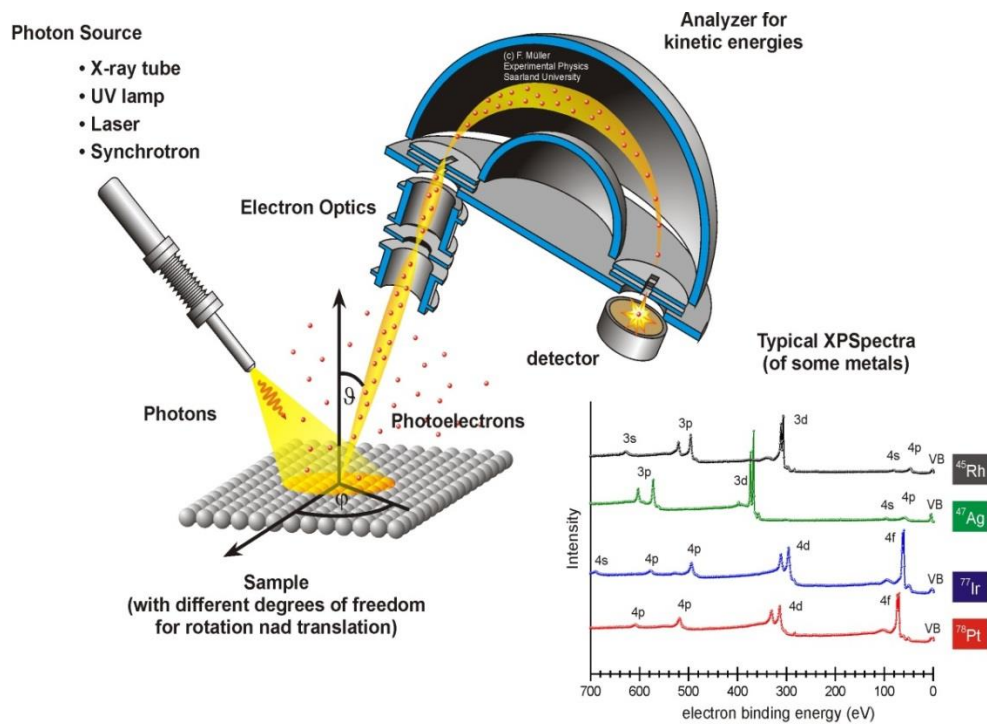


Fig 2. 7 Schematic of XPS and "Photoelectric Effect

The XPS spectrum consists of the intensity plot as function of the irrespective of the binding energy value and the scheme is presented in Fig 2.7. Each element has a specific and characteristic binding energy peak. The electrons which are emitted from the shell originate XPS peaks. The attenuation length of the XPS probes is very small and emits only the photoelectron at the few layers of the samples. The electrons only emit and escape elastically from the top

layers of the sample. In addition to XPS core-level peaks, the XPS spectra consists Auger electron peaks.

X-ray photoelectron spectroscopy was used to determine the elemental composition and the component interaction of the prepared samples. X-ray photoelectron spectroscopy was carried with a Scienta ESCA 200 spectrometer with a monochromatic Al K α x-ray source (1486.6eV).The XPS data were analyzed with the R Studio software. No special surface treatments were carried out for any of the samples. The spectra have been fitted with a Gaussian peak shape, after a Shirley-type background subtraction. The chemical composition and stoichiometry have been derived by applying Scienta sensitivity factors for the core levels.

3.5.4 Transmission Electron Microscopy

The transmission electron microscopy is widely used technique to investigate the structural, surface morphology and the crystallinity of the composite material. The average size of the particle and particles nature of the prepared or synthesized sample can be measured by employing transmission electron microscopy (TEM).A high resolution transmission electron microscopy can measure the sample having size in the range of 1 nm due to the shortening in de Broglie wavelength of the high energetic electron beam. This gives us useful information about to measure the crystalline or amorphous structures and also can be used to find the structural defects such as lattice expansion or dislocation within nanoparticles. Other information can be examined by employed the TEM analysis such as the atomic spacing distance, growth direction of the nanostructures material and the crystalline planes orientation. The schematic diagram of TEM components are presented in Fig 2.45. The working principle of the TEM is like this, the high energy electrons are accelerating by applying the high voltage up to 300 kV. The speed of accelerating electrons has nearly equal to the speed of light and these electrons behave like a

Chapter #2 Experimental methods

wave front having wavelength shorter than the light waves. The electron are scattered with interaction of the thin specimen of the material. The electromagnetic lenses are used to focus the electron beams to the sample. With interaction of the electron beam onto the sample the transmission takes place. The electrons beam is further focused to the objective lens into the image which is then passed through the intermediate and projector lenses, and then projected on the fluorescent screen.

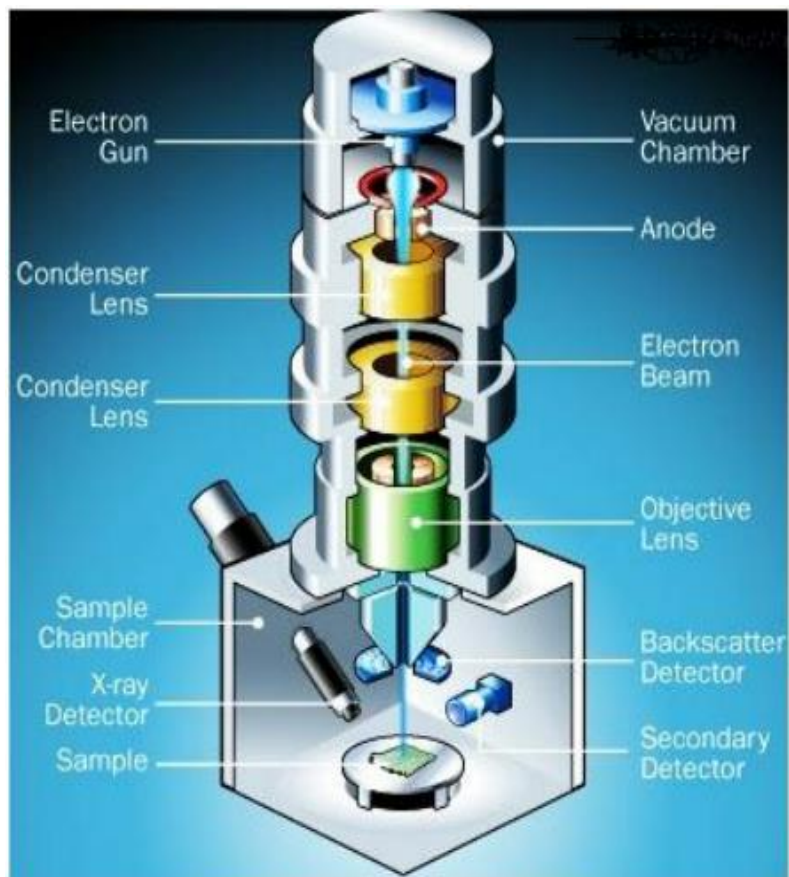


Fig 2. 8 Schematic diagram for TEM analysis [169]

Chapter # 3

The influence of Nb₂O₅ deposited by RF sputtering on the structural chemical and electronic properties of graphite nanoplatelets

3.1 Introduction:

The aim of this chapter is to reconnoiter an approach to decorate graphite nanoplatelets with layers of Nb₂O₅ using deposition process parameters. For this intention, different deposition process parameters (RF power, process pressure and powder vibration frequency) were varied to decorate graphite nanoplatelets with layers of Nb₂O₅ film in Ar plasma. Based on the variation of deposition parameters used, this chapter is divided into four sections.

In the 1st section, we will present the results of the decoration of graphite nanoplatelets with Nb₂O₅ layers by varying the RF power and discuss the chemical, structural, morphological and electronic properties of the interface between the graphene sheets and Nb₂O₅ layers.

In the 2nd section, the influence of Nb₂O₅ concentration on the structural and chemical properties of graphite nanoplatelets studied by varying the process pressure will be discussed.

In the 3rd section, the effect of Nb₂O₅ concentration on the structural and chemical properties of graphite nanoplatelets studied by varying powder vibration frequency will be presented.

In the last section, the decoration of graphite nanoplatelets with Nb₂O₅ layers by varying the deposition time will be described.

3.2 Experimental details:

Nb₂O₅ thin films were deposited on fine graphite nanoplatelets (GNPs) powder with specific surface area-80 m²/g, purity 99.2% and average flake thickness 12 nm (30-50 monolayer graphene) by Radio frequency (13.5 MHz) sputtering. The graphite nanoplatelets powder was provided by Graphene Supermarket. A commercially available high purity Nb₂O₅ disc (99.99%)

with 10 cm diameter was used as a sputtering target. Typically a base pressure of about 2×10^{-5} Pa was established before each deposition. The distance was fixed 50 mm between the target and substrate.. For the uniform distribution of the Nb₂O₅ nanostructures onto graphene surface a powder vibration system was developed. The sputtered particles were deposited on the vibrating powder; the powder vibration frequency is an important parameter and plays a vital role for uniform decoration. More specific details are given below:

- For the results presented in section I, in order to obtain different amounts of Nb₂O₅ on the GNPS surface, the power applied to the Nb₂O₅ target was varied from 40 W to 100 W. The total pressure and powder vibration frequency were fixed at 10 Hz (with amplitude of 32 μm) and 6 Pa respectively. The deposition time was fixed at 15 min.
- For the results reported in section II, the GNPs powders were decorated with Nb₂O₅ layers deposited with a range of process pressure of (2 Pa -8 Pa). The self-bias voltage and power applied to the target was fixed at -72 V and 40 W respectively. The powder vibration frequency and deposition time were kept constant at 10 Hz and 15 min respectively.
- For the results described in section III. We decorated the GNPs with Nb₂O₅ layers deposited with powder vibration frequencies $0 \leq \omega \leq 100$ Hz with vibrating amplitude of 32 μm. The process pressure and power applied to Nb₂O₅ target were fixed at 40 W and 6 Pa respectively. The deposition time for each sample was kept as 15 min.
- For the results presented in section IV, in order to obtain different amounts of Nb₂O₅ contents on the surface GNPs powder, the GNPs powder was decorated with Nb₂O₅ layers deposited by stepping up the deposition time from (10 to 45 min) at a constant power. The powder vibration frequency and power applied to Nb₂O₅ target were kept

constant at 10 Hz and 40 W respectively. The decoration of GNPs powder with Nb₂O₅ layers was performed at 6 Pa process pressure in Ar plasma.

3.3 The influence of Nb₂O₅ concentration on the properties of graphite nanoplatelets deposited by varying the RF power

Different Nb₂O₅ concentrations on the surface of the GNPs were obtained by varying the power applied to Nb₂O₅ target. In this section the interaction of high energy sputtered particles with GNPs will be discussed. These energetic plasma species and sputtered particles generated defects in the structure of GNPs. The structural defects and disorderness were characterized by using the Raman spectroscopy and X-ray diffraction (XRD) techniques. The surface morphology of the decorated Nb₂O₅ layers was investigated by Transmission Electron Microscope (TEM). The chemical state and composition of the deposited Nb₂O₅ layers were evaluated by using X-ray photoelectron spectroscopy (XPS). Furthermore the detail process parameters are presented in table 3.1.

Table 3.1 the process condition of decorated GNPs with Nb₂O₅ films

Sample #	RF Power (W)	Process pressure (Pa)	Deposition Time (min)	Powder vibration frequency (Hz)
1	40	6	15	10
2	60	6	15	10
3	80	6	15	10
4	100	6	15	10

3.3.1 XPS analysis of pristine GNPs and Nb₂O₅ decorated GNPs at different RF powers

The C 1s and Nb 3d core-level spectra shown in Fig 3.1 were used for the chemical analysis of the GNPs before and after the decoration by Nb₂O₅ at different RF power values. The C 1s spectrum de-convoluted by using Gaussian peak was performed after performing a Shirley

background correction. The C 1s signal of GNPs is shown in Fig 3.1 (a) the de-convolution of the C 1s spectra yields three peaks. In addition to the strong peak at 284.69 eV attributed to the graphitic carbon [¹⁷⁰, ¹⁷¹], a peak around 285.40 eV corresponds to defect structure arising from C-H related sp³ hybridized structure or hydrocarbon contamination [¹⁷², ¹⁷³, ¹⁷⁴], and a peak around 286.3 eV related to C-O bonding, probably from adsorbed impurities is also observed [¹⁷⁵]. Interestingly the C 1s binding energy for Nb₂O₅ decorated GNPs is shifted toward lower values relatively to that of pristine GNPs as shown in Fig 3.1(a).

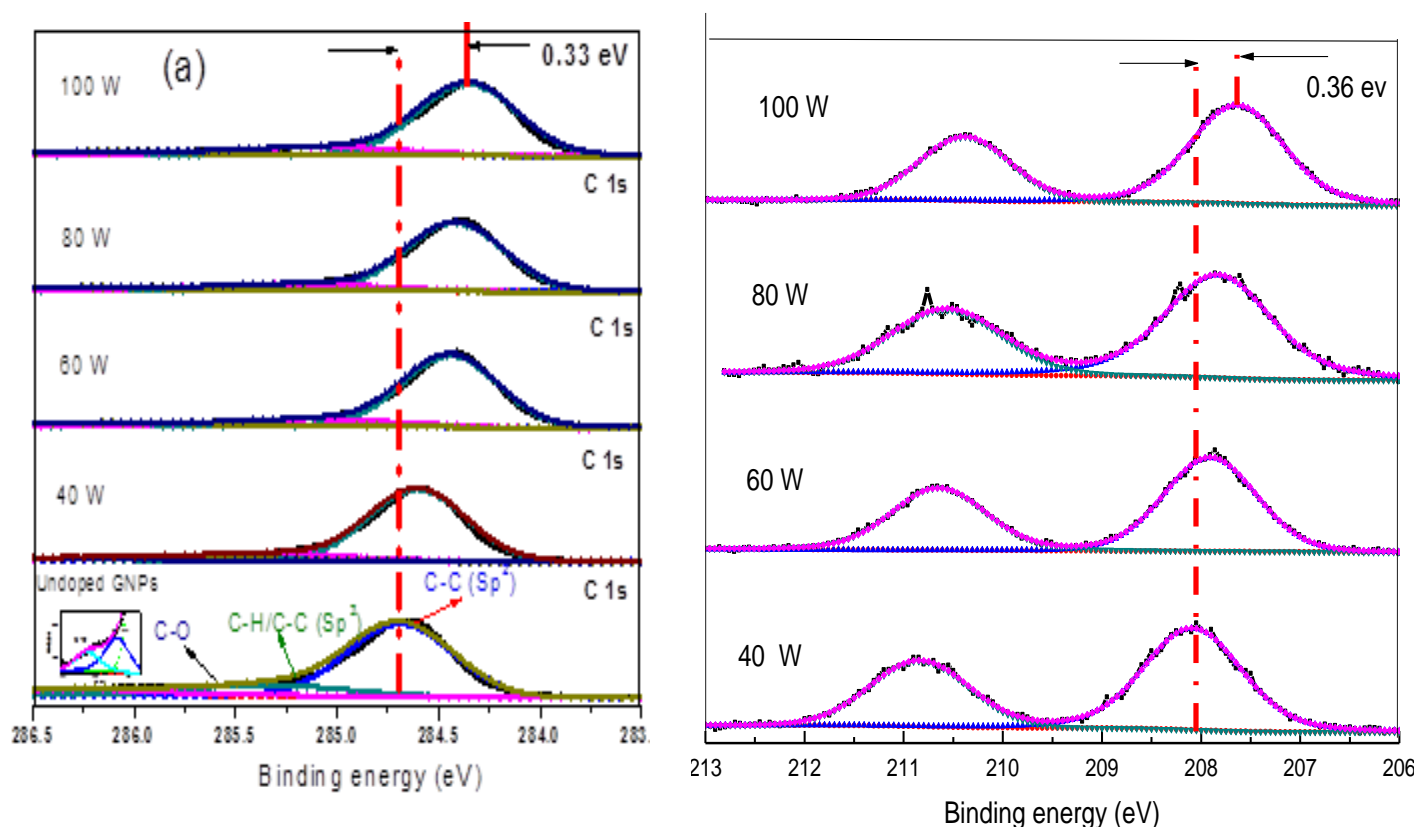


Fig 3. 1 XPS spectra of GNPs with incrementally increased of Nb₂O₅ contents through RF power variation (a)

(a) Shift in the C 1s core levels position upon Nb₂O₅ deposition (b) Nb 3d core level spectra with positions of the Nb⁺⁵ peaks. [Process pressure = 6 Pa, Time=15 min, Frequency = 10 Hz]

The downshift in the C 1s core level could be due to the interface charge transfer between the of the graphene sheets and metal oxide nanostructures, even there is no chemical bonding between the graphene sheets and metal oxide nanostructure, in this scenario charges are expected to be

transferred between the interface of the graphene sheets and metal oxide nanostructures in order to align the Fermi levels. In XPS measurement, Fermi level is the reference energy level for core level binding energy. Consequently a shift in the Fermi level is the origin of an equal shift in the C 1s core level binding energy.

The shift of the C 1s core level of Nb₂O₅ decorated GNPs relative to the C 1s core level in GNPs is understood as an equivalent shift of the Fermi level of GNPs. It can be seen that C 1s peak position shifts gradually toward the lower binding energies after deposition of Nb₂O₅ layers with the increasing RF power values. The maximum down shift was observed in the C 1s peak of 0.33 eV after the decoration of Nb₂O₅ onto GNPs at 100 W. Subsequently the shifts of C 1s peak suggest that Fermi level shift downward due to p type doping of GNPs due to charge transfer from GNPs to Nb₂O₅ layers. Charge transfer can be explained by the work function difference between the Nb₂O₅ and GNPs. Because Nb₂O₅ has a much higher electron affinity (3.90 eV) and work function (4.70 eV) than GNPs (1.26 eV and 4.33 eV) [176, 177], electrons are expected to transfer from GNPs to the Nb₂O₅. Similar phenomenon has been reported in a previous work concerning the deposition of MoO_{3-x} on graphene surface [100, 101].

Figure 3.1 (b) shows the Nb 3d XPS spectra with Nb₂O₅ layer deposited on GNPs at different RF power values. The binding energy values for Nb 3d at 208.1 eV and 210.12 eV correspond to Nb 3d_{5/2} and Nb 3d_{3/2} peak of Nb⁺⁵ [178]. XPS analysis confirmed that only one chemical state has been observed for the Nb. In addition, we observed a shift of 0.36 eV in the Nb⁺⁵ 3d_{5/2} states toward lower binding energies values with increasing Nb₂O₅ contents through RF power variation from 40 W to 100 W. It is another indication that the electrons transfer from the GNPs to the metal oxide i.e. a p-type doping of GNPs. It suggest that by increasing Nb₂O₅ layer thickness with rising RF power values the valance band edge of the metal oxide moves 0.36 eV

closer to the Fermi level which can be attributed to band bending. A similar phenomenon has been explained by Meyer, J. *et al* [100].

Fig 3.2 (a) presents the O 1s spectrum of the decorated GNPs with Nb₂O₅ films at 100 RF power value in Ar plasma. The O 1s spectrum were de-convoluted into three components due the presence of the asymmetric components towards the higher binding energy (BE) with respect to main component (O I), which suggest that oxygen exist in different chemical state. The peak is de-convoluted into three peaks: the first and main peak at lower B.E (530.84 eV) indicated as OI can be attributed to the O 1s core peak of O⁻² bound to Nb⁺⁵ [179], whereas a second component (OII) located at 531.82 eV, may arise due to the oxygen contribution in possible C=O or C-O-C [180]. A 3rd component (O III) at higher BE of 533.62 eV is from C-O bonding in O-C=O [181].

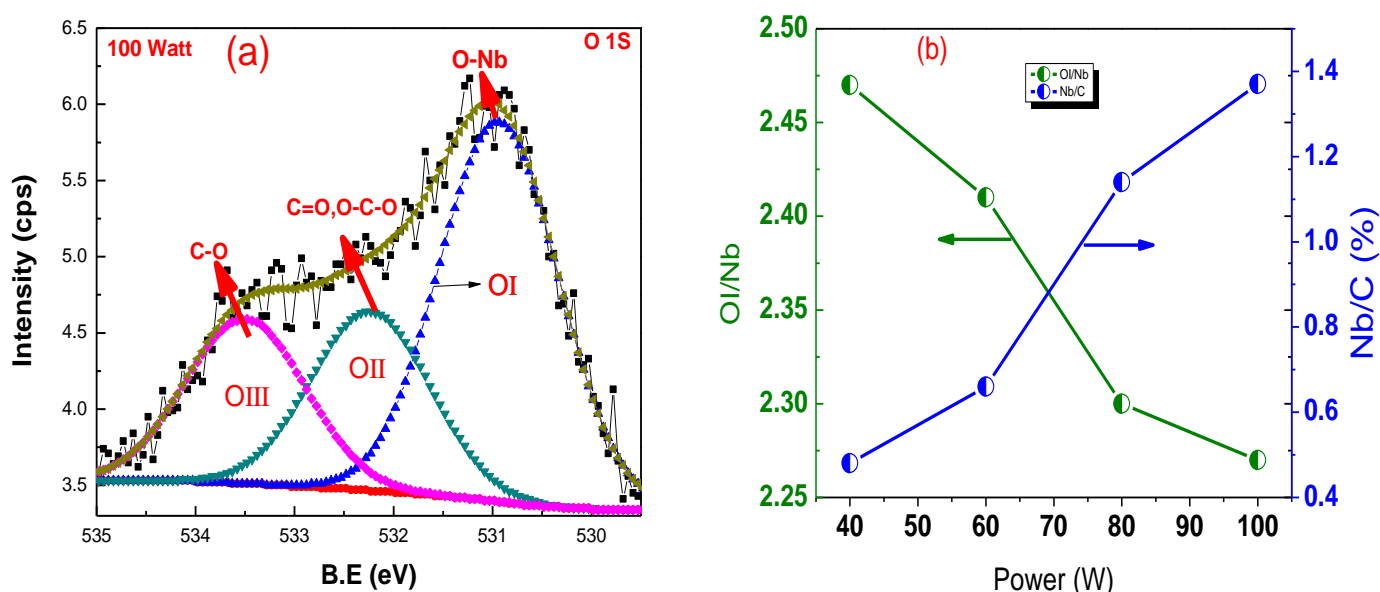


Fig 3. 2 (a) O 1s core peak and its de-convolution (b) variations of Nb/C and OI/Nb atomic ratio with RF power

The OI/Nb ratios were measured for the all samples on the basis of the area under the main component of the oxygen (OI) and the area under the Nb 3d_{5/2} component. The calculated values of the OI/Nb are presented in Fig 3.2 (b). It was found that the OI/Nb ratio decreased from 2.48 to 2.26, when the Nb₂O₅ were deposited onto GNPs in a ratio of 1.37 at. %. The Nb/C sp²

increases steadily with the rising RF power values the results are presented in Fig 3.3 (b). This suggests that with rising RF power values the sputtered particles energy increased and reached at the surface of the GNPs with high kinetic energy. These high energy sputtered particles generated the oxygen vacancies in the lattice of Nb₂O₅ structure during the deposition process.

The oxygen vacancy formation mechanism can be explained as follows, as already discussed in the above text, with increasing RF power values the sputtered particles and plasma species gain more kinetic energy during the deposition process. These energetic sputtered particles may direct remove the oxygen from the lattice of the Nb₂O₅ or might be due to the high collision of the sputtered particles with the high energetic plasma species induced the oxygen vacancy in the lattice of Nb₂O₅ during the deposition process.

3.3.2 XRD analysis of pristine GNPs and Nb₂O₅ decorated GNPs at different RF power values

The XRD patterns of the pristine GNPs and Nb₂O₅ decorated GNPs at different RF power values (40 to 100 Watt) are shown in Fig 3.3 (a). The peak positions in XRD patterns at 26.44°, 42.41°, 44.53°, 54.62°, 77.63° and 83.43° are assigned to reflections of the planes (002), (100/101), (004), (110) and (112) respectively [182]. The strongest intensity of the (002) diffraction peak indicates a preferred oriented hexagonal graphitic polycrystalline structure [183]. There is no extra peak observed in the XRD spectra related to Nb₂O₅ impurities due to low concentration or more likely to an amorphous state due to the low temperature growth. The enlarged view of peak (002) inset as shown in Fig 3.4 (a) shows that by the deposition of the low amount of Nb₂O₅ onto the GNPs produced notable change in the structure of GNPs. In the XRD patterns for the low Nb₂O₅ content sample (Nb/C sp²=0.48 at. %) obtained with a 40 W power the peaks slightly broadened indicating a deterioration of the crystallinity of the GNPs. Higher contents Nb/C sp² = 1.37 at.

%) obtained at 100 W produced a further increase of the FWHM and an intensity reduction of the peaks. We observed a shift in the position of the (002) peak toward lower angle values with increasing contents of Nb₂O_{5-x} in GNPs through rising RF power as shown in Fig. 3.3 (b). It shows that the interlayer d spacing between the layers of graphene is increased.

The interplaner spacing d values of un-decorated GNPs and Nb₂O₅ decorated GNPs powders were calculated for the (002) plane using Bragg's relation.

$$d_{002} = \frac{\lambda}{2 \sin \theta} \dots \dots \dots (1)$$

Where λ is the wavelength of X-ray radiation (equal to 0.1541 nm) and θ is the diffraction angle.

The calculated d spacing evaluation with the increasing Nb/C sp² is shown in Fig 3.6.

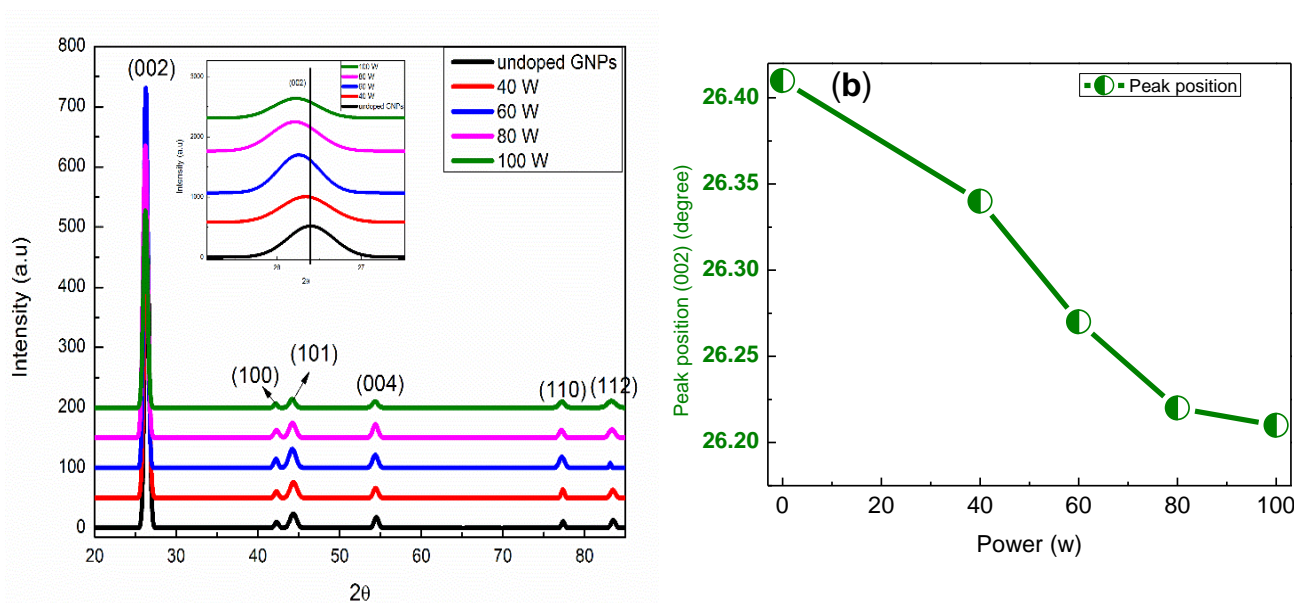


Fig 3.3 (a) XRD patterns of undoped and Nb₂O₅ doped GNPs **(b) Variation of the 2θ angle of the (002 at different RF powers**

The increasing d spacing of GNPs for samples with Nb/C sp² indicates that Nb₂O_{5-x} molecules induced stress in the layers of GNPs [184]. This caused the lattice distortion and expansion.

According to the hexagonal symmetry the lattice constants can be evaluated using the following equation,

$$\frac{1}{d_{hkl}^2} = \frac{4}{3} \left(\frac{h^2 + hk + k^2}{a^2} \right) + \frac{l^2}{c^2} \dots\dots\dots(2)$$

Where a -and c are the lattice parameters h, k and l are the Miller indices of the plane and d_{hkl} is the inter-planar spacing. The lattice parameters "a" and "c" of undoped GNPs and Nb₂O₅ doped GNPs were calculated from the reflection of the planes (100) and (002) using equation (2). Fig.3.4 shows the evolution of the lattice parameters ("a" and "c") of the GNPs when changing the Nb/C (sp²) through increasing the RF power. A small Nb₂O_{5-x} amount of introduction changed the "c" and "a" parameters. "The maximum elongation along 'c' axis is about 0.071 Å from 6.734 Å (for 0 % Nb) to 6.797 Å (for Nb/C of 1.37 at. %).

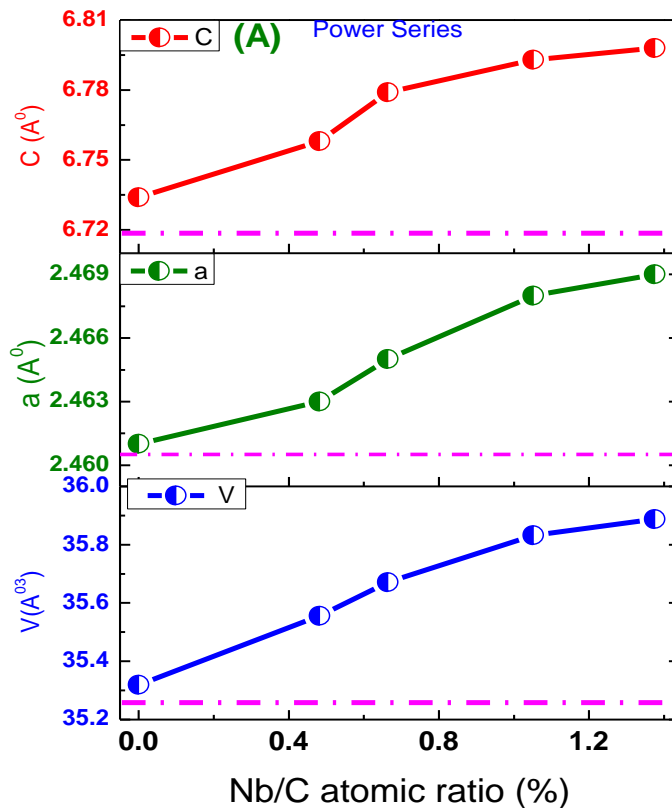


Fig 3. 4 Lattice parameters "a", "c" and cell volume V of GNPs with various Nb/C at. % levels

More likely reason for the expansion along the c axis is that, by the deposition of Nb₂O₅ onto graphene sheet with increasing RF power values the sputtered particles interacted with GNPs sheets more energetically and generates the stress in the layers of GNPs. With interaction of the sputtered particles and plasma species the planes of the GNPs are distorted, which might be caused by the expansion of the lattice of the GNPs or it might be due to the large difference between ionic radii of the Nb (0.70 Å) compared to the spacing between the layers of graphene (3.35 Å), which Nb intercalated randomly in the first two layers of GNPs.

Generally XRD is the bulk analysis technique; it gives the information about whole GNPs structure. The low expansions along “c” axis of GNPs after the deposition of the Nb₂O_{5-x} onto GNPs sheets might be due to the intercalation of Nb in the first two layers of GNPs. Consequently it can be considered that Nb atoms are randomly intercalated in the first two layers of GNPs, which might be cause the expansion along the c axis. Moreover Nb₂O_{5-x} deposition onto GNPs had also an observable influence on the lattice parameter ‘a’. The lattice parameter ‘a’ is also expanded with increasing of Nb/C atomic ratio (%) (sp²).

Microstrain (\mathcal{E}) and crystalline size (L_c) (the crystalline coherence length in the 002 direction) of un-decorated GNPs and Nb₂O₅ decorated GNPs were calculated using Williamson Hall equation [185].

$$\beta_{hkl} \cos \theta = \frac{K\lambda}{L_c} + 4\mathcal{E} \sin \theta \dots \dots \dots (4)$$

Where β_{hkl} is represented the FWHM (the full width at half-maximum) of the 002 peak of the GNPs, θ is the Bragg angle and L_c is the average crystallite size of GNPs, K is approximately equal to 0.9 [186]. Here the peak widening (β_{hkl}) is considered to be induced by both the strain and the crystallite size.

Using this equation a plot of $\beta\cos\theta$ in a function of $4\sin\theta$ was applied to the peaks (002), (004) and (112). The crystallite size was extracted from y-intercept and microstrain from the slope of linear fit. Fig 3.5 shows that the crystallite size linearly decreased with the increase of Nb/C (Sp²). The crystalline size L_C of pristine GNPs before decoration by Nb₂O₅ was (12.9±0.32) nm and the basal planes of graphene were stacking in order. The decrease of the crystalline size of GNPs after the decoration for Nb₂O₅ might be due to the basal plane bending or dislocations. Similar result was also reported in previous work by Zhang, B. et al [187]. The possible explanation for this is that the sputtered particles interact with GNPs, reduce the orientation and stacking order of the basal planes along c axis. From this, it is concluded that the crystalline size L_c of GNPs decreases due to the deprivation of ordered of basal planes or less graphitization part due the higher Nb₂O₅ contents on the GNPs. Similar result is also reported by Anjana Asthana using the neutron irradiation on highly oriented pyrolytic graphite [188]

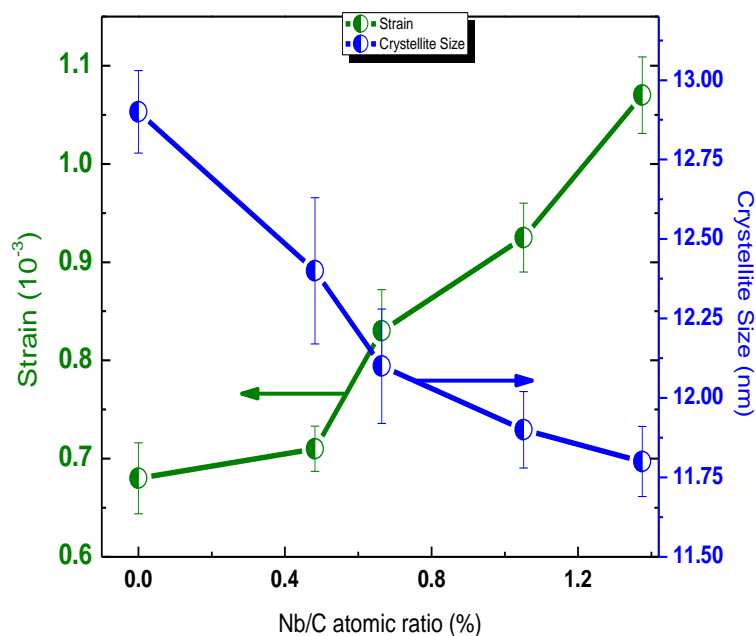


Fig 3. 5 Crystallite size and strain of undoped GNPs with Nb₂O₅ doped GNPs in function of Nb/C atomic ratio as obtained by varying the RF power during the deposition [Process pressure = 6 Pa, Time=15 min, Frequency = 10 Hz RF power value (40 W to 100 W).

The shifts in the 2θ values for GNPs corresponding to the (002) peak are well reflected in the variation of the residual strain with Nb/C (Sp²) as shown in Fig 3.5. This can be correlated with the variation of the cell volume of the undoped GNPs and Nb₂O₅ doped GNPs as shown in Fig 3.4. It is observed that the strain in Nb₂O₅-doped samples was higher than that of undoped GNPs. Also the strain increased as the dopant amount increased.

The graphitization index is used to describe quantitatively the degree of similarity between a carbon material and a perfect single crystal of graphite. The higher graphitization index indicates a more ordered graphitic structure.

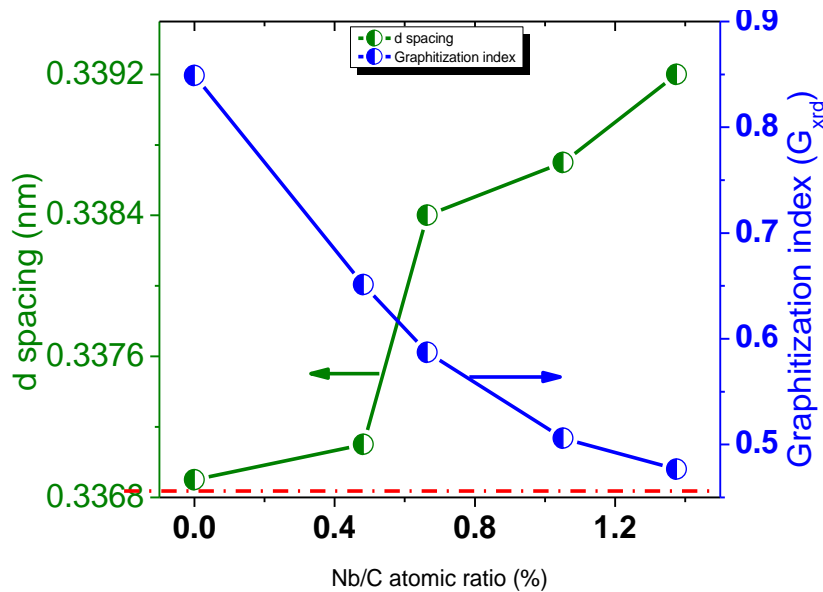


Fig 3. 6 Degree of graphitization and d spacing of undoped GNPs with Nb₂O₅ doped GNPs through RF power values variation [Process pressure = 6 Pa, Time=15 min, Frequency = 10 Hz RF power value (40 W to 100 W)].

The graphitization index derived from the average interplaner spacing between two successive graphite layers according to the equation [189].

$$G_{XRD} = \frac{3.440 - d_{002}}{3.440 - 3.354} \dots\dots\dots(3)$$

The interplaner spacing (d_{002}) of undoped GNPs and Nb₂O₅ doped GNPs calculated from equation (1), where 3.440 is interplanar spacing in carbon with a turbostratic structure, and 3.354 interplanar spacing in a defect-free single crystal of graphite.

Graphitization indices (G_{xrd}) and d spacing of the GNPs and decorated GNPs with Nb₂O₅ by varying RF powers are shown in Fig 3.6. The interlayer spacing d_{002} gradually increased with rising Nb/C (sp^2). The graphitization index (G_{xrd}) of GNPs before the Nb₂O₅ decoration was 0.85, which suggest that the stacking layers of the GNPs were well ordered. However, after decoration with Nb₂O₅ the degree of graphitization of GNPs decreased with increasing Nb/C (Sp^2). It shows that with increasing of Nb/C (Sp^2) through RF power variation, the large amount defects were induced onto GNPs, due to induced defects the basal plane of the GNPs loss their initial ordering, decreasing the degree of graphitization. This shows that high Nb/C (sp^2) atomic ratio values transformed the ordered GNPs structure to disordered GNPs structure.

3.3.3 TEM analysis of undoped and Nb₂O₅ doped GNP at 100 W RF power value

The surface morphology of the undoped GNPs and Nb₂O₅ deposited onto GNPs surface were examined using Transmission electron microscopy (TEM) to determine average size of the Nb₂O₅ layer on the GNPs. TEM images in Fig.3.7 (A–B, C-D) show the undoped and Nb₂O₅ deposited at 100 W onto GNPs surface. Fig 3.7 (C, D) depicts a GNPs surface decorated with uniform layers of the Nb₂O₅ nanoparticles. Around 5 to 10 nm homogeneously distributed nanoparticles were successfully deposited onto GNPs surface and these nanoparticles make aggregates on the surface of GNPs. High coverage of the Nb₂O₅ layers was obtained onto GNPs by using high deposition rate. As discussed in above text, with increasing the power values the deposition rate increased and more sputtered particles are deposited onto GNPs. The sputtered particles were agglomerated onto GNPs with increasing RF power values. However, a certain

amount of agglomeration of Nb₂O₅ was observed. A highly dispersed Nb₂O₅ layer on the GNPs surface with large surface area is favorable to promote their interfacial contact. A uniform decoration of the Nb₂O₅ layer on the GNPs surface has potential advantage in catalytic activity and other application.

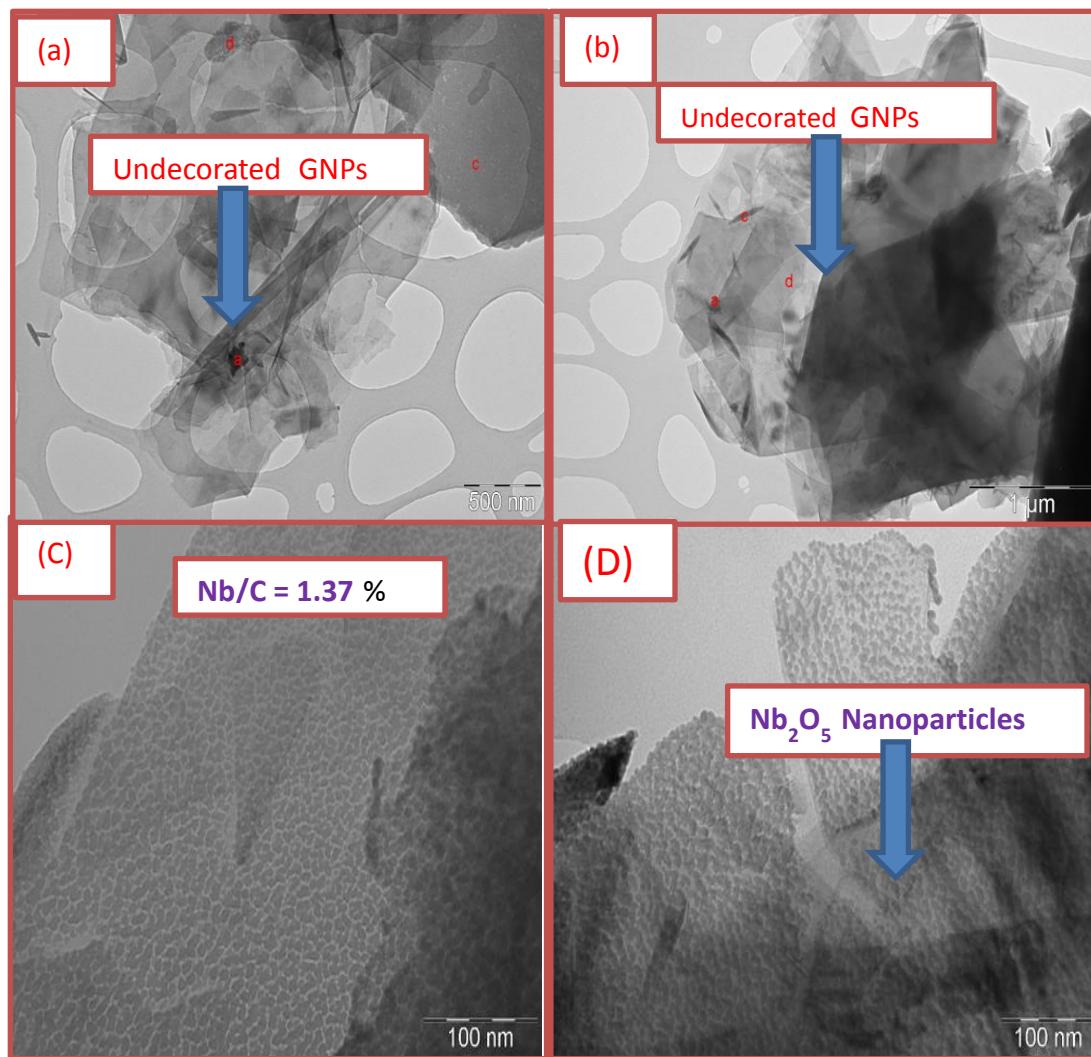


Fig 3. 7 TEM images (A-B) undoped GNPs and (C-D) Nb₂O₅ doped GNPs at 100 W

3.3.4 Raman study of undoped GNPs and Nb₂O₅ doped GNPs

The Raman spectra of Nb₂O₅ deposited at different RF powers shown in Fig. 3.8 (a) consist of four peaks. The so called D, G, D' and 2D peaks appear around 1330 cm⁻¹, 1580 cm⁻¹, 1610 cm⁻¹ and 2675 cm⁻¹ respectively. The G peak corresponds to the E_{2g} phonon at the Brillion zone

center. The G-band is highly sensitive to strain effects in sp² systems. The D band is a sign of either the existence of the disorder or the presence of any type of defects such as vacancy defects and the edges of the crystallite (i.e., the boundaries of the crystallite) [190,191,]. The 2D peak is originates in the process of the double resonance in which momentum conservation is accomplished by two phonon which are opposite wave vectors. Generally, 2D peak is always present in Raman spectra and it's required no defects to be originated. 2D peak is very sensitive to the electronic structure and the stacking order along the *c*-axis [192]. The Raman spectra of undoped GNPs and Nb₂O₅ doped GNPs at different RF power values are shown in Fig 3.8 (a).

The G and 2D peaks of Nb₂O₅ doped GNPs shifted to lower frequencies compared to undoped GNPs. The shift in G and 2D modes towards lower wavenumbers increased with rising of Nb/C sp² through RF power variation as shown in Fig 3.8 (b). The highest red shift is 10.8 cm⁻¹ and 24.68 cm⁻¹ for G and 2D peaks, respectively. There are several possible reasons reported in the literature for the shift of Raman peaks, including the effects of doping [193] and strain [194] The electron/hole doping in GNPs can affect the transition across the band gap with the interactions of optical phonons [195]. Hence the G band shows softening as well as bandwidth sharpening with doping [196]. G and 2D bands shift caused by charge doping through phonon-electron coupling in GNPs were reported by Kim e tal [197].

In case of a charge doping the shift in G band should be greater than the shift in 2D band [198]. Therefore, the red shift of G and 2D peaks observed in our case cannot be explained by charge doping and there should be other mechanisms. Tensile stress is reported to cause the red shift in graphene sheets [199]. The tensile strain lowering the vibration frequency of the phonon of GNPs due to the elongation of the elongation of C-C bonds [200]. More importantly lattice of the GNPs were distorted by the deposition of Nb₂O_{5-x}. Consequently by the deposition Nb₂O_{5-x} layers onto

GNPs the lattice constants of GNPs were enlarged, which lead to tensile strain in GNPs layers, which is in good agreement with the XRD results.

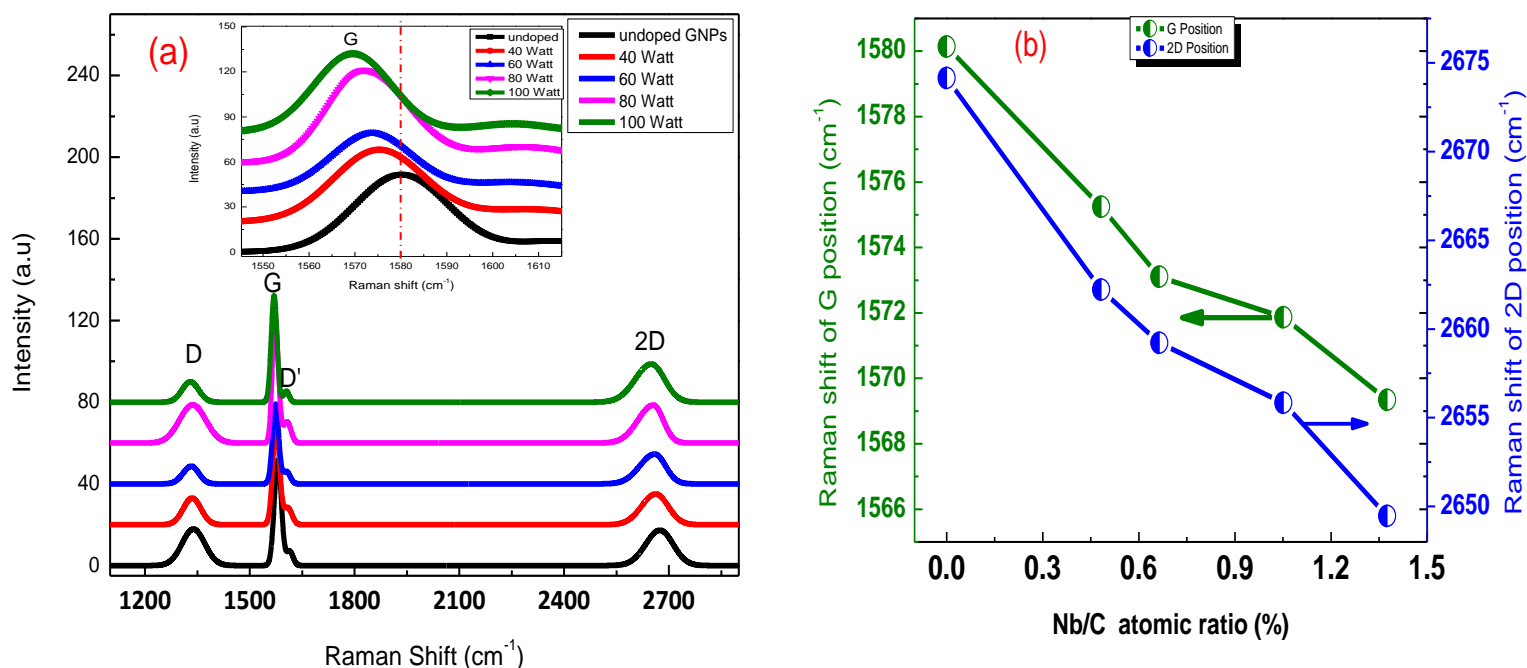


Fig 3. 8 (a) Raman spectra of undoped GNPs and (b) positions of the G and 2D peaks vs Nb/ C (sp²) at. ratio Nb₂O₅ doped GNPs at different RF powers

It is well established that the I_D/I_G peak ratio is used to measure the level of disorder, which is directly related to the diameter of the crystalline cluster (L_a) in the graphite system. For low disorder I_D/I_G ratio is known to be proportional to $1/L_a$ and to L_a^2 for high disorder. Ferrari and Robertson introduced a three-stage model of disorder in carbon materials, which allows to simply evaluating the disorder in carbon [201]. The first stage leads to nanocrystalline graphite (nc-G phase) from crystalline graphite. The second stage is related to the transformation of the nanocrystalline graphite into low sp³ amorphous carbon (a-C phase), and third stage is lead to low sp³ amorphous carbon (a-C phase) to high sp³ (tetrahedral) amorphous carbon. In the following, we refer to these three stages to quantify the impact of deposition of Nb₂O₅ on the structural quality of GNPs.

The first stage of disorder graphene sheets Raman spectrum can be explained as follow [124, 136]. I_D/I_G increases and D band appears b) all peaks broaden. In the case of graphite, the D and 2D peaks lose their doublet structure [202, 203]. However in the second stage of disorder graphene sheets can be evolved as follows ²⁰⁴a) the G peak position decreases b) Tuinstra and Koenig relation fails and I_D/I_G decreases. Tuinstra and Koenig relation is used for the measurement of in plane crystallite size $\propto (1/L_a)$ from the I_D/I_G ratio [205].

Fig.3.9 plots the ratio of the integrated area of the D and G peak for GNPs as function of Nb/C (sp²) obtained by the RF power. The intensity ratio of D band to G band (I_D/I_G) can serve as a convenient measurement of the amount of defects in graphitic materials [206]. It is noticeable that I_D/I_G ratio gradually decreased with increasing Nb/C (Sp²) atomic ratio (%). This corresponds to the second stage at which I_D/I_G ratio decreases as a function of increasing defects, which can be ascribed to a steady evolution from the sp² -bonded carbon found in graphene sheets into amorphous carbon with low sp³ bonding [207,208]. It can be explained as follows; with an increasing number of defects on the surface of GNPs through sputtered particles and plasma species interaction, hexagons in the honeycomb lattices are more distorted. More importantly with the interaction with the sputtered particles the I_D peak begins to attenuate with respect to I_G as a function of increasing defects and disorderness. Thus, with the loss of sp² rings, I_D will decrease and the I_D/I_G $\propto 1/L_a$ relation will no longer hold [208].

It means that the decrease of I_D/I_G is due to the main disordering related to the decrease in the number of sp² ordered rings [136]. Furthermore we can exclude the possibility of high sp³ bonding formation because in our case I_D/I_G does not go to zero and remain in the range 0.31 to 0.18 even for the highest RF power values. Also the FWHM of the G peak is found to be in the range

between $\sim 24.1\text{cm}^{-1}$ and 18.4 cm^{-1} , whereas the amorphous carbon with high sp^3 content would give a FWHM of $200\text{-}300\text{ cm}^{-1}$ [209, 210].

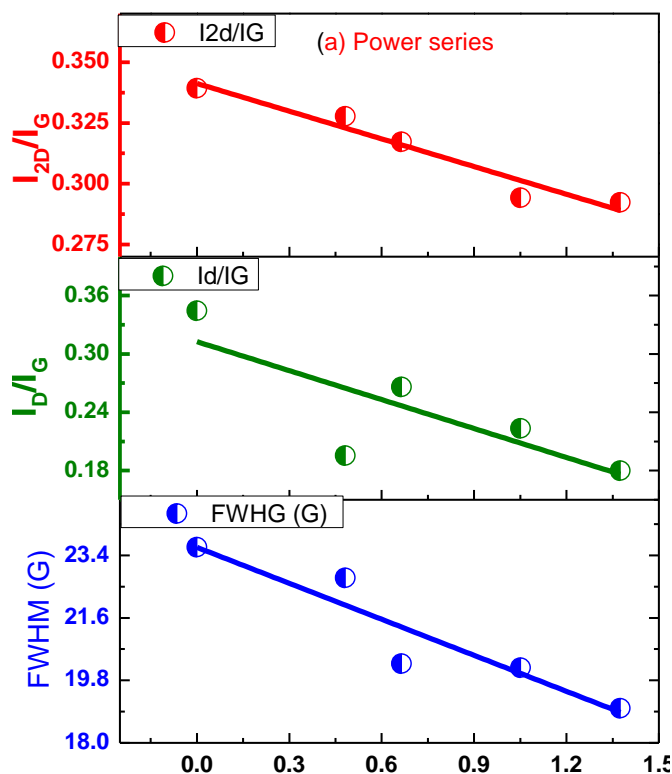


Fig 3. 9 Variation of Raman peak intensity ratios of I_D/I_G , I_{2D}/I_G and FWHM of the G peak plotted against the Nb to C atomic ratio (%).

Fig. 3.9 shows the changes of I_{2D}/I_G with the increase of Nb/C (sp^2). As can be seen, I_{2D}/I_G decreased almost linearly with the increasing of Nb/C (sp^2). In GNPs, the ratio I_{2D}/I_G decreases strongly with increasing doping level due to the additional electron-electron scattering contribution [211]. The intensity of 2D peak is strongly affected by the electron/hole and electron defects scattering rate. The defects generated into the lattice of GNPs with deposition of Nb₂O_{5-x} may increase the electron scattering rate and hence the intensity of 2D peak may decrease with the increase of defect/dopant concentration. Therefore, the I_{2D}/I_G decreases with increasing doping by Nb₂O₅ contents, i.e. defect density. Recent theoretical calculation predicted that

resonant scattering of electrons with short-range defects in GNPs dramatically increase the scattering cross section [212]. Such resonant scattering of electrons may arise in GNPs with high Nb₂O₅ doping, where the short-range defects are induced in GNPs by Nb₂O₅ doping.

The structural disorderness in disorder carbon can be measured by evaluating the FWHM of the G peak and the topological disorder can be measured by evaluating the shift in the position of the G peak [213]. More over the structural disorderness in graphene structure arises from the distortion of C-C bond length and bond angle. Topological disorder arises from the size and shape distribution of sp² clusters. FWHM (G) of the undoped GNPs and Nb₂O₅ doped GNPs as a function of Nb/C sp², are shown in Fig 3.9. It is found that FWHM (G) decreased from 23.63 cm⁻¹ and reached 19 cm⁻¹, when the Nb₂O₅ were deposited onto GNPs in a ratio Nb/ C sp²=1.37 atomic ratio (%). Meng et al is also reported that FWHM of GNPs decreased with charge doping[184]. This indicates that with deposition of Nb₂O₅ onto GNPs not only induced tensile strain in the plane of GNPs but also shows the doping behavior with deposition of the Nb₂O₅ layers.

3.4 The influence of Nb₂O₅ concentration on the structural and chemical properties of graphite Nanoplatelets deposited by varying the process pressure

In the section 3.3, the Nb₂O₅ were deposited onto GNPs surface by varying the RF power values and the deposition of Nb₂O₅ were carried at a constant process pressure value (6 Pa). It was found that defects were generated in the GNPs structure by the interaction of the high energy sputtered particles and plasma species. The process pressure one of the important deposition process parameter was used to deposit the Nb₂O₅ onto GNPs. The main goal of this section is to study the effect of the Nb₂O₅ concentration obtained on the surface of the GNPs by the variations of the process pressure. It is well established that the sputtered particles that are extracted from

the target adopt straight route during the deposition or either they are scattered in the plasma by single or multiple collisions with gas particles. In this perspective Nb₂O₅ were deposited onto GNPs surface at range of process pressures values from 2 Pa to 8 Pa. It was found that at low process pressure more defects and disorderness are induced in the structure of the GNPs compared to high process pressure. The defects and disorderness of decorated GNPs with Nb₂O₅ were characterized by Raman, XRD and XPS. Moreover the process parameters are described in table 3.2

Table 3.2 the process condition of decorated GNPs with Nb₂O₅ films

Sample #	RF Power (W)	Process pressure (Pa)	Deposition Time (min)	Powder vibration frequency (Hz)
1	40	2	15	10
2	40	3	15	10
3	40	4	15	10
4	40	5	15	10
5	40	7	15	10
6	40	8	15	10

3.4.1 XPS analysis of undoped GNPs and Nb₂O₅ doped GNPs at different process pressure values

Fig. 3.10 presents the XPS spectra of GNPs before and after deposition of Nb₂O₅ at different plasma process pressure values. The main peak with a binding energy 284.69 eV is attributed to carbon in C-C bond with sp² hybridization. Two other small components which have binding energies of 285.34 eV and 286.20 eV correspond to C-H /C-C bond with sp³ hybridization and C-O bond respectively. A shift toward the lower binding energy in the C 1s core level was

observed after the deposition of Nb₂O₅ onto GNPs at different process pressure values. The downshift of the C 1s core level increased with deposition of the Nb₂O₅ onto GNPs at low process pressure.

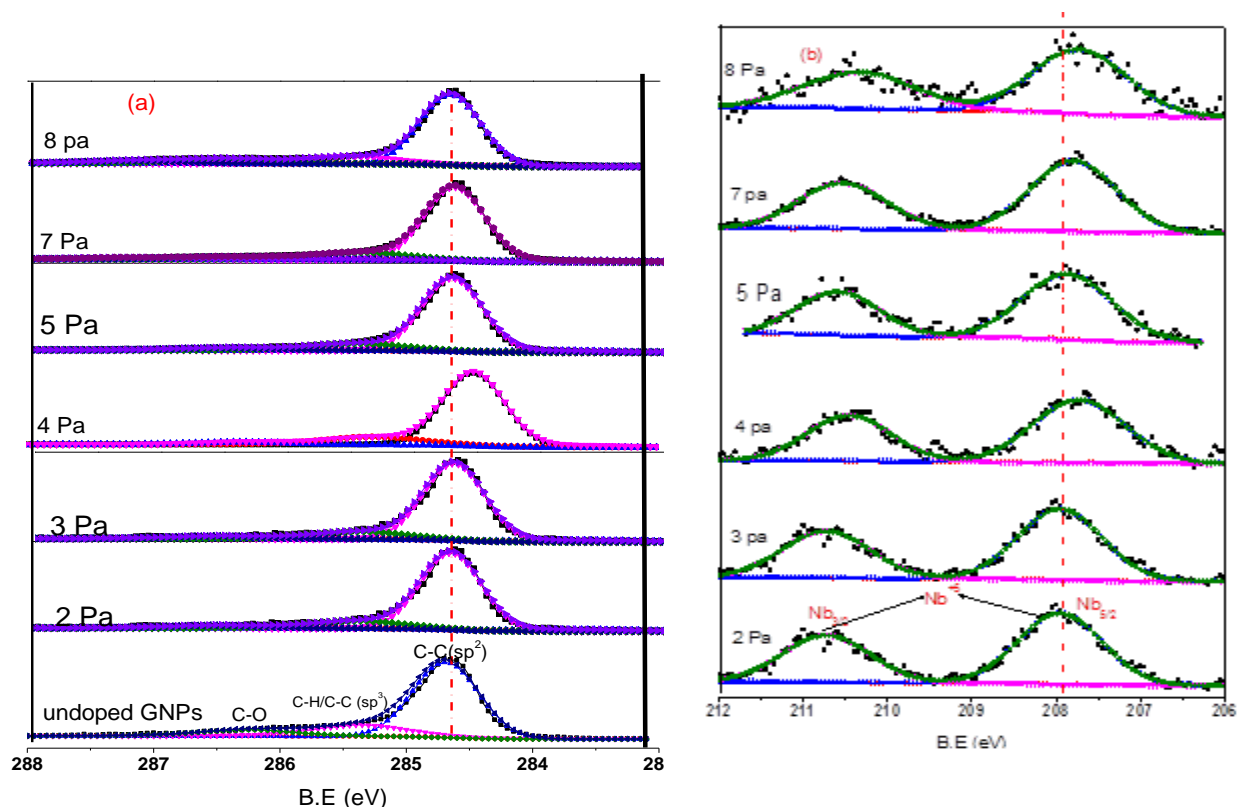


Fig 3. 10 XPS spectra of GNPs with incrementally increased of Nb₂O₅ contents through process pressures variation (a) (a) Shift in the C 1s core levels position upon Nb₂O₅ deposition (b) Nb 3d core level spectra with positions of the Nb⁺⁵ peaks. [Process pressure = 6 Pa, Time=15 min, Frequency = 10 Hz].

The downshifts in the C 1s core level were further increased with increasing of Nb₂O₅ concentration onto GNPs surface with variation of the process pressures values. The C 1s core level were further shifted to lower binding energy by 0.23 eV with respect to the undoped GNPs, when the Nb₂O₅ were deposited onto GNPs at 4 Pa process pressure in a ratio Nb/C sp²=0.53 at. %. The downshift of the C 1s core level after the deposition of the Nb₂O₅ layers onto GNPs is the indication of the p-type doping of graphene, where the electrons are transferred from the GNPs to Nb₂O₅ layers at interface. The maximum downshift of the C 1s core level after the deposition

of Nb₂O₅ layers onto GNPs at 4 Pa could be in agreement with increasing structural disorderness due to the disruption in the sp² carbon framework upon the deposition of Nb₂O₅. The similar phenomenon has been explained by the C. Coletti²². They described that the structural defects and disorderness is also shift the Fermi level from its position.

Figure 3.11 (b) shows the Nb 3d XPS core level for Nb₂O₅ layer deposited on GNPs at different process pressure values. The binding energy of the Nb 3d_{5/2} and 3d_{3/2} were 207.89 and 210.72 eV respectively, which corresponds to the Nb⁺⁵ state. Nb 3d peaks were shifted to the lower binding energies values by the deposition of the Nb₂O₅ onto GNPs at different process pressure values. The maximum downshift of 0.26 eV was observed in the Nb 3d core level with deposition of Nb₂O₅ onto GNPs at 4 Pa. The downshift of the Nb 3d core level suggests that the charge is transferred from graphene to the Nb₂O₅ layer due to the difference of the work function. The band of the Nb₂O₅ bends towards the interface after the charge accumulation in the band of Nb₂O₅.

Fig 3.11 (a) shows the O 1s peak deposited at 4 Pa process pressure. After the deposition of the Nb₂O₅ the O 1s spectra has been de-convoluted into three components. The component OI which has a BE of 530.973 eV is assigned to oxygen bonded with Nb (O-Nb). A second component OII having a BE energy of 532.18 eV, may arise due to the oxygen contribution in possible C=O bond [¹⁸⁰] The 3rd component (O III) at higher BE 533.62 eV is from C-O bond [¹⁸¹].

Furthermore, the oxide stoichiometry of deposited Nb₂O₅ on GNPs surface and atomic ratio of Nb/C (Sp²) is also assessed form the XPS analysis and the values are presented in Fig 3.11 (b). It can be seen that OI/Nb are in the range 2.18 -2.39 corresponding to the stoichiometry of Nb₂O_{5-x}. It was found that the calculated OI/Nb ratio at low process pressure values (2 Pa to 4 Pa) was in the range of 2.18 to 2.24 and the evaluated OI/Nb ratio for the high process pressure values (5 to

8 Pa) was in the range (2.28 to 2.42). This shows that more oxygen vacancies are generated in the lattice of Nb₂O_{5-x} with respect to high process pressure values

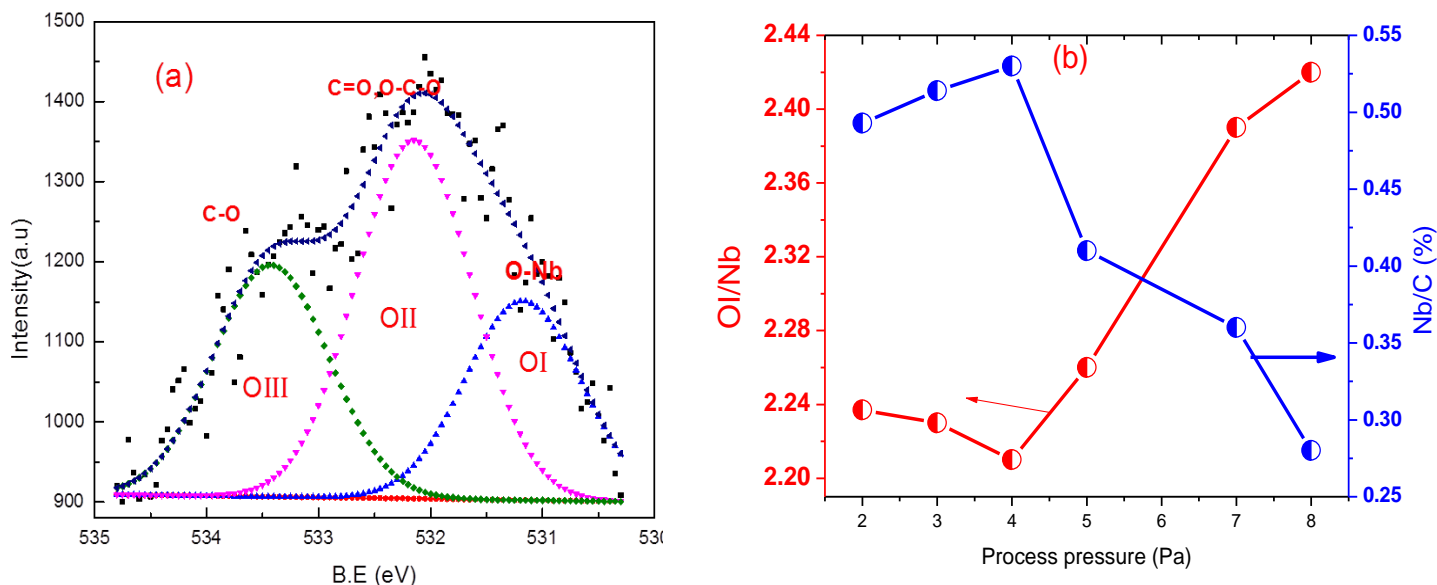


Fig 3. 11 (a) De-convolution of the O 1s core level (b) Variations of Nb/C and OI/Nb with respect to process pressure

This can be elucidated by the fact that at low process pressure values the sputtered particles and the plasma species interacted with layers of graphene more energetically generating oxygen vacancies in the lattice of Nb₂O₅. Also the Nb/C ratio at low process pressure values (2 Pa to 4 Pa) was obtained onto the GNPs surface in a ratio from (0.51 to 0.53 at. %) and for the high process pressure values (5 to 8 Pa) the Nb/C ratio was obtained in the (0.38 to 0.25 at. %).

3.4.2 XRD analysis of undoped GNPs and Nb₂O₅ decorated GNPs at different working pressure values

Fig 3.12 (a) shows the XRD patterns of undoped and Nb₂O₅ doped GNPs at different working pressure values. The XRD spectra shows that the crystal structure is hexagonal for all diffraction peaks that are indexed to the peaks of graphite (hexagonal) structure (ICDD card # 65-6212)

with lattice constants $a = 2.464 \text{ \AA}$ and $c = 6.71 \text{ \AA}$. We observed significant changes in the XRD patterns with Nb₂O₅ doping into the GNPs at different working pressures. The enlarged view of (002) peak of undoped GNPs and Nb₂O₅ doped GNPs shows two different behaviors with working pressure variation. One is at low working pressures (2-4 Pa), in which the (002) diffraction peak for the Nb₂O₅ doped GNPs was shifted towards the lower angle values with respect to the undoped GNPs. The second is at high working pressures (5 - 8 Pa), in which the (002) the peak shift is less pronounced with respect to lower pressure range (2-4 Pa) as shown in Fig 3.12 (b). These two behaviors can be explained as follows; in plasma process sputter deposition plasma is used as the source of charged species (electrons, ions). These high energetic ions extract few clusters and atoms from the target during the sputtering process, which are subsequently deposited on substrate [40]. The said scenario successfully explained the so-called Keller-Simmons (K-S) formula, a well-known empirical equation [214].

$$r = r_o \left(1 - \frac{K}{P} \exp \left\{ -\frac{P}{K} \right\} \right) \dots \dots \dots (5)$$

$$K = \frac{(Pd)_o}{d}$$

Where r is the deposition rate, p is the total pressure, d is the distance between target (cathode) and substrate, r_o is the deposition rate without scattering losses, and $(Pd)_o$ is an adjustable parameter called characteristic pressure-distance product.

The above equation illustrates the scattering of sputtered particles by gas atoms and molecules between the target and the substrate. The equation 5 shows that how deposition rate can vary with pressure when the substrate and target distance is fixed. Addition to this, concerning the sputtering theory, particles emitted from the target hold an energy spectrum

$\phi_o \propto E(E + U)^{-3} \cos \theta$ with the kinetic energy E, the surface binding energy U and the emission angle θ [215, 216].

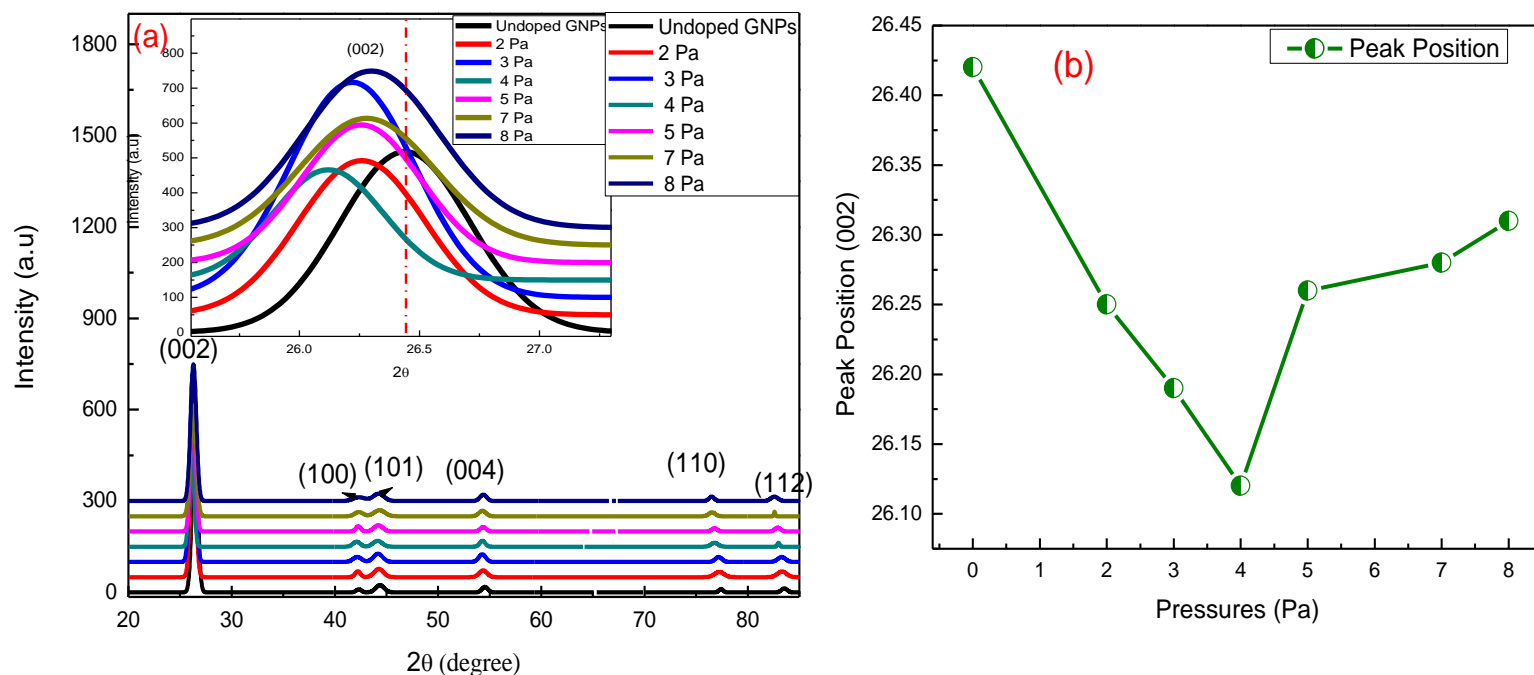


Fig 3.12 (a) XRD patterns Nb₂O₅ doped GNPs (b) Variation of the 2θ angle of the (002) at different working pressure peak with different working pressure process pressures

This indicates that sputtered particles are highly directed in the direction perpendicular to the cathode with high kinetic energies. In this way, equation (5) satisfies two main contributions i) the arrival of sputtered atoms which have conserved their original kinetic energy and directionality at the substrate surface, and ii) the arrival of sputtered atoms that have been thermalized by the plasma gas. Our XPS results showed that the deposition rate of Nb₂O_{5-x} was higher at low working pressures, (ratio of Nb/C is higher). At low pressure, the rate of deposition increases with total pressure until 4 Pa, where a maximum was reached. For higher pressure, the deposition rate decreases with pressure. The impact of the energetic sputtered particles does not only lead to a change in the deposition rate, but also has a noticeable influence on the structure of GNPs. The enlarged view of the (002) peak (inset) shows that the FWHM of (002) peak at low

working pressure broadened, indicating deterioration of the crystallinity of the GNPs. Also at low working pressures, the (002) peak intensity of GNPs became weaker, implying an increase of the disorder in GNPs. Furthermore, the bombardment of the sputtered particles and plasma species induced a significant strain in the GNPs, (as it will be described in the next section). At last we can conclude that the XPS result show that the Nb/C (sp²) increased at low working pressures. Also from the XRD analysis results it was observed that the disorderness increased at low working pressure.

The lattice parameters “a” and “c” of undoped and Nb₂O₅ decorated GNPs at different process pressure were calculated from the reflection of the planes (100) and (002) using equation (2). Fig. 3.13 shows the dependence of the calculated lattice parameters (“a” and “c”) of the GNPs with Nb₂O_{5-x} amount obtained by varying working the pressure values. The lattice parameter c’ and ‘a’ of GNPs linearly increased with rising Nb/C (sp²). The maximum elongation along ‘c’ axis is about 0.081 Å when Nb₂O_{5-x} incorporated to the lattice of GNPs in an atomic ratio (0.58 %) to C (sp²) at low working pressure. The possible reason for the elongation along ‘c’ and ‘a’ axis is that at low working pressure the plasma species and sputtered particles interacted with layers of GNPs more energetically. More possible reason for the elongation of the of ‘c’ and ‘a’ axis are that, by interaction of the GNPs with high energetic species and sputtered particles strain were induced in the planes of the GNPs.

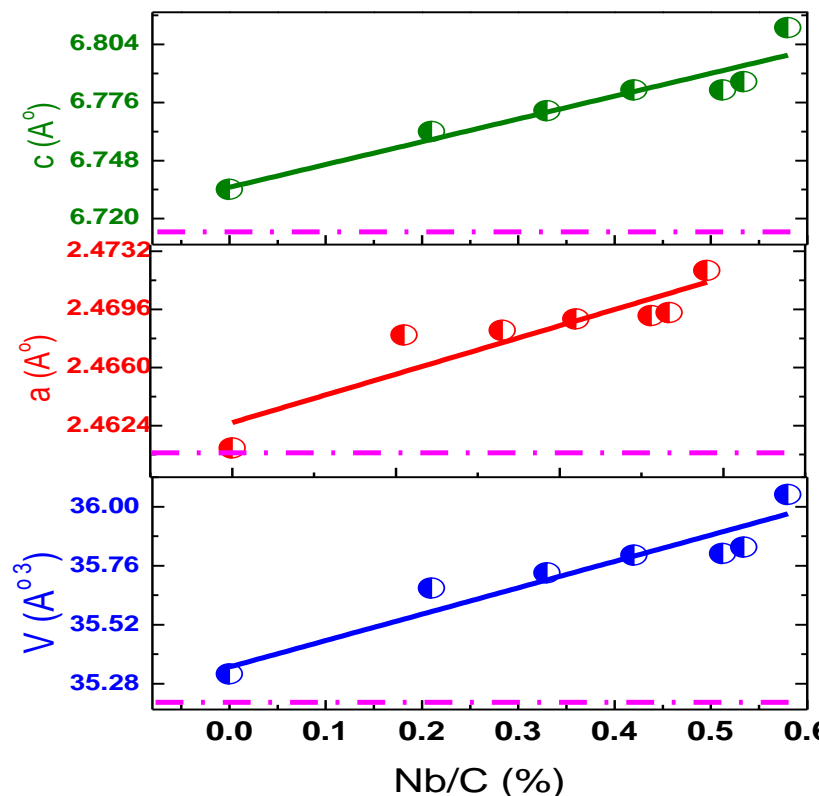


Fig 3. 13 Lattice parameters “a” “c” and cell volume V of GNPs with various Nb₂O₅-doping levels through variation of process pressure (the dashed line indicate a, c, and v values of bulk graphite).

3.4.3 Raman study of undoped GNPs and Nb₂O₅ doped GNPs at different process pressure values

Fig 3.14 (a) shows the Raman spectra of undoped GNPs and Nb₂O₅ doped GNPs at different working pressure values. The working pressure had a strong influence on the structure of GNPs. Two different behaviors were observed in Raman spectra (inset shown in Fig 3.14 (a)) for the deposition of Nb₂O_{5-x} onto GNPs by varying the process pressure. At lowest process pressure values (2 to 4 Pa), for lower process pressures values the G and 2D bands of the decorated GNPs with Nb₂O₅ are shifted toward lower wavenumbers with respect to the undecorated GNPs. The Nb/C (sp²) ratios increased from 0.50 at. % and reached 0.58 at. %, when the Nb₂O₅ deposited onto GNPs at lower process pressure values (2 to 4 Pa). The shift in G

and 2D for the decorated graphene with Nb₂O₅ layers as a function of Nb/C sp² are presented in 3.15 (b).

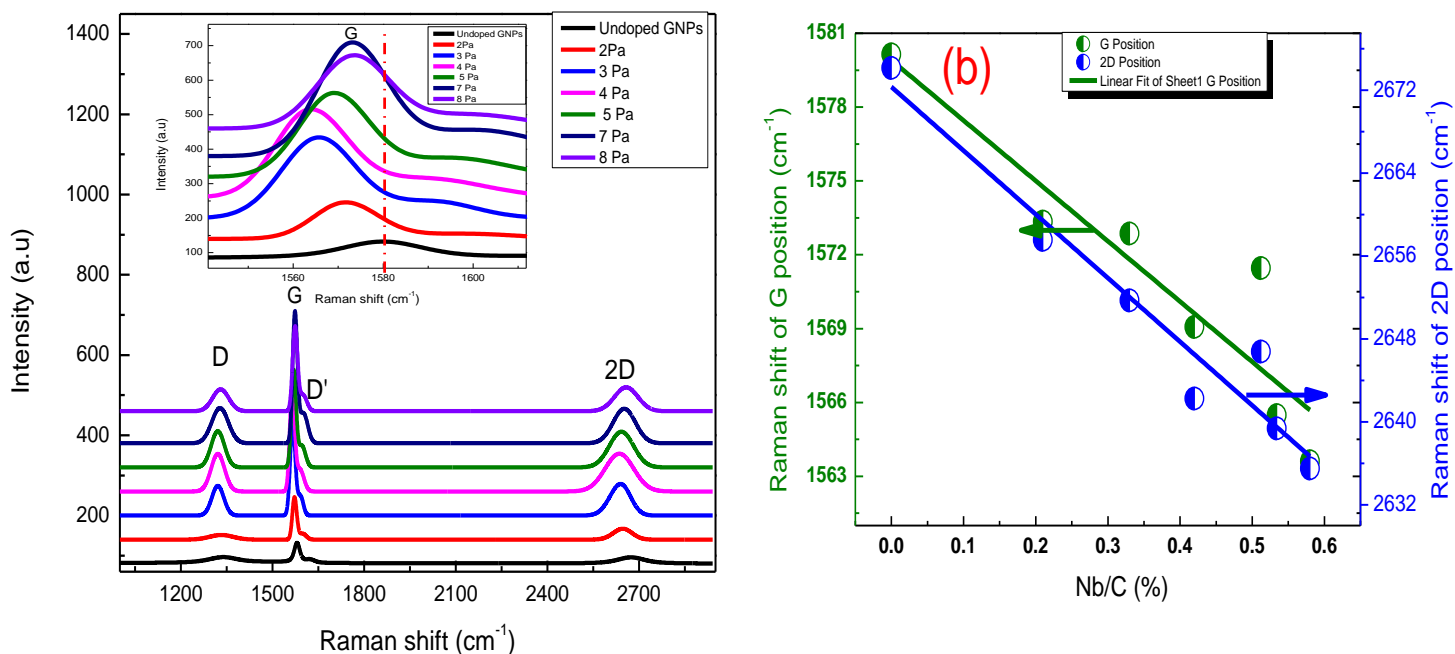


Fig 3. 14 (a) Raman spectra of undoped GNPs and Nb₂O₅ doped GNPs at different working pressure

(b) position of the G and 2D peaks vs Nb/C (%)

The highest red shift of G and 2D are 16.53 cm⁻¹ and 30.5 cm⁻¹ respectively, when Nb₂O_{5-x} deposited on GNPs in a ratio of Nb/C equal to (0.58 at. %) obtained at low working pressure values. This high red shift can be explained as follow, at low working pressures the mean free path λ for the sputtered particles, which accounts for the typical average distance covered by the sputtered atoms in the plasma gas species, is longer. Consequently, the sputtered particles undergo less-frequent collisions with plasma species and these sputtered particles deposited on the GNPs surface with higher energy [217]. Deposition of the Nb₂O₅ onto GNPs at low process pressure values generates the stress in the layers of GNPs due to the interaction of energetic plasma species and sputtered particles. As already discussed that at low process pressure values

the sputtered and plasma species are less frequent collision during the deposition process. Direct interaction of the energetic sputtered particles and plasma species with GNPs layers induced the stress the in the lattice of the GNPs. Accordingly by the interaction of the energetic sputtered particles with layers of the GNPs, the tensile strain was established in the planes of GNPs and eventually breaks the A-B symmetry of GNPs, which could effectively change the electronic band structure of GNPs. Likewise for higher working pressure values from (5 Pa to 8 Pa), the red shift for G and 2D bands are 6.81 cm⁻¹ and 15.5 cm⁻¹ respectively, when Nb₂O_{5-x} contents was deposited onto GNPs in ratio of (0.25 at. %) to C (sp²). This behavior can be explained by the fact that with increasing the working pressure, thermalization mean free path λ for the sputtered species was decreased. The sputtered species undergo many collisions inside the plasma and as a result, fewer low energy sputtered particles arrive at the surface of GNPs produced less red shift in G and 2D modes compared to low working pressure (2-4 Pa). These consequences are consistent with the XRD results.

3.5 Effect of Nb₂O₅ concentration on the structural and chemical properties of graphite nanoplatelets decorated by varying powder vibration frequencies

In the above two sections (3.3-3.4), the influence of Nb₂O₅ concentration onto GNPs by varying RF power values and process pressure values were discussed. In both sections Nb₂O₅ films were decorated on the surface of the GNPs with low vibration frequency of the powders. The powder vibration frequency is an important parameter and plays a vital role for the uniform decoration. The main objective of this work was to study the decoration of the Nb₂O₅ layer onto GNPs surface and the influence of the Nb₂O₅ concentration by varying different powder variation frequencies during the deposition process. For this purpose a sample holder stage previously designed to vibrate GNPs powder during the deposition process was used. In this context, Nb₂O₅

layers were deposited onto GNPs surface with powder vibration frequencies $0 \leq \omega \leq 100$ Hz with constant amplitude of 32 μ m. It was found that with high powder vibration frequencies, more sputtered particles were deposited on the GNPs with respected to the deposition of Nb₂O₅ onto GNPs without moving the GNPs powder. The detailed structural and chemical properties were studied using XRD, Raman and XPS techniques. Moreover the process parameters are presented in table 3.3.

Table 3.3 the process condition of decorated GNPs with Nb₂O₅ films

Sample #	RF Power (W)	Process pressure (Pa)	Deposition Time (min)	Powder vibration frequency (Hz)
1	40	6	15	0
2	40	6	15	10
3	40	6	15	50
4	40	6	15	100

3.5.1 Chemical analysis of undoped GNPs and Nb₂O₅ doped GNPs deposited at different powder vibration frequencies

The high resolution XPS spectra of undecorated graphene and decorated graphene with Nb₂O₅ layers at different powder vibration frequencies are illustrated in Fig 3.15. Fig.3.15 (a) shows de-convolution of the C1s peak of the GNPs and decorated GNPs with Nb₂O₅ films deposited at different powder vibration frequencies.

The C 1s core level were de-convoluted the three Gaussian peaks one centered at BE 284.69 eV corresponding to C-C Sp² hybridized carbon, the other peaks centered at binding energy at 285.32 eV to sp³ hybridized carbon (C-C)/C-H [218] and at 286.24 eV are attributed to C-O bonding configurations due to oxidation from the moisture

Fig.3.15 (b) shows the high resolution XPS spectra of Nb 3d for Nb₂O₅ decorated on GNPs surface at different powder vibration frequencies. To study the chemical state of Nb₂O₅, the peaks of the Nb 3d_{5/2} and Nb 3d_{3/2} core levels are at binding energies of 208.07 eV and 210.72 eV respectively. This suggests that one chemical state has been observed for the Nb which is designated to Nb⁺⁵[²¹⁹].

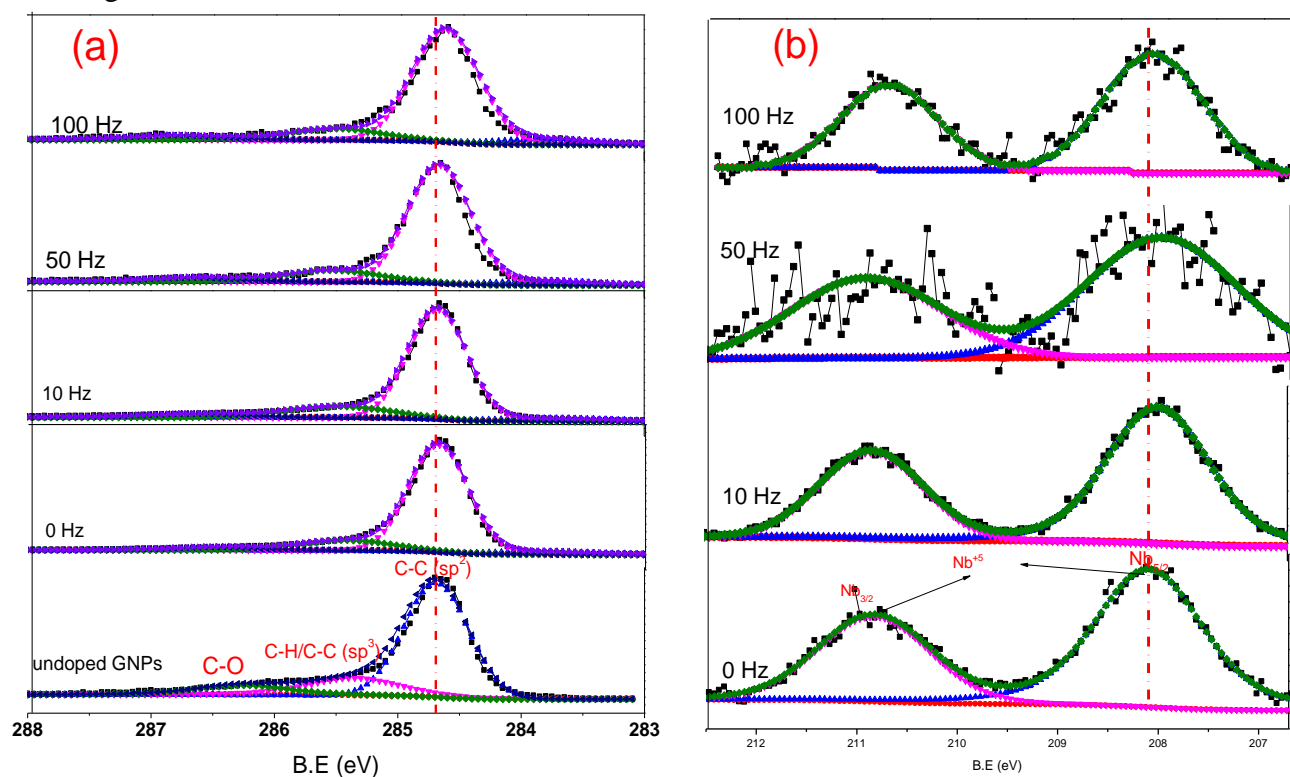


Fig 3. 15 (a) XPS spectra of GNPs with incrementally increased of Nb₂O₅ contents through different powder vibration frequency (a) C 1s core levels with marked positions of the C-C (sp²) bond and the shift of this position upon Nb₂O₅ deposition. (b) Nb 3d core level spectra with o positions of the Nb⁺⁵. [Process pressure = 6 Pa Time=15 min, Frequency = (0 to 10 Hz) RF power value =40 W]

The O 1s XPS spectrum of decorated GNPs with Nb₂O₅ films deposited at 100 Hz powder vibration frequency is presented in Fig 3.16 (a). The O 1s core level was de-convoluted into three components. The component OI which has BE energy of 530.92 eV corresponds to bond O-Nb. The second component has a BE energy position of 532.182 eV, it may arise due to the oxygen

contribution in possible C=O [65]. The 3rd component (O III) at higher BE 533.96 eV is from C-O bonding [65]. The OI/Nb and ratio was measured for all samples on the basis of the area under the main component of the oxygen (OI) and the area under the Nb_{5/2} component and sensitivity factors. The evaluated OI/Nb ratio as a function of powder vibration frequencies is presented in Fig 3.16 (b). The stoichiometry of the deposited Nb₂O_{5-x} lowers than ideal value (2.5), which suggests that, the deposited Nb₂O₅ layers onto GNPs were under stoichiometric. Also Nb/C sp² ratios as function of the powder vibration frequencies are also presented in Fig 3.16 (b). It was found that the Nb/C sp² ratio increased with rising powder vibration frequencies.

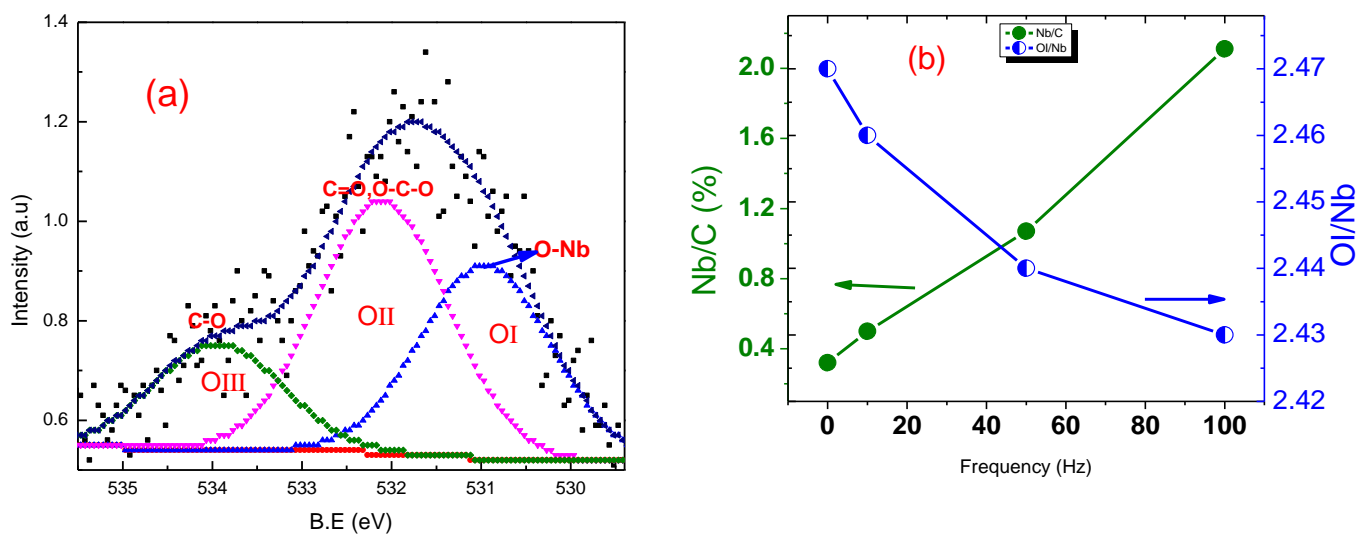


Fig 3. 16 (a) De-convolution of the O 1s core level (b) variations of Nb/C and OI/Nb as a Function powder vibration frequencies

3.5.2 Structural analysis of undoped GNPs and Nb₂O₅ doped GNPs at different powder vibration frequencies

Fig.3.17 (a) depicts the XRD patterns of undoped and Nb₂O₅ decorated onto GNPs with different powder vibration frequencies. The characteristic peaks of the undoped GNPs at position 26.44°, 42.41°, 44.53°, 54.62°, 77.63° and 83.43° correspond to the reflections of the planes (002), (100/101), (004), (110) and (112) respectively. It can be seen that with high powder vibration

frequency noticeably variation was observed in the intensity of GNPs peaks with respected to without moving GNPS powder. Here we compared the impact of the Nb₂O₅ on the moving GNPs powder and without moving GNPs powder during the deposition. The (002) peak became broader and less intense for the powder vibration frequency of 100 Hz, which indicates a less graphitic ordered of GNPs. However the enlarged view of the peak (002) in the inset in Fig 3.17 (a) shows that the peak is more shifted toward lower angle values with high powder vibration frequencies compared to undoped GNPs.

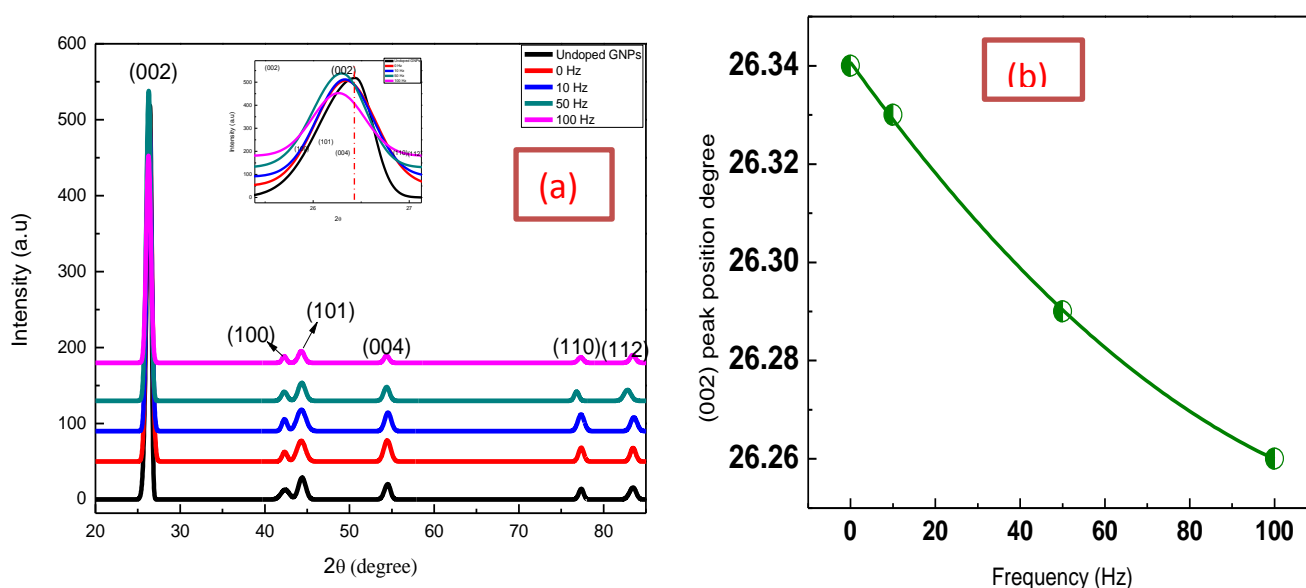


Fig 3. 17 (a) XRD patterns Nb₂O₅ doped GNPs (b) Variation of the 2θ angle of the (002) at different powder vibration frequencies peak with through varying powder vibration frequencies (RF power =40 W deposition time =15 min and process pressures =6 Pa)

This suggests that the interlayer d –spacing of the GNPs increased with raising the Nb₂O₅ concentration. Significant enhancement in the deposition rate was observed for the high powder vibration frequency with respect to the case without moving GNPs powder. At $\omega = 0$ Hz (no vibration to the GNPs powder) the sputtered particles were deposited at certain areas of the GNPs flakes. For the low vibration frequency at $\omega = 10$ Hz, the GNPs powder starts vibration

motion with respect to the sputtered particles by means of fixed amplitude of 32 μm during the deposition process. Consequently there is more possibility for the sputtered particles to deposit at large surface area of the GNPs with respect to the case of without moving (0 Hz) GNPs powder. It should be noted that, in both process of deposition the same deposition parameters were used to deposit Nb₂O₅ films onto GNPs. But the Nb₂O₅ films were coated only the surface powder and the beneath surface of the GNPs flakes were not covered with sputtered particles in case of without moving (0 HZ) GNPs powder. With high powder vibration frequency (100 Hz) the sputtered particles coated the whole GNPs surface. High surface area of the GNPs exposed to the sputtered particles during the deposition process. The above mentioned phenomenon can be explained as follows, our XPS analysis shows that by increasing the powder vibration frequencies more Nb₂O₅ concentration were obtained onto GNPs., XPS is a surface technique and gives the information of the coated surface of the GNPs upto 100 nm. Therefore, it can be considered that, the decoration of the GNPs with Nb₂O₅ films by means of high powder vibration frequency, the sputtered particles anchored over larger area of the GNPs surface with respect to the case without moving GNPs powders. These observations indicate that with deposition of Nb₂O₅ onto GNPs by increasing powder vibration the planes of GNPs are more distorted with increasing powder vibration frequencies.

The calculated lattice parameters “a” and “c” of undoped GNPs and Nb₂O₅ doped GNPs at different powder vibration frequencies from the reflection of the planes (100) and (002) are presented in Fig.3.18. The lattice parameters “a” &”c” increased linearly with rising of Nb/C (sp²). The increase of lattice parameters values suggest that, with interaction of the sputtered particles the planes of the GNPs were distorted and the tensile strain were established in the plane of GNPs.

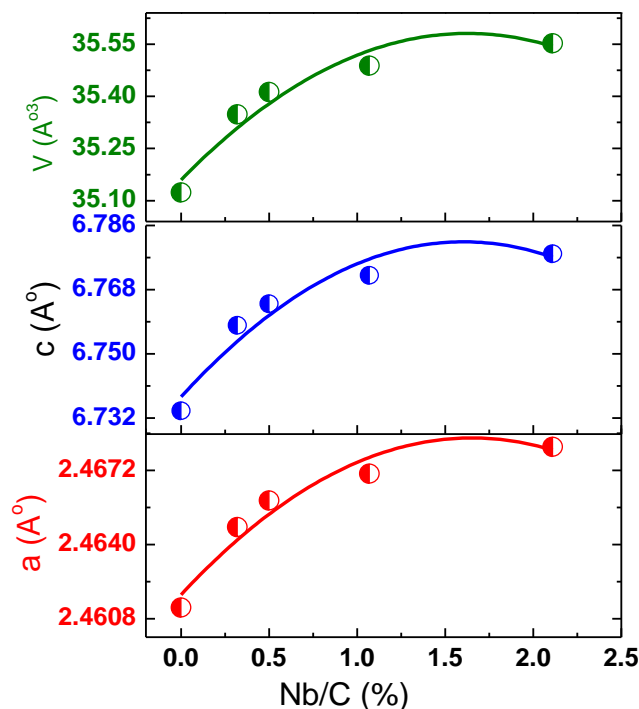


Fig 3. 18 Lattice parameters “a” “c” and cell volume V of GNPs with various Nb₂O₅-doping levels through varying powder vibration frequencies

Microstrain (\mathcal{E}) and crystalline size (L_c) (the crystalline coherence length in the 002 direction) of undoped GNPs and Nb₂O₅ decorated onto GNPs at different powder vibration frequencies were calculated using equation (4).

The crystallite size of undoped GNPs and Nb₂O₅ films decorated onto GNPs at different powder vibration frequencies are presented in Fig.3.19. The crystallite size of the GNPs decreased with rising of Nb/C (sp²) atomic ratio (%). The decrease of the crystallite size can suggest that with decoration of the GNPs by Nb₂O₅ at different powder vibration frequencies the more sputtered particles and plasma species interact to the basal plane of the GNPs. During the deposition process the sputtered particles and plasma species interacted with basal planes of the GNPs. These plasma species and sputtered particles degraded basal plane of the GNPs. Consequently, due to the degradation of order of the basal plane the crystallite sizes of decorated GNPs along

the c-axis decreased. Moreover the strain induced in the lattice of the GNPs after the deposition of Nb₂O₅ films onto GNPs.

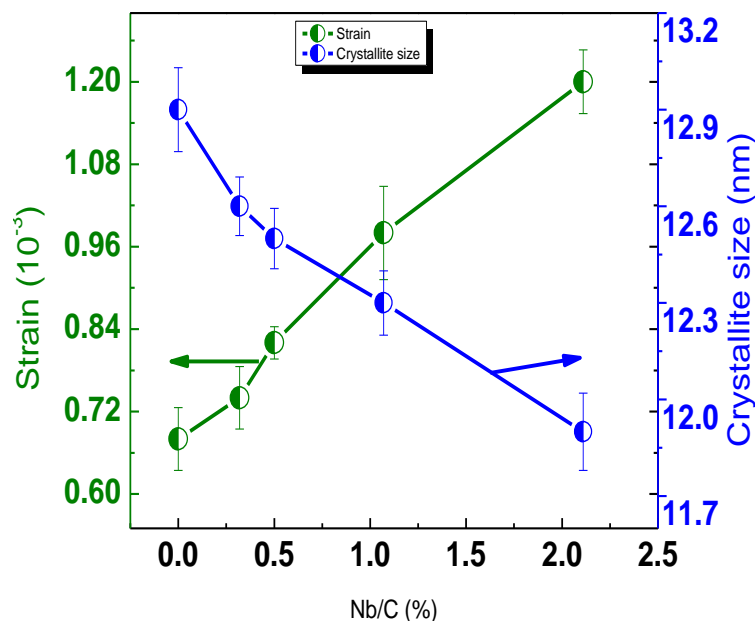


Fig 3. 19 Crystallite size and strain of the GNPs as function of Nb/C atomic ratio (%).

Williamson Hall plot confirmed that the Nb₂O₅ induced a tensile strain in the lattices of the GNPs. This suggests that after decoration of Nb₂O₅ films the lattice constant of the GNPs increased. From the Fig 3.20 it can be seen that strain increases with rising of Nb/C (sp²). It is correlated with cell volume of the GNPs. The cell volume of the GNPs increases with rising of the Nb/C (sp²).

3.5.3 Raman study of undoped GNPs and Nb₂O₅ doped GNPs at different powder vibration frequencies

Fig 3.20 (a) presents the Raman spectra of undoped GNPs and Nb₂O₅ deposited on GNPs with different powder vibration frequencies. The deposition of Nb₂O₅ with variation of the powder vibration frequencies strongly affected the structural and electronic properties of GNP, as the Raman spectra show that with high powder vibration frequencies the D, G and 2D bands

position, intensity and FWHM drastically changed. We observed a red shift in G and 2D bands after the deposition of Nb₂O₅ on GNPs using high powder vibration frequencies. Also this red shift increases with rising of Nb₂O_{5-x}, when varying the powder vibration frequencies as shown in Fig 3.21 (b).

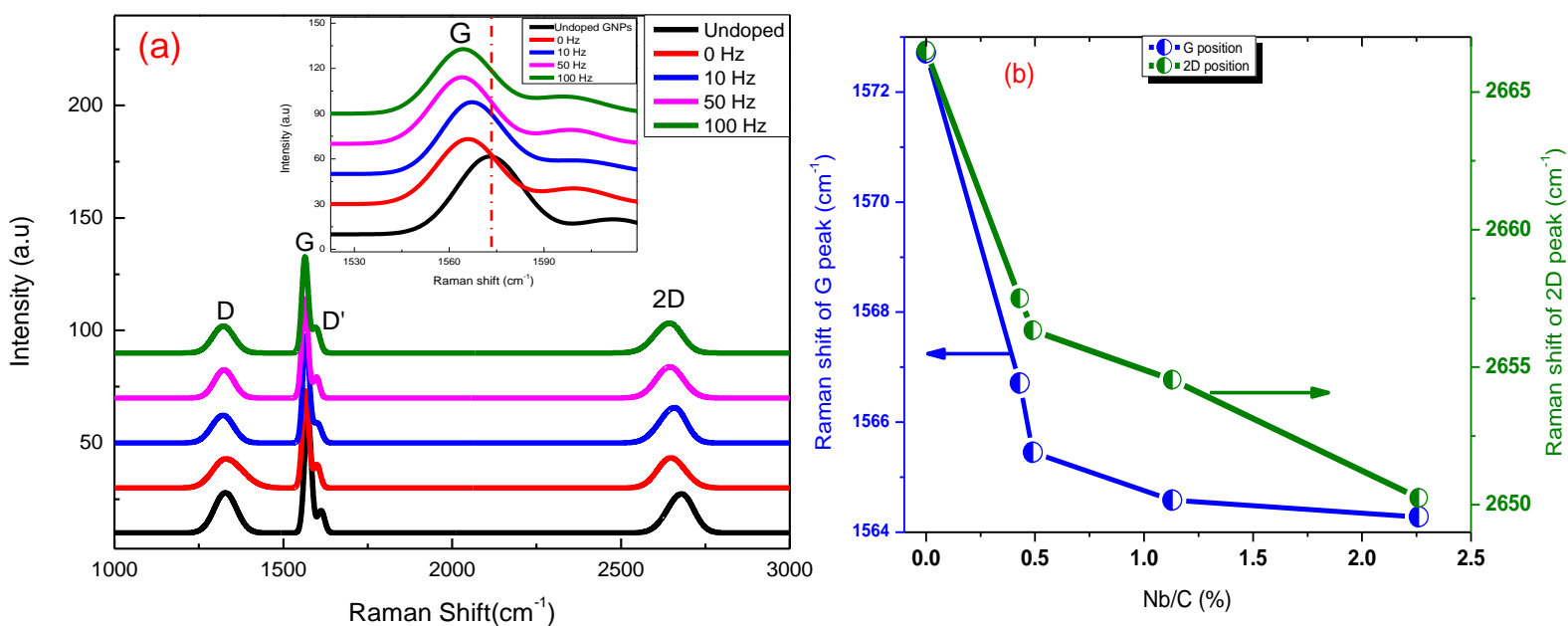


Fig 3. 20 (a) Raman spectra of undoped GNPs

(b) position of the G and 2D peaks vs. Nb/C (%)

and Nb₂O₅ doped GNPs at different sample vibration frequencies.

The red shift in G and 2D were also observed for the decorated GNPs with Nb₂O₅ without moving powder (0 Hz). But the red shift observed in the G and 2D in case of without moving GNPs powder was less than with respect to the red shift observed for the decorated graphene with Nb₂O₅ by means of high powder vibration frequency (100 Hz). The maximum red shift of G and 2D in the case without moving powder was 6.80 cm⁻¹ and 9 cm⁻¹ with respect to undoped GNPs. However in the case of high powder vibration frequency (100 Hz), the maximum red shift in G and 2D was 8.5 cm⁻¹ and 16.4 cm⁻¹ observed., This high red shift in G and 2D peaks for

GNPs bands with high powder vibration frequencies compared to the case without moving powder vibration (0 Hz) could be due to the more Nb₂O₅ deposited onto the GNPs.

As explained in the XPS section with high powder vibration more sputtered particles are decorated on the surface of the GNPs. This high redshift of the G and 2D in case of high powder vibration frequencies can be explained as follows, by the deposition of Nb₂O₅ films onto GNPs at different powder vibration frequency generates the structural defects in the plane of the GNPs and these structural defects modified the lattice of the GNPs, which could change the electronic properties of the GNPs. Accordingly, the crystal phonon energy of the lattice of GNPs with interaction of Nb₂O₅ films is lowered due to the due the enlarged the lattices of GNPs.

3.6 Effect of Nb₂O₅ concentration on the structural and chemical properties of graphite nanoplatelets decorated by varying deposition time

The influence of the Nb₂O₅ contents onto GNPs studied by the variation of the sputtered ions energies and plasma species by varying RF powers and process pressures was studied in the above section. Also we concluded that the high energy sputtered particles induced large disorderness in the structures of the GNPs. In this section the Nb₂O₅ films were deposited onto GNPs by keeping constant ion energy at constant RF power value and only increased the amounts of the Nb₂O₅ onto GNPs surface. The different amounts of Nb₂O₅ onto GNPs were obtained by stepping up the deposition time. The structural disorderness and the defects were characterized by XRD and Raman techniques and the chemical analysis of decorated graphene with Nb₂O₅ was characterized by XPS analysis. The condition of the process parameters are presented in table 3.4

Table 3.4 the process condition of decorated GNPs with Nb₂O₅ films

Sample #	RF Power (W)	Process pressure (Pa)	Deposition Time	Powder vibration frequency (Hz)
1	40	6	10	10

2	40	6	20	10
3	40	6	30	10
4	40	6	45	10

3.6.1 Chemical analysis of undoped GNPs and Nb₂O₅ doped GNPs at different time of deposition

Fig 3.21 depicts the XPS core levels of undecorated GNPs and decorated GNPs with Nb₂O₅ films at different times of deposition. The high resolution C 1s core level of the undecorated GNPs and decorated GNPs with Nb₂O₅ films at different times of deposition are presented in Fig

3.21 (a).

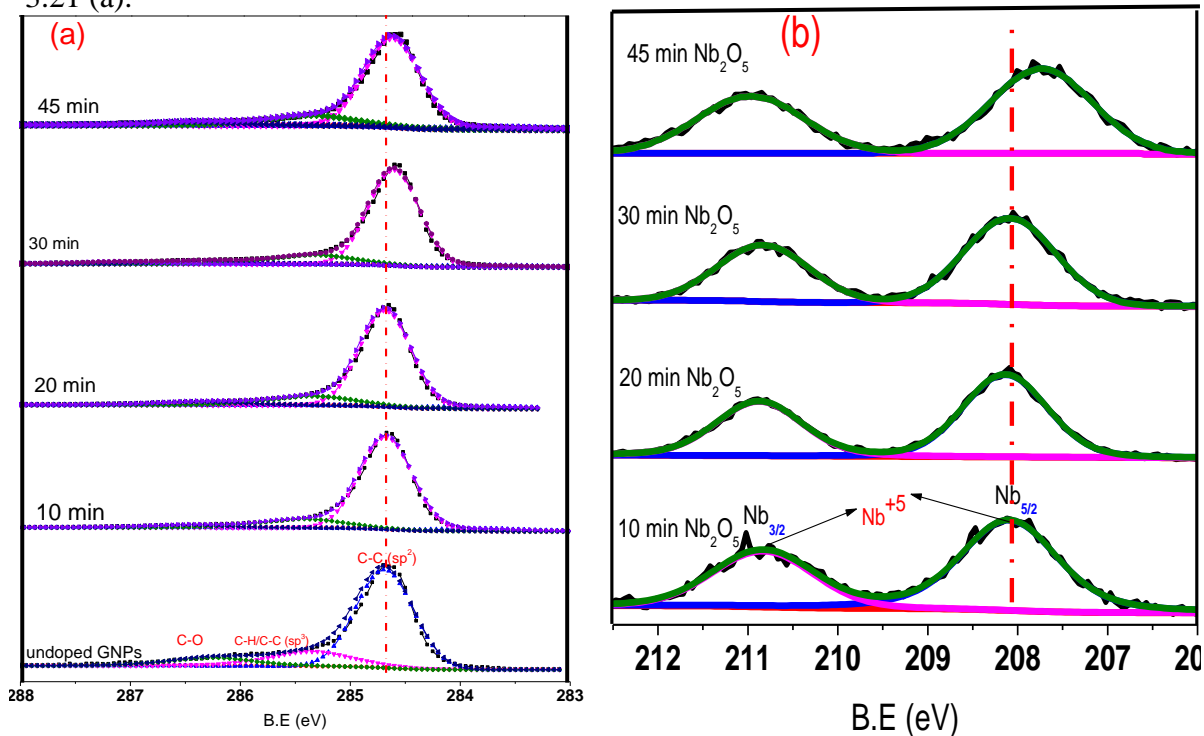


Fig 3.21 XPS spectra of GNPs with incrementally increased Nb₂O₅ contents through different times of deposition (a) Shift in the C 1s core levels position upon Nb₂O₅ deposition (b) Nb 3d core level spectra with positions of the Nb⁺⁵ peaks. (RF power =40 W deposition time =10 min to 45 min) process pressures =6 Pa, Powder vibration= 10 Hz)

The C 1s core level of the undoped and Nb₂O₅ doped GNPs samples were de-convoluted into three components. The binding energies of the components of the undecorated GNPs C 1s spectrum are 284.69, 285.23 and 286.2 eV respectively, which are attributed to C-C (sp²), C-H/C-C (sp³) and C-O bonds respectively.

Nb 3d XPS spectra of Nb₂O₅ layers deposited on GNPs at different times of deposition are shown in Figure 3.21 (b). The binding energy values for Nb 3d at 208.1 eV and 210.12 eV represent the Nb 3d_{5/2} and Nb 3d_{3/2} states of Nb⁺⁵. It is confirmed from the XPS spectra that only one chemical state has been observed for the Nb.

Fig 3.22 (a) shows the O 1s XPS core level of Nb₂O₅ decorated on GNPs at 45 min of deposition in Ar plasma. The Gaussian line function was used to de-convolute the O 1s core level. The O 1 core level was de-convoluted into three components. The component OI which has BE energy of 530.92 eV corresponds to bond O-Nb. The second components OII BE position at 532.16 eV allocated to the oxygen contribution in possible C=O. The 3rd component (O III) at higher BE of 533.62 eV is from C-O bonding.

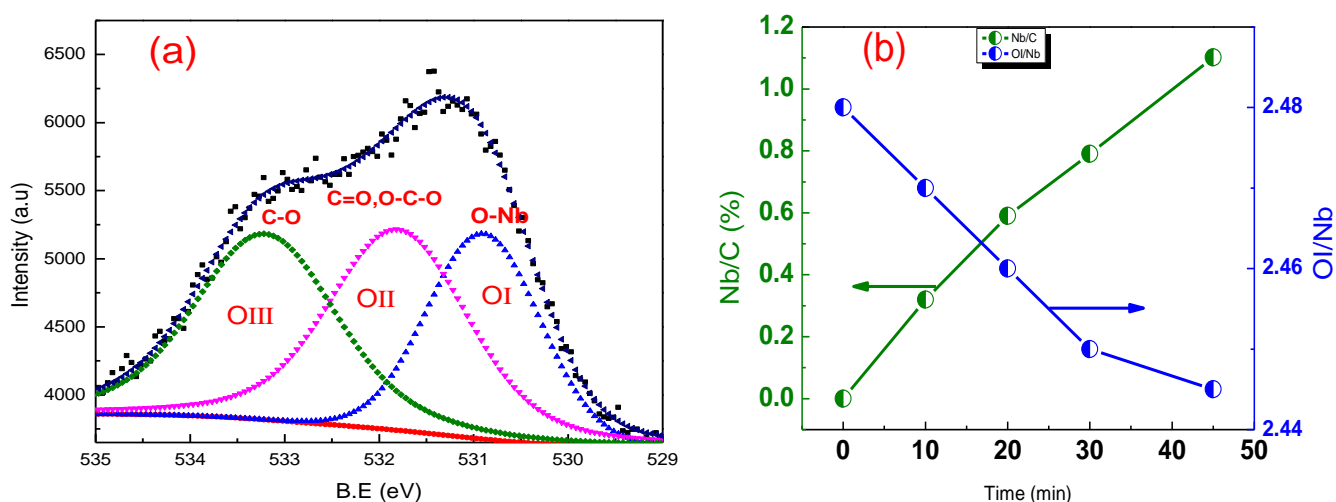


Fig 3. 22 (a) De-convolution of the O 1s core level (b) variations of Nb/C and Stoichiometry with respect to different time of deposition

Additionally, the stoichiometry and concentration of the decorated Nb₂O₅ onto GNPs surface at stepping up the deposition time were evaluated from the XPS analysis and the results are shown in Fig.3.22 (b). It can be seen that the Nb/C (sp²) ratio increased with stepping up deposition time however the OI/Nb ratio linearly decreased with rising of the deposition time. This indicates that the decorated Nb₂O₅ is under stoichiometric with respect to the ideal of 2.5.

3.6.2 XRD analysis of undoped GNPs and Nb₂O₅ doped GNPs at different times of deposition

Figure 3.23 (a) depicts the XRD patterns of undoped and Nb₂O₅ deposited on GNPs at different times of deposition. In this case the amount of Nb₂O₅ onto GNPs increased by stepping up deposition time. The peaks are identified as (002), (100)/ (101), (004) (110) and (112) planes of hexagonal graphite.

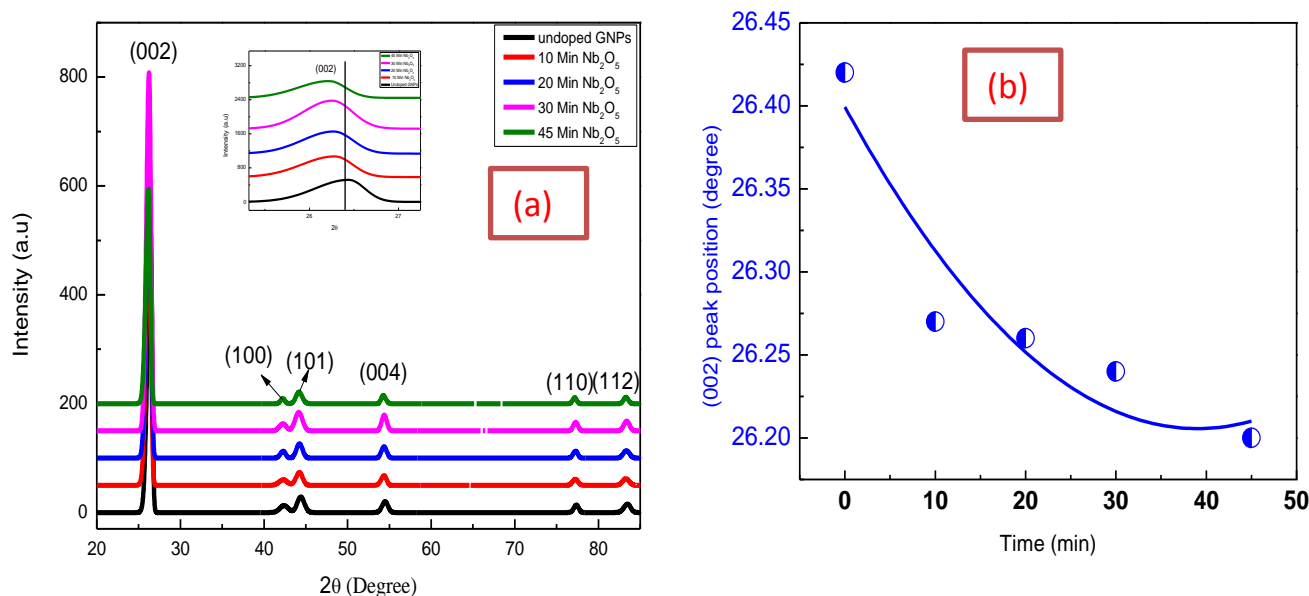


Fig 3. 23 (a) XRD patterns Nb₂O₅ doped GNPs (b) Variation of the 2θ angle of the (002) at different time of deposition peak with different time of deposition

With increasing of Nb₂O₅ concentration onto GNPs the intensity of the (002) peak was attenuated. The full width at half maximum of (002) peak became higher by increasing the Nb₂O₅ concentration onto GNPs. The shift in (002) peak of the GNPs toward lower angle values

increased with stepping up the deposition time and the results are presented in Fig 3.24 (b). This indicates that the interplaner spacing between the layers of GNPs is increased. The increase in the lattice spacing between the layers of graphene suggests that the planes of the GNPs are distorted with interaction of the sputtered particles and plasma species.

Furthermore the lattice parameters “a” and “c” of undoped GNPs and Nb₂O₅ deposited onto GNPs at different times of deposition were calculated from the reflection of the planes (100) and (002) using equation (2)

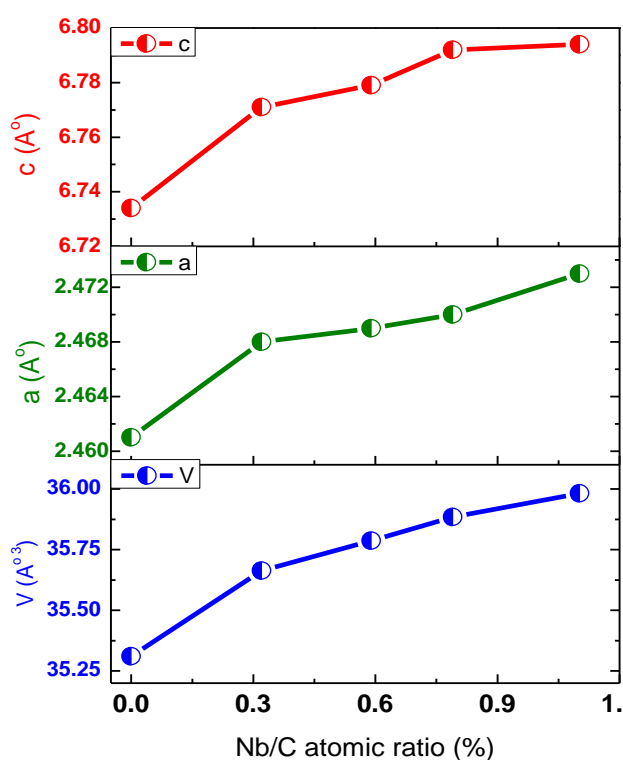


Fig 3. 24 Lattice parameters “a”, “c” and cell volume V of GNPs in function of Nb/C at. ratio

Fig. 3.24 shows the dependence of the calculated lattice parameters (“a” and “c”) of the GNPs when changing the Nb₂O₅ concentration by stepping up deposition time. The “c” and “a” parameters increased, when a small amount of Nb₂O₅ was deposited onto GNPs in atomic ratio Nb/C (sp²) = 1.2 %. The enhancement of the “c” and “a” parameters can suggest that, the

planes of GNPs were distorted with deposition of the Nb₂O₅ and the tensile strain were developed in the planes of GNPs with interaction of the plasma species and sputtered particles. Due to the tensile strain the lattice parameters of the GNPs increased.

Moreover, to characterize the similarity between the GNPs and perfect single crystal graphite the Mering–Meire (G_{xrd}) index was used [220].

Fig 3.25 shows the graphitization indices (G_{xrd}) and d spacing of the GNPs and decorated GNPs with Nb₂O₅ by stepping up the deposition time. With raising of Nb contents to the C (Sp^2) the interlayers spacing d_{002} is increased.

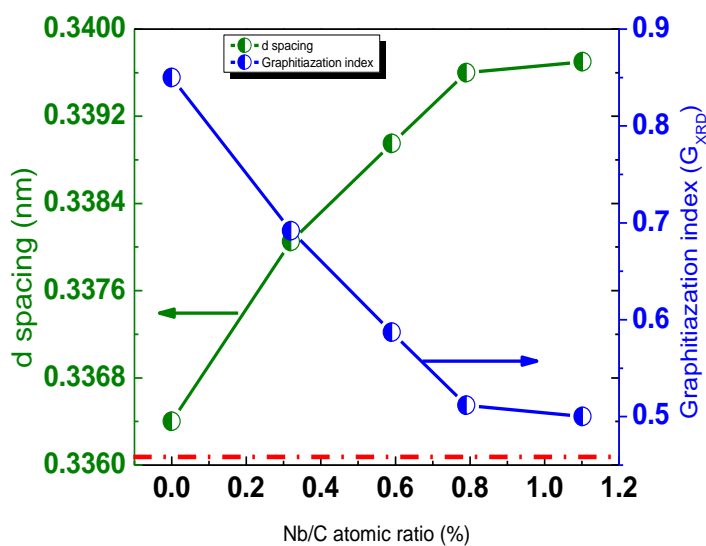


Fig 3. 25 Degree of graphitization and d spacing of undoped GNPs with Nb₂O₅ doped GNPs at different time of deposition

Graphitization index G_{xrd} of the GNPs before the decoration was 0.85, this suggest that the basal planes were well aligned. However after the decoration of Nb₂O₅ the graphitization index of GNPs decreased from the 0.85 to 0.5, when the Nb₂O₅ layers were deposited onto GNPs sheets with a Nb/C (sp^2)= 1.2 atomic ratio (%). It can be explained like as follows; by increasing the deposition time more sputtered particles were deposited and plasma species interacted with

GNPs sheet generates the structural defects in the planes of the GNPs. The stacking orders of basal planes were degraded with interaction of the sputtered particle and plasma species. Due to the degradation of the stacking order of the basal planes of GNPs gradually loss their initial ordering, decreasing the degree of graphitization.

3.6.3 Raman study of undoped GNPs and Nb₂O₅ doped GNPs with different times of deposition

We have further studied the Raman analysis of undoped and decorated GNPs with Nb₂O₅ films deposited by varying the deposition time. Three main peaks corresponding the D, G and 2D bands dominated all the spectra. The enlarged view of the position G inset shows that G peak shifted to lower wavenumber with increasing the deposition time as shown in Fig 3.26 (a). The position of the G peak started at 1572.1 cm⁻¹ before the Nb₂O₅ deposition and decreased up to 1567.06 cm⁻¹ after the deposition of Nb₂O₅ for 45 min. Similarly the position of the 2D peak shifted to a lower wavenumber from 2666.7 to 2651.3 cm⁻¹ after deposition of Nb₂O₅ for 45 min as shown in Fig 3.26 (b). Literature survey points to several possible explanations for this red shift in GNPs. This includes the effects of charge doping [221] and mechanical strain [222]. The relatively shift in G and 2D bands gives us information whether the shift due to charge transfer or strain effect dominates [223, 224]. The shift in G and 2D band will be due to charge transfer if shift G band is stronger than that of 2D band [225, 226]. However if the shift in 2D band is greater than G bands then the mechanical strain dominates. Therefore downshift of G and the 2D bands of Nb₂O₅ doped GNPs are attributed to tensile strain [227]. This effect can be explained as follows, when the C-C bond length and angles of sp² ring are modified through tensile strain, the hexagonal symmetry of the graphene layers is broken due to the enlarging of the lattice constants and the lowering of vibration frequency of the crystal phonon [200]. This is in good agreement

with XRD findings in which lattice constants of GNPs increased after decoration of Nb₂O₅. Hence, for increasing tensile strain in GNPs both pos (G) and Pos (2D) shifted to lower wavenumbers [68].

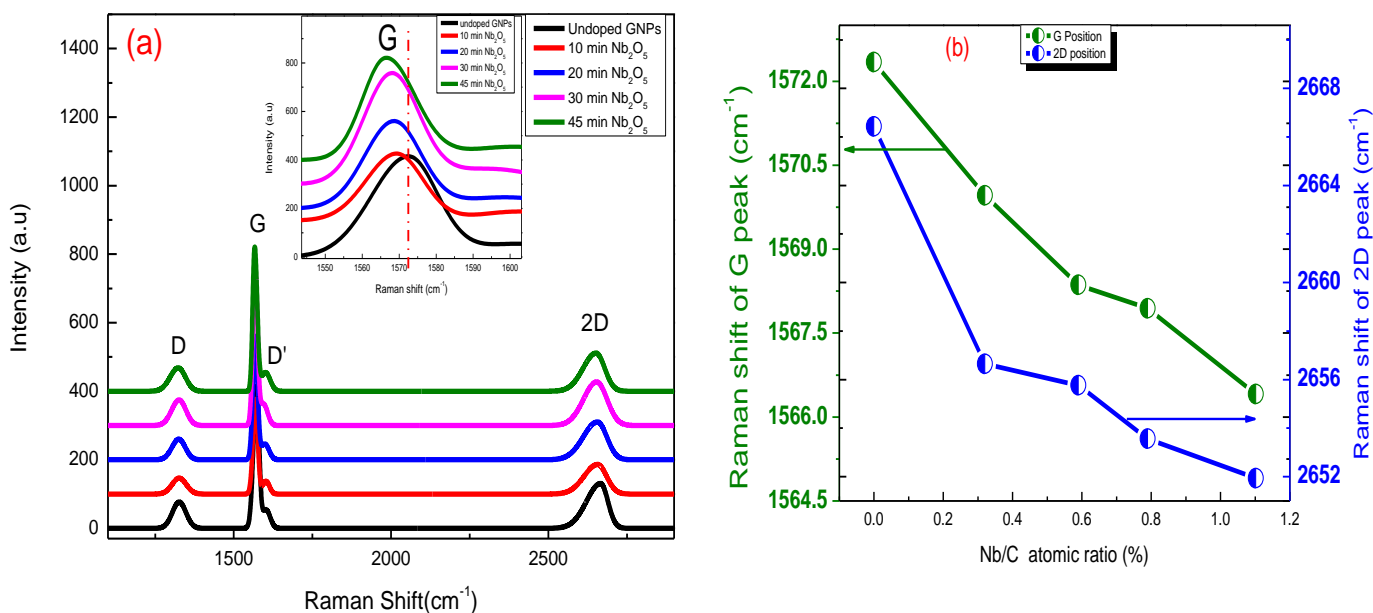


Fig 3. 26 (a) Raman spectra of undoped GNPs and

(b) position of the G and 2D peaks vs Nb/C (%)

Nb₂O₅ doped GNPs at different time of deposition.

More importantly the level of defects and disorderness induced in the planes of GNPs by the interaction of the Nb₂O₅ were evaluated using the intensity ratios of D and G peaks. As in the section (3.3.4) it has been explained that, there are two regimes in the defected GNPs structures.

One is low density defect regime where I_D/I_G ratio increased with respect to the high defects density and for this regime the lattice phonon scattered elastically. The second regime is related to the high defects density, whereas I_D/I_G begins to attenuate as a function of increasing the defects density, this regime can be attributed to a gradual evolution from the sp² -bonded carbon found in graphene sheets into amorphous carbon with low sp³ bonding [207]. The I_D/I_G ratio of the decorated GNPs with Nb₂O₅ films as a function of Nb/C (sp²) atomic ratio (%) is illustrated in

Fig.3.27. It can be seen that I_D/I_G ratio gradually decreased with rising of Nb/C (Sp^2) atomic ratio (%). This can be attributed to the second regime of the defects at which I_D/I_G ratio decreases as a function of induced defects in GNPs structures, whereas the sp^2 bonded carbon of the GNPs is transformed into low sp^3 amorphous carbon (a-C phase). This effect can be explained like this, when the sputtered particles and plasma species interacted with GNPs surface, they generate the structural defects in the structure of the GNPs. Also these defects on the surface of the GNPs increased with stepping up the deposition time. This is confirmed from XPS analysis, with stepping up deposition time more sputtered particles deposited on the surface of the GNPs.

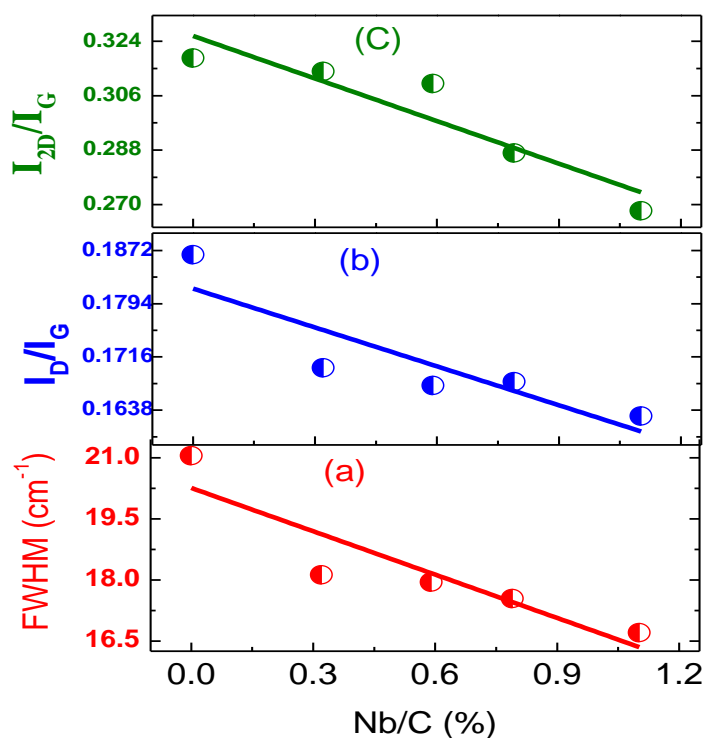


Fig 3. 27 Variation of Raman peak intensity ratios of I_D/I_G , I_{2D}/I_G and FWHM of the G peak plotted against the Nb to C atomic ratio (%).

The I_{2D}/I_G ratio of the decorated GNPs with Nb₂O₅ as a function of Nb/C (%) ratio is presented in Fig 3.27(c). I_{2D}/I_G ratio is very sensitive to the doping level GNPs. From the Fig.3.28 (c) it can

be seen that with raising Nb/C (Sp²) by stepping up the deposition time the I_{2D}/I_G ratio decreased. According to the previous reported data suggest that the I_{2D}/I_G ratio decreases with increasing doping concentration due the additional electron-hole or electron-defect scattering contribution. As discussed in the section 3.3 that the intensity of the 2D bands strongly depend on the doping concentration and also affected with extra electron/hole or electron defects scattering rate. In our case the defects induced in the structure of the GNPs with interaction of sputtered particle and plasma gas species. The intensity of the 2D bands more affected with these defects with respect to G peak. More importantly the defects increased on the surface of GNPs with rising of deposition time. The intensity of 2D of the GNPs attenuated with these short range defects induced by Nb₂O₅ contents.

Furthermore the full width at half maximum (FWHM) of the G peaks of GNPs decreased as a function of changing Nb/C (sp²) with rising deposition time are presented in Fig 3.28 (a). The FWHM of the GNPs is very sensitive to the doping level due to the reduction of the Kohn anomaly [228]. The reduction of the FWHM of the GNPs after the interaction of the Nb₂O₅ could be due to charge doping at the interface. Actually the sharpening of FWHM (G) of the GNPs could be decaying into electron-hole pair due to the Pauli Exclusion Principle. Addition to this reduction of the FWHM of the G peak occurred when the electron hole gap becomes higher than the phonon energy, then phonons is decayed [229].

3.7 Concluding Remarks

In this chapter we presented the experimental study results about Nb₂O₅ deposition on GNPs by the variation of the deposition process parameters. Based on the variation of deposition parameters used, this chapter is divided into four sections (i) the decoration of the GNPs with Nb₂O₅ at different RF power values have been discussed. (ii) The structural disorderness of the

decorated GNPs with Nb₂O₅ by varying process pressures was studied. (iii) The powder vibration frequencies were used to decorate the GNPs powder with Nb₂O₅ films uniformly and the structural and chemical are presented. (iv) Different amounts of Nb₂O₅ nanoparticle were deposited by varying the deposition time.

In section 3.3, decoration of the Nb₂O₅ onto GNPs by varying the RF power values (40 -100 W) was presented. The structural, chemical properties and morphological investigations were carried out of the decorated samples. It was found from the XRD investigations that tensile strain was developed in the planes of the GNPs with deposition of Nb₂O₅. Also with interaction of the high energy sputtered particles and plasma species the defects on the surface of the GNPs are increased. Raman studied revealed that the frequencies of the GNPs G and 2D modes were found to undergo red shifts with decoration of Nb₂O₅. We explained the red shift of GNPs from the Raman frequencies in terms of tensile strain and doping induced by Nb₂O₅. TEM images demonstrated that GNPs decorated with around 5 to 10 nm uniform layer of Nb₂O₅ at 100 W on their surface were successfully fabricated. From the XPS analysis it was confirmed that, by increasing Nb₂O₅ layer thickness on the GNPs surface with rising RF power values downshift in C 1s peak suggests a p-type doping of GNPs due to charge transfer at the interface as a consequence of the higher work function difference between the Nb₂O₅ (4.70 eV) and GNPs (4.3 eV).

In section 3.4, the structural disorderness of the Nb₂O₅ decorated onto GNPs by varying process pressure has been discussed. It was noted from the Raman and XRD result that at low working pressure values the high energy of sputtered particles and plasma species bombardment onto GNPs, induced large disorder onto graphene layers. Also at low working pressure more sputtered

particles were deposited on the GNPs surface, these sputtered interacted with basal plane of the GNPs more energetically, which degraded stacking order of the basal planes of GNPs.

In section 3.5 for the uniform decoration of the GNPs with Nb₂O₅ film the powder vibration was used. From the XPS analysis it has been confirmed that with high powder vibration frequency more sputtered particles deposited on the surface of the GNPs compared to the case without moving powder. Furthermore the Raman and XRD studied reveal that with powder vibration the tensile strain was induced in the lattice of GNPs.

In section 3.6 the structural defects of the decorated GNPs with Nb₂O₅ at different times of deposition were discussed in detail. The XRD results shown that, the introduction of low concentration of Nb/C (sp²) led to a significant lattice distortion along the c-axis and a-axis, which reveals that Nb₂O₅ generated a tensile strain in and between the planes of GNPs. The stacking order of the basal plane and the crystalline thickness of the GNPs along c-axis were degraded upon the deposition of Nb₂O₅. The redshift in G and 2D peak of GNPs after the decoration of Nb₂O₅ is due to the tensile strain induced in the plane of GNPs with increasing the Nb₂O₅ concentration.

Concluding, decoration of Nb₂O₅ onto GNPs powders by the variation of RF parameters were discussed in detail. In this chapter, the interaction of the Nb₂O₅ concentration with GNPs which consist of 30 to 40 layers of graphene sheets was presented. The interaction of the graphene flakes (1.6 nm) consisting of average three to five layers of graphene sheet in average with Nb₂O₅ nanoparticles will be discussed in next chapter #4 and the interface between the graphene flakes and Nb₂O₅ nanoparticles will be presented.

Chapter # 4

Effect of Nb₂O₅ concentration on the structural electronics and chemical properties of graphene powder

4.1 Introduction:

The main aim of this work is to study the interaction of graphene powder with Nb₂O₅ nanoparticles deposited by RF sputtering technique. In chapter # 3 the effect of Nb₂O₅ concentration on the structural and chemical properties of graphite nanoplatelets (consist of 30 to 40 layers of graphene) by varying deposition process parameters, like RF power, powder vibration frequency and process pressure was presented. It was found that, the tensile strain was established into the GNPs planes upon the deposition of the Nb₂O₅. The tensile strain in the planes of the GNPs increased with rising of Nb₂O₅ concentration. The tensile strain and doping were confirmed from the XRD, Raman study and XPS analysis. In this chapter the interface between graphene powder and deposited Nb₂O₅ nanoparticles by RF sputtering technique will be discussed. Different deposition parameters were adjusted during the deposition process to achieve the uniform distribution of the Nb₂O₅ nanoparticles onto graphene sheets. Interface between the graphene powder and a dissimilar material is needed for different kinds of applications [²³⁰,²³¹] Moreover the influence of Nb₂O₅ concentrations on the chemical, structural and electronic properties of graphene will be described in this chapter. Based on the study of the decoration of Nb₂O₅ on the surface of graphene powder with different deposition process parameters, this chapter is divided into three sections:

- For the results presented in section I, the structural chemical and electronic properties of the decorated graphene with Nb₂O₅ nanoparticles will be discussed. In this study, no vibration frequency was given to the graphene powder during the deposition process.

- For the results reported in section II, different amounts of Nb₂O₅ nanoparticles were obtained onto graphene by increasing the deposition time. A powder vibration frequency of 10 Hz was used to deposit the Nb₂O₅ nanoparticles onto graphene powder. The influence of Nb₂O₅ concentration on the structural, chemical and electronic properties of GNPs will be presented.
- For the results described in section III, the influence of Nb₂O₅ nanoparticles on the structural, chemical, morphological and electronic properties of graphene will be studied.

4.2 Experimental details

The Nb₂O₅ nanoparticles were deposited onto graphene powder by varying three different deposition parameters. The Powder vibrations frequency, RF power and deposition time parameters were used to deposit the Nb₂O₅ nanoparticles onto graphene powders. The other deposition parameters like substrate to target distance base pressure and target used for the deposition are the same as described in chapter#3. More specific details for each section are given below:

- In order to obtain different amounts of Nb₂O₅ contents on the surface graphene powder, the graphene powder was decorated with Nb₂O₅ nanoparticles deposited by stepping up the deposition time (8 to 32 min). The Nb₂O₅ nanoparticles were deposited onto graphene surface without moving powder. The RF power and process pressure values were kept constant at 6 Pa and 40 W respectively.
- The graphene powders were decorated with Nb₂O₅ nanoparticles at different time of deposition (8 to 32 min). In this study, 10 Hz powder vibration frequency with fixed amplitude of 32 μm was used to deposit the Nb₂O₅ nanoparticles onto graphene sheets. The self-bias voltage and power applied to Nb₂O₅ target was fixed at -72 V and 40 W

respectively. The total process pressure for the decoration of Nb₂O₅ nanoparticles onto graphene surface was fixed at 6 Pa.

- In order to obtain different concentration of Nb₂O₅ on the graphene surface power applied to Nb₂O₅ target was varied from 40 W to 100 W. The total pressure and powder vibration frequency were fixed at 10 Hz and 6 Pa respectively. The deposition time were fixed at 15 min.

4.3: The influence of the Nb₂O₅ concentrations on the properties of graphene deposited by

RF sputtering technique on static graphene powders:

The main objective of this work is to investigate the influence of Nb₂O₅ concentrations on the structural, chemical and magnetic properties of graphene powder. The different amount of Nb₂O₅ concentrations were obtained on the graphene surface by stepping up the deposition time. It is well established that due to the presence of numerous topological defects graphene shows a weak ferromagnetic behavior in long range ordering [²³²,²³³]. By the deposition of Nb₂O₅ onto graphene powder structural defects were generated in the plane of graphene and the structural defects and disorderness increased with rising of Nb₂O₅ contents onto graphene powder. These structural defects enhanced the ferromagnetic property of the graphene. The ferromagnetic property of the decorated graphene with Nb₂O₅ nanoparticles will be presented in chapter# 7. The structural defects, ferromagnetic behavior and chemical composition of decorated graphene with Nb₂O₅ nanoparticles were characterized by X-ray diffraction (XRD), Raman spectroscopy, vibrating sample magnetometer from PPMS (Dyna Cool) and X-ray photoelectron spectroscopy (XPS). Moreover the process parameters are presented in table 4.1.

Table 4.1 the process condition of decorated graphene with Nb₂O₅ nanoparticles

Sample #	RF Power (W)	Process pressure (Pa)	Deposition Time (min)	Powder vibration frequency (Hz)
1	40	6	8	0
2	40	6	16	0
3	40	6	24	0
4	40	6	32	0

4.3.1 XPS Analysis of undoped graphene and Nb₂O₅ doped graphene:

XPS is a potential technique for exploring the chemical composition, element states, and the nature of heteroatom functionalized or doped graphene supported nanocomposites. The C 1s and Nb 3d XPS spectra of the undecorated graphene and decorated graphene with Nb₂O₅ nanoparticles at different times of deposition are illustrated in Fig.4.1. The high resolution C 1s XPS spectra of undecorated graphene and for the decorated graphene with Nb₂O₅ nanoparticles at different times of deposition are shown in Fig.4.1 (a). The C 1s core levels spectra were deconvoluted into three components. The XPS C 1s spectra of the undoped graphene has characteristic peaks at 284.81, 285.58 and 286.72 eV respectively that correspond to sp² carbon bonded (C-C) [233,234] sp³ hybridized carbon (C-C)/C-H [235] and C-O bonding configurations due to oxidation from the moisture. It is interesting to see that after the decoration of Nb₂O₅ nanoparticles on the surface of graphene the C 1s peak shifts toward the lower binding energies. The downshift in C 1s peak can be explained as, when graphene make interface with weakly interacting material like Nb₂O₅, the charge are expected to transfer across the interface in order align the Fermi level of the contacted material. The downshift of the C 1s peak increased with

stepping up the Nb₂O₅ concentration. The maximum downshift was observed in the C 1s peak about 0.10 eV after the decoration of Nb₂O₅ onto graphene at 32 min of deposition.

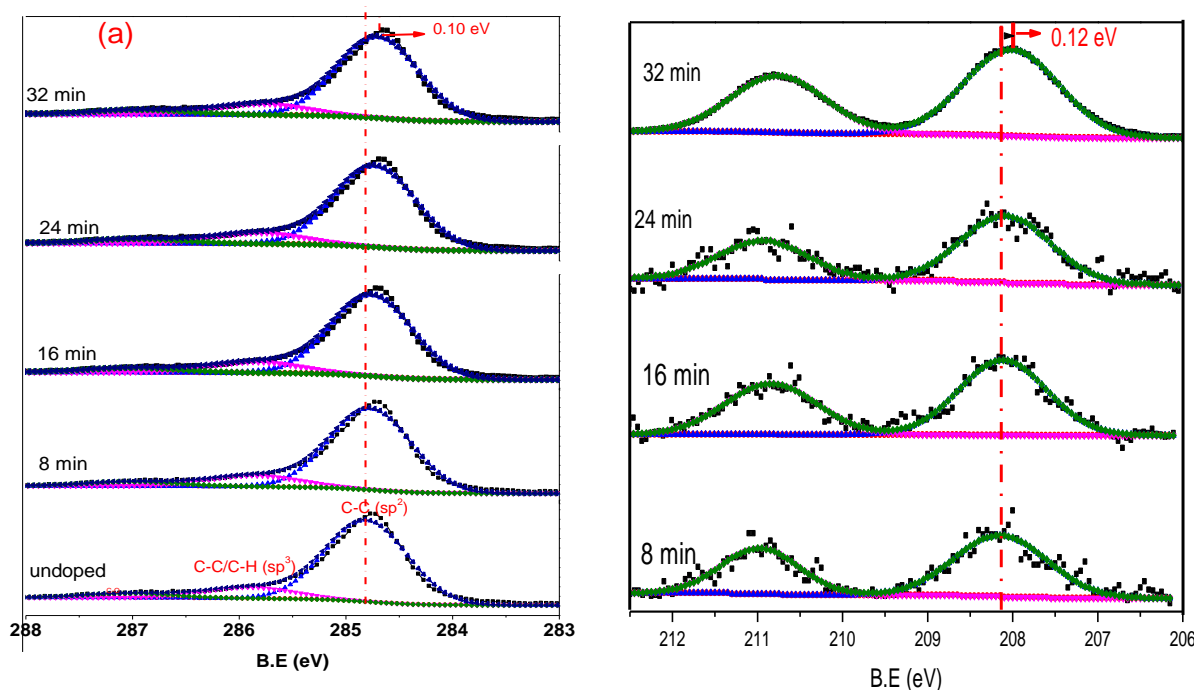


Fig 4.1 XPS spectra of graphene powder with incrementally increased Nb₂O₅ contents by varying the deposition time (a) Shift in the C 1s core levels position upon Nb₂O₅ deposition (b) Nb 3d core level spectra with positions of the Nb⁺⁵ peaks. [Process pressure = 6 Pa, Time= 8 to 32 min, Frequency = 0 Hz RF power= 40 W]

Actually the downshift of the C 1s core level binding energy is equal shift in the Fermi level. However the Fermi level shift is the consequence of the charge transfer between interfaces of the two materials. Therefore, the downshift in the C 1s core level of the graphene is due to p doping upon the deposition of Nb₂O₅ nanoparticles, whereas the electrons are transferred from graphene to Nb₂O₅ nanoparticles due to difference of work function between the graphene and Nb₂O₅.

Fig 4.1 (b) depicts the high resolution XPS spectra of Nb 3d for decorated graphene surface with Nb₂O₅ nanoparticles by stepping up the deposition time. To study the chemical state of Nb₂O₅, there are two main peaks of the Nb 3d_{5/2} and 3d_{3/2} core level centered at 208.14 eV and 210.68

eV respectively, which designates that the peaks are originated from Nb⁵⁺ state [236]. The binding energies of these photoelectrons are characteristic of Nb₂O₅ [237]. The downshifts in the Nb 3d were observed with the increasing of Nb₂O₅ concentration on the surface of graphene by stepping up deposition time. The maximum downshift of 0.12 eV was noted upon the deposition of Nb₂O₅ nanoparticles onto graphene at 32 min. The downshift of the Nb 3d core level upon the deposition of Nb₂O₅ nanoparticles suggest that, the band of Nb₂O₅ bending toward the interface with accumulation layers of the electrons from the graphene.

The O1s XPS spectrum of decorated Nb₂O₅ nanoparticles on graphene surface in Ar plasma is presented in Fig. 4.2 (a). The O 1s peak is de-convoluted into three components the first peak OI at lower binding energy (BE), 530.91 eV can be ascribed to the O1s core peak of O²⁻ bound to Nb⁺⁵ in graphene sheets. Whereas the other two peaks at higher BE located at 532.13 eV, and 534.15 eV may probable come from the (C=O, COO) and from C-O bonding [238].

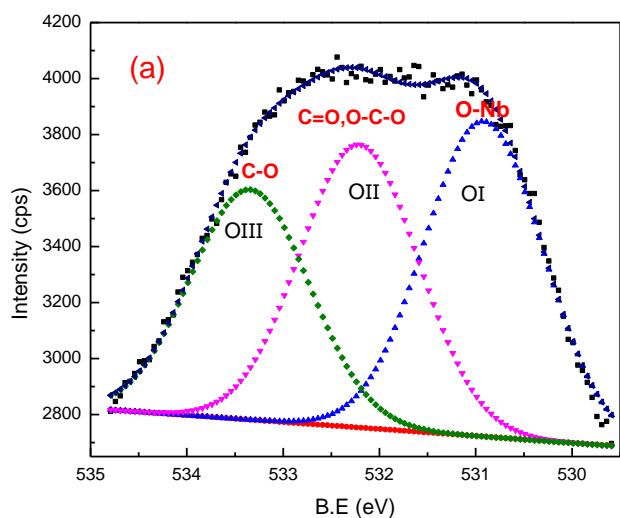
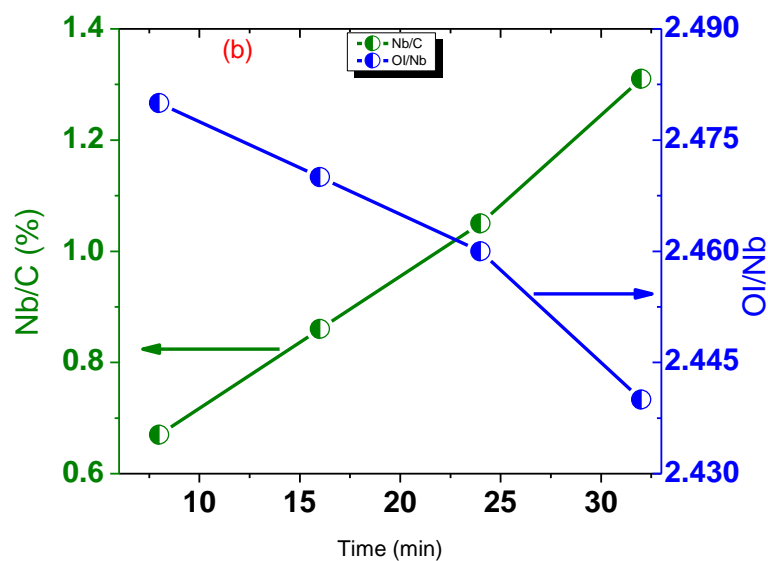


Fig 4. 2 (a) De-convolution of the O 1s core level



(b) variations of Nb/C and Stoichiometry with respect to different time of deposition

The OI/Nb ratio was evaluated for the decorated graphene with Nb₂O₅ nanoparticle to determine the oxygen vacancy. The measured OI/Nb ratios for the decorated graphene with Nb₂O₅ nanoparticles at different times of deposition are presented in Fig 4.2 (b). The calculated value of the OI/Nb ratios indicates that the deposited Nb₂O₅ nanoparticles are under stoichiometric. The Nb/C sp² ratio increased by rising the deposition time and the results are shown in Fig 4.3 (b). The Nb/C sp² ratio increased from 0.63 and reached to 1.37 atomic ratios (%), when the decoration time was varied from 8 min to 32 min.

4.3.2 XRD analysis of undoped Graphene and Nb₂O₅ doped graphene

X-ray diffraction was used to characterize the undoped graphene and Nb₂O₅ decorated graphene powders. Fig.4.3 (a) shows the XRD patterns of undoped graphene and Nb₂O₅ decorated graphene powder by stepping up deposition time. There is strong influence of the Nb₂O₅ concentration onto the structure of the graphene.

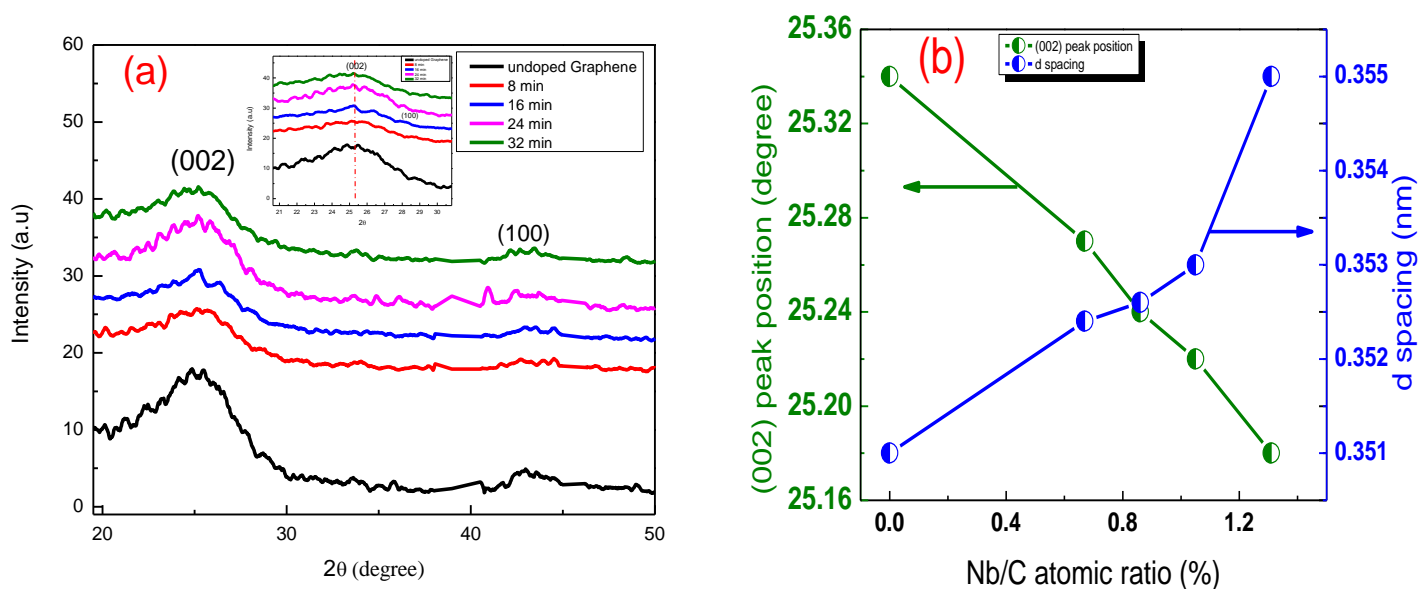


Fig 4. 3 (a) XRD patterns of undoped and Nb₂O₅ doped graphene at (b) Variation of the 2θ angle position of the (002) different time of depositions and d-spacing as function of Nb/C at. %

By the deposition of Nb₂O₅ onto graphene sheets, the FWHM and position of the graphene plane was drastically changed. A broad and low intensity of (002) peak was observed for the

undecorated graphene and decorated graphene with Nb₂O₅ nanoparticles, which suggests that graphene flake consist of very few layers of graphene [239]. The (002) peak of the graphene gradually shifted toward the lower 2θ values by increasing the deposition time as shown in Fig (a) (enlarged view). This indicates that the interlayer distances of graphene sheet increased with rising of the Nb₂O₅ concentration. The measured values of the d –spacing as a function of Nb/C sp² is presented in Fig 4.4 (b). The d-spacing values of graphene increased from the 0.351 nm to reach 0.355 nm, when the graphene were decorated with Nb₂O₅ nanoparticles in a ratio Nb/C sp²=1.31 at. %. Furthermore, the FWHM of the (002) peak for the undecorated graphene and decorated graphene with Nb₂O₅ nanoparticles were evaluated using the Lorentzian line function. It was found that the FWHM of the (002) peak of graphene became broadened with increasing the Nb₂O₅ concentration. The evaluated FWHM of graphene as function of Nb/C sp² are depicted in Fig 4.4

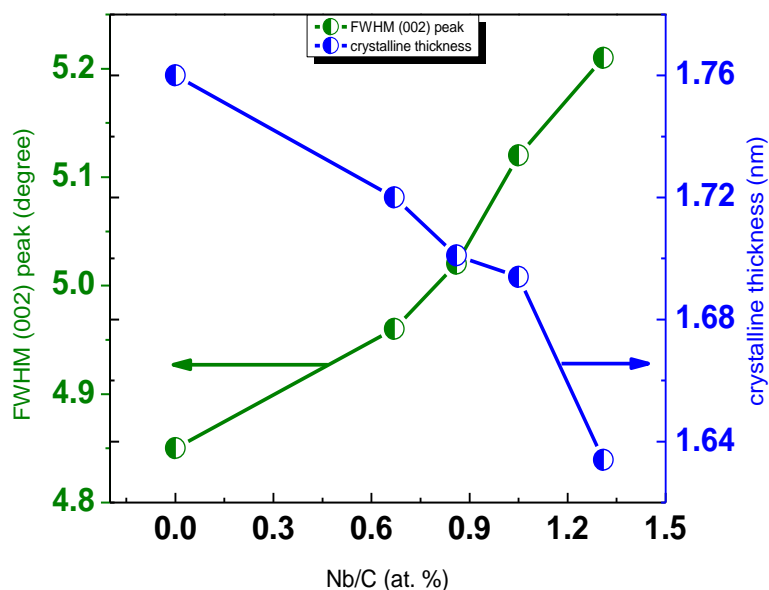


Fig 4.4 Variation in the FWHM of the (002) peak and crystallite thickness as function of Nb/C sp² atomic ratio

The FWHM of the (002) peak for graphene increased from the 4.85 to 5.20 with the deposition of Nb₂O₅ nanoparticles in a ratio Nb/C sp²=1.31 at. %. The broadening of the FWHM of

graphene upon the deposition of Nb₂O₅ nanoparticles suggest that the defects were pronounced in the plane of the graphene. The crystalline thickness of the graphene was calculated using the Scherer equation [²⁴⁰].

$$D = \frac{K\lambda}{\beta \cos \theta} \dots\dots\dots(1)$$

Where D is the average crystalline thickness of the graphene, λ is the wave length of the X-ray source, β_{hkl} is the full width at half-maximum (FWHM) of the peak considered (in rad), θ is the Bragg angle. The crystalline size of the graphene flakes as a function of Nb/C sp² are shown in fig 4.4. The crystalline thickness decreased from 1.76 nm to 1.62 nm with deposition of the Nb₂O₅ nanoparticles onto graphene sheet in a ratio Nb/C sp²=1.31 at. %. The reduction of the crystalline thickness of the graphene sheet indicates that the stacking order of the graphene sheet was reduced due to the interaction of the sputtered particles and plasma species.

4.3.3 Raman analysis of undecorated graphene and decorated graphene with Nb₂O₅ nanoparticles

Raman spectroscopy is a powerful tool to extract the identification about the graphitic systems including the defects, strain and disorderness present in the graphitic material [¹⁹⁴]. The Raman spectra of undoped graphene and Nb₂O₅ decorated graphene at stepping up the deposition are shown in Fig 4.5(a). We can see characteristic bands for all samples. Four characteristic bands for the undecorated graphene and decorated graphene with Nb₂O₅ nanoparticles were observed.

The bands around at 1585.89, 1327, 2636 and 2920 cm⁻¹ are attributed to the G-band, D-band, 2D band and D+G band respectively. The G peak arises at the Brillouin zone center and corresponds to the E_{2g} phonon. The D peak which is related to the breathing modes of sp² atoms and defects are required for its activation. The 2D peak is the second order of the D peak it

appears around 2646 cm^{-1} and originates in the process of the double resonance in which momentum conservation is accomplished by two phonon in opposite wave vectors. The D+G band is the combination band originated in the presence of disorderness in the system [241]. It is interesting to note that blue shifts were observed in the G and 2D of graphene after the deposition of the Nb₂O₅ nanoparticles. The upshift in G and 2D bands were observed upon the deposition of Nb₂O₅ nanoparticles onto graphene. The upshift in the G and 2D increased by rising the deposition time the results are shown in Fig 4.5 (a) (enlarged view). The maximum upshifts of 5.8 cm^{-1} and 4.5 cm^{-1} in the G and 2D were noted, when the Nb₂O₅ nanoparticles were deposited onto graphene in a ratio Nb/C $\text{sp}^2=1.31\text{ at. \%}$ and the results are illustrated in Fig 4.5 (b). Several possible explanations were reported in the literatures related to the shift in G and 2D bands. It includes charge doping, mechanical strain and disorderness generated in the plane of the graphene. The shift in G and 2D bands in the Raman spectra due to the charge transfer has been explained by Ferrari et al [210]

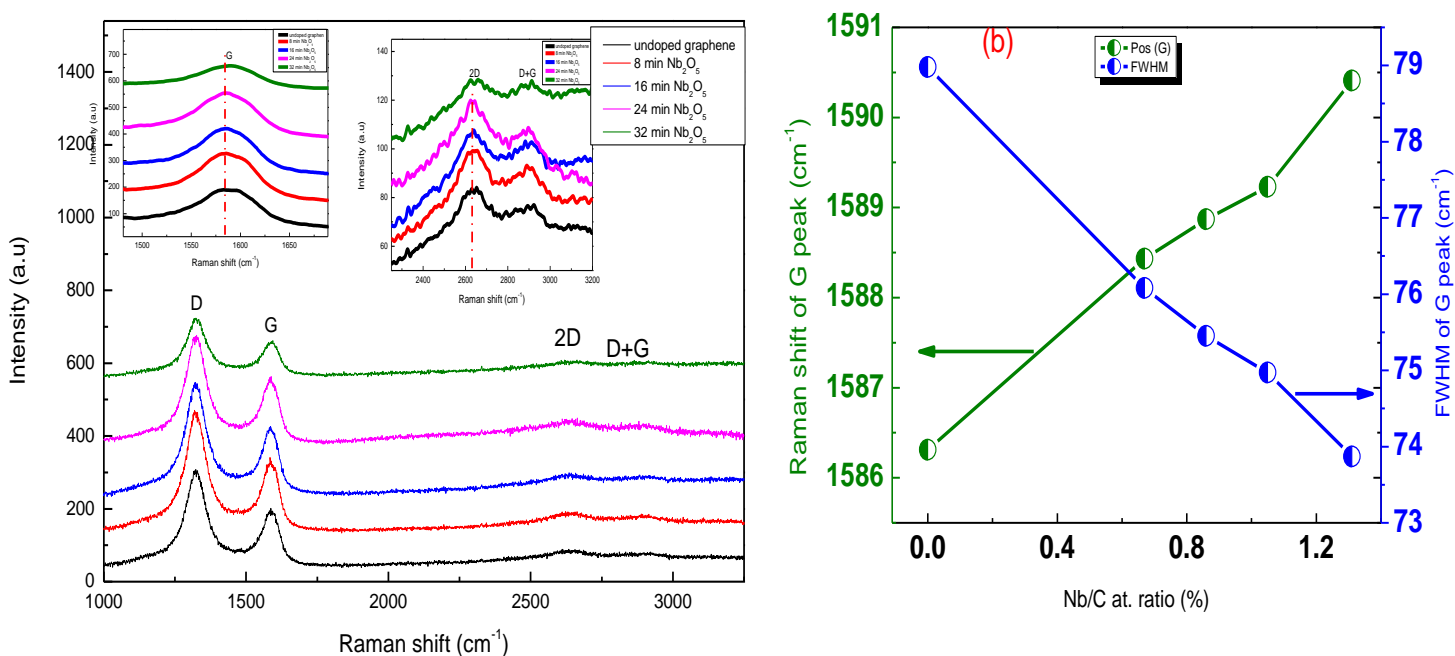


Fig 4. 5 (a) Raman spectra of undoped graphene and (b) positions of the G and FWHM (G) vs Nb to C (%) Nb₂O₅ doped GNP at different times of deposition

It can be considered that with deposition of Nb₂O₅ onto graphene the strain is established in the plane of graphene. Our XRD result demonstrates that tensile strain was developed into the plane of graphene upon the deposition of Nb₂O₅ nanoparticles. The shift in the G and 2D bands due to the tensile strain is also reported by Elena del Corro et al [242]. But in our case, less than 2 % strain was established in the plane of the graphene. It is also well established in the literatures that, the upshift in G and 2D band of graphene with metal oxide interaction is due to the p doping [243]. . With deposition of the Nb₂O₅ nanoparticles onto graphene sheet the upshift in G band is greater than the shift in 2D band. Phan Thanh Luan et al also reported that the upshift of the G and 2D is due to the p doping [244]. This suggest that the upshift in G and 2D band is not due to the strain, but doping phenomenon was dominates. Therefore, the upshifts G and 2D bands position of graphene after the decoration of Nb₂O₅ corresponds to the charge transfer between the graphene and Nb₂O₅ nanoparticles, where electrons being transferred from graphene to Nb₂O₅ nanoparticles. Consequently it is a clear that Nb₂O₅ nanoparticles interacted with graphene sheet the charge transfer from graphene to Nb₂O₅ nanoparticles. This result is good agreement with XPS analysis.

Moreover the full width half maximum (FWHM) of the G peaks of graphene were evaluated by means of Gaussian line of shape. The evaluated FWHM of the G peak as function of Nb/C sp² are presented in Fig 4.5 (b). It was observed that, the FWHM of the G peak decreased from 78.7 cm⁻¹ to 73.8 cm⁻¹, when the Nb₂O₅ nanoparticles were introduced in a ratio in a ratio Nb/C sp²=1.31 at. %. The reduction in FWHM (G) of graphene after the interaction of Nb₂O₅ nanoparticles are attributed the charge doping. The sharpening of the FWHM is actually decayed into electron-hole pairs due to the Pauli Exclusion Principle. Magdalena Onyszko et al is also reported the similar phenomenon and explained that with decoration of the reduced graphene

oxide with metal oxide nanoparticles, the FWHM of G peak decreased upon the doping of graphene with metal oxide nanoparticles [245].

The defects and disorderness induced in the graphene structure with the interaction of the sputtered particles and plasma species were evaluated by using the I_D/I_G ratio [246]. Generally, the I_D/I_G is used to measure the density of defects in disorder graphene. The estimated I_D/I_G ratio of undecorated graphene and decorated graphene with Nb₂O₅ nanoparticles as function of Nb/C sp² are depicted in Fig. 4.6. The I_D/I_G ratio increased from 1.65 and reached 1.75 with deposition of Nb₂O₅ nanoparticles onto graphene sheet in a ratio Nb/C sp²=1.31 at. %. This shows that, the structural defects were enhanced in graphene plane with deposition of the sputtered particles.

Furthermore, the I_D/I_G ratio is also used to measure the in-plane crystalline size of the graphene.

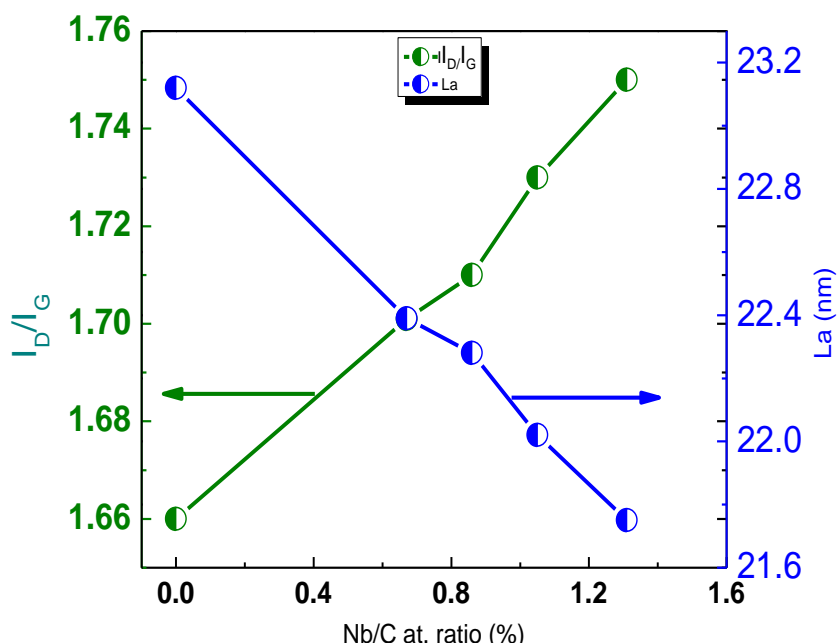


Fig 4. 6 Variation of Raman peak intensity ratios of I_D/I_G plotted against the Nb to C atomic ratio (%)

The in-plane crystallite size of undecorated graphene and decorated graphene with Nb₂O₅ nanoparticles were calculated by using the by using Tuinstra - Koenig relation [247].

$$La(nm) = 2.4 \times 10^{-10} \lambda^4 \left(\frac{I_D}{I_G} \right)^{-1} \dots\dots\dots(2)$$

The calculated in-plane crystallites sizes of the undecorated graphene and decorated graphene with Nb₂O₅ nanoparticles as a function of Nb/C sp² are shown in Fig 4.6. The in-plane crystallites size of graphene flakes decreased from 23.2 to 21.4 nm, when the Nb₂O₅ nanoparticles were deposited onto graphene sheet in a ratio Nb/C sp²=1.31 at. %. The reduction of the in-plane crystalline size of the graphene upon the deposition of Nb₂O₅ nanoparticles suggests that, the sp² domain of the graphene were broken. As already discussed before, structural defects increased by stepping up deposition time. It is well proven that, when the structural defects increased to the sp² domain, the hexagon of the graphene were more distorted with increasing defects density. Therefore, the reduction of the sp² domain size of the graphene upon the deposition of Nb₂O₅ nanoparticles could be increasing the structural defects.

4.3.4 TEM analysis of decorated graphene at 16 and 32 min.

The morphology and size distributions of the decorated Nb₂O₅ nanoparticles on the graphene powder were examined by TEM analysis. Fig. 4.7 (a-d) shows graphene sheets decorated with Nb₂O₅ nanoparticles at 16 and 32 minute of depositions. The distribution of Nb₂O₅ nanoparticles onto the graphene sheets and their intimate contact can be seen clearly from the TEM images. Fig 4.8 (a-b) shows the decoration of Nb₂O₅ on the graphene surface at 16 min of deposition. The dispersion of the Nb₂O₅ nanoparticles on the graphene sheets are uniformly distributed even at low decoration of time. Fig 4.8(c-d) depicts that, Nb₂O₅ nanoparticles were deposited onto graphene sheet for 32 min of deposition. The deposited Nb₂O₅ nanoparticles were made aggregates onto graphene sheet. As discussed in the above text that, the graphene sheets were decorated with Nb₂O₅ nanoparticles onto static graphene flakes. The sputtered particles were deposited onto graphene sheets at specific area of flakes and make aggregates onto graphene

sheets. The agglomerations of the deposited Nb₂O₅ nanoparticles were increased with high deposition time. The size of the decorated Nb₂O₅ nanoparticles on the graphene sheet is around 15 to 20 nm.

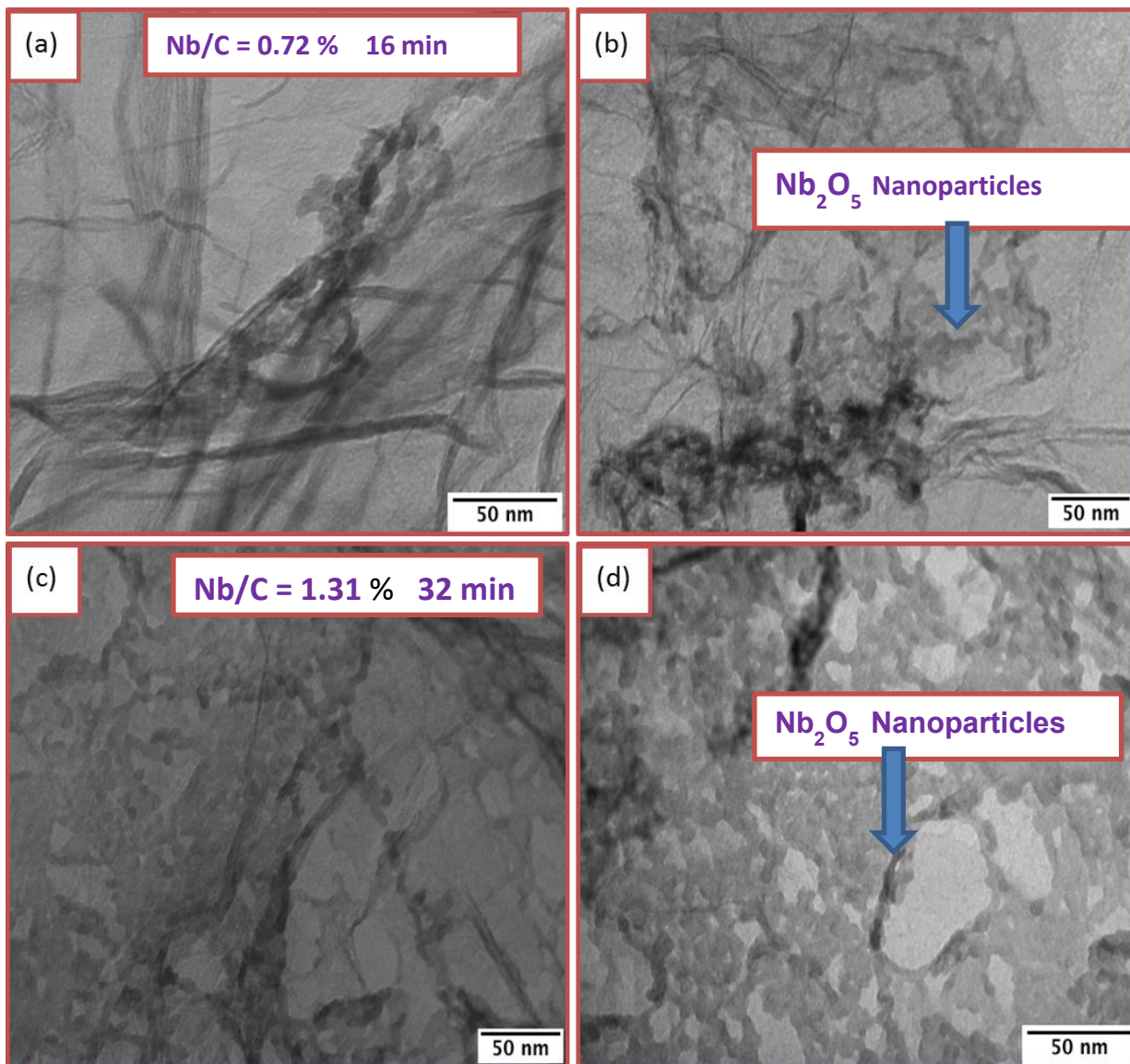


Fig 4. 7 TEM images (A-B) decorated graphene at 16 min of deposition and (C-D) Nb₂O₅ decorated graphene at 32 min of deposition

4.4: The effect of the Nb₂O₅ concentration on the structural and chemical properties of graphene powder via given 10 Hz vibration to the graphene powder

In the section 4.1 we discussed the deposition of Nb₂O₅ nanoparticles on the graphene without moving powder during the deposition process and studied the interaction of the graphene with Nb₂O₅ nanoparticles. In this section, we presented the decoration of graphene with Nb₂O₅ nanoparticles via given 10 Hz vibration with amplitude of 32 μm to the graphene powder. The powder vibration plays important role in the uniform decoration of the Nb₂O₅ nanoparticles on the surface of graphene powders. To see the influence and interaction of the sputtered particle on the moving graphene powder various characterizations techniques were used. The structural defects, chemical composition of decorated graphene with Nb₂O₅ nanoparticles were characterized by X-ray diffraction (XRD), Raman spectroscopy and X-ray photoelectron spectroscopy (XPS) Moreover the process parameters are presented in table 4.2.

Table 4.2 the process condition of decorated graphene with Nb₂O₅ nanoparticles

Sample #	RF Power (W)	Process pressure (Pa)	Deposition Time (min)	Powder vibration frequency (Hz)
1	40	6	8	10
2	40	6	16	10
3	40	6	24	10
4	40	6	32	10

4.4.1 XPS analysis of undoped graphene and Nb₂O₅ doped graphene

Fig 4.8 (a) (b) shows the XPS signal of C 1s and Nb 3d core level were measured for undecorated graphene and decorated graphene with Nb₂O₅ nanoparticles deposited by stepping up the deposition time. The C 1s core levels of the undoped graphene were de-convoluted into three components which described into above section 4.8 (a). It is important to note that after the

interaction of graphene with Nb₂O₅ nanoparticles the C 1s core levels shifts toward the lower binding energy values. Graphene can be doped with electron if the work function of the dopant is lower than graphene, otherwise it will be doped with hole under the opposite condition. The shift in the C 1s core level toward the lower binding energies increased as by the raising of Nb₂O₅ concentrations. The maximum downshift in the C 1s core level of 0.11 eV was observed after the deposition Nb₂O₅ nanoparticles onto graphene powders at 32 min of deposition. The downshift of the carbon C 1s core level is clear indication of the p-type doping of graphene due to the electron being transferred from the graphene to Nb₂O₅ nanoparticles at the interface in order to align the Fermi level of the contacted materials.

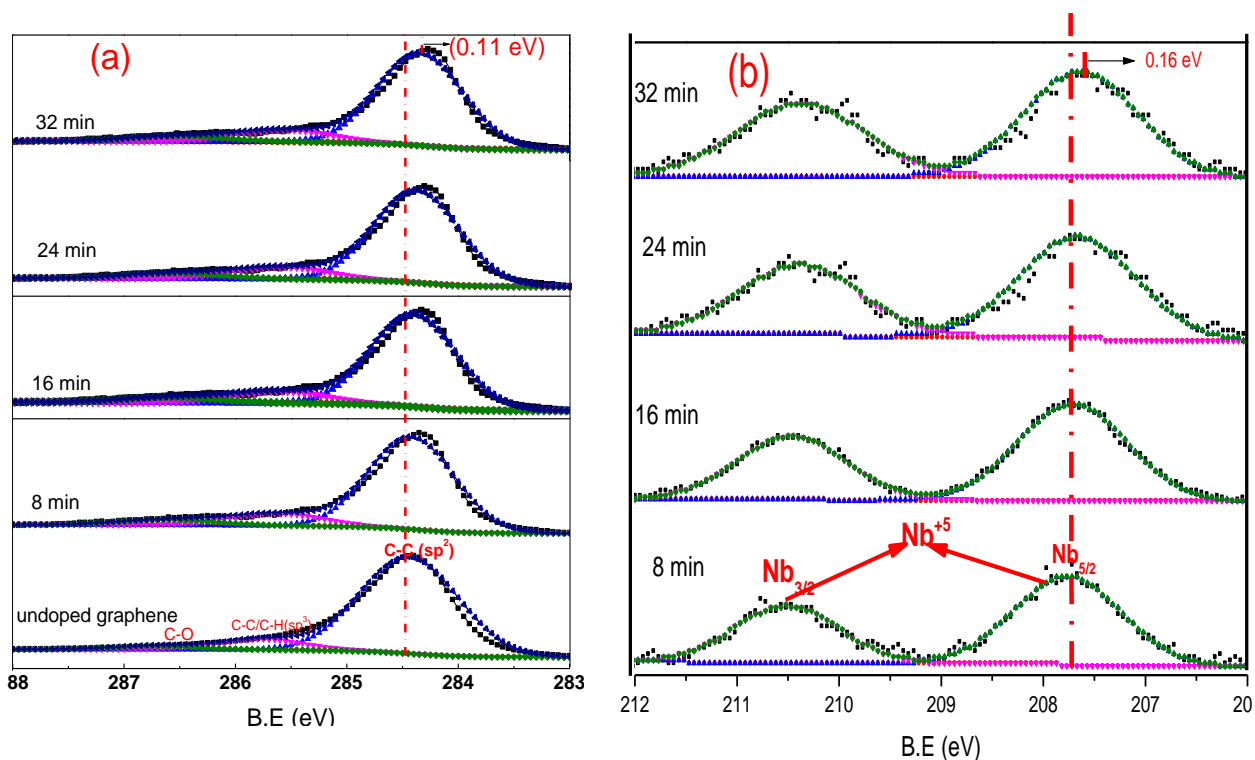


Fig 4.8 XPS spectra of graphene powder with incrementally increased Nb₂O₅ contents by varying the deposition time (a) Shift in the C 1s core levels position upon Nb₂O₅ deposition (b) Nb 3d core level spectra with positions of the Nb⁺⁵ peaks. [Process pressure = 6 Pa, Time= 8- 32 min, Frequency = 10 Hz RF power= 40 W]

The composition of the decorated Nb₂O₅ nanoparticles were examined by using the XPS measurements and the results are presented in Fig 4.9 (b). The binding energies of Nb 3d_{5/2} and 3d_{3/2} core level were 208.14 eV and 210.68 eV respectively. The spin-orbit splitting between Nb 3d_{5/2} and 3d_{3/2} core level was 2.6 eV, which perfectly matched the reported values for Nb₂O₅ [248]; thus, this result suggested that the chemical state of the decorated nanoparticle is in the Nb⁺⁵. The similar shift of the 0.16 eV were observed in the Nb 3d_{5/2} peak towards the lower binding energies with increasing of Nb₂O₅ concentration which suggests that electron transfer from graphene to the Nb₂O₅, i.e. a p-type charge transfer doping of graphene. This can be explained as follow, the band of Nb₂O₅ move closer to the Fermi level with accumulation of the electrons from the graphene in the bands of the Nb₂O₅. As discussed in chapter #3 the band of the Nb₂O₅ bends toward the interface after the charge is transferred from graphene to Nb₂O₅. Therefore, the Nb 3d core level shifted toward the lower binding energy due to the band bending of the Nb₂O₅ upon interface with graphene sheets.

A Gaussian fit was performed on the O 1s peaks of deposited Nb₂O₅ nanoparticles onto graphene at 32 min of deposition and three components centered at ~530.92 eV (OI), ~532.4 eV (OII) and ~533.80 eV (OIII), respectively are displayed in Fig 4.9 (a). The OI sub peak is attributed to O²⁻ bound to Nb⁺⁵, while the two other components OII and OIII at higher binding energy values, 532.13 eV, and 534.15 eV, may come from the (C=O, COO) and from C-O bonding.

Additionally, the oxide stoichiometry (OI/Nb), and Nb/C (%) atomic ratios were also estimated from the XPS analysis. The measured the OI/Nb as function of deposition time is presented in Fig 4.9 (b). The measured values of OI/Nb indicate that the deposited Nb₂O₅ nanoparticles onto graphene sheets are under stoichiometric with respect to the ideal value of Nb₂O₅, which is 2.5

As expected Nb/C sp^2 atomic ratio increased from 0.93 and reached 1.51 atomic ratio %, when the decoration times of the Nb₂O₅ nanoparticles onto graphene powder was varied from 8 min to 32 min. It was found that with decorated graphene Nb₂O₅ nanoparticles with 10 Hz is that, more Nb/C atomic ratio % was obtained with respect to the case of without moving graphene powder (0 Hz). This is described in section 4.1.1.

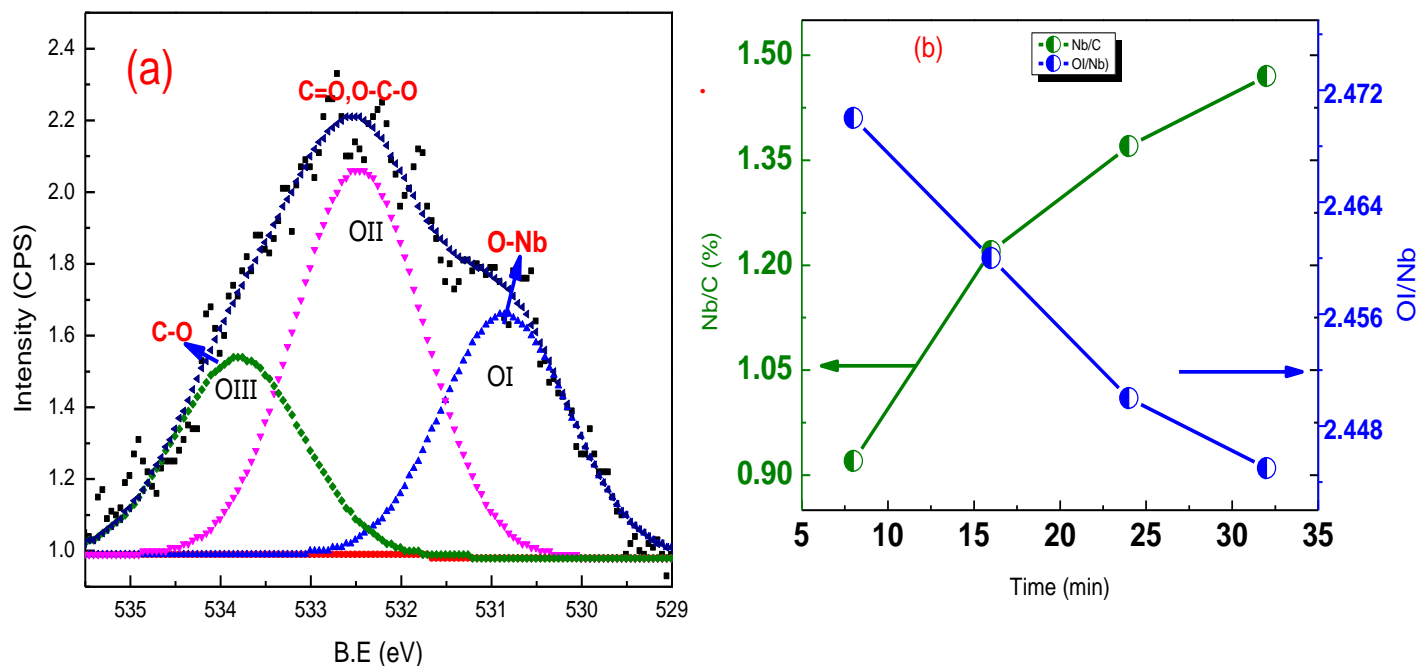


Fig 4. 9 (a) De-convolution of the O 1s core level (b) variations of Nb/C and Stoichiometry with respect to different time of deposition

4.4.2 XRD analysis of undecorated Graphene and Nb₂O₅ doped graphene

Fig 4.10 (a) illustrates the XRD patterns of the undecorated graphene and decorated graphene with Nb₂O₅ nanoparticles at different times of deposition. Fig4.11 (a) shows a broad diffraction peak around 25.11° which corresponds to the (002) diffraction peak of few layer graphene. The weak peak intensity suggests that the graphene sheets consist of less than 5 layer of graphene. The inset of Fig 4.11 (a) depicts that (002) peak of graphene sheet was shifted toward lower 2θ values after Nb₂O₅ deposition. This shows that the d-spacing of the graphene sheet increased

upon the deposition of Nb₂O₅ nanoparticles. The calculated d-spacing values in accordance with 2θ values are 0.354, 0.355, 0.356, 0.3564 and 0.357 nm respectively. This can suggest that distortions in the lattice of graphene induced with increasing of Nb₂O₅ concentration. Moreover the XRD patterns show linear trend in the full width at half-maximum (FWHM) of (002) peak as a function of Nb/C (sp²). The evaluated of the values of the (FWHM) of the 002 peak of the graphene as function of Nb/C (sp²) ratio are presented in Fig 4.10 (b). The FWHM of the (002) peak increased from 4.54 and reached 4.92 with deposition of Nb₂O₅ nanoparticles in a ratio Nb /C (sp²) = 1.51 at.ratio (%).The broadening of the (002) peak indicates that, structural defects were pronounced in the structure of graphene with decoration of Nb₂O₅ nanoparticles onto graphene sheets.

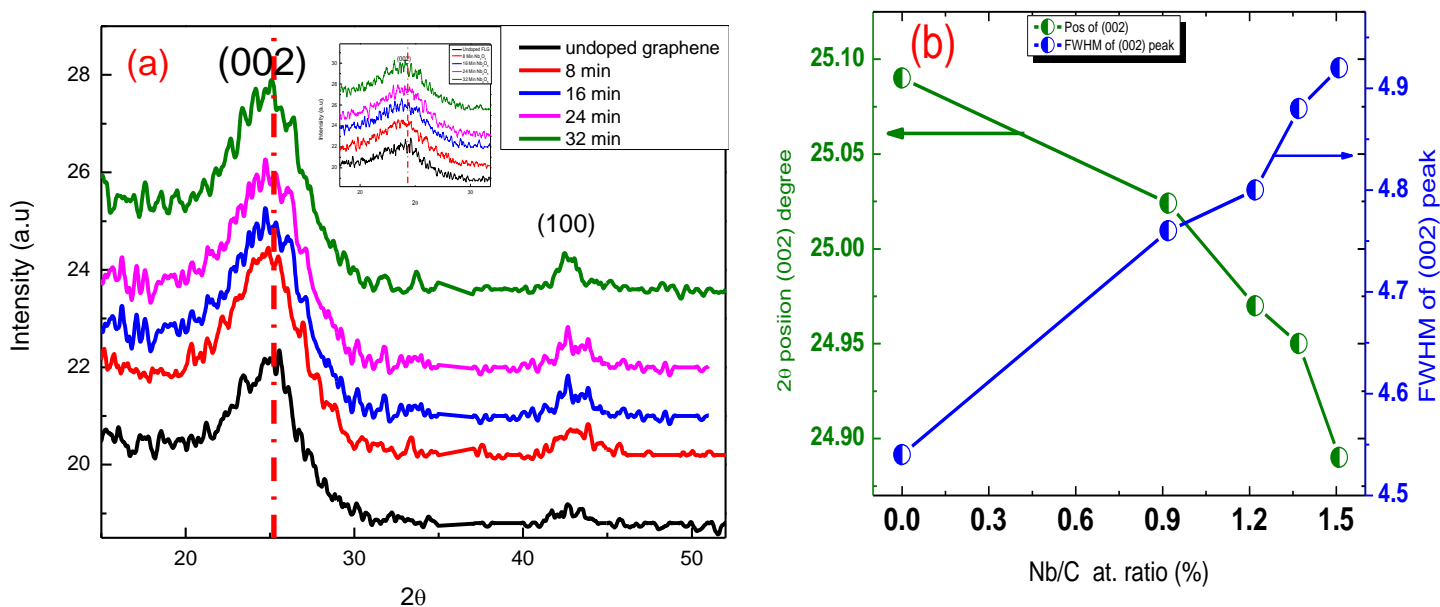


Fig 4. 10 (a) XRD patterns of the undoped graphene and Nb₂O₅ doped graphene at different times of deposition (b) Variation of the 2θ angle of the (002) and FWHM (002) as a function Nb/C atomic ratio (%)

The notable feature in the XRD pattern is that 002 peak shifted more towards lower angles values with respect to the decorated Nb₂O₅ nanoparticles without moving graphene powder, which have been discussed above in section(4.1.2). The same deposition times were used in both

cases. The more likely reason of this high shift is due to fact that with vibration of graphene powders more Nb₂O₅ contents are deposited to the graphene rings, which generates more distortion in the plane of graphene.

4.4.3 Raman Spectroscopy of Nb₂O₅ decorated graphene via given vibration to graphene powder

The Raman spectra of undecorated graphene and Nb₂O₅ decorated graphene by rising deposition time are shown in Fig 4.11 (a). In the previous section (4.1.3) we presented the Raman spectra of decorated graphene with Nb₂O₅ nanoparticles without moving the graphene powder during the deposition and discussed the upshift of G and 2D peaks upon the deposition of the Nb₂O₅ nanoparticles. Now in this section 10 Hz powder vibration frequency with 32 μm amplitude was given to the graphene powder during the deposition.

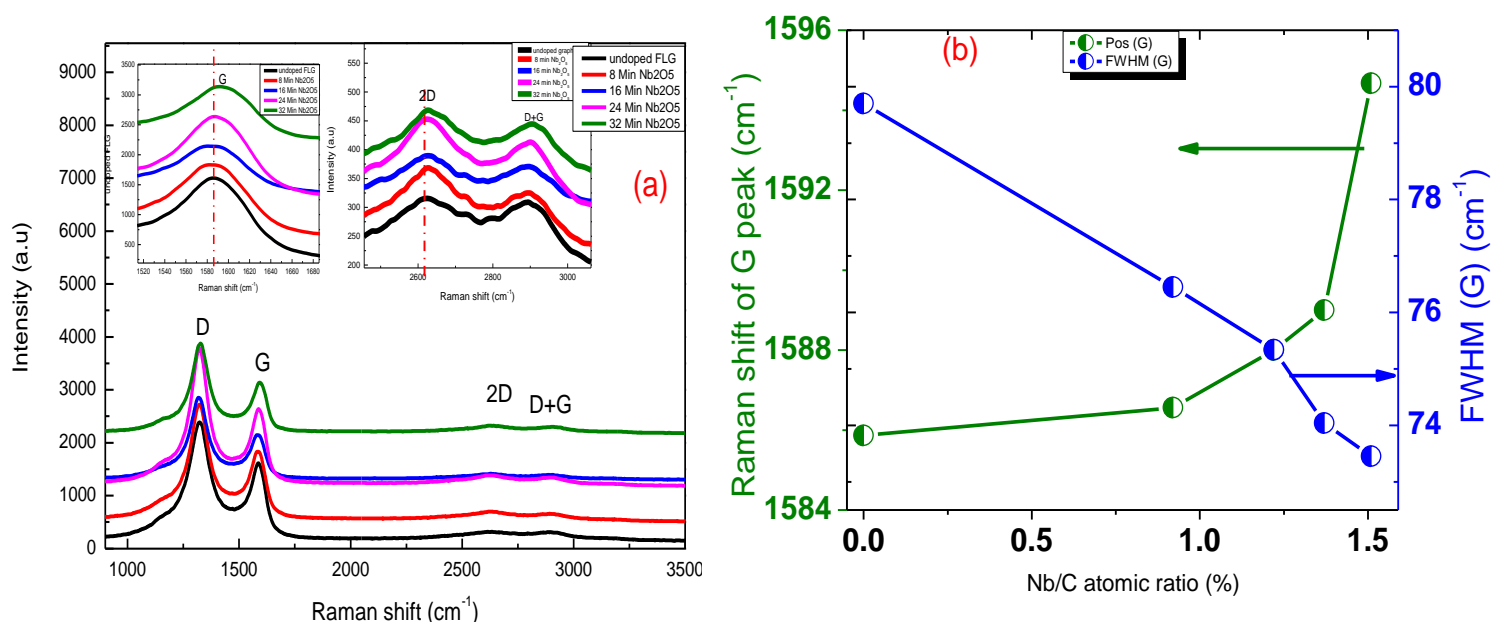


Fig 4. 11 (a) Raman spectra of undoped GNPs and (b) positions of the G and FWHM (G) vs Nb to C (%) Nb₂O₅ doped GNPs at different time of deposition

Again four peaks were observed for all samples, which correspond to the D, G, 2D and D+G bands respectively. More likely, strong variation in the FWHM and position of the G and 2D were observed of graphene powder after the deposition of Nb₂O₅ nanoparticles.

The upshift in the G and 2D were detected after the deposition of the Nb₂O₅ nanoparticles. The upshift in the G and 2D increased with the stepping up the deposition time. The maximum upshift in the G and 2D of 9.21 cm⁻¹ and 7.8 cm⁻¹ were observed after the deposition of the Nb₂O₅ nanoparticles onto graphene powder in a ratio Nb/C (sp²) = 1.51 at.ratio (%). The upshift of G and 2D bands after the deposition of Nb₂O₅ nanoparticles suggest that, there is strong electronic interaction between the graphene and Nb₂O₅ nanoparticles due to which the bands of graphene shifted to higher wavenumbers. Based on the reported observation about the upshifted of the G and 2D bands are due to the hole doping and opposite for the electronic doping. Accordingly, the upshift in the G and 2D bands of the graphene upon the deposition of Nb₂O₅ nanoparticles are due to p doping, whereas the electrons being transferred from graphene to the Nb₂O₅ nanoparticles and this result is well consistent with XPS analysis.

Additionally, it is interesting to note that the FWHM (G) peak decreased with rising of Nb/C (sp²) atomic ratio (%) and the results are presented in Fig 4.11 (b). The FWHM of G peak decreased from 79.7 cm⁻¹ and 73.43 cm⁻¹, after the deposition of Nb₂O₅ nanoparticles in ratio Nb/C (sp²) = 1.51 at.ratio (%). It is well understood that doping has major influence on the Raman spectra. Doping in graphene shifts the Fermi level away from the Dirac point, which decreased the probability of the excited charge carrier recombination [207]. It is also well established that the lattice strain can also modify the FWHM of the G peak. Zhen Hua Ni, et al reported that the FWHM of G peak varied with both compressive and tensile strain [249]. For the compressive strain the FWHM of the G peak increased and opposite for the tensile strain[228]. In

addition to this it has been also reported that the FWHM (G) decreases and the G peak position increases for both electron and hole doping. The FWHM (G) sharpening is due to Pauli blocking of phonon decay into e – h pairs when the e – h gap is higher than the phonon energy [250, 251]. Therefore, it can be considered that the reduction FWHM of the G peak is not only due to the doping, but might due to the tensile strain induced in graphene by decoration of Nb₂O₅ nanoparticles.

Generally the intensity ratio of D to G peak I_D/I_G can be used to measure the level of disorder and defects in graphitic materials. It is noticeable that the intensity of the D peak becomes very strong after the deposition of Nb₂O₅ nanoparticles. This indicates that after interaction of graphene with Nb₂O₅ nanoparticles the symmetry of the graphene was broken and which induced the structural defects in the graphene.

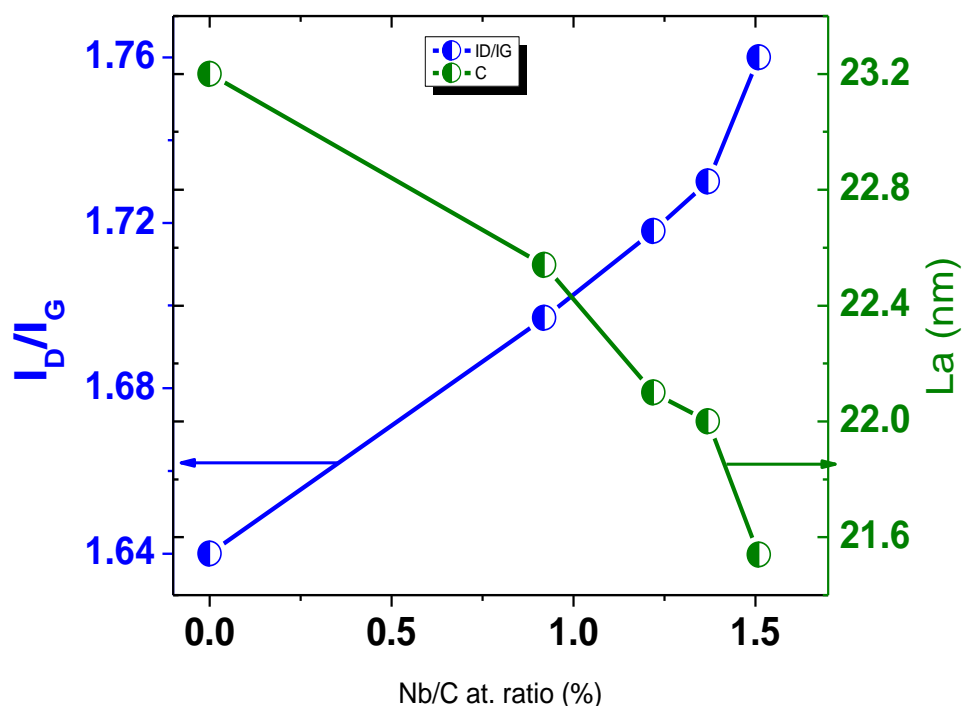


Fig 4. 12 Variation of Raman peak intensity ratios of I_D/I_G plotted against the Nb to C atomic ratio (%).

Fig 4.12 shows I_D/I_G the intensity (area) ratio of the decorated graphene with Nb₂O₅ nanoparticles as a function of Nb/C (sp²) atomic ratio (%). The I_D/I_G ratios are linearly increased with rising of Nb/C (sp²). The I_D/I_G ratios values increased 1.76, when Nb₂O₅ nanoparticles were deposited onto graphene sheets with a ratio Nb/C (sp²) = 1.51 at.ratio (%) to the value obtained for undoped graphene I_D/I_G 1.64. This suggests that with deposition of the Nb₂O₅ nanoparticles onto graphene sheets the structural defects in the sp² framework were enhanced. The in-plane crystalline size was calculated for the decorated graphene with Nb₂O₅ nanoparticles by using the equation (1). The in-plane crystalline size as a function of Nb/C (sp²) is presented in Fig 4.12. By increasing the Nb/C (sp²) ratio the in-plane crystalline size of graphene decreased. The in-plane crystalline size decreased from the 23.2 nm to 21.2 nm, when the Nb₂O₅ nanoparticles deposited in a ratio Nb/C (sp²) = 1.51 at.ratio (%)

4.5 Effect of Nb₂O₅ nanoparticles on the structural and chemical properties of graphene powder deposited by varying the RF power values

In the above two sections, the interaction of the sputtered particles with graphene by keeping constant the sputtered particles energy with constant RF power value was presented. The structural defects induced in graphene plane with interaction of the sputtered and plasma species. The main goal of this work is to study the interaction of the Nb₂O₅ nanoparticles with graphene sheet deposited by varying the RF power values. By changing the RF power values to Nb₂O₅ target different amounts of Nb₂O₅ nanoparticles were obtained on the graphene sheets. The Raman and X-ray diffraction techniques were used to investigate the structural defects. The chemical analysis of the decorated graphene with Nb₂O₅ nanoparticles were performed by using XPS. Moreover the process parameters are presented in table 4.3.

Table 4.3 the process condition of decorated graphene with Nb₂O₅ nanoparticles

Sample #	RF Power (W)	Process pressure (Pa)	Deposition Time (min)	Powder vibration frequency (Hz)
1	40	6	15	10
2	60	6	15	10
3	80	6	15	10
4	100	6	15	10

4.5.1 Chemical analysis of undoped graphene and Nb₂O₅ doped graphene at different RF power

XPS analysis was performed for the decorated graphene with energetic sputtered Nb₂O₅ nanoparticles. Fig 4.13 depicts the XPS spectra of decorated graphene with Nb₂O₅ nanoparticles deposited at different RF power values. The high resolution XPS spectra of the undecorated graphene and decorated graphene at different RF power values are presented in Fig 4.13 (a). The C 1s peak is asymmetric with a long tail extending to the high binding energy region. The C 1s core levels were de-convoluted into three components. The characteristic and features of the de-convoluted components are similar to those which are explained in the section of 4.3.1. More importantly, downshifts in the C 1s core levels of graphene were observed after the deposition of Nb₂O₅ nanoparticles. The downshift in the C 1s core levels of graphene increased by the increasing the RF power values. The maximum downshift of 0.18 eV of C 1s core level was observed upon the deposition of Nb₂O₅ nanoparticles in a ratio (Nb/C sp²= 2.09 at. %), at 100 W RF power value. Literature surveys suggest that, when graphene interacted with metal oxide the charge is expected to transfer at the interface between the contacted materials due to the difference of work function. Using the C 1s peak of undoped graphene as a reference for the

neutral charge transfer graphene, then the shift of 0.18 eV to lower binding energy after the interaction of Nb₂O₅ corresponds to a p type doping of graphene. The doping of graphene by metal oxide at interface is well established phenomena [23]. Consequently the charge transfer between the Nb₂O₅ and graphene due to the difference of the work function.

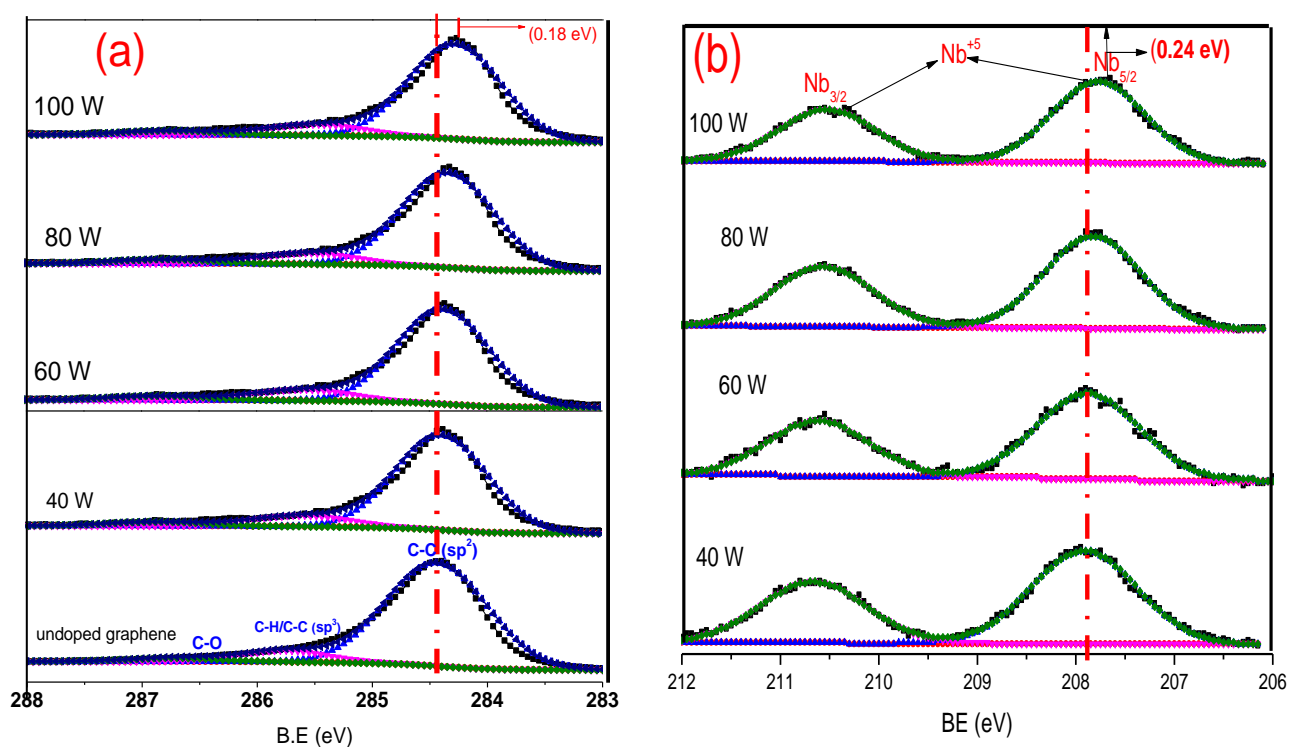


Fig 4. 13 XPS spectra of graphene powder with incrementally increased Nb₂O₅ contents by varying the RF power values (a) (a) Shift in the C 1s core levels position upon Nb₂O₅ deposition (b) Nb 3d core level spectra with positions of the Nb⁺⁵ peaks. [Process pressure = 6 Pa, Time=15 min, Frequency = 10 Hz]

Fig 4.13 (b) shows XPS spectra of the Nb 3d peaks for the Nb₂O₅ nanoparticles decorated he graphene surface with rising RF power values. The Nb3d_{3/2} and Nb3d_{5/2} peaks are located at 207.89 eV and 210.64 eV, respectively. The binding energies of these photoelectron peaks are characteristic of Nb⁺⁵ states. It is interesting to note that, the Nb 3d core level shifted toward the lower binding energy by increasing the RF power values. The maximum downshift of 0.24 eV in the Nb 3d_{5/2} was observed after the deposition of Nb₂O₅ nanoparticles at 100 W. More likely

reason for the downshift of the 3d_{5/2} is that, charge transfer between the graphene and Nb₂O₅ nanoparticles are occurred at the interface. Due to the difference of the work function between graphene (4.3 eV) and Nb₂O₅ nanoparticles (4.70 eV) electrons are transferred from the graphene to Nb₂O₅ band. Therefore, in order to align the band between the graphene and Nb₂O₅ the band of Nb₂O₅ bend towards the interface happened and the binding energy values of the Nb₂O₅ decreased.

The O1s XPS core level of decorated Nb₂O₅ nanoparticles on graphene surface at 100 W are presented in Fig. 4.14 (a). The O 1s core level displays an asymmetric shape at higher binding energy values. The O 1s peak was fitted by three Gaussian components. The main component (OI) located at binding energy (530.89 eV) is assigned to the O⁻² bound to Nb⁺⁵. Two shoulder components towards the higher binding energies values located at 532.12 eV and 533.3 eV can be assigned to the C=O and C-O bonds respectively.

More interestingly, OI/Nb ratios for the decorated graphene with Nb₂O₅ nanoparticles at different RF power values were estimated from the XPS analysis. The measured values of the OI/Nb ratio as a function of RF power values are depicted in Fig 4.14 (b). The OI/Nb ratio decreased from 2.47 and reached 2.26, when RF power values were varied from 40 W to 100 W

Also the Nb/C sp² atomic ratio (%) increased from 0.69 and reached to 2.09 atomic ratios (%) upon the deposition of Nb₂O₅ nanoparticles at 100 W. These results indicate that by the deposition of Nb₂O₅ nanoparticles the oxygen vacancies generates into the lattice of Nb₂O₅. The oxygen vacancies in the lattice Nb₂O₅ increased by raising the RF power values. To address this point, the vacancy formation mechanisms involve direct removal of oxygen from Nb₂O₅ lattice by the interaction plasma energetic species.

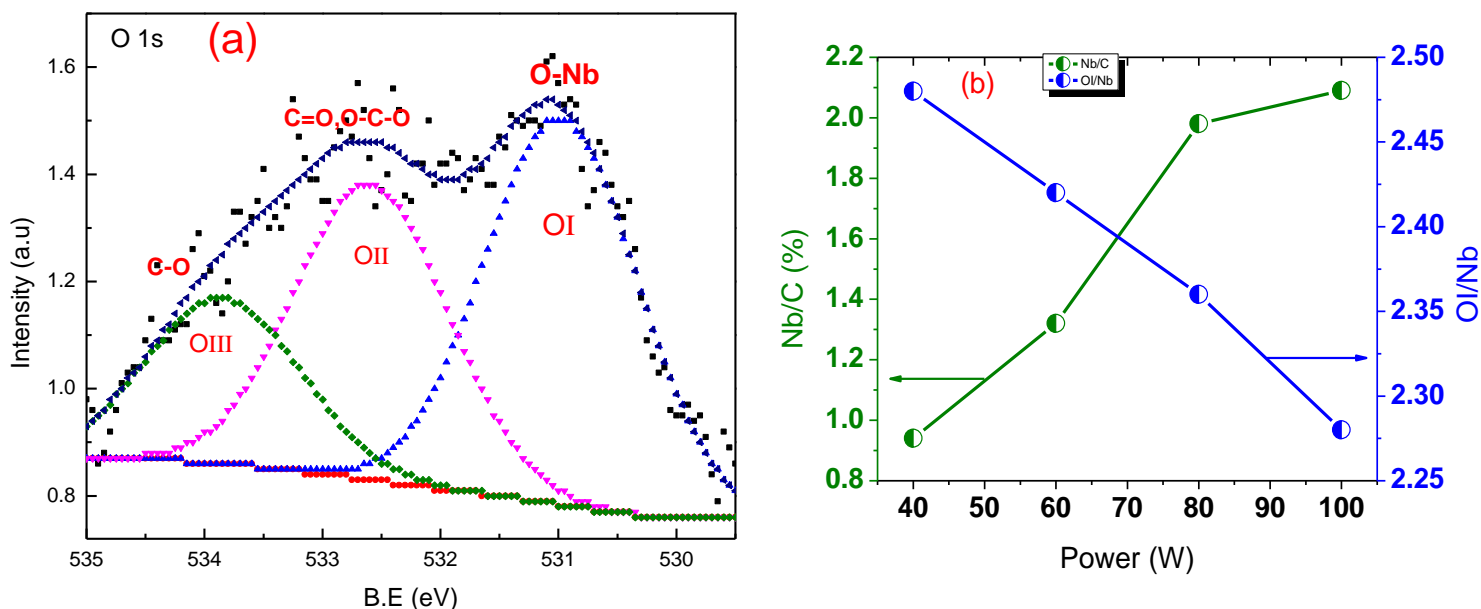


Fig 4. 14 (a) De-convolution of the O 1s core level (b) variations of Nb/C and with respect to RF power values

4.5.2 XRD of undoped Graphene and Nb₂O₅ decorated graphene at different RF power

The XRD patterns of undoped graphene and decorated graphene with Nb₂O₅ films deposited by varying the RF power values are presented in Fig 4.15 (a). The undoped graphene powder shows a broad and low intensity peak centered at $2\theta = 25.36^\circ$ which corresponds to the few layers graphene planes. The 2θ position of (002) of graphene powder gradually shifts toward the lower angle value by increasing the RF power values. The evaluated values of the undecorated graphene and for the decorated values as a function of Nb/C sp² are presented in Fig 4.15 (b). The shift of (002) peak toward the lower angle values after the deposition of the Nb₂O₅ nanoparticles suggest that, the d spacing of the graphene sheets increased by raising the Nb/C sp². The calculated d-spacing values in accordance with 2θ values are 0.351, 0.3524, 0.3526, 0.353 and 0.355 nm respectively. More importantly the XRD patterns show systematic changes in the full width at half-maximum (FWHM) of the (002) peak as a function of Nb/C (Sp²) are depicted in Fig 4.15 (b). The broadening of (002) peak of graphene powder after the interaction

of Nb₂O₅ nanoparticles deposited by varying the RF power values indicates that the defects are pronounced in the graphene framework.

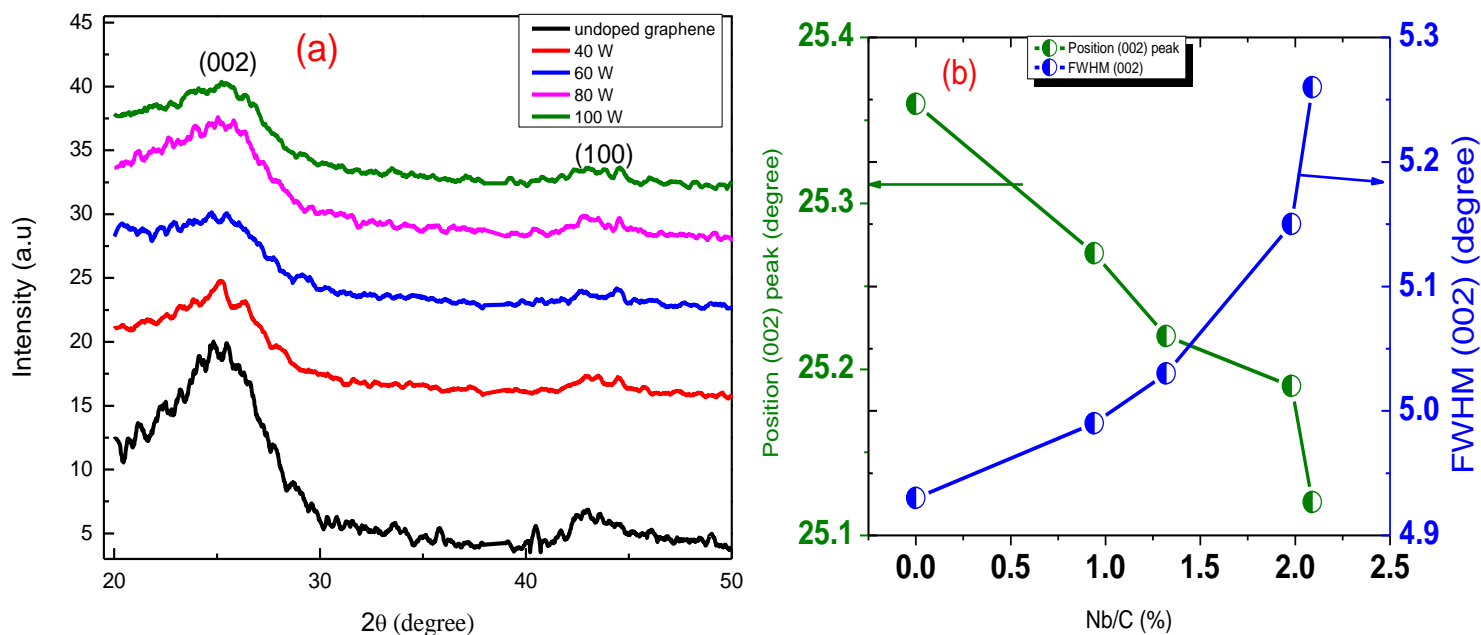


Fig 4.15 (a) XRD patterns of the undoped graphene (b) Variation of the 2 θ angle of the (002) and Nb₂O₅ and doped graphene at different RF Power FWHM (002) as a function of Nb/C atomic ratio (%)

4.5.3 Raman Spectroscopy of undoped graphene and Nb₂O₅ doped graphene at different RF power values.

Fig 4.16 (a) present the Raman spectra of the undecorated graphene and decorated graphene with Nb₂O₅ nanoparticles deposited at different RF power values. In all Raman spectra, the characteristic G and 2D bands of graphene (centered at ≈ 1586 cm⁻¹ and ≈ 2646 cm⁻¹, respectively) are present. The D and D+G bands (≈ 1330 cm⁻¹ and ≈ 2920 cm⁻¹, respectively) are also present in the spectra and typically suggest the presence of defects in the graphene lattice like edges and disordered carbon.

It is reported that significant changes occur in the properties of graphene, in specific its electronic structure and phonon frequencies when holes or electron are added by the interaction

with metal or metal oxide [26]. It was recently revealed that due to the charge transfer mechanism the Fermi level of graphene modulated [252]. The charge transfer between the graphene and metal oxide interaction is a well-known phenomenon [253, 254]. The induced charge transfer between the graphene and metal oxide which modifies the electronic properties of graphene can be understood by using characteristic Raman spectra of graphene. The confirmation of the charge transfer between the graphene and metal oxide can be identified by measuring the position of D, G or 2D bands or their ratios. It is also well established that the, the G and 2D bands of the graphene was shifted to higher frequency upon the p doping graphene with metal oxide [255]. A low blue shift of 4 cm⁻¹ and 3 cm⁻¹ were observed upon the deposition of Nb₂O₅ nanoparticles at 40 W RF power values. The upshifts in G and 2D bands increased with raising RF power values. The maximum upshift of G and 2D by 11.5 cm⁻¹ and 9.5 cm⁻¹ were observed, when the Nb₂O₅ nanoparticles were deposited onto graphene sheets in ratio Nb/C sp²=2.09 atomic ratio (%) at 100 W RF power value. The blue shift in G and 2D peaks of graphene after the decoration of Nb₂O₅ nanoparticles suggest that, the charge are transferred between the graphene and Nb₂O₅ nanoparticles, where the electron being transferred from graphene to Nb₂O₅ nanoparticles. It is therefore clear that Nb₂O₅ films interact with graphene as electron acceptor and the charge is the transfer between the graphene and Nb₂O₅ nanoparticles.

Interestingly the FWHM of G peak decreased with interaction of Nb₂O₅ nanoparticles. Further the doping confirmation can be extracted from the FWHM of G peak. It has been reported that the FWHM of G peak decreases with electrons and holes doping. Fig 4.16 (b) depicts the FWHM of G peak as a function of the Nb/C sp² atomic ratio. The FWHM of G peak is decreased as a function of increasing Nb/C (sp²) by varying the RF power values. The FWHM of G peak

decreased from 78.68 and reached to 71.8 cm⁻¹ when the Nb₂O₅ nanoparticles were deposited in a ratio of Nb/C (sp²) = 2.09 % to C (Sp²).

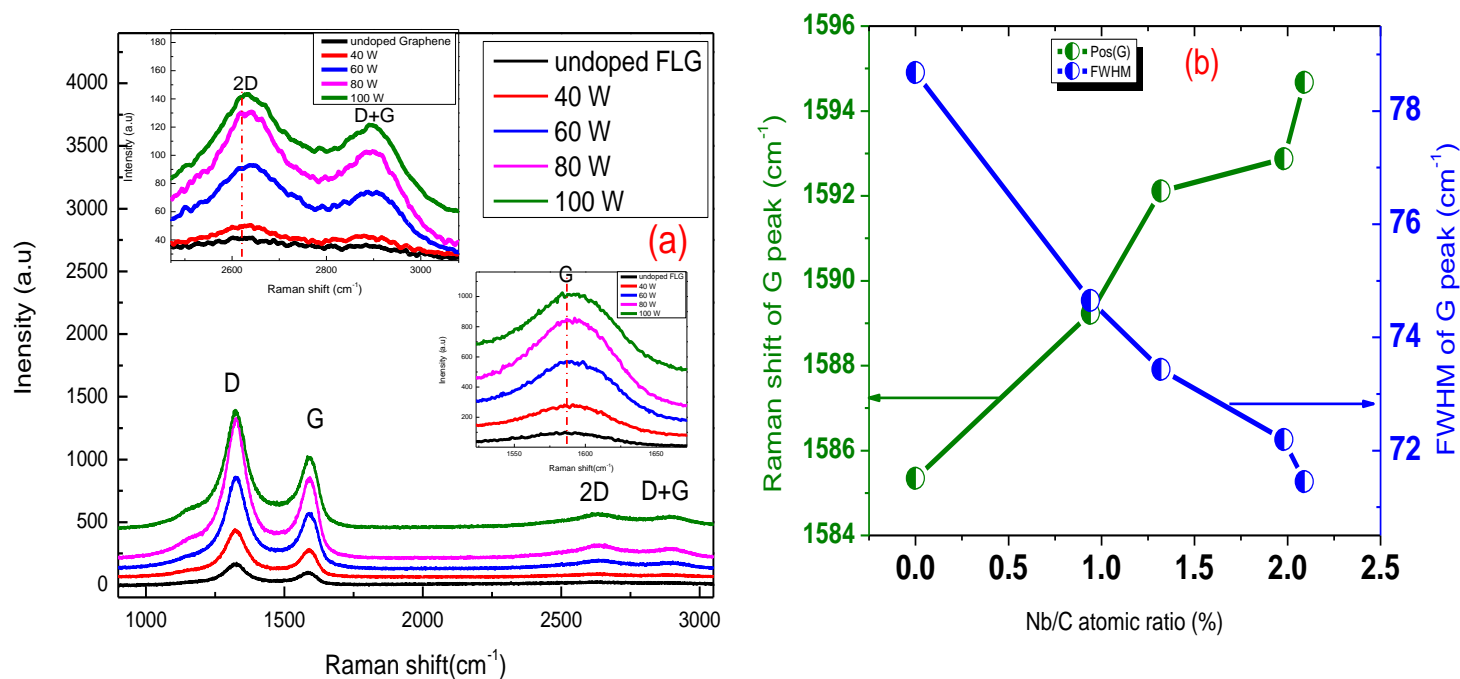


Fig 4.16 (a) Raman spectra of undoped GNPs and (b) positions of the G and FWHM (G) vs Nb to C (%) Nb₂O₅ doped GNPs at different RF powers

The sharpening of the FWHM of G peak after the interaction Nb₂O₅ films corresponding to the doping. In the section 4.4.3, we discussed that the FWHM of G peak decreased, when the tensile or compressive strain was developed in the lattice of graphene sheets. Our XRD results demonstrate that with deposition of the Nb₂O₅ nanoparticles onto graphene sheets the tensile strain was established in the lattice of graphene sheets. From these observations, it can be considered that the reduction of FWHM of G peak not only doping also might be due to the tensile strain induced in graphene sheets.

It is well known that the intensity ratio of D band to G band (I_D/I_G) was used to quantify the level of defects and disorderness induce in the structure of the graphene. The I_D/I_G is directly related to the diameter of the crystalline cluster (L_a) in the graphite system. Fig. 4.17 presents the I_D/I_G ratios as a function of the Nb/C (sp²), when Nb₂O₅ nanoparticles were deposited onto to graphene sheets by increasing the RF power values. .

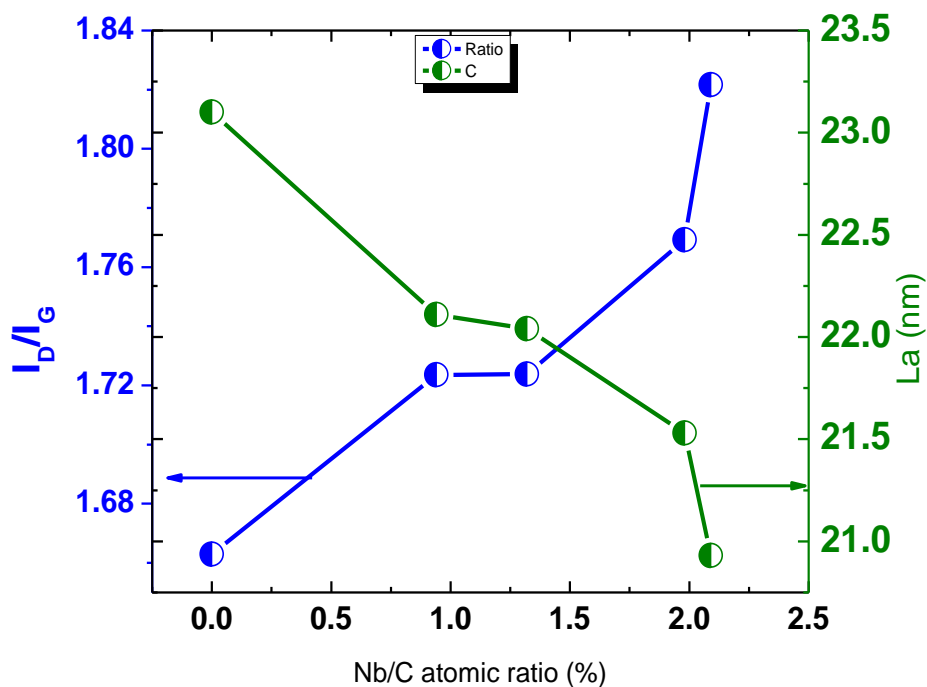


Fig 4. 17 Variation of Raman peak intensity ratios of I_D/I_G plotted against the Nb to C atomic ratio (%).

The I_D/I_G ratio of the increased from 1.66 and reached to 1.82, when the Nb₂O₅ nanoparticles were deposited in a ratio Nb/C (sp²) = 2.09 atomic ratio (%). This can suggest that with interaction of sputtered particles and energetic plasma species induced defects in the sp² framework of graphene. To address this point, it has been well established that by increasing RF power values the sputtered particles and plasma species gain more kinetic energy during the deposition and interact with graphene surface more energetically. Due to the interaction of the energetic plasma species and sputtered particles with graphene the defects are introduced in the

graphene rings. The defects are increased with interaction of the high energetic species and sputtered particles.

4.6 Conclusion Remarks:

In summary, the influence of the Nb₂O₅ concentrations on the structural, chemical, morphological and magnetic properties of graphene deposited by varying the deposition process parameters were investigated. Based on the variation of Nb₂O₅ concentrations by varying the deposition process parameters the chapter was categorized in three sections.

In section 4.3, the effect of Nb₂O₅ concentrations on the structural, chemical and magnetic properties were studied. The Nb₂O₅ nanoparticles were deposited on the surface of graphene by varying the deposition time via no vibration given to graphene powders. The structural properties of the decorated graphene were investigated using X-ray diffraction and Raman spectroscopy. From the X-ray diffraction analysis it was observed that by decoration of graphene with Nb₂O₅ nanoparticles the lattice of graphene distorted and the d-spacing of the layers of graphene increased. Raman study revealed that the frequency of the G band undergoes blue shift after the interaction of Nb₂O₅ nanoparticles. The blue shift can suggest that Nb₂O₅ nanoparticles interact with graphene as an electron acceptor and the charge transfer from graphene to Nb₂O₅ nanoparticles. Also defects and disorderness in the graphene were increased after the decoration of Nb₂O₅ nanoparticles. X-ray photoelectron spectroscopy analysis shows that electron transfer from graphene to Nb₂O₅ nanoparticles is responsible for the p-type doping of graphene. The morphology and size distributions of the decorated Nb₂O₅ nanoparticles on the graphene powder were confirmed by transmission electron microscopy (TEM). The size of the decorated Nb₂O₅ nanoparticles on the graphene sheet is around 15 to 20 nm. The magnetic data indicate that

formation of Nb₂O₅ nanoparticles anchored to the graphene matrix. The ferromagnetic behaviors of graphene are significantly changed by the interaction of Nb₂O₅ nanoparticles.

In section 4.4, the influences of the Nb₂O₅ nanoparticle on the structural and chemical properties of the graphene were discussed. The interactions of the graphene with Nb₂O₅ nanoparticle deposited by RF sputtering via given 10 Hz vibration to the graphene powder during the deposition process were investigated by X-ray diffraction (XRD), Raman spectroscopy and X-ray photoelectron spectroscopy. The XRD result demonstrates that the d-spacing of the graphene sheets increased with the interaction of the Nb₂O₅ nanoparticle. The strong p-doping effect was clearly evident in the Raman spectroscopy data where the positions of the G of graphene progressively upshifted after the increasing the Nb₂O₅ concentrations. Increasing intensity of the D peak of graphene after the interaction of Nb₂O₅ nanoparticles suggest that the defects and disorderness were induced in the structure of graphene. The chemical environment of the surface composition of the decorated graphene with Nb₂O₅ nanoparticles was recorded by X-ray photoelectron spectroscopy. By stepping up the deposition time the Nb percentage in host graphene was regulated ranging 0.48 to 1.51 %. The downshift shift in C 1s peak after decoration of the Nb₂O₅ on the surface of the graphene powder due to charge transfer i.e P type doping of the graphene with the Fermi level downshifted by 0.11 eV.

In section 3.5 the graphene powders were decorated with Nb₂O₅ films by varying the RF power values ranging from (40-100 W). Different amount of Nb₂O₅ concentrations were obtained on the graphene surface by varying the RF power value to Nb₂O₅ target. It has been reported that by increasing the RF power values during the plasma deposition, more sputtered particles extracted from the target having high kinetic energies. The interaction of the high energetic sputtered particle with graphene sheet induced structural defects. The chemical and structural properties of

decorated graphene with energetic sputtered particles were characterized by Raman spectroscopy; X-ray diffraction X-ray photoelectron spectroscopy. The XRD investigation shows that with the interaction of the energetic sputtered particles the lattice of the graphene was distorted. The d spacing of graphene was linearly increased with interaction of the energetic sputtered particles. Raman study revealed that with interaction of the graphene with Nb₂O₅ films blue shift of the G band observe, which are consistent with p-type doping. Finally, XPS measurements of the graphene/Nb₂O₅ interface suggest p-type doping of graphene due to charge transfer at the interface as a consequence of the high work function of Nb₂O₅.

Concluding this chapter, the interface between Nb₂O₅ nanoparticle and graphene sheets were presented. The detailed structure, chemical, morphological and electronic properties were discussed. In next chapter # 5, the structural, chemical, morphological and electronic properties of the decorated graphene sheets with Mg nanoparticle will be presented.

Chapter # 5

Effect of Mg crystalline nanoparticles and crystalline film on the structural and chemical properties of graphene powder

5.1 Introduction:

Recently, owing to the exceptional material's properties, a remarkable research attention has been focused on graphene. Meanwhile it is believed that the graphene, which has high surface area, serves as an ideal support for anchoring well-dispersed nanoparticles for the improvement of its catalytic action toward the hydrogen dissociation. It has been reported that Magnesium based hybrid materials a promising candidates for the hydrogen storage, because of their high gravimetric and volumetric hydrogen storage capacities. In this chapter we demonstrate different approaches to employ graphene as hydrogen storage materials. First, strategy is to decorate the graphene with very small Mg nanoparticles to enhance the hydrogen sorption. In parallel, different RF process parameters will be varied to achieve the well dispersed nanoparticles onto graphene sheets in the range in the range of 5-10 nm. On such scale, quantum size effects enter at play lowering the H₂ desorption temperature from 350°C typical of bulk Mg hydrides to 140°[²⁵⁶]. In order to achieve the small Mg nanoparticles on the surface of graphene powder different depositions process parameters like RF power, Powder vibration frequency and deposition time were varied. Based on the deposition conditions used, this chapter is divided into three sections; this is categorized like this;

- ❖ For the results described in section I, the chemical structural and electronic properties of decorated graphene with Mg nanoparticles will be discussed.
- ❖ For the results reported in section II, different levels of Mg nanoparticles were obtained onto graphene sheets by increasing the deposition time. The structural, chemical and electronic properties of the decorated graphene with Mg nanoparticles will be displayed.

- ❖ For the results described in section III, Mg nanoparticles were decorated onto graphene sheet by varying the powder vibration frequencies. Structural analysis was investigated by Raman and x-ray diffraction and chemical analysis were performed with XPS analysis.

5.2 Experimental details

The crystalline Mg nanoparticles and crystalline films were deposited onto graphene powders by radio frequency sputtering in Ar plasma. A high purity Mg disc (99.99%) with 5 cm diameter was used as a sputtering target. Powder vibrating stage was developed for the uniform distribution of Mg nanostructures onto graphene surface. More specific details for each section are given below:

- To obtain different level of Mg contents onto graphene sheets the power applied to the Mg cathode was varied from 30 to 75 W, corresponding to self-bias voltage ranging between -157 to -273 V. The powder vibration frequency and deposition time was fixed at 10 Hz and 18 min respectively. The total process pressure was fixed at 6 Pa.
- In order to achieve different amounts of the Mg nanoparticles onto graphene, the graphene powder was decorated with Mg nanoparticles deposited by stepping up the deposition time (6 to 27 min). The self-bias voltage and power applied to Mg target was fixed at -158 V and 40 W respectively. The total process pressure and powder vibration frequency for each deposition were kept at 6 Pa and 10 Hz respectively.
- The Mg nanoparticles were deposited onto graphene sheets by using different powder vibration frequencies. For the well distributed Mg nanoparticles onto graphene sheet the powder vibration frequency was varied from $0 \leq \omega \leq 100$ Hz with constant amplitude of 32 μm . The process pressure and power applied to Mg target were fixed at 6 Pa and 40 W respectively. The deposition time were kept constant at 27 min.

5.3 The effect of crystalline Mg nanoparticles on the properties of graphene powder deposited at different RF power values

The main goal of this work is to decorate graphene with well dispersed Mg nanoparticle and study the interaction of the energetic sputtered particles deposited by increasing RF power values. Different amount of Mg concentrations were obtained by changing the RF power values. By increasing the RF power values the energy of the sputtered ions were increased and reached at surface of the graphene with high kinetic energy. The influence of the energetic sputtered particles and plasma species on the structural and chemical properties of the graphene will be discussed in this section. Different characterization techniques were used to investigate the structural defects induced in graphene by the interaction of the energetic sputtered particles. The Raman and XRD were used to study the structural defects and for the chemical analysis XPS was used. The morphology of the deposited Mg nanoparticles onto graphene was examined by TEM analysis. Moreover the process parameters are presented in table 5.1.

Table 5.1 the process condition of decorated graphene with Mg nanoparticles

Sample #	RF Power (W)	Process pressure (Pa)	Deposition Time (min)	Powder vibration frequency (Hz)
1	30	6	18	20
2	45	6	18	20
3	50	6	18	20
4	60	6	18	20
5	75	6	18	20

5.3.1 TEM analysis of graphene sheets decorated with Mg nanoparticles at 27 min of deposition.

The surface morphology of the decorated graphene with Mg nanoparticles was investigated using Transmission electron microscopy (TEM). Fig 5.1 (a, b) presents the TEM micrographs of the deposited Mg nanoparticles onto graphene 27 min of deposition. TEM micrograph of Mg/graphene composite shows that Mg nanoparticles are uniformly distributed onto graphene sheet. These nanoparticles were deposited at powder vibration frequency (10 Hz). Fig (b) shows that the deposited particles distributed uniformly onto graphene sheets. However, the deposited Mg nanoparticles made aggregates onto graphene sheets. Moreover the deposited Mg nanoparticles are in spherical shape and having an average particles size of 20-25 nm.

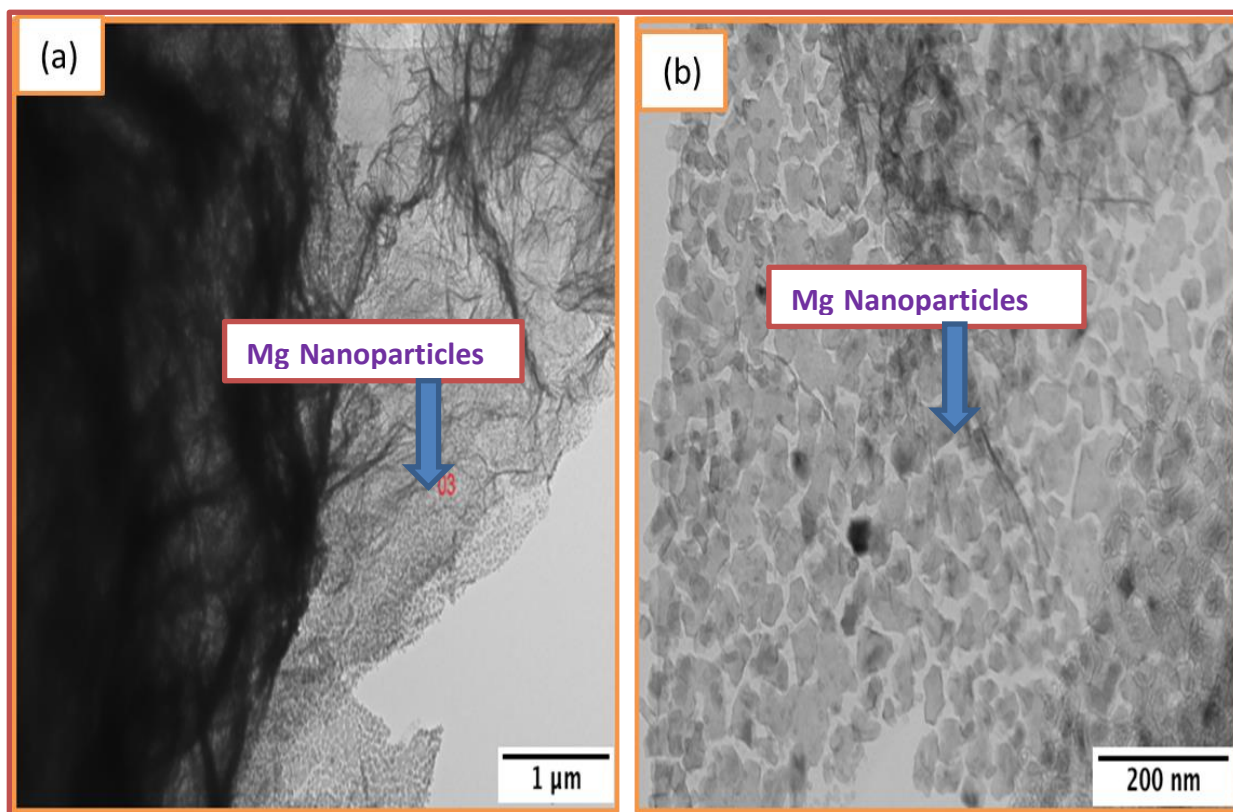


Fig 5.1 TEM images (A-B) of Mg decorated onto graphene at 27 min of deposition

5.3.2 XPS analysis of undoped graphene and Mg doped graphene at different RF power values

To evaluate the influence of energetic sputtered particles onto graphene X-ray photoelectron spectroscopy (XPS) measurements were performed. Fig 5.2 (a) shows the XPS spectrum of the C 1s core level of the undoped graphene and decorated graphene with Mg nanoparticles deposited at different RF power values. The high resolution C 1s XPS spectra of the undoped graphene were de-convoluted into three components. The de-convoluted components of the undecorated graphene are centered at 284.45, 285.23 and 286.2 eV, which are assigned to the C-C (sp^2), C-H/C-C (sp^2) and C-O bonds respectively.

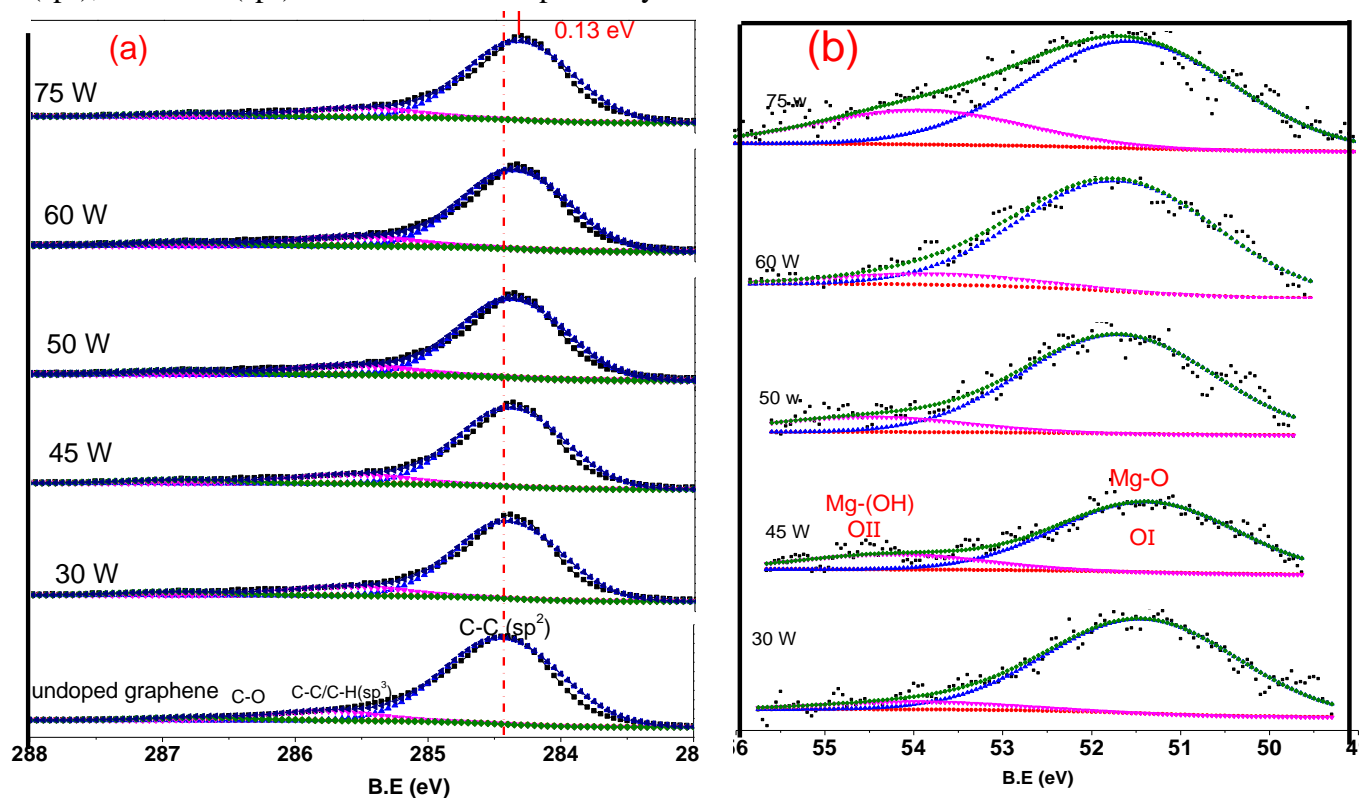


Fig 5. 2 (a) XPS spectra acquired on graphene powders with incrementally increased of Mg contents by varying the RF power values (a) Shift in the C 1s core levels position and the shift of this position upon Mg deposition (b) Mg 2p core level spectra (RF power =30 to 75 W, Process pressure=6 Pa, Time= 18 min and powder vibration frequency= 10 Hz)

More interestingly, the C 1s core level of graphene shifted towards the lower binding energy values upon the deposition of the Mg nanoparticles onto graphene. The downshift of the C 1s core level of the graphene toward the lower increased after increasing the RF power values. The downshift of C 1s peak about 0.13 eV were observed after the deposition of Mg nanoparticles onto graphene at 75 W of deposition. The shift in the C 1s core level is the consequence of the charge transfer (n-type or p-type) between interfaces of the graphene and nanostructure. It is also revealed that for the doping, the charge is transferred between the various nanostructures and graphene due to the difference of work function values. It is well understood that the work function of the metal is dramatically changed by the unintentional metal oxidation, when it was exposed to the air and also to change the doping type i.e from n-type to p-type doping or vice versa [257]. The reported work function value for the Mg is 3.68 eV and further increased to 4.94 eV due to the native surface oxide [258, 259]. From the XPS analysis it was found that, the deposited Mg nanoparticles onto graphene sheets are oxidized by exposed to the air moisture. Consequently the downshift of C 1s core level of the deposited Mg nanoparticles onto graphene sheets suggests that graphene is p doped with Mg nanoparticles upon the surface oxidation of the Mg nanoparticles, where the electrons are transferred from graphene (4.33 eV) [260] to MgO due to the high work function of the MgO (4.96 eV).

The high resolution spectra of the Mg 2p peak for the decorated graphene with Mg nanoparticles deposited by increasing the RF power values are presented in Fig 5.2 (b). The Mg 2p spectra were de-convoluted into two components, located at 50.93 eV and 52.85 eV respectively. The peak located at 51.43 eV belongs to the Mg-O bond [261, 262], and the component which is located at 52.85 eV is assigned to the Mg-OH bond [263], meanwhile no metallic Mg peak was observed in the XPS spectra. This suggests that the deposited Mg nanoparticles were surface oxidized due

to exposing to the air. The peak position of Mg 2p, C 1s and the O 1s spectra and chemical composition for the decorated graphene with Mg nanoparticles are shown in table 1. The composition of the Mg-O and Mg-OH component for all the decorated graphene sheets with Mg nanoparticles at different RF power values were determined on the basis of the area under the whole component of the Mg-O (I) and area under the component of Mg-(OH) (II) of the Mg 2p spectrum and the results are presented a in table 1. It can be seen that, with increasing RF power values, the composition of Mg-O and Mg-(OH) gradually increased. This suggests that as deposited Mg nanoparticles are mainly consisting of MgO and as well as few residual OH group adsorbed from the air moisture.

The O 1s high resolution XPS spectrum of Mg nanoparticles deposited onto graphene in Ar plasma is shown in Fig 5.3 (a).

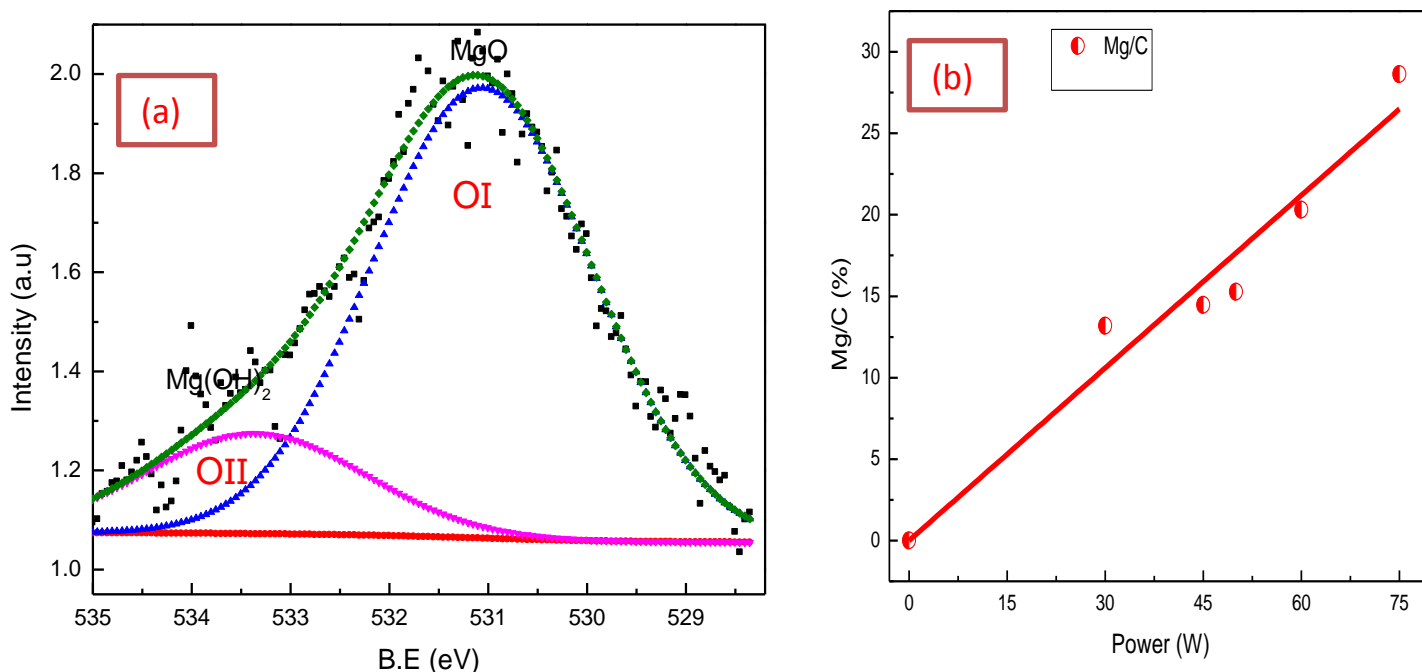


Fig 5. 3 (a) O 1s core peak and its de-convolution b) variations of Mg/C sp² atomic ratio with RF Power

It is shown that after the deposition of Mg nanoparticles onto graphene the O 1s spectra become asymmetric toward the higher binding energy side. The O 1s spectrum is de-convoluted into two

components. The main component at lower B.E 531.09 eV is assigned to O⁻² bound to Mg⁺²[²⁶⁴], whereas toward the higher B.E 533.45 eV is attributed to the Mg-OH bond [²⁶⁵].

Moreover the O/Mg ratio was calculated to estimate the stoichiometry of oxidized Mg nanoparticles onto graphene sheet. The stoichiometries of the decorated graphene with Mg nanoparticles at different RF power values are present in table 1.

The OI/Mg ratio OI which bonded to Mg (I) in the Mg 2p spectrum for the deposited samples were estimated on the bases of the area under the Mg components and area under the OI component of the O 1s spectra. The measured OI/Mg(I) ratios were found between 0.99 and 0.94 (see Table 1) and 1 is the ideal values for the MgO crystal. This shows that deposited Mg nanoparticles on graphene surface under-stoichiometry; this might be due to the adsorbed of (OH) group. Moreover, the Mg/C sp² as a function of the RF power values is presented in Fig 5.3 (b). The Mg/C sp² ratio increased from 13.5 atomic ratios (%) and reached to 28.37 atomic ratios (%), when the RF power values varied from 30 W to 75 W for the deposited of Mg nanoparticles onto graphene sheets.

Table 1: Binding energy values of C 1s and Mg 2p core-levels, O/Mg atomic ratio MgO and Mg(OH)₂ concentration for increasing power applied Mg target

Power (W)	BE (C 1s)	BE (Mg-O) (eV)	OI/Mg(I)	MgO (%)	Mg(OH) ₂ (%)	Mg(OH) ₂ / MgO
0	284.45	0			0	
30	284.40	51.43	0.96	8.62	0.71	0.082367
45	284.39	51.26	0.95	8.97	1.2	0.133779
50	284.39	51.22	0.95	9.20	1.26	0.136957
60	284.38	51.11	0.94	11.21	1.86	0.16132
75	284.32	50.98	0.92	13.05	2.87	0.219923

Additionally, the obtained ratio between the MgO and Mg(OH)₂ are presented in table (1). It was found that the ratio between the MgO and Mg(OH)₂ ratio linearly increased by raising RF power values. This behavior can be explained like this, in the above text, we discussed that Mg/C sp² ratio increased and the OI/Mg(I) ratio under stoichiometric. This behavior indicates that the deviation from stoichiometry of MgO nanoparticles at different RF power values might be due the hydroxylation. Hydroxylation increased onto the surface of Mg nanoparticles by rising RF power values. Therefore, the ratio between the MgO and Mg(OH)₂ increased linearly by rising RF power values.

5.3.3 XRD analysis of undoped graphene and Mg doped graphene at different RF power values

The XRD pattern of the undoped graphene and decorated graphene with Mg nanoparticles deposited at different RF power values (30 to 75 Watt) are shown in Fig 5.4(a). The peak positions of the undoped graphene in the XRD pattern at 25.11° and 42.85° are assigned to the reflection of the plane (002) and (100) respectively, which corresponds to the diffraction peaks of few layers graphene [266]. On the other hand for the decorated graphene with Mg films additional diffraction peaks at $2\theta = 31.83^\circ$, 34.05° , and 36.35° were also observed. These peaks can be indexed to the three reflection peaks (001), (002) and (101) planes of hexagonal Mg structure (JCPDS 04-0770) [267]. The crystalline nature of the Mg nanostructure in the Mg/graphene composite was confirmed by XRD investigation. The characteristic peak (101) plane confirmed that the Mg metal is deposited onto graphene sheet. No other impurities peaks were observed in the XRD pattern. This suggests that only Mg nanoparticles were anchored to the graphene sheet. The intensity of Mg (101) monotonically increased with gradual increase RF

power values from 30 to 75 W. The average crystallite size of the decorated Mg nanoparticles was estimated using the Scherer's formula [268].

$$D = \frac{K\lambda}{\beta \cos \theta} \dots\dots\dots(1)$$

Where β_{hkl} is the full width at half-maximum (FWHM) of the peak considered (in rad), θ is the Bragg angle and D is the average crystallite size where k is the shape factor and K has a typical value is approximately equal to 0.9 [12].

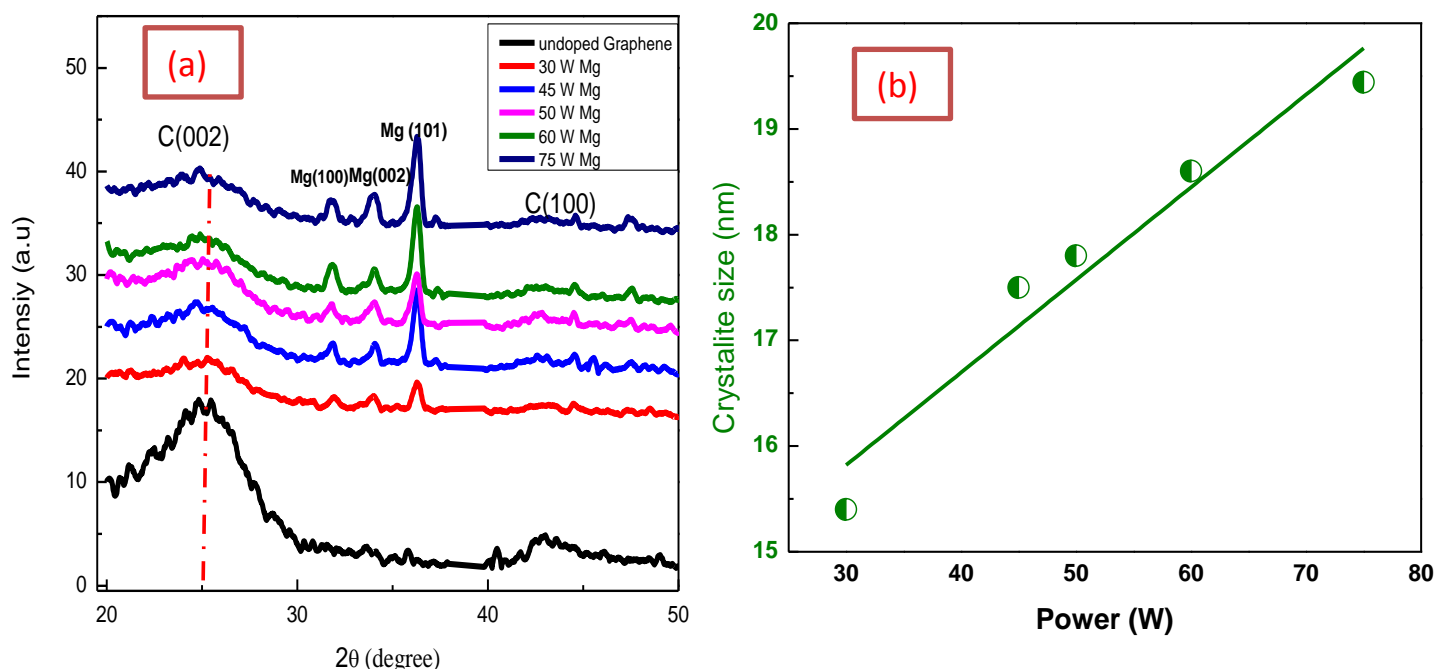


Fig 5.4 (a) XRD patterns of decorated graphene with Mg b) crystallite sizes of the decorated Mg nanoparticles at different RF power values nanoparticles as function of RF power

The average crystallite size of the Mg films as a function of the RF power values are shown in Fig 5.4 (b). We observed that with increasing the RF power values from 30 W to 75 W the FWHM of the characteristic peaks were reduced and a slight increase in the average crystallites size of the Mg crystal The crystallite sizes of the deposited Mg nanoparticles onto graphene sheet as a function of RF power values are presented in Fig 5.4 (b). It can be seen that crystallite size of deposited Mg nanoparticles increased from 15.4 nm and reached 19.44 nm, when the RF

power values varied from 30 W to 75 W. It is well presumed that by increasing the RF power values the more sputtered particles were extracted from the target. Addition to this the energy of the sputtered particles increased with rising RF power values. Also it is well known that the deposition rate increased with rising RF power values. The improvement of the crystallite size of the deposited Mg nanoparticles can be explained as follows, by increasing RF power values the plasma species gain more kinetic energy and interacted with target with high kinetic energy and extracted larger particles from target with respect to lower RF power values, or it might be with increasing RF power values more Mg nanoparticles were deposited onto graphene sheets and these nanoparticles made aggregation onto graphene sheet. Consequently with increasing RF power values the growth of the Mg nanoparticles was enhanced.

The (002) peak of the graphene gradually shifted toward lower 2θ values after the deposition of Mg nanoparticles at different RF power values as shown in Fig 5.5. This shows that d spacing of graphene sheets increased by raising the Mg concentration onto graphene sheets. The calculated values of the d- spacing of graphene as a function of Mg/C sp^2 are illustrated in Fig 5.5.

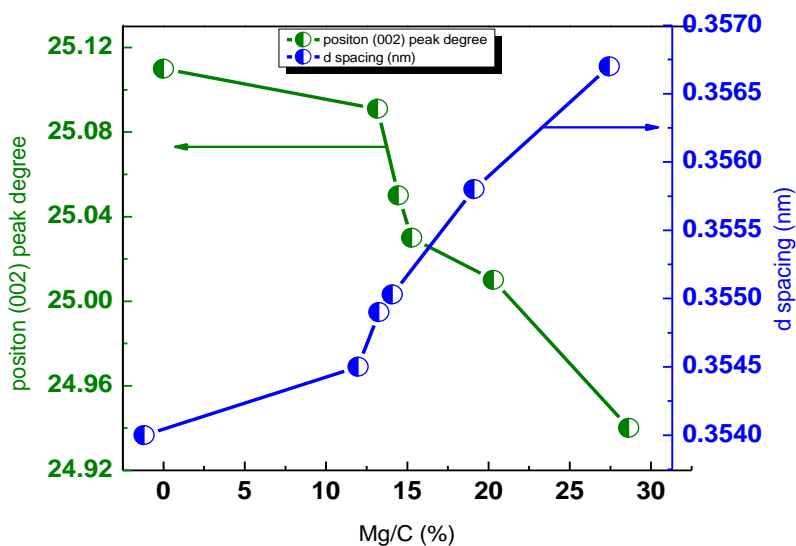


Fig 5. 5 Variation of the 2θ angle position of the (002) and d-spacing as function of Mg/C at. %

The d- spacing increased from 3.54 nm and reached 3.57 nm, when the Mg nanoparticles were deposited onto graphene sheets in a ratio Mg/C $sp^2=28.37$ atomic ratio (%). The FWHM of the (002) peak for decorated graphene with Mg nanoparticles were evaluated using the Lorentzian line function. It was found that the (002) peak of graphene became broadened with rising of Mg concentration onto graphene sheets.

This shows that with increasing amounts of the Mg nanoparticles onto graphene surface weak signal were detected from the (002) plane. The weak intensity of the (002) peak suggest that the crystallite thickness of graphene sheets were reduced upon the deposition of the Mg nanoparticles. The peak around 2θ position 42.85° corresponding to (100) plane of graphene was weak peak detected after the deposition of Mg nanoparticle at 75 W, which shows that sheet of the graphene were fully anchored by Mg nanoparticles, resulting in lowered degree of graphitization. The behavior can correlate with TEM analysis; Fig 5.1 (b) shows the deposited Mg nanoparticles were anchored over the larger surface area of the graphene sheets.

5.3.4 Raman study of undoped graphene and Mg doped graphene at different RF power values

Raman analysis was carried out for the undoped graphene and decorated graphene with Mg nanoparticles to examine doping and mechanical strain. The Raman spectra of the undecorated graphene and decorated graphene with Mg nanoparticles at different RF power values are presented in Fig 5.6 (a). Four characteristic peaks (G, D, 2D and D+G) were detected in the Raman spectra for the undoped graphene and decorated graphene with Mg nanoparticles. The relative shift in the position of G and 2D bands can be used to evaluate the combined the effect of doping and mechanical strain induced in the graphene sheets [6-8]. For the undoped graphene the G band is at 1584.86 cm^{-1} and the 2D band position is at 2636.87 cm^{-1} . After the deposition

of the Mg nanoparticles at 30 W, the G band shifts to high wavenumbers at 1589.56 cm^{-1} and the 2D bands of the graphene comparatively unchanged (within standard error) at 2637.76 cm^{-1} . The G and 2D bands were shifted to higher wavenumber by 10.87 and 8.5 cm^{-1} respectively upon the deposition of Mg nanoparticles onto graphene sheet at 75 W RF power value. These shifts could be attributed to doping or mechanical strain induced in the graphene sheets. Recently, it is reported that metal with high lattice mismatch on graphene lead to a significant shifts in G and 2D bands (due to increased strain) [6].

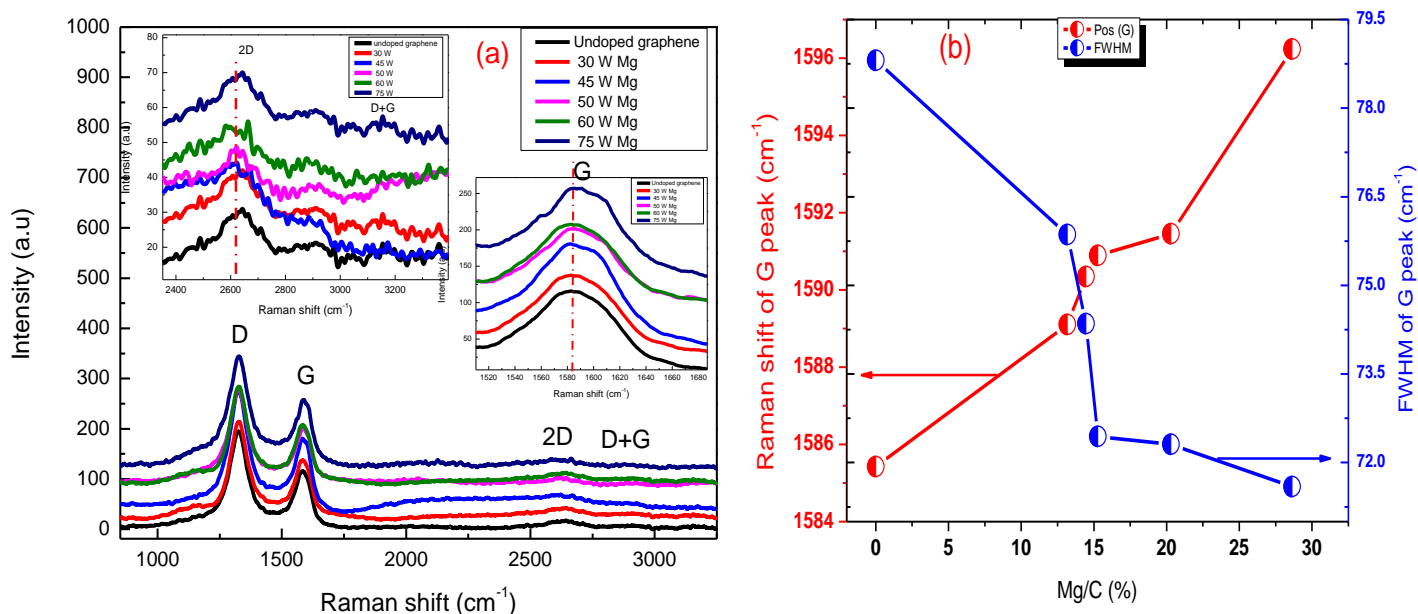


Fig 5. 6 (a) Raman spectra of undoped graphene and (b) positions of the G and FWHM (G) as a function of Mg/C (%) Mg doped graphene at different time of deposition

When mismatched lattice indices metal like Au (4.08 \AA) and Ag (4.05 \AA) were deposition onto graphene (2.46 \AA) sheet, where (4.08 \AA), (4.05 \AA) and (2.46 \AA) are the lattice constant values of Au, Ag and graphene. For these metals the G and 2D peak Raman shifts are attributed to the mechanical strain and doping is hard to conclude from the Raman studies [269]. In this case of study, it is reported that the shift in 2D band is always greater than the shift in G band, which indicates that mechanical strain dominates over the doping phenomenon. However by the

deposition of metal with matching lattice indices to the graphene like Co, Ni and Mg, the shifts in the G peak is larger compared to the shift in the 2D band and this comparative shift in the position suggested to a successful doping in graphene. It is also reported that the upshifted of G and 2D bands of graphene is due to p doping [²⁶]. Based on this observation, the upshift of G and 2D bands of graphene after the deposition of Mg nanoparticles suggests that the graphene is p doped with Mg nanoparticles. The Gaussian function line shape was used to evaluate the FWHM (G) peak of undecorated graphene and decorated graphene with Mg nanoparticles. The evaluated values of FWHM of G peak as function of Mg/C atomic ratio are presented in Fig 5.6 (b). The FWHM of G peak decreased from 78.5 cm⁻¹ to 71.5 cm⁻¹ upon the deposition of Mg nanoparticles onto graphene sheets at 75 W RF power values in a ratio Mg/C= 28.37 at. % . It is reported that reduction of FWHM (G) is due to the charge doping [²⁷⁰].

The I_D/I_G ratio was used to quantify the defects and disorderness level induced in the graphene by the interaction of the energetic sputtered particles. The relationship between the I_D/I_G and obtained values of Mg/C (sp²) atomic ratio by increasing RF power is shown in Fig 5.7. The I_D/I_G ratios of the decorated graphene with Mg nanoparticles increased as a function of the Mg/C atomic ratio (%). The measured I_D/I_G ratio for the undecorated graphene was 1.66, suggesting that structural defects were present in the graphene. However after the deposition of Mg nanoparticles onto graphene sheets by increasing RF power the I_D/I_G ratio were further increased. The I_D/I_G ratios values were increased to 1.76, when the Mg was deposited in a ratio Mg/C sp²= 28.37 %), at 75 W RF power value. This suggests that the structural defects further increased by rising the Mg concentrations onto graphene sheets. The in-plane crystalline sizes of the decorated graphene with Mg nanoparticles were calculated using the using Tuinstra - Koenig relation [²⁴⁷]. It was found that the in plane crystalline size of decorated graphene with Mg nanoparticles

decreased from 23.2 nm to 21.5 nm upon the deposition of Mg nanoparticles onto graphene sheets at 75 W RF power value in a ratio Mg/C $sp^2 = 28.37\%$. This suggest that the sp^2 domain of graphene decreased by the deposition of Mg nanoparticles onto graphene sheets. The sp^2 domain of the graphene was distorted with interaction of the Mg nanoparticles. It is well proven that the sp^2 domain become smaller with increasing the structural defects to graphene plane. L. G. Canado et al reported that the sp^2 domain become smaller and more distorted upon the increasing the structural to graphene sheets^[136].

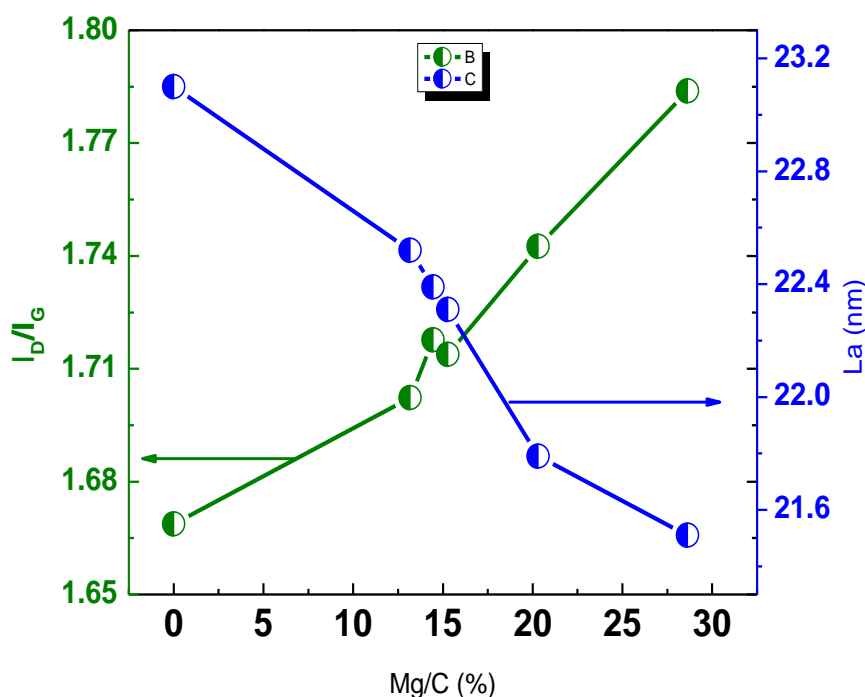


Fig 5.7 Variation of Raman peak intensity ratios of I_D/I_G and L_a plotted against the Mg to C atomic ratio (%)

5.4 The effect of crystalline Mg nanoparticles on the properties of graphene powder decorated deposited at different times of deposition

In the above sections (5.3) we discussed the deposition of Mg nanoparticles onto graphene by increasing RF power values. The structural defects were investigated by Raman and XRD techniques for the decorated graphene with Mg nanoparticles deposited at different RF power

values. It was found that by increasing the RF power structural defects increased. In this process of deposition we kept the sputter ion energy constant and only increase the amount of Mg nanoparticle onto graphene surface by increasing the deposition time. XRD and Raman were used to investigate the structural defects induced in the sp^2 framework by the deposition of Mg nanoparticles. For the chemical analysis X-ray photoelectron spectroscopy was used. Moreover the process parameters are presented in table 5.2.

Table 5.2 the process condition of decorated graphene with Mg nanoparticles

Sample #	RF Power (W)	Process pressure (Pa)	Deposition Time (min)	Powder vibration frequency (Hz)
1	40	6	6	20
2	40	6	9	20
3	40	6	12	20
4	40	6	18	20
5	40	6	27	20

5.4.1 XPS analysis of graphene and Mg deposited onto graphene at different times of deposition

Fig 5.8 (a) shows the XPS spectrum of the C 1s core level of the undoped graphene and decorated graphene with Mg nanoparticles deposited at different time of deposition. The high resolution XPS spectra of the undoped graphene were de-convoluted into three components. The main peak with a binding energy 284.69 eV is assigned to carbon in C-C bond with sp^2 hybridization. Two other small components which have binding energies of 285.34 eV and 286.20 eV correspond to C-H /C-C bond with sp^3 hybridization and C-O bond respectively. Fig 5.8 (b) shows the high resolution spectra of the Mg 2p peak for the decorated Mg nanoparticles

deposited by varying the deposition time. It can be seen that by increasing the deposition time the Mg spectra became asymmetric and broadened toward the higher binding energy side. The Mg spectrum was de-convoluted into two peaks. The following two components were observed one at 50.94 eV and the other at 53.7 eV. The peak of 50.90 eV may be ascribed to MgO and the peak of 53.78 eV correspond to Mg(OH)₂ [271, 272].

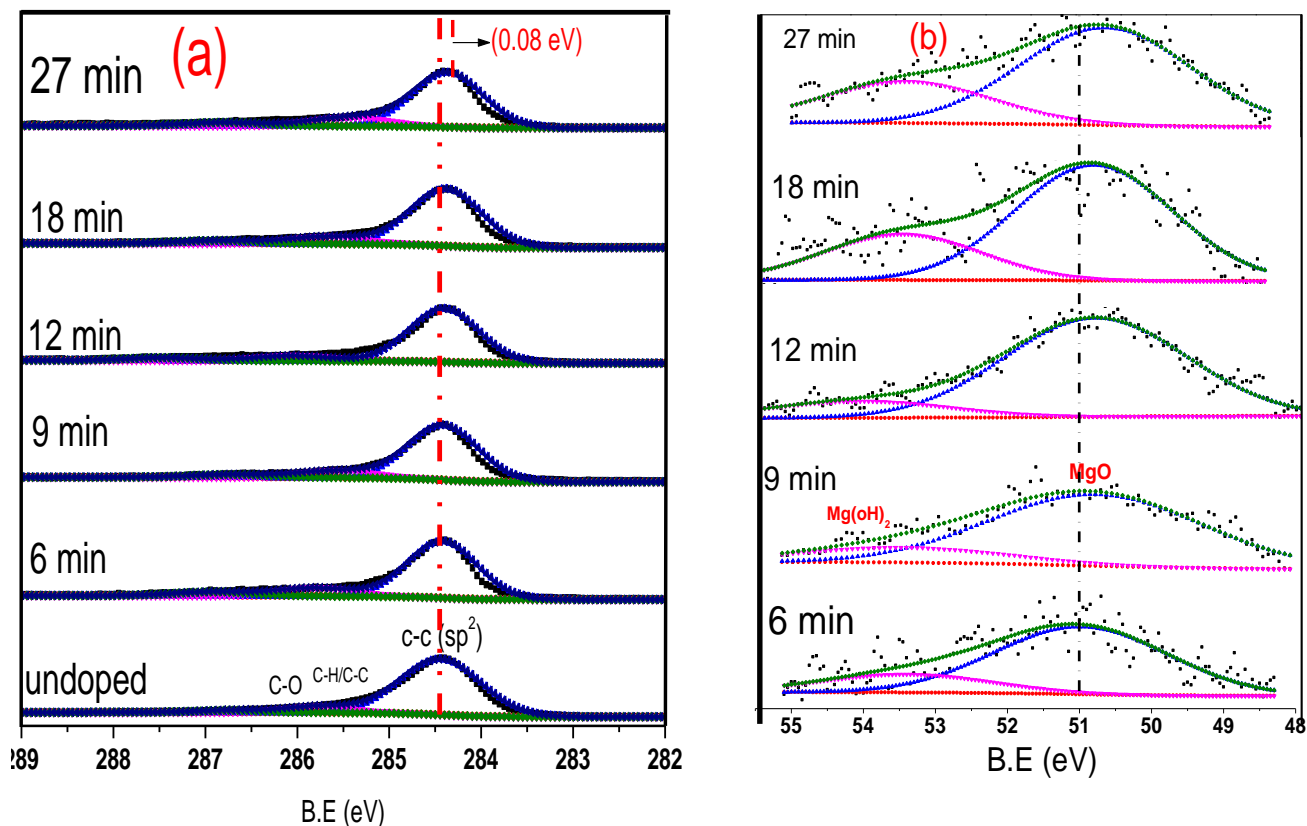


Fig 5. 8 (a) XPS spectra of graphene powder with incrementally increased of Mg contents by varying the deposition time (a) a Shift in the C 1s core levels position and the shift of this position upon Mg deposition (b) Mg 2p core level spectra (RF power =40 W, Process pressure= 6 Pa, Time= (6 to 27 min and powder vibration frequency= 0 Hz).

Fig 5.9 (a) depicts a high-resolution spectrum of the O 1s peak of decorated graphene with Mg nanoparticles. The O 1s spectra were de-convoluted into two components. The first and main peak at lower binding energy (531.1 eV) can be attributed to the O 1s core peak of O²⁻ bound to

Mg^{+2} [²⁷³], whereas a second component (OII) is located at 533.82 eV correspond to $\text{Mg}(\text{OH})_2$ peak [²⁷⁴, ²⁶²].

Additionally, the Mg/C sp² atomic ratio was assessed from the XPS analysis. The evaluated values of Mg/C sp² ratio as function of the different deposition times are presented in Fig 5.9 (b). It was found that Mg/C sp² ratio increased from 6.73 and reached 18.3 atomic ratios (%), when the deposition time varied from 6 min to 27 min of deposition.

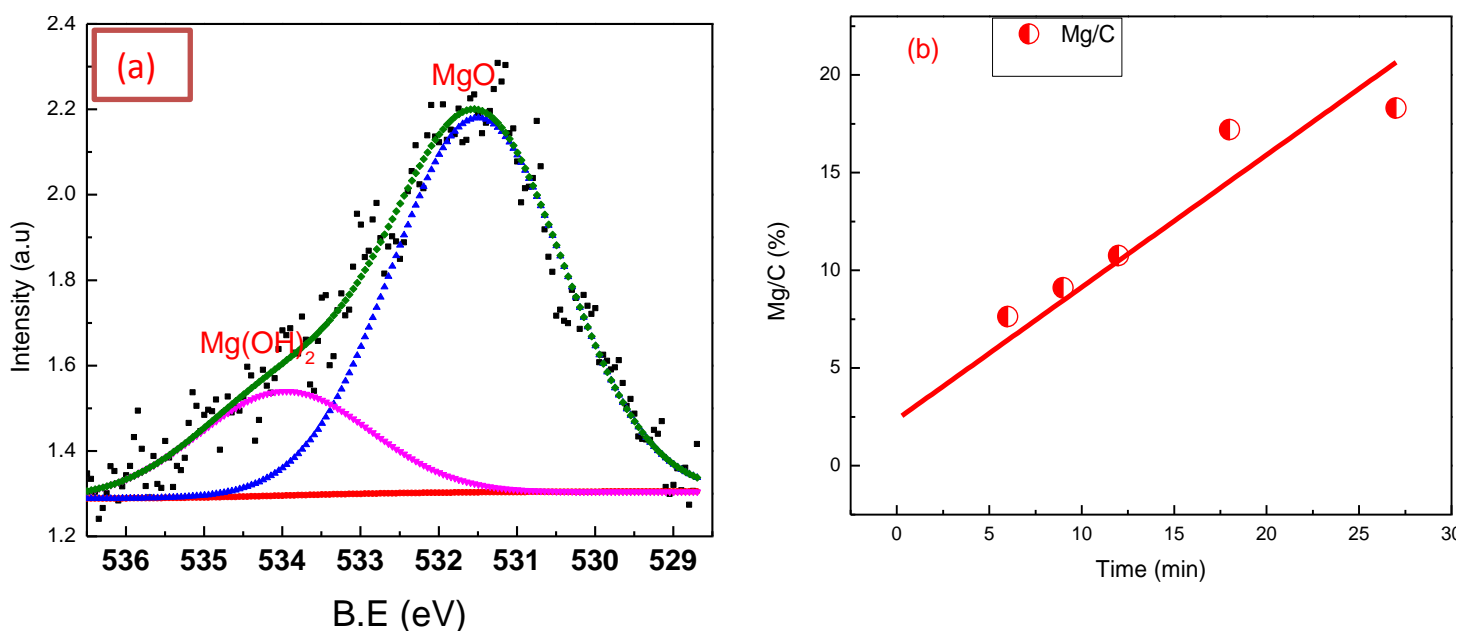


Fig 5. 9 (a) O 1s core peak and its de-convolution

(b) variations of Mg/C and atomic ratio with time

5.4.2 XRD analysis of undecorated graphene and Mg decorated graphene at different times of deposition

The X-ray diffraction (XRD) patterns of undoped graphene and Mg doped graphene decorated by stepping up the deposition time are shown in Fig. 5.10. The characteristic C (002) peak undoped graphene centered at $2\theta = 25.11^\circ$ belongs to few layers graphene plane. The characteristic C (100) peak is also visible in the XRD patterns. In the case of Mg nanoparticles modified graphene three characteristic peaks were observed. The characteristic peaks are corresponding to (001), (002) and (101) planes of hexagonal structure of metallic Mg, which is

observed at 31.83° , 34.05° , and 36.35° . The average crystallite size of the decorated crystalline Mg nanoparticles was calculated using equation (1).

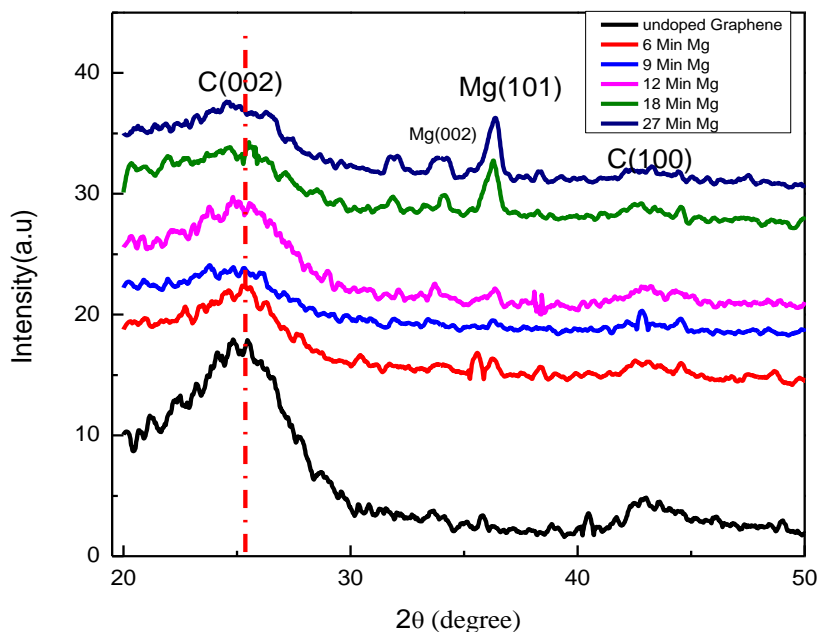


Fig 5.10 XRD patterns of the undecorated graphene and decorated graphene with Mg nanoparticles at different times of deposition

The crystallite sizes of the Mg nanoparticles onto graphene sheet were in the range of 14 to 16 nm. Addition to this 2θ position of C (002) peak is slightly shifted toward the lower 2θ values by increasing the Mg concentration to the graphene plane. The position of (002) peak of graphene as function of the Mg/C sp² are shown in Fig 5.11. This indicates that the d spacing of graphene sheet increased by raising the Mg concentration to graphene plane. The calculated d-spacing value increased from 0.354 nm and reached 0.357 nm upon the deposition of Mg nanoparticles at 27 min of deposition in a ratio Mg/C sp² = 18.3 atomic ratio (%). Moreover the FWHM of the (002) peak of graphene becomes broadened by the deposition of Mg nanoparticle onto graphene sheet. The broadening of (002) peak after the deposition of the Mg nanoparticles indicates the

structural defects were induced in the graphene framework. The structural defects increased by raising the Mg concentration to the graphene plane.

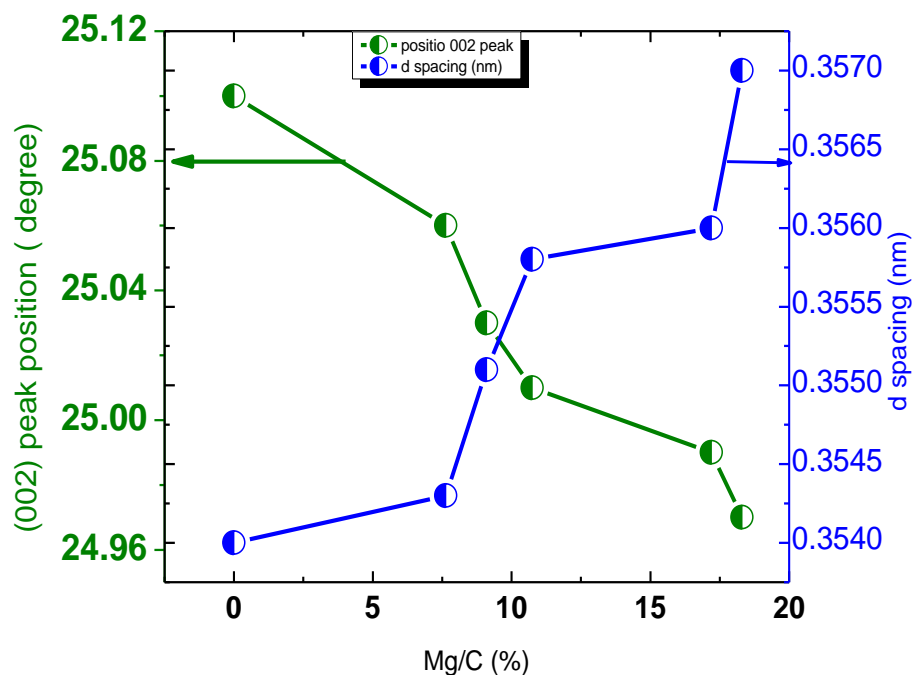


Fig 5. 11 Variation of the 2θ angle position of the (002) and d-spacing as function of Mg/C at. %

5.4.3 Raman study of undecorated graphene and Mg doped graphene at different times of deposition

Various amounts of the Mg nanoparticles were deposited on the surface of graphene to study the interaction between the Mg nanoparticles and graphene. Fig 5.12 (a) shows the Raman spectrum of undoped graphene and decorated graphene with Mg nanoparticles by increasing the deposition time. Four characteristic peaks at 1327.89, 1585.85, 2635 and 2920 cm^{-1} were observed in the Raman spectrum for undoped graphene. These peaks correspond to the G-band, D-band; 2D band and D+G band respectively. It is a well effective process for distinguishing the doping type or mechanical strain by comparing G and 2D peaks position between decorated graphene with Mg nanoparticles and undoped graphene [¹¹⁰]. It is also well reported that the mechanical strain is dominates over on doping, if the shift in 2D band is larger than the shift in G band. Our XRD

results shows that the tensile strain induced in the plane of graphene, but in case of tensile strain the G and 2D band is shifted toward the lower wavenumbers. The evaluated Raman spectrum for the decorated graphene with an increasing amount of Mg nanoparticles is presented in Fig 5.12 (a) (enlarged view) with a comparison to the undoped graphene. When the amount of Mg nanoparticles increased onto graphene sheet the G peak blue-shifts gradually from 1586 to 1590.56 cm^{-1} as a function of the increasing Mg/C (sp²) are shown in Fig 5.12 (b) suggesting p-type doping. Similar result is also reported by the Xiuyi Lin et al [111].

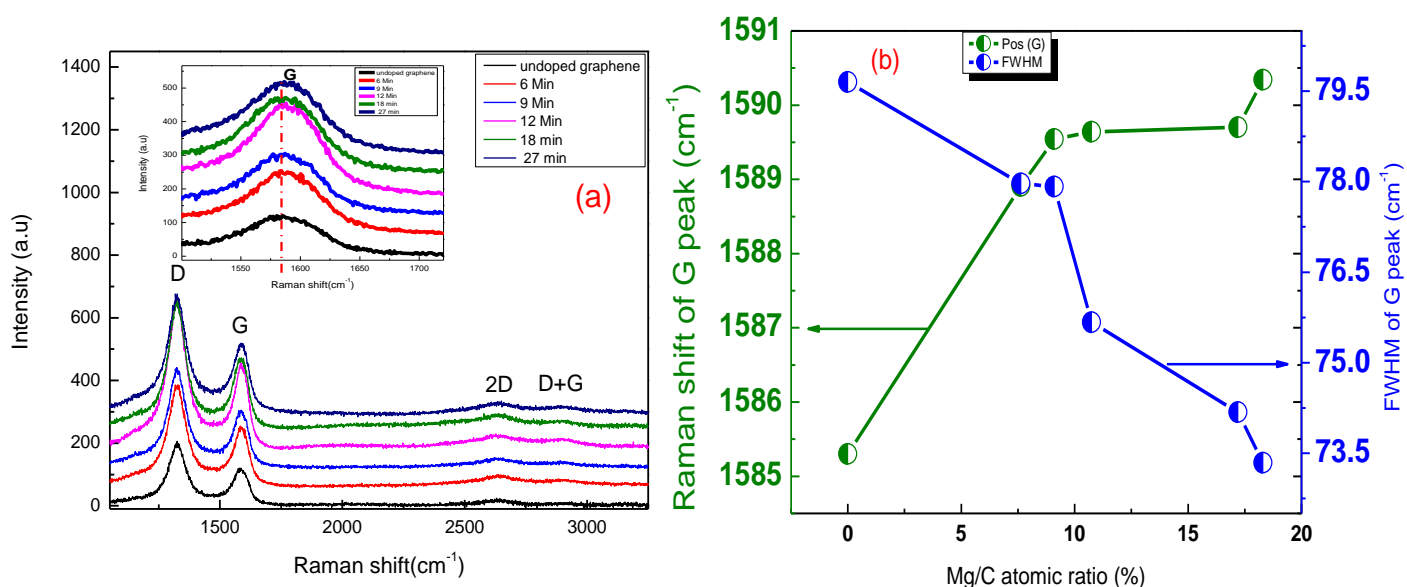


Fig 5. 12 (a) Raman spectra of undoped graphene and (b) positions of the G and FWHM (G) vs Mg to C (%) Mg doped graphene at different time of deposition

This shows that there is strong interaction between the Mg nanoparticles and graphene sheet, which change the electronic properties of the graphene upon the deposition of Mg nanoparticles. Furthermore by using the Lorentzian function to evaluate the FWHM of G peak, we found that with raising of amount of Mg contents to graphene Sp² framework, the full width half maximum (FWHM) of the G peaks is gradually decreased as a function of increasing the Mg/C Sp² as shown in Fig 5.12 (b). The FWHM of G peak is decreased from 79.56 to 73.6 cm^{-1} , when Mg

contents were deposited in a ratio 18.3 % to C (Sp^2). The sharpening in FWHM (G) of graphene after the deposition of Mg nanoparticles onto graphene is attributed to the charge doping [207]. Magdalena Onyszko et al is also explained that the FWHM of G peak of the reduced graphene oxide decreased due to the charge doping [245].

The intensity ratio of D and G (I_D/I_G) were used to quantify the degree of disorderness (including defects and edges) and average size of the Sp^2 domains. It was observed that the intensity of the D peak of graphene increases as function of the Mg contents.

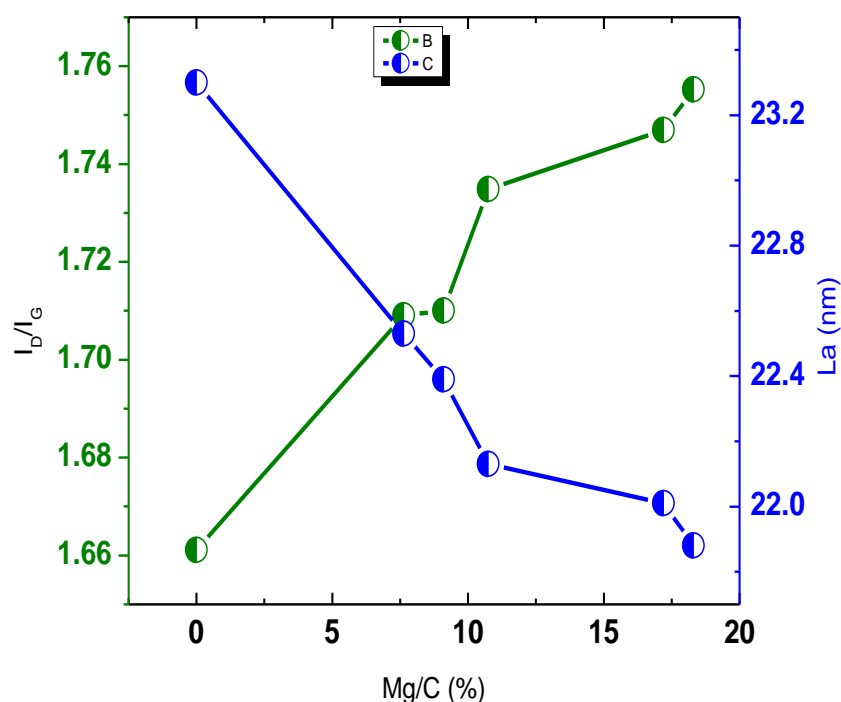


Fig 5.1 3 Variation of Raman peak intensity ratios of I_D/I_G and L_a plotted against the Mg to C atomic ratio (%).

This suggests that the symmetry of graphene was broken and induced the structural defects in the structure of graphene. The calculated intensity ratio of the D and the G band (I_D/I_G) were varied from 1.66 to 1.75 as a function of the increasing Mg/C (sp^2). The evaluated values of I_D/I_G as a function of the Mg/C (sp^2) are illustrated in Fig 5.13. Moreover, the in-plane crystalline size was calculated using the I_D/I_G ratio and the obtained values as function Mg/C sp^2 atomic ratios are presented in Fig 5.12. It can be seen that L_a decreased by increasing the Mg/C atomic ratio (%).

This suggests that by the deposition of Mg nanoparticles onto graphene the size of the sp^2 domain decreased.

5.5 The influence of Mg crystalline nanoparticles on the structure and chemical properties of graphene powder via given different vibration frequencies to graphene powders

In the above two sections (5.3, 5.4), the deposition of Mg nanoparticles were discussed by varying two deposition parameters RF power and deposition time. In both processes we deposited the Mg nanoparticles onto graphene at low powder vibration frequency (20 Hz). It was found that at low powder vibration frequency, the deposited Mg nanoparticles make aggregates on the graphene sheet. Recently different chemical and physical approaches were used to decorate graphene well dispersed metal nanoparticles [275, 276, 277]. However the decorated nanoparticles onto graphene sheets were not homogeneous sizes and these nanoparticles easily tend to agglomerate due to the high surface energy of the nanoparticles onto graphene sheet and lose their catalytic activities. In this section of thesis, the well dispersed Mg nanoparticles were deposited onto graphene sheet by given high vibration frequency to graphene powder during the deposition process. A range of powder vibration frequencies from 0 to 100 Hz was used to decorate the graphene with Mg nanoparticles. The Raman and X-ray diffraction techniques were used to study the structural disorderness induced in graphene by the deposition of Mg nanoparticles. For the chemical analysis X-ray photoelectron spectroscopy (XPS) were used. The surface morphology of the deposited Mg nanoparticle was examined by TEM analysis. Moreover the process parameters are presented in table 5.3.

Table 5.3 the process condition of decorated graphene with Mg nanoparticles

Sample #	RF Power (W)	Process pressure (Pa)	Deposition Time (min)	Powder vibration frequency (Hz)
1	40	6	27	0
2	40	6	27	20
3	40	6	27	30
4	40	6	27	40
5	40	6	27	50
6	40	6	27	80
7	40	6	27	100

5.5.1 TEM analysis of decorated graphene with Mg nanoparticles deposited at 0 Hz and 80 Hz

The surface morphology of the decorated Mg nanoparticles was examined by TEM. Fig 5.14 (a-d) presents the TEM micrographs of the decorated Mg nanoparticles deposited onto graphene sheet without moving (0 Hz) the graphene powder during the deposition process. Fig 5.14 (a) shows the low magnification of the decorated Mg nanoparticles. The deposited Mg nanoparticles are homogeneously distributed onto graphene sheets. The high magnification TEM micrograph, as shown in Fig 5.14 (b-c), indicates that deposited Mg nanoparticles onto graphene flake are distributed with high density. The deposited Mg nanoparticles are anchored to the graphene sheet, even after the ultra-sonication used to disperse the Mg/graphene composite for the TEM characterization. From the Fig 5.14 (d) indicates that the deposited Mg nanoparticles make aggregates by the deposition of Mg nanoparticles onto graphene sheets without moving (0 Hz) graphene powder. The average size of the deposited Mg nanoparticles are around 10-15 nm.

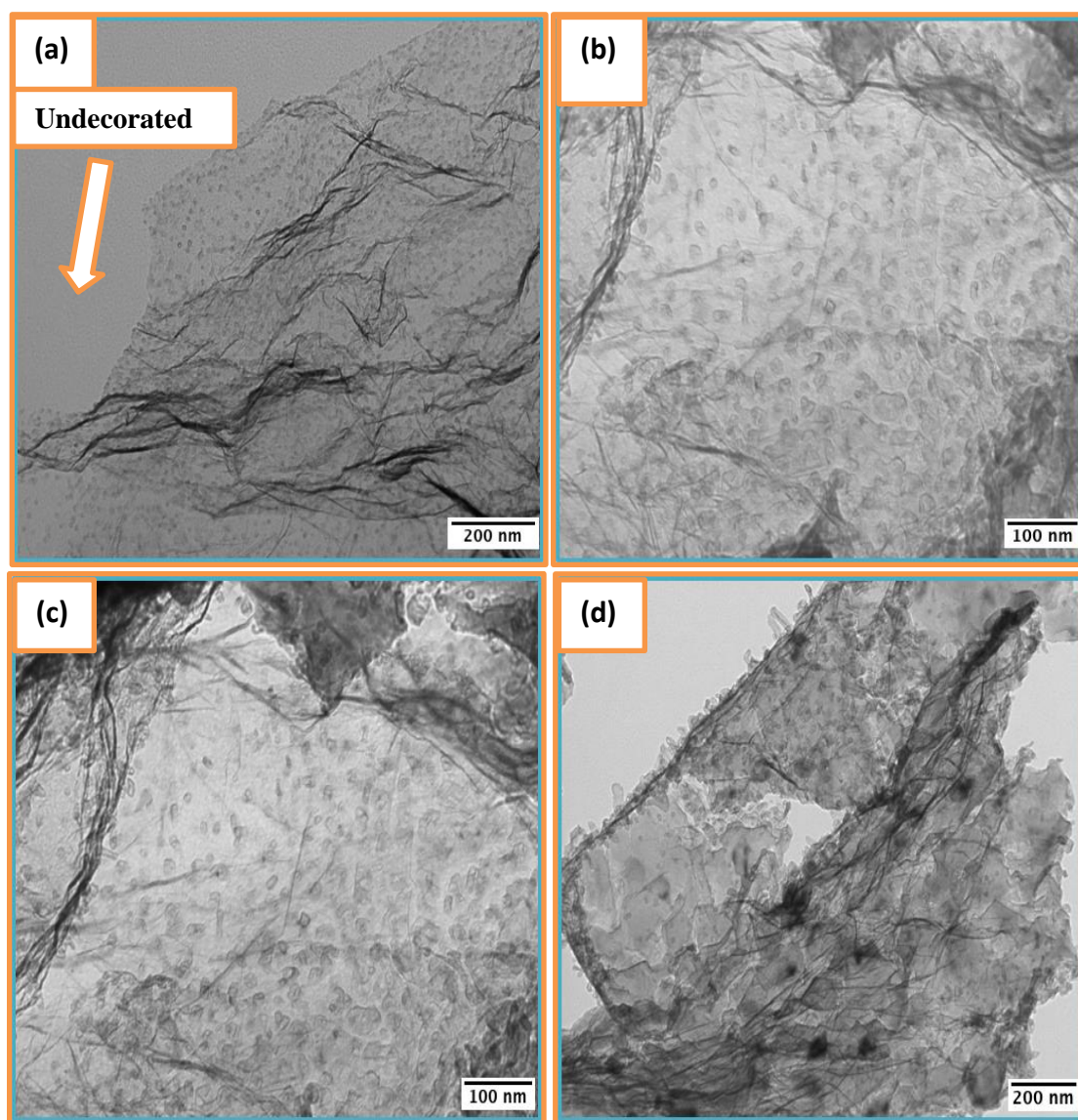


Fig 5. 14 TEM images (a-d) of deposited Mg nanoparticles without moving powder (0 Hz)

TEM micrographs of the deposited Mg nanoparticles onto graphene at high powder vibration frequency (80 Hz) are shown in Fig 5.15. Low magnification micrographs as shown in Fig 5.15 (a,d), indicates that the deposited Mg nanoparticles are homogeneously distributed onto graphene sheet. This shows that with high powder vibration frequency the graphene flake are almost completely covered by Mg nanoparticles. Well dispersed small Mg nanoparticles were deposited onto graphene sheets with high powder vibration frequency. Notably feature for the deposited

Mg nanoparticles at high vibration frequency is that, less agglomeration of the Mg nanoparticles was observed. This is confirmed that by the deposition of the Mg nanoparticles onto graphene with high powder vibration the sputtered particles decorated over the entire graphene sheet. The average particles size of the deposited Mg nanoparticles at high powder vibration frequency (80 Hz) from the micrographs are about 8-12 nm.

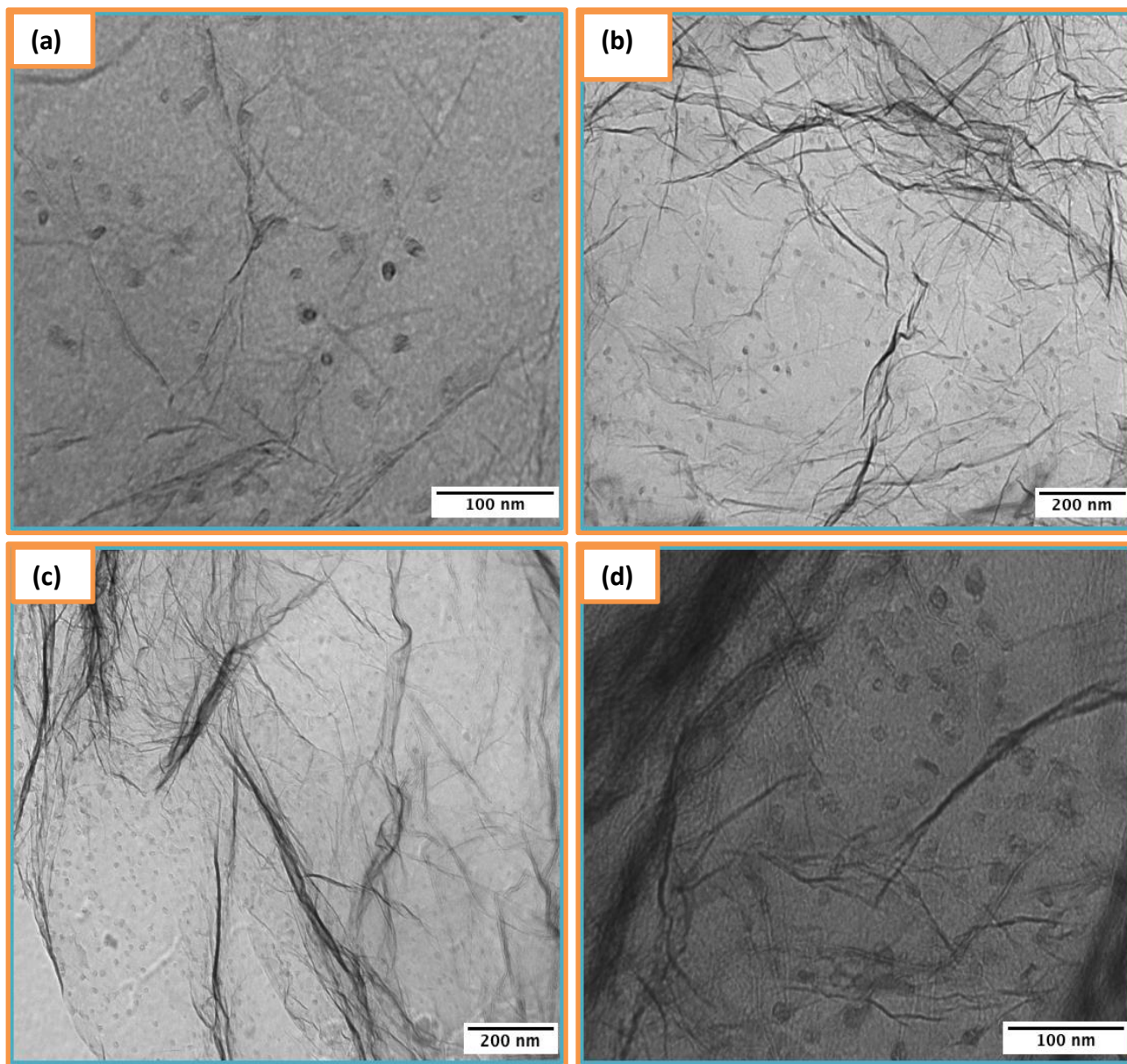


Fig 5. 15 TEM images (a-d) of deposited Mg nanoparticles at high powder vibration frequency (80 Hz)

5.3.2 XPS analysis of undoped graphene and Mg doped graphene at different powder vibration frequencies.

The C 1s spectra of the undecorated graphene and decorated graphene with Mg nanoparticles at different powder vibration frequencies are displayed in Fig 5.16 (a). The C 1s spectra of the decorated graphene with Mg nanoparticles become asymmetric toward the higher binding energy (B.E) regime. The Gaussian line shapes were used for the de-convolution of the C 1s spectra. The C 1s spectra are de-convoluted into three components. The main peak at 284.46 eV is allocated to sp^2 C-C bonds and other two low intensity peaks at 285.6 and 286.3 eV are assigned to defects or sp^3 bond (C-H/C-C) and C-O bond respectively. More importantly by the deposition of Mg nanoparticles onto graphene sheet at different powder vibration frequency the shift in the C 1s core level were observed. The C 1s core level spectra shifts towards the lower binding from the 284.45 eV to 240.41 eV after the deposition of the Mg nanoparticles onto graphene without moving powder (0 Hz). The shift in C 1s core level towards the lower the binding energy increased with raising the powder vibration frequencies. The C 1s core level is shifted 0.10 eV toward lower binding energy upon the deposition of Mg nanoparticles at 100 Hz powder vibration frequency. The peak shifts in the C 1s core-level position are strongly related to Fermi-level. The shift in the C 1s core level is equal shift in the Fermi level. But the Fermi level is shifted from its position by the charge doping. It is also reported the charge is transfer between the graphene and metal interface due to the difference of the work function. The shift in C 1s core level of the deposited Mg nanoparticles onto graphene can be explained as follow, the XPS analysis shows that the deposited Mg nanoparticles are oxidized by exposing to the air. M. Giangregorio et al is reported that the oxidation of the metal surface dramatically change the

work function of the metal. The work function of the Mg metal is 3.68 eV and increased to 4.96 eV by the unintentional oxidation [278].

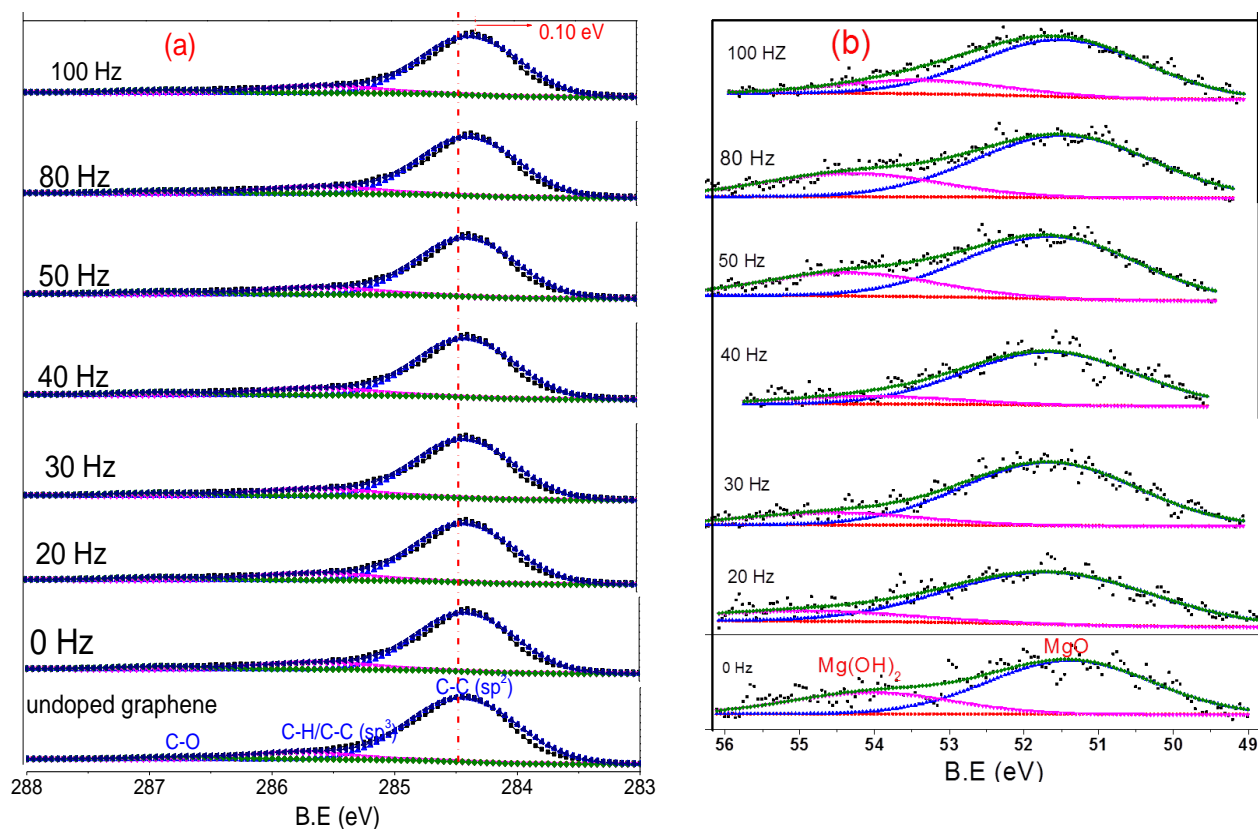


Fig 5.10 (a) XPS spectra of graphene powder with varying the powder vibration frequencies (a) a Shift in the C 1s core levels position and the shift of this position upon Mg deposition (b) Mg 2p core level spectra (RF power =40 W, Process pressure=6 Pa, Time= 27 min and powder vibration frequency= (0 to 100 Hz).

The work function of metal is known to depend on its structure, crystalline orientation and oxidation state [279, 280, 281]. The reported work function for the graphene is 4.33 eV. It would be presumed that graphene is doped with electron if the works function of graphene (WG) > work function of the metal (WM) or its oxide and doped with holes if WG < WM. Due to the surface oxidation of the Mg nanoparticles, the work function of the MgO is greater than that of graphene, the graphene is p doped with MgO nanoparticles, whereas electrons are transferred from graphene to the MgO in order to aligned the Fermi level between the interface of the two

composite materials. The high-resolution spectra of the Mg 2p peak for the deposited Mg nanoparticles onto graphene at different powder vibration frequencies are shown in Fig 5.16 (b). The Mg 2p peak is contained within two components located at 51.38 eV and 53.73 eV respectively. The main components at the lower binding energy side is assigned to Mg-O bond from MgO and with a chemical shift of 2.3 eV with respect to Mg-O component is attributed to Mg bonded to the -OH groups.

The Mg concentration onto the graphene surface increased with a variation of the powder vibration frequency. The obtained Mg concentration onto graphene sheet by varying the powder vibration frequency is presented in Fig 5.17 (b). At 0 Hz vibration, the Mg/C is 12.94 at. % and further increased to 32.23 at. %, when the Mg nanoparticles were deposited at 100 Hz powder vibration frequency. The same other deposition parameters were used in both cases (RF power =40 W, Process pressure=6 Pa, Time= 27 min and powder vibration frequency= (0 to 100 Hz). With powder vibration frequency more sputtered particles were deposited onto graphene sheet compared to the case without moving powder vibration frequency (0 Hz). This phenomenon can be explained as follows, by the deposition of the Mg nanoparticles onto graphene without moving powder the sputter particles were deposited only one face of the graphene sheet. Only surface graphene flakes were coated during the deposition process. The beneath graphene powder were not decorated by the Mg nanoparticles. Also, the Mg nanoparticles not covered the whole surface area of the graphene sheet during the deposition process. However, at 100 Hz powder vibration frequency, the powder vibrated with respect to sputtered particles during the deposition process, more sputtered particles are line of sight to the graphene sheet. It can be expected that both faces of the graphene sheets were covered with Mg nanoparticles during the deposition process. It is also confirmed from the TEM analysis that; Mg nanoparticles were

uniformly distributed over the graphene sheet at high powder vibration frequency. Larger surface area of graphene sheets were covered by the Mg nanoparticles during the deposition process with using of high powder vibration frequency. As discussed in Chapter#3, XPS is a surface technique and analyzes the surface of the decorated graphene upto a few nanometers. Consequently, the XPS detects more Mg nanoparticles, when it was deposited onto graphene sheets by using high powder vibration frequency compared to the case without moving graphene powder (0 Hz). The O 1s XPS spectra of the deposited Mg nanoparticles at 100 Hz powder vibration frequency is presented in Fig 5.17 (a). The O 1s spectrum is de-convoluted into two components. The main component OI located at 531.08 eV is assigned to the Mg-O bond; with shoulder on the high binding energy side corresponding to (OII) peak is also observed, about 2.1 eV higher than the main peak (OI) at 531.08 eV. The peak located at 533.32 is attributed to the surface hydroxyl group formed by adsorption of moisture on oxidized magnesium surfaces [14].

The composition of the Mg-O and Mg-OH component for all the decorated graphene sheets with Mg nanoparticles at different powder vibration frequencies were measured on the basis of the area under the whole component of the Mg-O (I) and area under the component of Mg-(OH) (II) of the Mg 2p spectrum and the results are presented in table 2. Moreover, to measure the stoichiometry, the O/Mg was firstly evaluated using the area of whole component OI of the O 1s peak and the Mg(I) 2p component. The measured ratios for the decorated graphene with Mg nanoparticles at different powder vibration frequencies are displayed in Table 2. The calculated O/Mg ratio indicates that the oxidized Mg nanoparticles were under stoichiometric (see table 2) and 1 is the ideal values for the MgO, which is might be due to the adsorption of the OH group at the surface of the MgO. Furthermore, XPS results also demonstrate that no metallic Mg components were observed, which suggest that all the deposited Mg nanoparticles were oxidized

at the surface. Since there is no protective layer on the top of the deposited Mg nanoparticles, the MgO was further hydroxylated easily, when it was exposed to air and Mg(OH)₂ was formed at the surface MgO. The amount of the Mg(OH)₂ increased by rising the powder vibration frequencies. The evaluated ratio of the Mg(OH)₂/MgO as a function of the powder vibration frequencies are displayed in a table (2).

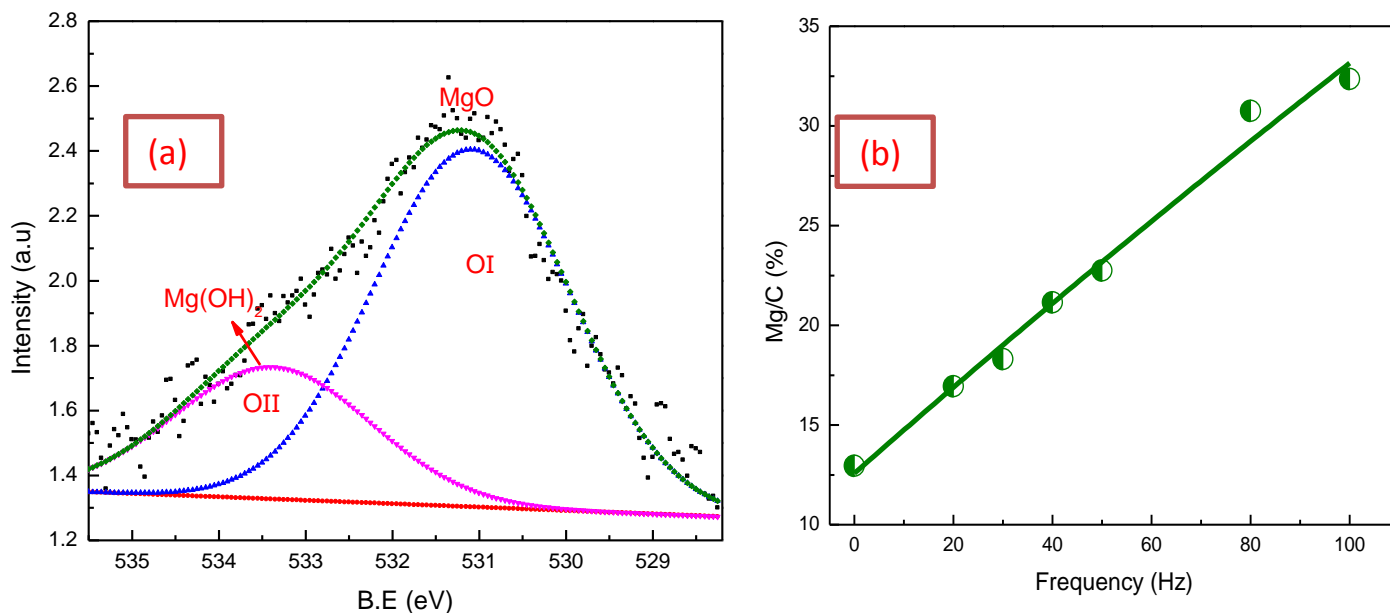


Fig 5.17 (a) O 1s core peak and its de-convolution (b) variations of Mg/C atomic ratio as function of powder vibration frequencies

This behavior can be explained as follows, this indicates that the deposited Mg nanoparticles deviated from the stoichiometry of MgO nanoparticles might be due to the hydroxylation and the hydroxylation increased by raising the powder vibration frequency. Because by using high powder vibration frequency more Mg nanoparticles were deposited onto graphene sheets.

Table 2: Binding energy values of C 1s and Mg 2p core-levels, O/Mg atomic ratio, MgO and Mg(OH)₂ concentration for the different powder vibration frequencies

Frequency Hz	BE (C 1s)	BE (Mg-O) (eV)	OI/Mg (I)	MgO (%)	Mg(OH) ₂ (%)	Mg(OH) ₂ / MgO
0	284.45	0			0	
0	284.41	51.38	0.94	9.06	1.48	0.161308
20	284.41	51.36	0.95	11.83	1.95	0.164835
30	284.39	51.34	0.94	12.06	2.28	0.189055
40	284.38	51.29	0.94	13.18	2.56	0.191638
50	284.38	51.29	0.93	13.78	3.90	0.283019
80	284.37	51.20	0.93	14.08	4.07	0.289063
100	284.35	51.05	0.94	16.10	4.67	0.290082

5.5.3 XRD investigation of undoped graphene and Mg-doped graphene decorated at different powder vibration frequencies

The XRD patterns of the graphene and decorated graphene with Mg nanoparticles deposited at different powder vibration frequencies are presented in Fig 5.18 (a). The broad and dominant diffraction peak centered at $2\theta=25.11^\circ$ in the XRD pattern of the graphene correspond to the reflection of the (002) plane [34]. In the XRD patterns, the characteristic (002) peak is broad and low-intensity peak, which indicates that the graphene powder contained only a few layers of graphene [57]. On the other hand for the decorated graphene with Mg nanoparticles additional three diffraction peaks at $2\theta = 31.83^\circ$, 34.05° , and 36.35° were also observed. These peaks can be indexed to the three reflection peaks (001), (002) and (101) planes, which are assigned to the reflection from the hexagonal phase of Mg with lattice constant of $a = 3.234 \text{ \AA}$ and $c = 5.204 \text{ \AA}$ ((JCPDS 04-0770). There was no other impurities peak observed in the XRD patterns. The characteristic peaks of Mg nanoparticles located at 31.83° , 34.05° , and 36.35° were obtained. It was observed that the (101) peak of the Mg nanoparticles deposited without moving powder (0

Hz) was narrower, which suggests that large nanocrystalline particles were deposited onto graphene sheet. The crystallite sizes of the deposited Mg nanoparticle were calculated using equation (1). The crystallite sizes of the deposited Mg nanoparticles decreased with increasing powder vibration frequencies and the results are presented in Fig 5.18 (b).

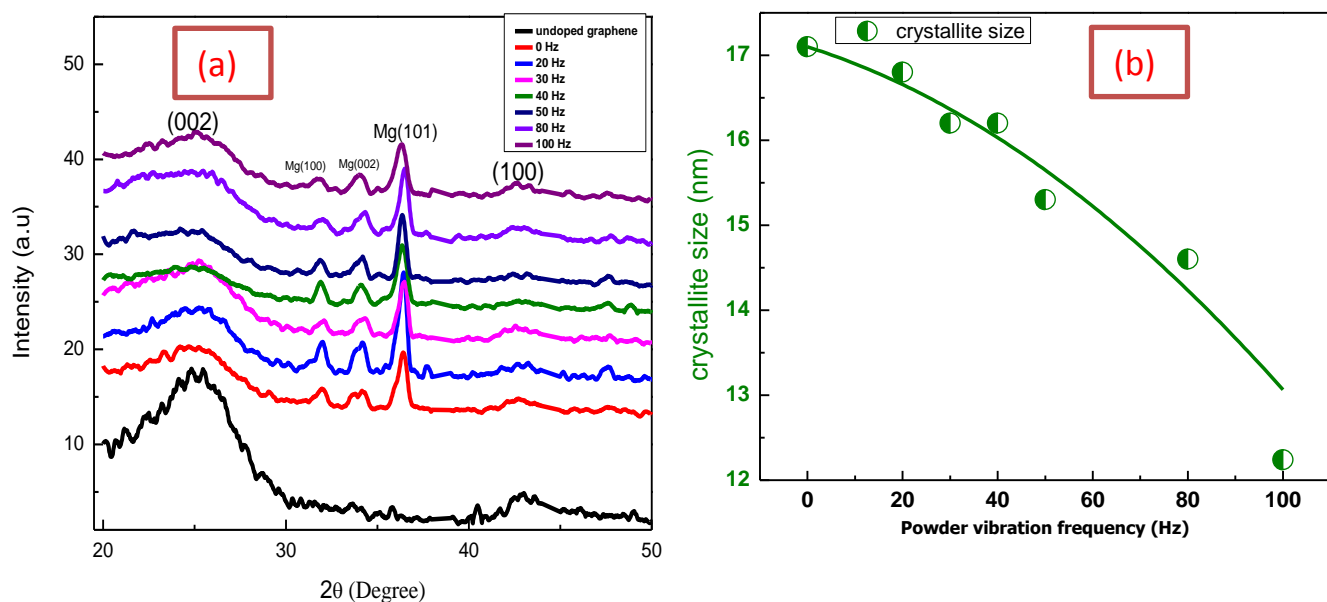


Fig 5. 18 (a) XRD patterns of decorated graphene with nanoparticles at different powder vibration frequencies

(b) crystallite sizes of the decorated Mg nanoparticles Mg as function of powder vibration frequencies

It can be seen in the XRD patterns, the FWHM of the (101) peak for deposited Mg nanoparticles are becoming wider as by increasing powder vibration frequencies. For comparison, the Lorentzian function was used to evaluate the FWHM of (101) peak for the deposited Mg nanoparticles without moving powder (0 Hz) and with powder vibration frequency at 100 Hz. It was found that the FWHM of the (101) peak without moving powder (0 Hz) and high powder vibration frequency (100 Hz) are 0.55 (degree) and 0.74 (degree) respectively. These results can be explained as follows, as discussed in the section 5.5.1 that, with deposition of Mg nanoparticles onto graphene sheets without moving powder (0 Hz), the sputtered particles were deposited onto graphene sheets at a certain area of the graphene surface and the graphene surface

were not completely covered by the sputtered particles. Also, it was found that the sputtered particles make aggregates onto graphene sheet. Due to the aggregation of the Mg nanoparticle on the graphene surface, the crystallite size of the Mg nanoparticles increased. However in the case of high powder vibration frequency (100 Hz) the crystallite size of the Mg nanoparticles obtained onto graphene sheet decreased with respect to that the crystallite size obtained without moving the powder (0 Hz). From the TEM image shown in Fig 5.15(a) indicates that well dispersed Mg nanoparticles were obtained onto graphene sheets by using high powder vibration frequency. The sputtered particles were anchored over the entire surface of the graphene flake. No aggregations of the sputtered particles were observed during the deposition process with high powder vibration frequency. Therefore, the crystallite size of the deposited Mg nanoparticles onto graphene sheet obtained in case of using high powder vibration was less than that of the crystallite size obtained onto graphene sheets without moving graphene powder.

Moreover the FWHM of the graphene (002) peak increased by the deposition of the Mg nanoparticles at different powder vibration frequencies and the values are presented in Fig 5.19. This suggests that the crystallinity of the graphene were reduced. The reduction of the crystalline thickness of the graphene after the deposition of the Mg nanoparticles suggest that, the stacking order of the graphene plane reduced due to the high concentration of Mg nanoparticles onto graphene plane. Additionally by the deposition of graphene with Mg nanoparticles the (002) peak of graphene were gradually shifted towards the lower angle values. This indicates that the plane of the graphene was distorted with the increasing amount of Mg nanoparticles onto graphene.

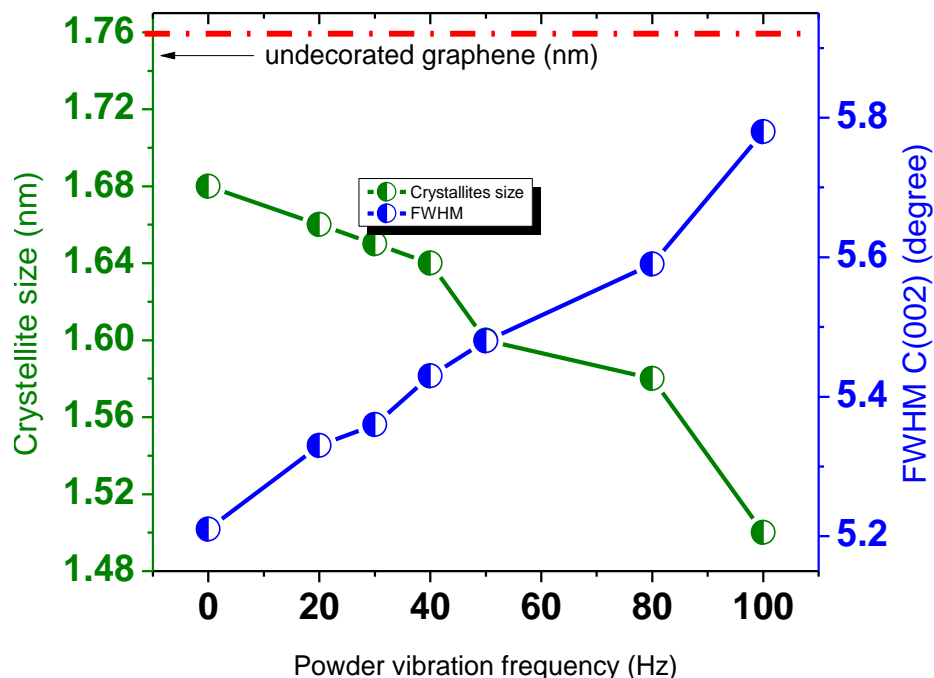


Fig 5.19 Crystallite sizes and FWHM of undecorated graphene and decorated graphene flakes with Mg nanoparticles as a function of powder vibration frequency

5.5.4 Raman study of undoped graphene and Mg-doped graphene decorated at different powder vibration frequencies

Fig.5.20 shows the Raman spectra undoped graphene and decorated Mg nanoparticles onto graphene deposited at different powder vibration frequencies. The Raman spectra of the undoped graphene and decorated graphene with Mg nanoparticles revealed characteristic G peak originating from in-plane vibration of sp^2 carbon atoms and D arising from the disorder induced mode. The Raman spectra of undoped graphene and deposited Mg nanoparticles onto graphene contain D and G peaks located at 1324 and 1585.67 cm^{-1} respectively. In addition to D and G peaks a broad low intensity 2D band is also observed at $\sim 2637.23\text{ cm}^{-1}$. A change in the positions, intensities and the full width at half maximum (FWHM) of the G, 2D and D peaks were observed. It is found that the G peak of graphene upshifted after the deposition of Mg nanoparticles at different powder vibration frequencies. The G peak of the graphene was shifted

from the 1585.67 cm^{-1} to 1588.78 cm^{-1} , when Mg nanoparticles were deposited onto graphene without moving graphene (0 Hz) powder.

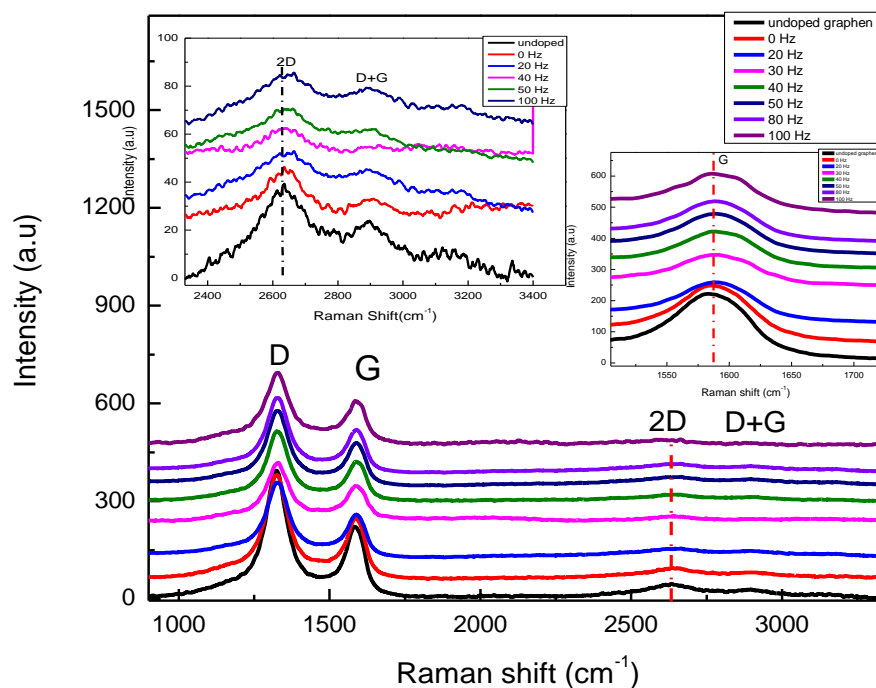


Fig 5.20 Raman spectra of undoped graphene and Mg-doped graphene at different of powder vibration frequencies

The shifts in G position toward higher wavenumbers were increased by increasing the powder vibration frequencies. The upshifts of the G peak were further increased from 1585.67 cm^{-1} to 1595.23 cm^{-1} after the deposition of Mg nanoparticles onto graphene at 100 Hz powder vibration frequency. Visible shifts in 2D bands toward the higher wavenumber were also observed after the deposition of Mg nanoparticles onto graphene as shown in Fig 5.20 (enlarged view).]The 2D bands were upshifted from 2637.23 cm^{-1} to 2645.43 cm^{-1} after the deposition of Mg nanoparticles at 100 Hz powder vibration frequency. The doping type and strain can be measured from the position shift of the G and 2D bands. [^{282, 26}]. It is known from literature that the downshift of the 2D peak and upshift of the G peak correspond to n-doping of graphene, while

the upshift of the G band position and the upshift of the 2D band position means p-doping [198, 283]. In our case the G band position and the of the 2D band position were shifted to higher wavenumbers by 9.81 cm⁻¹ and 8.2 cm⁻¹ respectively. This result suggest p-doping of graphene with Mg nanoparticles depositions. The blue shift of G peak in the graphene peak by the deposition of the Mg nanoparticles suggesting phonon stiffening due to charge transfer.[284

The I_D/I_G of the decorated graphene with Mg nanoparticles as function of the Mg/C is presented in Fig 5.21. Normally I_D/I_G ratio was used to measure the defect density induced in the sp² domain by the interaction of the metal or other impurities [285]. From the Fig 5.21, it is asserted that as the Mg contents increased by increasing the powder vibration frequency, the defects in the decorated graphene were pronounced. Moreover by the deposition of the Mg nanoparticles onto graphene scattering of phonon from the defects sites were increased, the Raman spectra display the noticeable increase of the D peak intensity. Fig 5.21 shows I_D/I_G of the of the deposited Mg nanoparticles onto graphene as function of the Mg/C atomic ratio. It was found that with increasing Mg/C atomic ratio obtained by increasing the powder vibration frequencies, the I_D/I_G ratios increased. The I_D/I_G ratios values increased to 1.767, when Mg nanoparticles were obtained in ratio Mg/C (sp²) = 32.34 atomic ratio (%) at high powder vibration frequency (100 Hz). This suggests that, the structural defects were pronounced in the sp² domain with increasing of Mg concentration onto graphene sheets. The intensity ratio of the D and G bands (I_D/I_G) is also used to calculate the in-plane crystallite sizes (La). The in-plane crystallite size is measured by using Tuinstra - Koenig relation [247].

$$La(nm) = 2.4 \times 10^{-10} \lambda^4 \left(\frac{I_D}{I_G} \right)^{-1} \dots\dots\dots(2)$$

Where La is the in-plane crystallite size and λ is the excitation wave length wavelength used in the Raman measurement. Fig 5.21 shows that the in-plane crystallite size decreased by increasing

the Mg/C sp^2 . This suggests that by increasing the Mg contents to C sp^2 domain, the sp^2 domain was broken and decreased from 23.2 nm to ~21.6 nm due to the deposition of Mg nanoparticles onto graphene sheets.

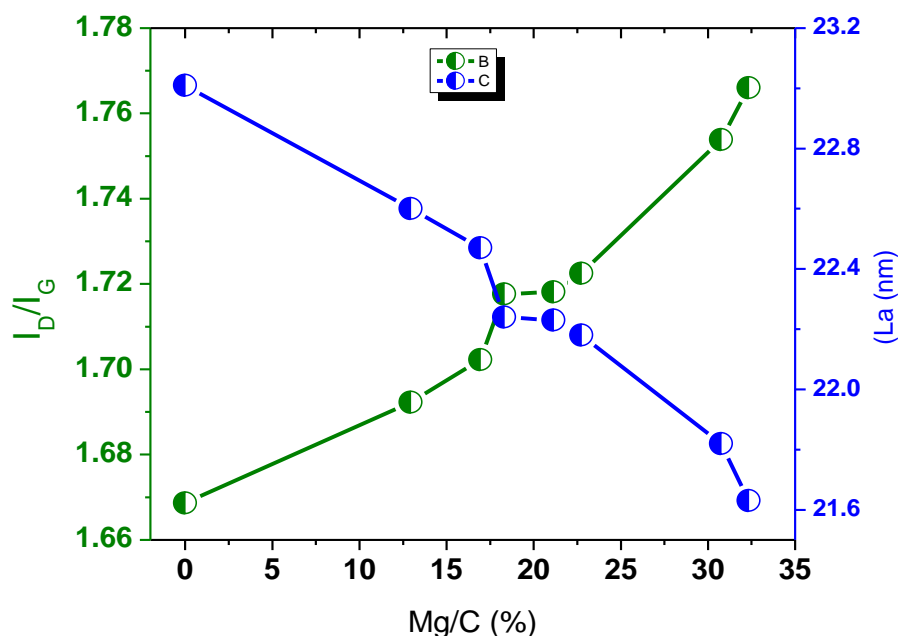


Fig 5. 21 Variation of Raman peak intensity ratios of I_D/I_G and in plane crystallites size (L_a) plotted against the Mg to C atomic ratio (%)

5.6 Concluding Remarks:

In this chapter, the influence of the Mg amount on the structural, chemical and morphological properties of the graphene are reported. The Mg nanoparticles were deposited onto graphene successfully by varying three deposition parameters RF power, deposition time and powder vibration frequency. By the variation of the deposition parameters different amounts of Mg concentration were obtained onto graphene sheet. On the bases of the variation of the deposition parameters, the following conclusions are drawn from this chapter and categorized in the following sections.

In the 5.3 section, the structural properties of the decorated graphene with Mg nanoparticles were investigated by X-ray diffraction and Raman spectroscopy. The chemical properties were

studied using the XPS technique. It was found from the XRD results, by increasing the RF power values the plane of the graphene were distorted with the interaction of high energetic sputtered particles and plasma species. Addition to this the crystalline nature of the Mg nanostructure in the Mg/graphene composite was confirmed by XRD investigation. The crystallites sizes of the deposited Mg nanoparticle were increased from (14 to 21 nm) by variation of the RF power values (30 to 75 W). Raman spectrum showed that with the interaction of graphene with Mg nanoparticles the G and 2D peak were shifted 11 cm^{-1} and 7 cm^{-1} to higher wavenumbers, suggesting p doped graphene by the deposition of Mg nanoparticles. The structural defects were increased in the graphene with interaction of Mg nanoparticle. The XPS results revealed that with the deposition of the Mg nanoparticles the C 1s core level shifts toward the lower binding energy. The charge is transferred from the graphene to the MgO due to the difference of work function.

In the 5.4 section, the interactions of graphene with Mg nanoparticles were characterized by XRD, Raman, XPS and TEM. XRD results demonstrated that by the interaction of the graphene with Mg nanoparticles the d spacing of the graphene was increased. Also the three characteristic peaks correspond to (001), (002) and (101) planes of hexagonal structure of metallic Mg were also observed. The crystallite sizes of deposited Mg nanoparticles were in the range of 14 to 16 nm. The p-doping effect was clearly evident in the Raman spectroscopy data of graphene upon the deposition of the Mg nanoparticles. The sp^2 domain of graphene was decreased due to the interaction of energetic species and sputtered particles. XPS analysis showed that the deposited Mg nanoparticles were oxidized due to exposure to the atmosphere. The p doping effect was also confirmed from the XPS analysis. TEM micrograph showed that Mg nanoparticles are uniformly

distributed onto graphene sheet. The deposited Mg nanoparticles are in spherical shape and having an average particles size of 20-25 nm.

In the last section, the well dispersed Mg nanoparticles onto graphene sheet were deposited by varying the powder vibration frequencies. The deposited Mg nanoparticles onto graphene at different powder vibration frequencies were characterized by XRD, TEM, Raman, and XPS techniques. TEM micrographs revealed that the deposited Mg nanoparticles onto graphene sheet without moving powder were aggregated at certain places of the graphene sheet. However by deposition of Mg nanoparticles onto graphene at high powder vibration frequency were uniformly distributed over the entire sheet of graphene. The well dispersed Mg nanoparticles onto graphene flake were confirmed from the TEM analysis. XRD results demonstrated that with deposition of Mg nanoparticles at high powder vibration frequency the plane of the graphene were distorted due to the interaction of energetic species. The crystallite sizes of the deposited Mg nanoparticles were decreasing by using high powder vibration frequency. By the deposition of Mg nanoparticles, the intensity ratio of D and G bands I_D/I_G of graphene was increased. The XPS analysis showed that with high powder vibration frequency more sputtered particles were deposited onto graphene sheet compared to the case of without moving powder.

Lastly, the structural, chemical and electronic properties decorated graphene sheets with different amount of the Mg nanoparticle were discussed in this chapter. Furthermore, the interaction of the graphene sheets with TiO_2 nanoparticles will be studied in next chapter# 6.

Chapter # 6

The influence of TiO₂ concentration on the structural, chemical and electronic properties of graphene powder by plasma processing

6.1 Introduction:

Graphene 2D nanostructure can potentially serve as supporting materials to anchor semiconductor nanoparticles onto graphene sheet and improve the performance of the composite materials in optoelectronic and energy conversion devices. Additionally, the graphene surface properties could be tuned via chemical modification. For the decoration of catalytic nanoparticles onto graphene sheets can be more useful in carrying out sensing or catalytic process. TiO₂ is a wide band gap semiconductor and active in its photocatalytic property under UV irradiation. The interaction of graphene with TiO₂ nanoparticles is capable to enhance the catalytic activity under UV irradiation [60]. Different chemical and physical methods were used to decorate with well distributed nanoparticles graphene sheets. However, by chemical methods the nanoparticles tend to aggregate onto graphene powder, which reduces the photocatalytic activity of the composite [286]. The main objective of this part of the work is to study the interaction of graphene with TiO₂ nanoparticles and the enhancement of catalytic activity of the composite. In this chapter, three different deposition parameters were used for the decoration of well dispersed TiO₂ nanoparticles onto graphene sheets. On the basis of variation of the deposition process this chapter is divided into three sections and following investigations are driven

- ❖ For the results presented in the first section, TiO₂ nanoparticles were deposited by varying RF power values and the interaction of the energetic sputtered particles and plasma species with graphene sheet will be discussed.

- ❖ For the results described in the second section, different amount of TiO₂ nanoparticles were obtained onto graphene by increasing the deposition time. The structural, chemical and electronic properties of the decorated graphene with TiO₂ nanoparticles will be studied.
- ❖ For the results reported in the last section, the influence of the TiO₂ concentration on the structural, chemical and electronic properties of the graphene will be presented.

6.2 Experimental detail:

The anatase TiO₂ nanoparticles were deposited onto graphene by RF sputtering in Ar plasma. High purity (99.99%) TiO₂ disc with 5 cm diameter was used as a sputtering target. The distance between the TiO₂ target and graphene powder were fixed at 50 mm. The powder vibration system was used to decorate the graphene powder with uniform TiO₂ nanoparticles. Three deposition parameters RF power, deposition time and powder vibration frequency were varied to deposit the TiO₂ nanoparticles onto graphene sheet and the specific details of the deposition parameters are given below.

Firstly, the TiO₂ nanoparticles were deposited onto graphene powder by varying the RF power values from 30 to 80 W corresponding to self-bias voltage ranging between -174 to -294 V. The total process pressure and powder vibration frequency were kept constant at 6 Pa and 20 Hz respectively. The deposition time was fixed at 40 min.

Secondly, in order to vary the amount of TiO₂ nanoparticles onto graphene sheet at constant RF power value, the TiO₂ nanoparticles were deposited by increasing the deposition time from (10 to 60 min). The RF power and self-bias voltage applied to the TiO₂ target were fixed at 40 W and 174 V respectively. The powder vibration frequency and total process pressures were kept constant at 20 Hz and 6 Pa.

At last, the graphene powders were decorated with well dispersed TiO₂ nanoparticles by varying the powder vibration frequency from 0 to 100 Hz with constant amplitude of 32 μm. The deposition time RF power and process pressure were kept at constant values of 60 min a 40 W and 6 Pa process pressure respectively.

6.3 Effect of TiO₂ nanoparticles on the structural, chemical and electronic properties of graphene powder deposited by varying RF power values

In this section, the results of the deposited TiO₂ nanoparticles onto graphene by varying the RF power values are presented. The main goal of this work is to study the interaction of graphene with TiO₂ nanoparticles, when the sputtered particles interact with graphene sheet with high kinetic energy. By the variation of the RF power values different amounts of TiO₂ nanoparticles onto graphene were obtained. The influence of the TiO₂ concentrations on the structural, chemical and electronic properties of the graphene is discussed in this section. The interaction of graphene with TiO₂ nanoparticles were characterized by the XRD, Raman, XPS and TEM techniques. Moreover the process parameters are presented in table 6.1.

Table 6.1 the process condition of decorated graphene with TiO₂ nanoparticles

Sample #	RF Power (W)	Process pressure (Pa)	Deposition Time (min)	Powder vibration frequency (Hz)
1	30	6	40	20
2	50	6	40	20
3	60	6	40	20
4	70	6	40	20
5	80	6	40	20

6.3.1 TEM analysis of decorated graphene with TiO₂ nanoparticles deposited at 80 W

The surface morphology and structure feature of the decorated graphene with TiO₂ nanostructures were examined by TEM analysis. Fig 6.1 (a-b) shows the decorated graphene with TiO₂ nanoparticles deposited at 80 W. It is observed from the TEM micrographs that very small TiO₂ nanoparticles anchored onto graphene. Fig (a) shows the high magnification of the decorated graphene sheet with TiO₂ nanoparticles. Graphene sheets were decorated with high coverage of TiO₂ nanoparticles and the deposited particles are well distributed over the graphene sheets. Fig (b) demonstrates the low magnification of the deposited TiO₂ nanoparticles onto graphene sheet, which indicates that a uniform layer of TiO₂ covered the graphene sheet. Due to deposition of the TiO₂ nanoparticles at high RF power value the small TiO₂ nanoparticles make aggregates onto graphene sheet and look like thin layer of TiO₂ nanoparticles. The sizes of the deposited TiO₂ nanoparticles are in the range of 5-10 nm.

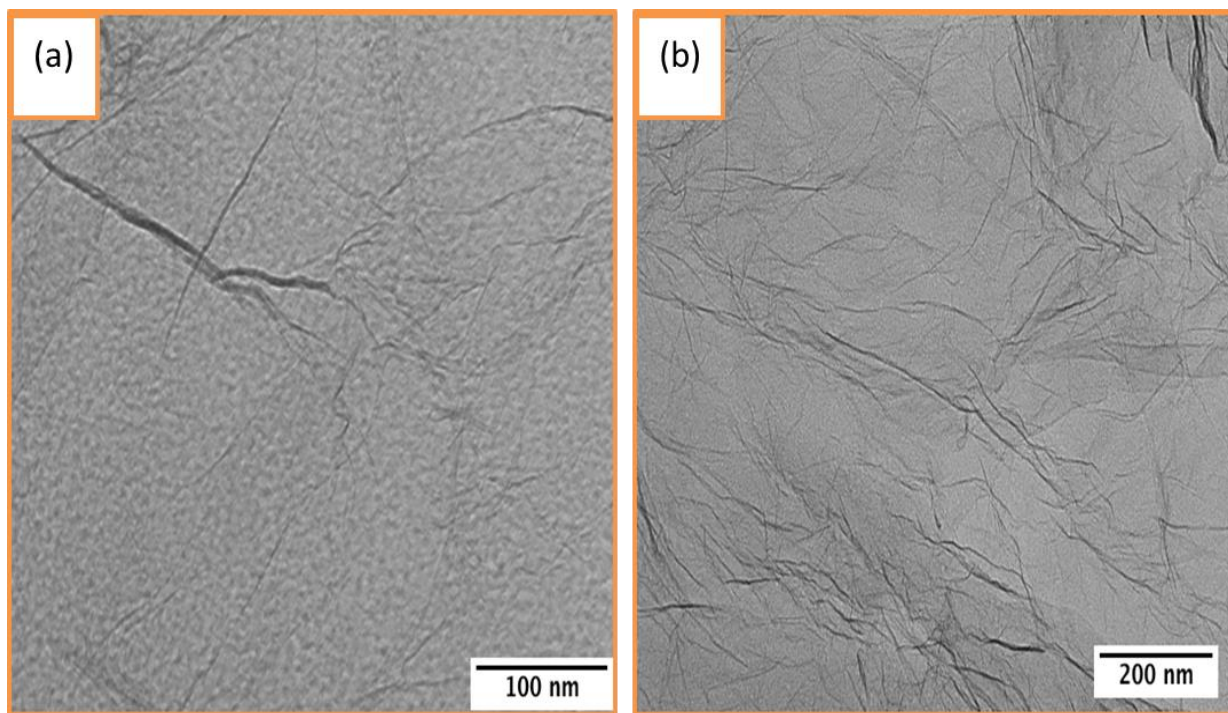


Fig 6. 1 TEM images (a-b) of deposited TiO₂ nanoparticles onto graphene sheet at 80 W

6.3.2 XPS analysis undoped graphene and TiO₂ doped graphene deposited at different RF power values

The interaction between the graphene and deposited TiO₂ nanoparticles are studied by using the XPS analysis. The high resolution XPS spectra of the C 1s core level of the undecorated graphene and decorated graphene with TiO₂ nanoparticles deposited at different power values are shown in Fig 6.2 (a). The C 1s core level were de-convoluted into three components. The binding energies of the components of the undecorated graphene C 1s spectrum are centered at 284.45, 285.23 and 286.2 eV respectively, which are attributed to C-C (sp²), C-H/C-C (sp²) and C-O bonds respectively.

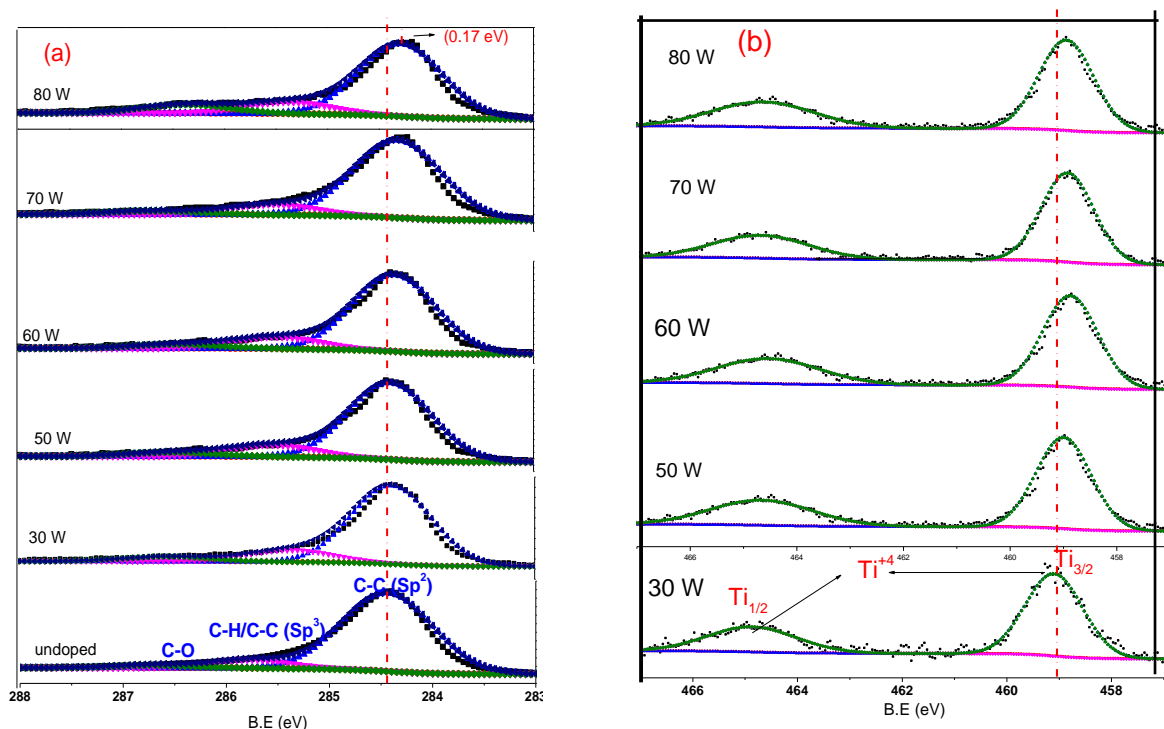


Fig 6. 2 (a)| XPS spectra for graphene powder and deposited TiO₂ nanoparticles at different RF power values (a)Shift in the C 1s core levels position and the shift of this position upon TiO₂ deposition. (b) Ti 2p core level spectra. [Process pressure = 6 Pa, Time=40 min, Frequency = 20 Hz RF power= 30 to 80 W]

By the deposition of TiO₂ nanoparticles the C 1s core level of the graphene shifted toward lower binding energies values. A low shift of 0.04 eV was observed in the C-C (sp²) bond with respect

to undoped graphene C-C (sp²) bond, when TiO₂ nanoparticles were deposited onto graphene at 30 W. The shifts in C-C (sp²) bond increased by raising the RF power values and reached 0.17 eV with the deposition of TiO₂ nanoparticles onto graphene at 80 W. Generally the photoemission spectroscopy are used to measure the core level, work function and valance band and this method is also useful for the determination of the interface band alignment. Recently it was reported that, when graphene interacted with high band gap semiconductor the C 1s core level is shifted toward the lower binding energies due to the charge transfer at the interface in order to align the Fermi level [287]. Youngkyu Chang et al demonstrated that the shift in the Fermi level is due to the difference of the work function [288]. Similar observation about the charge transfer between the interactions of graphene and TiO₂ due to the difference of work function is reported by Aijun Du et al using density function theory [116]. He described that charge is transferred from graphene to TiO₂ due to large difference in work function values between the TiO₂ (5.50 eV) and graphene (4.3 eV). In our case, after the deposition of TiO₂ nanoparticles onto graphene sheet the C 1s core level of the graphene is shifted towards the lower binding energies values. Therefore, the shift in the C 1s core level of the graphene after the deposition of TiO₂ nanoparticles is due to p doping, whereas the electrons are transferred from graphene to TiO₂ nanoparticles at the interface in order to align the Fermi level between the TiO₂ and graphene.

The high resolution XPS spectra of the Ti 2p peak for the decorated graphene with TiO₂ nanoparticles deposited at different RF power values are presented in Fig 6.2 (b). The Ti 2p XPS spectra were fitted by two components one is Ti 2p_{1/2} and the second Ti 2p_{3/2} [289]. The spin orbit split components of Ti 2p_{1/2} and Ti 2p_{3/2} is located at binding energy positions of 459.08 and 464.95 eV respectively. The separation between the Ti 2p_{1/2} and Ti 2p_{3/2} is 5.87 eV and this split

orbit coupling suggests that the oxidation state of Ti is +4 [290]. Moreover with increasing RF power values, the Ti 2p core level is shifted towards the lower binding energy values. The maximum downshift of 0.26 eV was observed, when graphene were decorated with TiO₂ nanoparticles at 80 W. The downshift of the Ti core levels suggest that charge is transferred from the graphene to TiO₂ due the difference of the work function of the contacted materials [291]. The band of the TiO₂ bends toward the interface upon the interface of TiO₂ films with graphene sheets. The band bending of TiO₂ is further explained in section 6.5.1.

Fig 6.3 (a) depicts the O 1s spectra for the deposited TiO₂ nanoparticles onto graphene at different power values in Ar plasma. The O 1s XPS spectra were de-convoluted into three components. The main component (OI) located at binding energy (530.69 eV) is assigned to the O⁻² bound to Ti⁺⁴ [181] Two shoulder components towards the higher binding energies values located at 532.12 eV and 533.3 eV can be attributed to the C–OH and C–O bonds respectively [292, 180].. There was a similar shift observed in the OI components like C 1s and Ti 2p by increasing the deposition RF power values. This indicates that surface dipoles were developed due to the charge transfer between TiO₂ and graphene and lead band bending of TiO₂ and also decreased the binding energies of the Ti 2p and O 1s [112].

Furthermore, the atomic ratio between oxygen and metal in oxide is one of the important and useful parameter to evaluate the stoichiometry of the oxide. The TiO₂ (OI/Ti) stoichiometry were measured on the basis of the area under the main component of the oxygen (OI) and the area under the Ti 2p_{3/2} component. The measured atomic ratio, OI/Ti, for the decorated graphene with TiO₂ nanoparticles at different RF power values are displayed in Fig 6.3 (b). It can be seen that by increasing the RF power values from 30 W to 80 W, the OI/Ti ratio decreased linearly

from 1.96 to 1.86. This shows that the deposited TiO₂ is more oxygen deficient at high RF power values than at low power deposition.

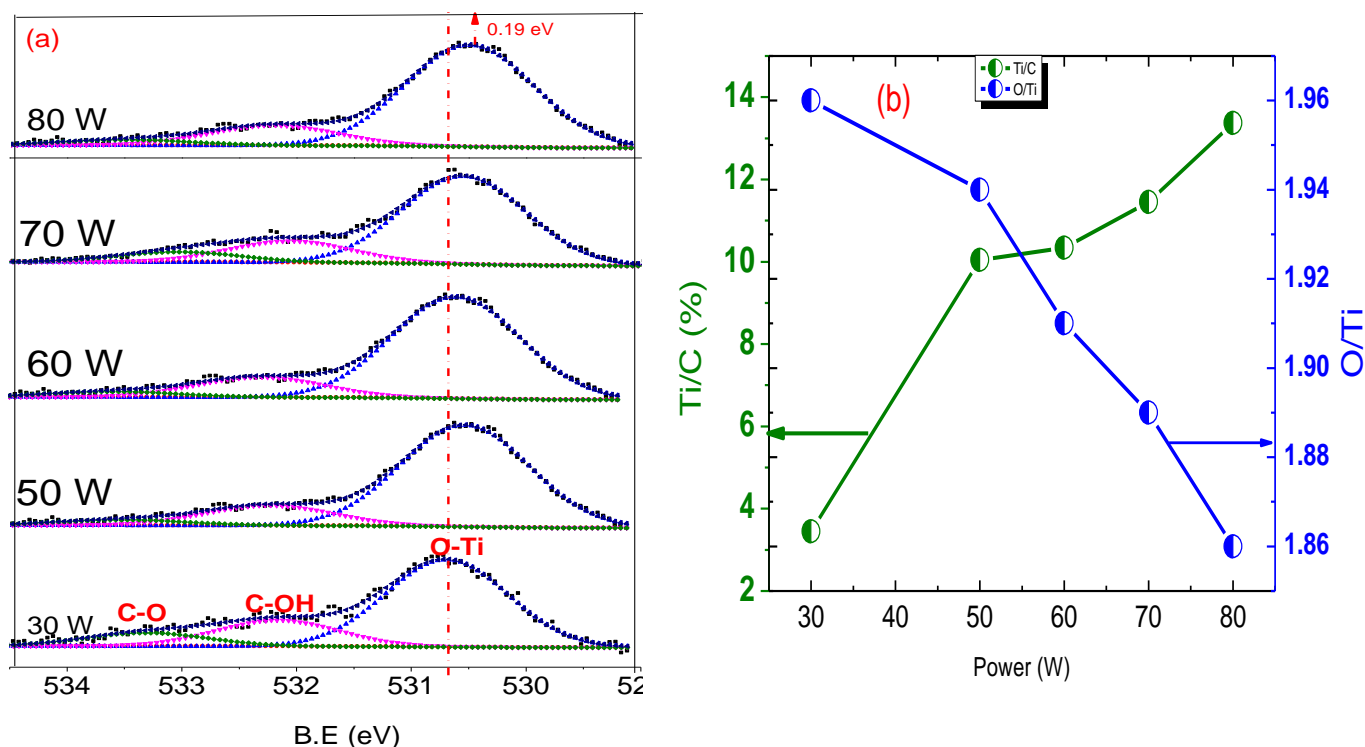


Fig 6.3 (a) XPS O 1s core peak of decorated graphene TiO₂ nanoparticles at different RF Power values (b) variations of Ti /C sp² and OI/Ti atomic ratio as a function of RF power values

Generally by deposition of the TiO₂ at higher power the ion flux and sputtered particles bombardment on the graphene powder was higher than at low power deposition. It is well known by increasing the RF power values, the sputtered particles extracted from the TiO₂ target having high kinetic energies and the interaction of these sputtered particles with graphene powder is more rigorously. Ti/C (sp²) atomic ratio also increased from 3.45 at. % and reached 13.37 at. %, when the RF power values varied from 30 W to 80 W. The results are presented in Fig 6.3 (b). The reduction of the OI/Ti ratio can be explained as follow, by increasing RF power values the sputtered particle and plasma species interact with lattice of TiO₂ more energetically generates the oxygen vacancies in the TiO₂ lattice.

The oxygen formation mechanism of the deposited TiO₂ nanoparticles onto graphene sheets at different RF power values can be explained as follows, as discussed in the above text that the sputtered particles gain more kinetic energy by increasing RF power values, these energetic sputtered particles remove the oxygen from the lattice of TiO₂ nanoparticles when it was deposited onto graphene sheets, or might be oxygen remove from the lattice of TiO₂ during the deposition process, when the sputtered particles coming from the target and collision takes place between the sputtered particles with energetic plasma species.

6.3.3 XRD analysis undoped graphene and TiO₂ doped graphene deposited at different RF powers

The XRD patterns of the undoped graphene and decorated graphene with TiO₂ nanoparticles deposited at different RF power values are presented in Fig 6.4 (a). The XRD pattern of the undecorated graphene shows a broad peak at $2\theta = 25.11^\circ$ attributed to the (002) reflection of few layer graphene. The numbers of graphene layers were calculated using the relation [²⁹³]

$$N = \frac{\text{Thickness}}{d_{(002)}} \dots\dots\dots(1)$$

The calculated number of layers from the above equation for the undoped graphene is 4.96. This shows that the graphene powder consist of very few layers of graphene. The characteristic (002) peak of the graphene is very broad, which indicates that graphene layers are not well ordered. By the decoration of graphene with TiO₂ nanoparticles, the (002) peak was shifted to higher 2θ values and the shift in (002) gradually increased by raising the TiO₂ concentration. This indicates that the spacing between the layers of graphene is reduced with increasing contents of the TiO₂. The calculated interplaner distances of the undecorated graphene and for the decorated graphene with TiO₂ nanoparticles as function of Ti/C (sp²) atomic ratio (%) are presented in Fig

6.4 (b). Moreover it is observed that FWHM of the graphene is becoming wider by increasing the TiO₂ concentration. FWHM of the (002) peak of all the samples were evaluated upon Gaussian shape fit. This suggests that by the deposition of TiO₂ nanoparticles onto graphene, the structural defects were pronounced in the graphene structure.

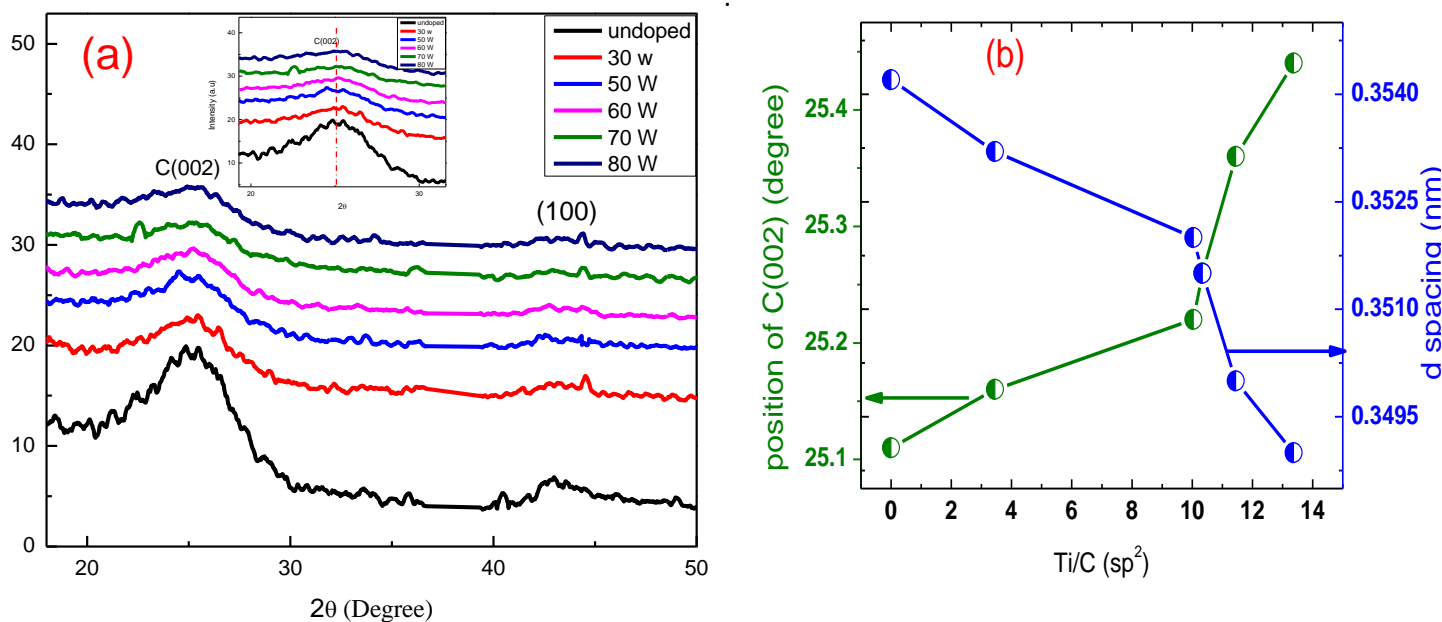


Fig 6. .4 (a) XRD patterns of undoped and TiO₂ doped graphene powers values (b) Variation of the 2θ angle of the (002) and RF d-spacing as function of Ti/C sp² atomic ratio.

The crystallite thickness of undoped graphene and for the decorated graphene with TiO₂ nanoparticles were measured by fitting the (002) peak [294]. The crystallite thicknesses were calculated by using the Scherer equation and the crystallite thickness decreased with increasing the TiO₂ concentration as shown in Fig 6.5. This can be explained as follows; by the deposition of TiO₂ nanoparticles onto graphene the stacking order of the graphene layer was reduced with the interaction of the high energetic sputtered particles.

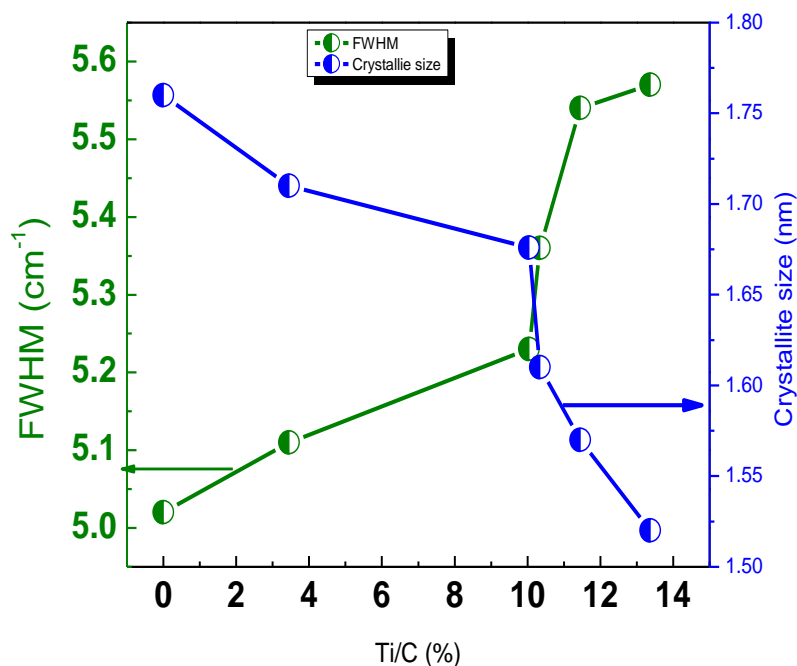


Fig 6. 5 Variation in the FWHM of the (002) peak and crystallite thickness as function of Ti/C atomic ratio

6.3.4 Raman analysis of undoped graphene and TiO₂ doped graphene deposited at different RF power values

Raman spectra of the undecorated graphene and decorated graphene with TiO₂ nanoparticles deposited by increasing RF power values are depicted in Fig 6.6. Four characteristics bands in the Raman spectrum of the undoped graphene were detected: the D band (defects band or disordered) band located at 1324 cm⁻¹ and the G (in-plane stretching of the sp² C-C bonds) band centered at 1586.45 cm⁻¹. The 2D band of the graphene centered at 2637 cm⁻¹ is originated from the second order zone boundary and D+G band located at 2876 cm⁻¹ is the combination band originated in the Raman spectra in the presence of disorders in the system. In addition, for the decorated graphene with TiO₂ nanoparticles, four characteristics bands of the TiO₂ were also observed in the Raman spectra. The peaks are centered at 154, 394, 510 and 632 cm⁻¹. These peaks can be attributed to the E_g, B_{1g}, A_{1g} and E_{1g} modes of the anatase phase of TiO₂, respectively [295, 296]. This is confirmed that anatase phase formation was established onto

graphene sheets. It is also shown that by the deposition of TiO₂ onto graphene at different RF power values, there were strong changes observed in the position, intensity and FWHM of the G, D and 2D peak respectively. The G and 2D peak were shifted by 5 and 4 cm⁻¹ to higher wave numbers, when the TiO₂ nanoparticles were deposited at 30 W. The shifts in G and 2D peaks increased with rising TiO₂ concentration obtained onto graphene at different RF power values. Further upshifts in G and 2D bands of 11.34 cm⁻¹ and 10.5 cm⁻¹ were observed, when the graphene was decorated with TiO₂ nanoparticles at 80 W and the results are presented in Fig 6.6 (enlarged view).

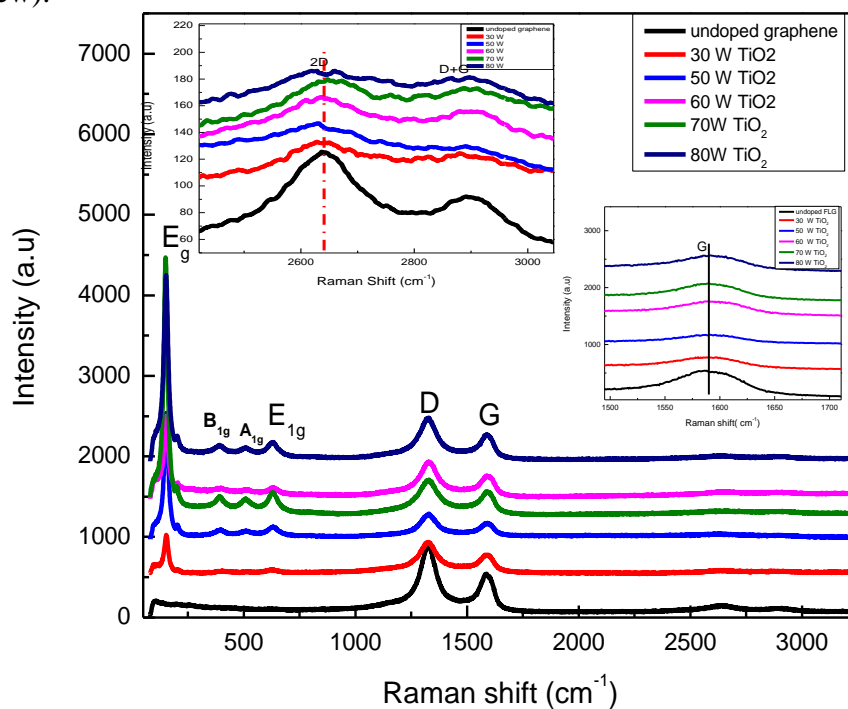


Fig 6.6 Raman spectra of undoped graphene and TiO₂ doped graphene at different RF power values

It is reported that the 2D band of the graphene was shifted to higher frequency upon the p doping graphene with metal oxide [297]. Likewise, the G peak of graphene is shifted to higher frequency with p doing and shifted toward the lower wavenumber with n-doping [298]. It is also possible that by the deposition of TiO₂ nanoparticles onto graphene the defects were generated in the plane of graphene and these defects scatter the electrons to non-adiabatic state [299]. However,

Denys Naumenko et al is reported that the upshift in G and 2D peaks are due to the p doping [300]. Similar observation was also reported by Jisook Lee et al [253]. Consequently, the dynamic effect in decorated graphene with TiO₂ nanoparticles was less dominant. In our case, the G and 2D bands of the graphene were shifted to higher wavenumbers upon the deposition of TiO₂ nanoparticles. This indicates that upshift of G and 2D bands are due to p doping. Hence, the interaction TiO₂ nanoparticle with graphene as an electron acceptor and the electrons are transferred from the graphene to the anatase TiO₂ nanoparticles. This phenomenon is further explained in the section (6.5.3).

The level of the disorders and defects can be evaluated in graphitic materials by measuring the relative intensities of D and G band, higher intensity I_D/I_G ratio indicating higher disorders and defects in the graphene planes. Fig 6.7 depicts that the I_D/I_G ratio as a function of Ti/C sp² atomic ratio obtained by increasing the RF power values. The I_D/I_G ratio increased with increasing the TiO₂ concentrations onto graphene planes.

The I_D/I_G ratio was 1.64 for the undoped graphene and increased to 1.80, when the TiO₂ nanoparticles were deposited at 80 W in a ratio of Ti/C sp² =13.37 atomic ratio (%). This indicates that the structural defects increased with deposition of TiO₂ onto graphene by increasing the RF power values.

In addition, the in-plane average crystallite size (La) were measured directly using the I_D/I_G ratio [301],

$$La(nm) = 2.4 \times 10^{-10} \lambda^4 \left(\frac{I_D}{I_G} \right)^{-1} \dots\dots\dots(2)$$

Where λ is the wavelength used for the analysis of the samples, (in our case is 633 nm). The calculated in-plane crystalline size of undecorated graphene and decorated graphene with TiO₂ as a function of Ti/C (sp²) is presented in Fig 6.7. The in-plane crystallites size of the graphene

were reduced from 23.1 to 21 nm when the TiO₂ were deposited onto graphene in the ratio of Ti/C (sp²) = 13.37 at. %. These suggest that with the deposition of TiO₂ nanoparticles onto graphene at different RF power values, the sp² domains of the graphene were broken or may be shrinking with the interaction of TiO₂ nanoparticles. The reduction of the sp² domain size is further explained as follows, the hexagons of the sp² domain were distorted with deposition of the TiO₂ nanoparticles and the distortion increased with raising the amounts of the TiO₂ nanoparticles. Consequently due to the distortion of the sp² domain by the interaction of the sputtered atoms the sp² domain was reduced.

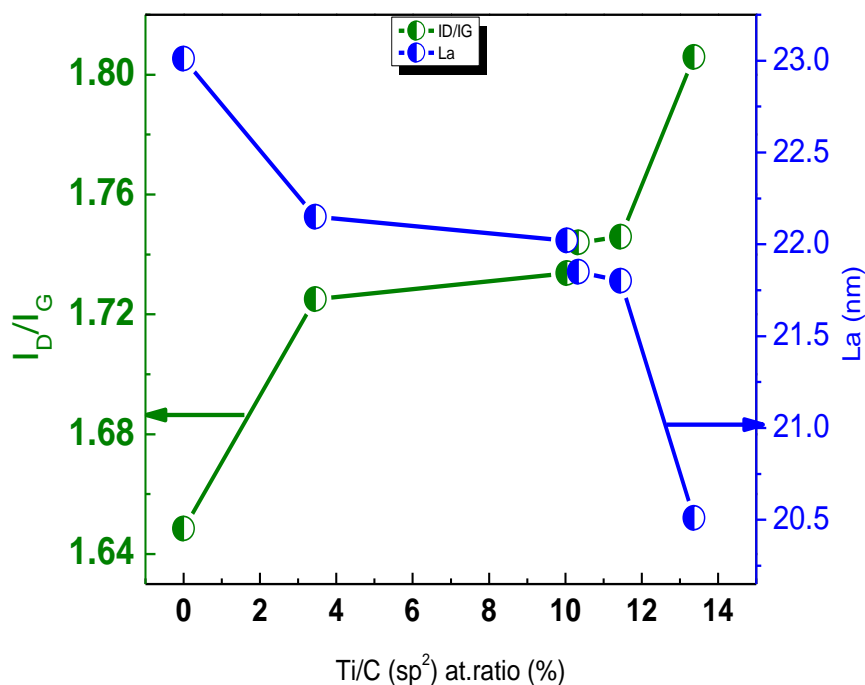


Fig 6. 7 Variation of Raman peak intensity ratios of ID/IG and in plane crystallites size (La) plotted against the Ti/C.a (%)

6.4 influence of TiO₂ on the structural, chemical and electronic properties of graphene powder deposited by varying the deposition time.

In section 6.3, we described the interaction of the graphene with TiO₂ nanoparticles deposited by increasing RF power values. It was found that by the deposition of the TiO₂ nanoparticles onto

graphene induced the structural defects and the structural defects were enhanced in the sp² domains with increasing the sputtered particles energies. In this section of thesis, we studied the influence of the TiO₂ concentration on the structural and chemical properties of the graphene. TiO₂ nanoparticles were deposited onto graphene by increasing the deposition time. For the structural characterization, the Raman and XRD analysis were used to investigate the types of defects. XPS analysis was used for the chemical analysis. Moreover the process parameters are presented in table 6.2.

Table 6.2 the process condition of decorated graphene with TiO₂ nanoparticles

Sample #	RF Power (W)	Process pressure (Pa)	Deposition Time (min)	Powder vibration frequency (Hz)
1	40	6	10	20
2	40	6	20	20
3	40	6	30	20
4	40	6	40	20
5	40	6	50	20
6	40	6	60	20

6.4.1 XPS analysis undoped graphene and TiO₂ doped graphene deposited with different times

The XPS analysis of the decorated graphene with TiO₂ nanoparticles are depicted in Fig 6.8. The high resolution C 1s core level spectra of the undecorated graphene and decorated graphene with different times are displayed in Fig 6.8 (a). The C 1s core levels of the undecorated and decorated graphene with TiO₂ were de-convoluted into three components by using the Gaussian shape line function after performing a Shirley background correction. The de-convoluted

components for the undecorated graphene are located at binding energy 284.45, 285.23 and 286.2 eV, which correspond to the C-C (sp²), C-H/C-C (sp³) and C-O bonds respectively. A small downshift was observed in the C 1s core level after the deposition of TiO₂ nanoparticles at 10 min. The shift in the C 1s core levels was further increased with increasing concentration of TiO₂ to graphene plane. The maximum downshift of 0.09 eV was observed with decoration of TiO₂ nanoparticles at 60 min of deposition. This observation suggests that with the interaction of graphene with TiO₂ nanoparticles the charge transfer occurring from graphene to TiO₂ due to the difference of work function. In this case the maximum down shift of 0.09 eV were detected with the deposition of the TiO₂ nanoparticles at 60 min in a ratio Ti/C sp² = 5.26 atomic ratio (%) at 40 W RF power value compared to the downshift of 0.19 eV in C 1s level were observed upon the deposition of TiO₂ nanoparticles at 80 W in a ratio Ti/C (sp²) = 13.37 atomic ratio (%) at 40 min of deposition. The reasonable explanation for this is that by increasing RF power values (40 to 80 W) more sputtered particles were deposited onto graphene sheet energy compared to the deposition at constant RF power (40 W) value. This observation indicates that by increasing the amount of the TiO₂ nanoparticles onto graphene sheet, the interaction between the graphene and TiO₂ increased.

Fig 6.8 (b) presents the XPS spectra of the Ti (2p) binding energy region for the decorated graphene with TiO₂ nanoparticle at different times of deposition. Two components centered at binding energies of 459.01 and 464.95 eV are attributed to the Ti (2p_{3/2}) and Ti (2p_{1/2}) respectively. The spin-orbital coupling of these photoelectrons was assigned to the chemical state Ti⁺⁴. The separation between the spin-orbital couplings is 5.94 eV indicates that TiO₂ was formed on the graphene sheet [302, 303].

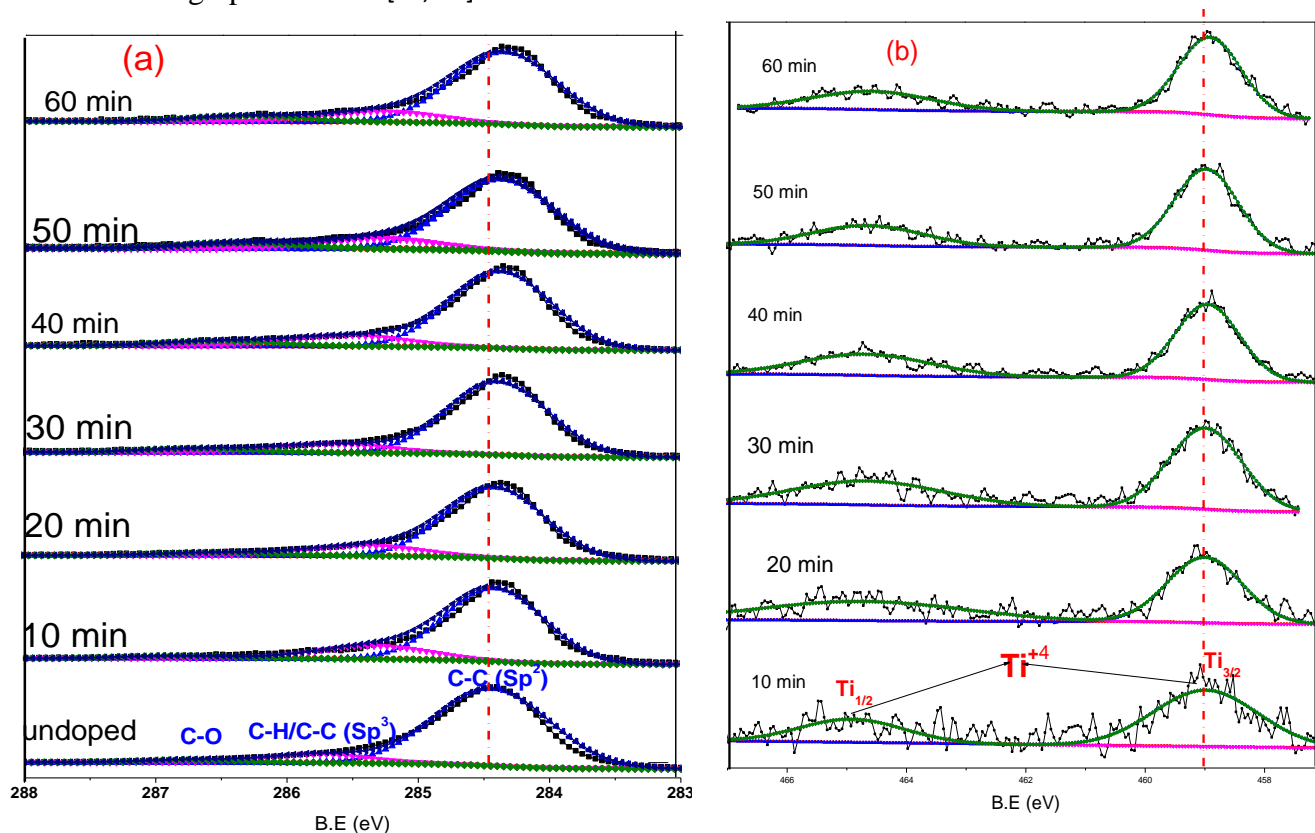


Fig 6. 8 (a) XPS spectra from graphene powder and deposited TiO₂ nanoparticles at different times of deposition (a) C Shift in the C 1s core levels position and the shift of this position upon TiO₂ deposition. (b) Ti 2p core level spectra. [Process pressure = 6 Pa, Time=40 min, Frequency = 20 Hz RF power= 30 to 80 W]

A shift of 0.10 eV in the Ti 2p was observed with deposition of the TiO₂ nanoparticles at 60 min. The downshift of the Ti 2p is related to charge transfer between the TiO₂ and graphene due to the difference of work function. Due to the charge transfer from graphene to the TiO₂, the band of

the TiO₂ bend toward the interface reduced the binding energy of the Ti core level and the result is shown schematically in Fig 6.14.

The O 1s XPS spectra for the decorated graphene with TiO₂ nanoparticles at different times of deposition are presented in Fig 8.9 (a). The decorated graphene with TiO₂ nanoparticles was deconvoluted into three components. The deconvoluted components centered at the binding energy positions of 530.59, 532.09 and 533.54 eV were consigned to Ti-O, C-OH, and C-O bonds respectively. The shifts in the OI component of O s binding energies were observed after the deposition of TiO₂ onto graphene.

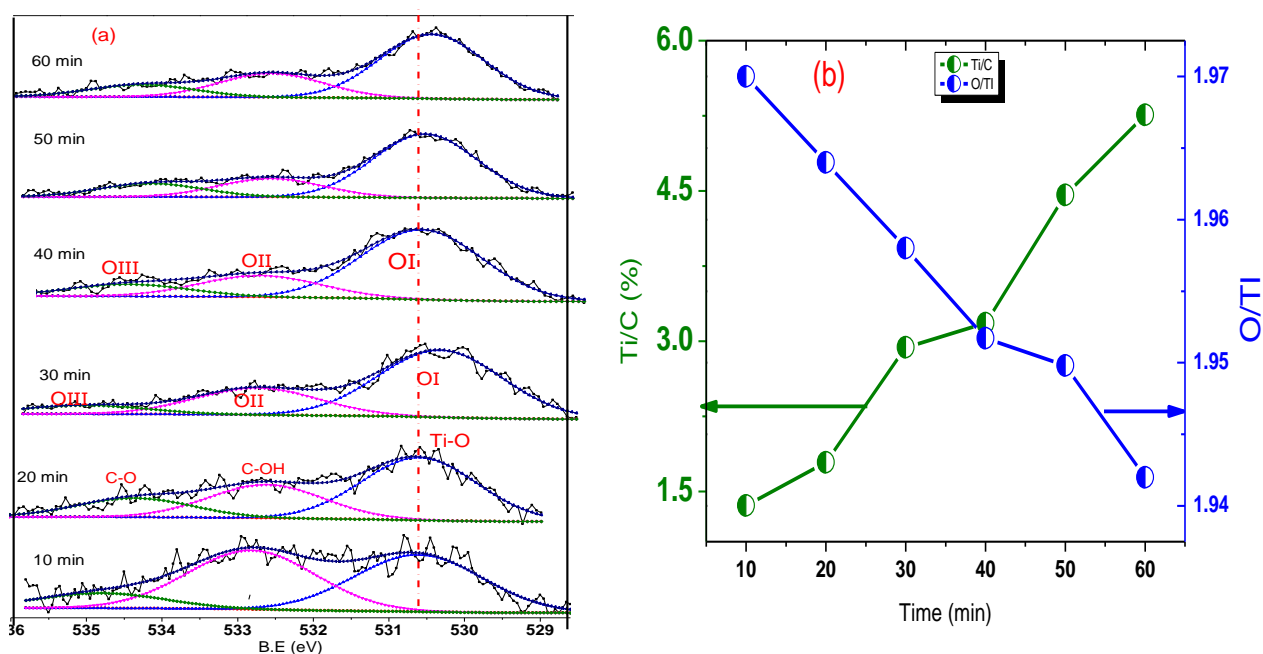


Fig 6. 9 (a) O 1s core peak of decorated graphene with TiO₂ nanoparticles at different time of deposition

(b) variations of Ti /C and OI/Ti atomic ratio as a function of different time of deposition

The downshift of the O 1s binding energies increased and reached 0.10 eV at 60 min of deposition of TiO₂ nanoparticles onto graphene. The shift in the O 1s core level is due to the charge transfer between the TiO₂ and graphene at the interface and reduced the binding energies

of the O core level. The band bending of the O 1s core level is further explained in the section 6.5.3

Additionally, OI/Ti ratio was evaluated for the decorated graphene with TiO₂ nanoparticles at different times of deposition and the results are illustrated in Fig 6.9 (b). It can be seen that the OI/Ti ratio is less than the ideal value of TiO₂ crystal, which suggest that the deposited TiO₂ nanoparticles onto graphene sheets are under stoichiometric Ti/C (sp²) atomic ratio were increased by stepping up the deposition times and reached in a ratio Ti/C sp² =5.26 atomic ratio (%) at 60 min of deposition.

6.4.2 Raman analysis of undoped graphene and TiO₂ doped graphene deposited with different times

Fig 6.10 (a) present the Raman spectra of the undecorated graphene and decorated graphene at different times of deposition. Four characteristic bands (G, D, 2D, and D+G) were observed for the undoped graphene located at 1324, 1585.45, 2637 and 2875 cm⁻¹ respectively. Additionally, the TiO₂ vibration modes were also observed with deposition of the TiO₂ nanoparticles onto graphene sheet. Four vibration modes for the decorated TiO₂ nanoparticles centered at 154, 394, 510 and 632 cm⁻¹ respectively. No vibration modes of TiO₂ were detected at low deposition time, which indicates that low amount of TiO₂, was deposited onto graphene sheets. By increasing the deposition time an intense peak at 151 cm⁻¹ and three other small vibration modes were observed in the Raman spectra, which are attributed to the E_g, B_{1g}, or A_{1g}, E_{1g} modes of the anatase phase of TiO₂, respectively [304]. Moreover, a small shift in the G and 2D band by 3 and 2 cm⁻¹ towards the high wavenumber were noticed at 10 min of deposition of TiO₂ nanoparticles onto graphene sheet as shown in Fig 6.10(a) (enlarged view). The shifts in the G and 2D bands increased with stepping up the deposition time. The shifts in G and 2D bands were further increased by 9.1 and

8.5 cm⁻¹, when the TiO₂ nanoparticles were deposited in a ratio Ti/C=5.26 atomic ratio (%) at 60 min of deposition as shown in Fig 6.10 (b).

It is explained in the literature that, the shift in the G and 2D peaks discriminated the type of doping either p-doping or n-doping [305]. Density functional theory revealed that the position of the 2D peak shifts toward the lower wavenumbers for the increasing electron concentration and shifts toward the higher wavenumber for increasing hole concentration [306].

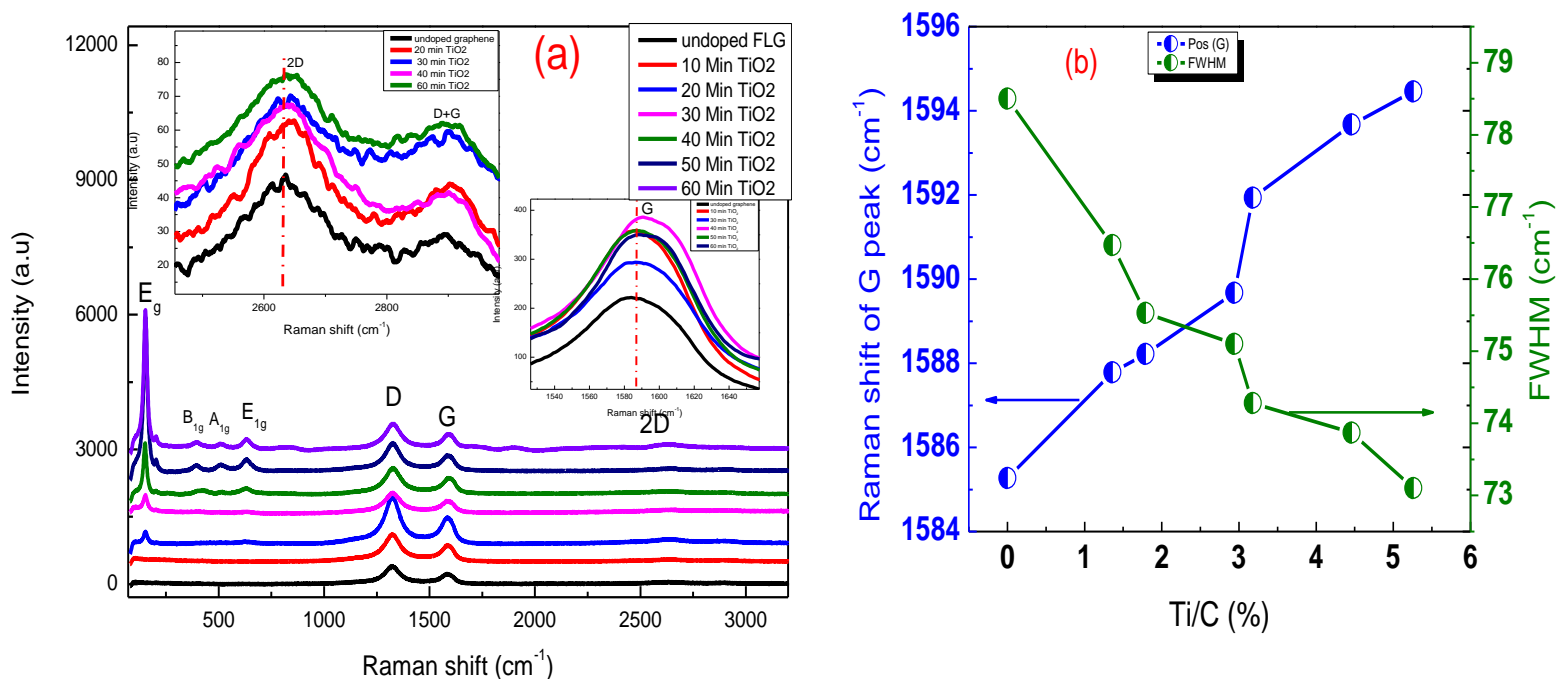


Fig 6. 10 (a) Raman spectra of undoped graphene and TiO₂ doped graphene at a different time of deposition

(b) positions of the G and FWHM (G) as a function of Ti/C at. %

Inset show the enlarged view of G and 2D bands.

In our case, with deposition of the TiO₂ nanoparticles onto graphene, the G and 2D peak were upshifted by 9.1 and 8.5 cm⁻¹ respectively. This upshifted of G and 2D indicates that graphene was p-doped with TiO₂ nanoparticles. This result is in good agreement with the XPS analysis.

The FWHM (G) of the undecorated graphene and decorated graphene with TiO₂ nanoparticles were evaluated using the Gaussian function line shape. The measured values of FWHM of G

peak as a function of Ti/C sp^2 atomic ratio are shown in Fig 6.10 (b). The FWHM of G peak decreased from 78.5 cm^{-1} to 73.1 cm^{-1} by the deposition of TiO₂ at 60 min in a ratio Ti/C=5.26 atomic ratio. (%). The reduction in the FWHM of the G peak is due to the doping. Pisani et al reported that, the Fermi level shifts from the Dirac point due to the doping in graphene and the excited charge carrier recombination probability were decreased. The reduction in the recombination of the excited charge also decreases the FWHM and sharpens the G peak [³⁰⁷].

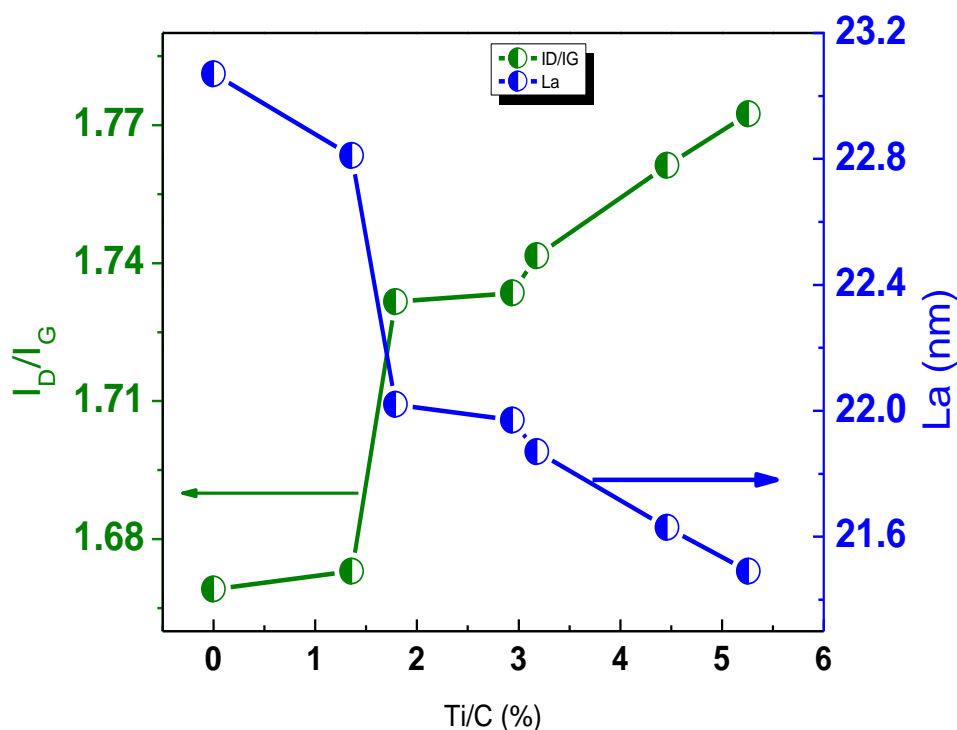


Fig 6. 11 Variation of G and D peak intensity ratio I_D/I_G and in plane crystallites size (L_a) plotted against the Ti/C atomic ratio(%)

The I_D/I_G ratio was used to measure the defects and disorders induced in the structure of graphene by the interaction of TiO₂ nanoparticles. The measured I_D/I_G ratio of undecorated graphene and decorated graphene with TiO₂ nanoparticles as a function of Ti/C (sp^2) are illustrated in Fig 6.11

The I_D/I_G ratio increased from 1.66 and reached to 1.77 when the TiO₂ nanoparticles were deposited onto graphene sheets in a ratio of Ti/C=5.26 at. %. This shows that the structural defects increased in graphene planes by increasing the TiO₂ concentrations.

The in-plane crystalline sizes of the decorated graphene with TiO₂ nanoparticles were calculated using equation [1]. The evaluated in-plane crystalline size as a function of Ti/C are presented in Fig 6.11. The in-plane crystallite size of graphene decreased from 23.1 to 21.49 nm with introduction of TiO₂ to graphene plane in a ratio Ti/C=5.26 at. %.

The more reasonable explanation for the reduction of the in-plane crystallite size of graphene after the interaction sputtered particles and plasma species could be shrinking of the sp² domain or may be the sp² domain of graphene is broken with increasing the amount of TiO₂ nanoparticles.

6.4.3 XRD analysis undoped graphene and TiO₂ doped graphene at different times deposition

Fig 6.12 (a) presents the XRD pattern of the undecorated graphene and decorated graphene with TiO₂ nanoparticles at different times of deposition. A broad and low-intensity peak of the (002) peak were observed at $2\theta = 25.11^\circ$ for the undoped graphene. For the decorated graphene with TiO₂ nanoparticles, the (002) peak shifted gradually to higher 2θ values by increasing the deposition time as shown in fig 6.12 (a) (enlarged view). The shift of the (002) toward the higher angles values suggests that the d-spacing between the sheet were decreased. The calculated d-spacing as a function of Ti/C (sp²) are depicted in Fig 6.12 (b). The d-spacing values decreased from 3.54 to 3.49 nm with deposition of the TiO₂ in a ratio Ti/C=5.26 at. %.

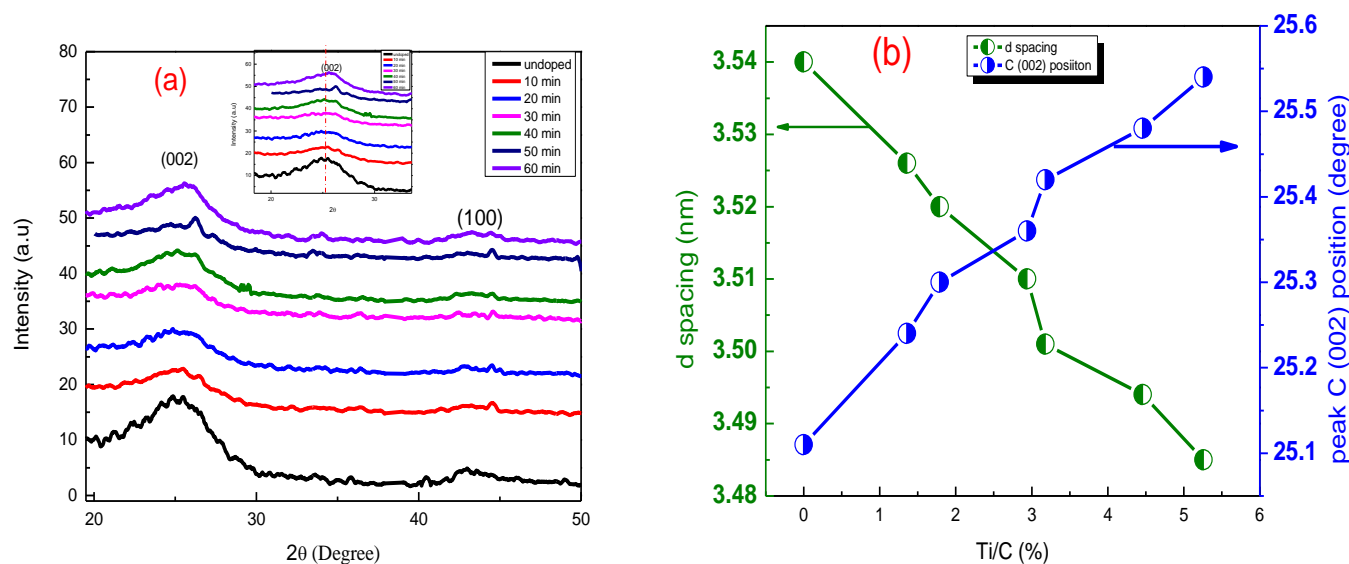


Fig 6. 12 (a) XRD patterns of undoped and TiO₂ doped graphene at different times of depositions (b) Variation of the 2θ angle position of the (002) and d-spacing as function of Ti/C at. %

Additionally, with rising of the TiO₂ concentration onto graphene the FWHM of the 002 peak of the graphene is becoming wider. The evaluated values of the FWHM of the (002) peak as a function of Ti/C (sp²) are presented in Fig 6.13. The FWHM of the 002 peak increased by raising the Ti/C (sp²) atomic ratio (%). This suggests that the structural defects increased with rising of TiO₂ concentration. The crystalline thicknesses of undecorated graphene and decorated graphene with TiO₂ nanoparticles were calculated using the Scherer equation and the values are illustrated in Fig 6.13. The reduction of the crystalline thickness of the graphene after the deposition of TiO₂ nanoparticles indicates that the stacking orders of the graphene sheets were decreased. Our graphene flakes contain very few layers of graphene. The stacking orders of the layers are very poor due to widening of the (002) peak. When the TiO₂ nanoparticles were deposited onto the graphene sheets, the interlayer separation between the graphene sheets decreased. Therefore it influences the staking order of the graphene sheets.

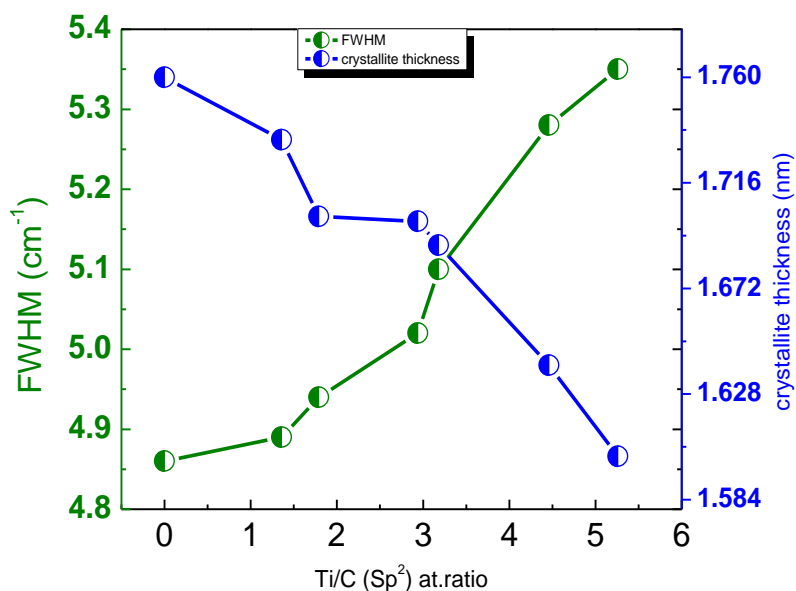


Fig 6. 13 Variation in the FWHM of the (002) peak and crystallite thickness as function of Ti/C atomic ratio

6.5 The influence of TiO₂ nanoparticles on the structure and chemical properties of graphene powder via given different vibration frequencies

In the above two section (6.3, 6.4), the TiO₂ nanoparticles were deposited onto graphene at low powder vibration frequency (20 Hz). It was found from the TEM micrographs that, by deposition of TiO₂ nanoparticles with low powder vibration frequencies the sputtered particles were aggregated onto graphene sheets. The main objective of this work is to decorate the graphene sheets with well dispersed TiO₂ nanoparticles. TiO₂ nanoparticles were deposited onto graphene sheet with variations of the powder vibration frequencies discussed in this section. The influence of the interaction of TiO₂ nanoparticle with vibrating graphene powder was characterized by various techniques. In term of structural study the Raman and XRD were used and the chemical composition was studied by XPS technique. Moreover the process parameters are presented in table 6.3.

Table 6.3 the process condition of decorated graphene with TiO₂ nanoparticles

Sample #	RF Power (W)	Process pressure (Pa)	Deposition Time (min)	Powder vibration frequency (Hz)
1	40	6	60	0
2	40	6	60	20
3	40	6	60	40
4	40	6	60	60
5	40	6	60	80
6	40	6	60	100

6.5.1 XPS analysis undoped graphene and TiO₂ doped graphene deposited at different powder vibration frequencies

Fig 6.15 presents the XPS spectra of the undecorated graphene and decorated graphene at different powder vibration frequencies. The high resolution C 1s XPS spectra of the undecorated graphene and decorated graphene with TiO₂ nanoparticles at different powder vibration frequencies are described in Fig 6.15 (a). The C 1s core level is considerably changed with the deposition of TiO₂ onto graphene powder at different powder vibration frequencies. Before the deposition the C 1s core level main peak C-C (sp²) was located at 284.45 eV. But upon the deposition at 0 Hz vibration the C 1s core level was shifted to lower binding energy position to 284.40 eV. The downshift in the C 1s core level increased with variation of the powder vibration frequencies. The maximum downshift of 0.12 eV in the C 1s core level was observed at 100 Hz powder vibration frequencies. Recently several approaches were reported concerning about the doping of graphene. Generally, when graphene is contacted with high work function material like, TiO₂, MoO₃ and WO₃ charge is expected to transfer at the interface due to the work function differences. The charge transfer phenomenon at the interface between the graphene and metal oxide (hfO₂, MoO₃) has been explained by Jens Mayer et al¹⁰⁰]. Simon Sanders et al is

also explained the same phenomenon. He described that shifts in the Fermi level of graphene from its Dirac point due to the charge transfer between the interface of metal oxide and graphene^[308]. The downshift of the C 1s core level from its Dirac position is presented schematically in Fig 6.14. The downshift of the Fermi level from its Dirac point is due to the p doping and opposite for the n doped graphene. Upon the deposition of TiO₂ nanoparticles onto graphene powder the C 1s core level shift toward the lower binding energy values and the downshift of the C 1s core level increased with rising of TiO₂ concentration. The downshift of the C 1s core level of graphene after the deposition of TiO₂ nanoparticles is indication of p-doping of graphene.

The high resolution XPS spectra of the Ti 2p for the decorated graphene with TiO₂ nanoparticles at different powder vibration frequencies are presented in Fig 6.15 (b). For the decorated graphene with TiO₂ nanoparticles two prominent peaks were observed, which are located at 459.08 eV and 464.93 eV respectively. The spin-orbit split of the photoelectron for the decorated graphene with TiO₂ nanoparticles is represented to the Ti 2p_{3/2} and Ti 2p_{1/2} peaks. The separation between the Ti 2p_{3/2} and Ti 2p_{1/2} is 5.87 eV, which indicates that the presence of the normal state of Ti⁺⁴ and is consistent with reported data ^[309]. Addition to this shifts in the Ti 2p was observed toward the lower binding energies values. A downshift in the Ti 2p core levels were noted upon deposition of the TiO₂ nanoparticles onto graphene sheets and the maximum downshift of 0.16 eV was obtained, when the TiO₂ nanoparticles were deposited onto graphene at 100 Hz powder vibration frequencies. The downshift of the Ti 2p core level can be explained as follows, as described in the above text. When graphene contacted with TiO₂ electrons are transferred from graphene to the TiO₂ due to the large work function of the TiO₂. This demonstrates that the electrons are lost in the graphene side produces positive space charge close

to the interface (space charge region) and the accumulation of the electrons in the TiO₂ induce negatively charged surface. This effectively generates an electric field between the graphene and TiO₂ at the interface.

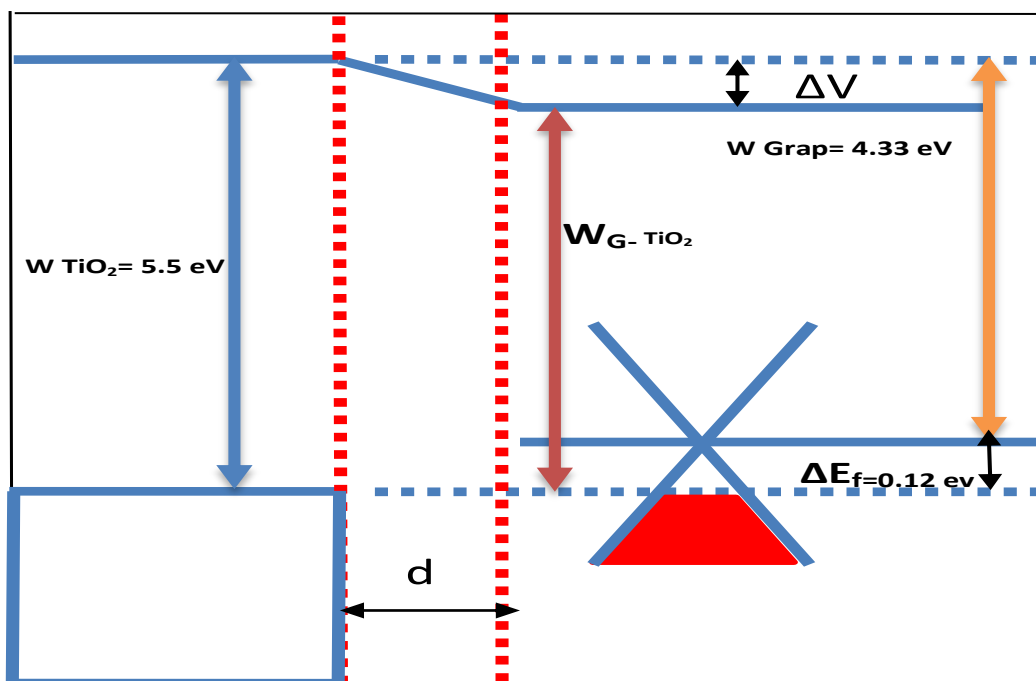


Fig 6.14 Band alignment of the graphene and TiO₂ nanoparticles

The generated electric field in the space charge region of the contacted material leads to the distortion of the electronic band of graphene and TiO₂ close to the interface and the band bending occurred at the interface. As the work function of the TiO₂ (5.50 eV) is larger than graphene (4.33 eV), the electrons are transferred from the graphene to the TiO₂ nanoparticles and the bands of the TiO₂ bend downwardly towards the interface with the formation of an accumulation layer in the TiO₂. However when the graphene is contacted with low work function metal oxide, then the electrons is transferred from the metal oxide to graphene and the band of the metal oxide bends upwardly. A similar phenomenon has been reported recently by Yongqing Cai. et al [³¹⁰].

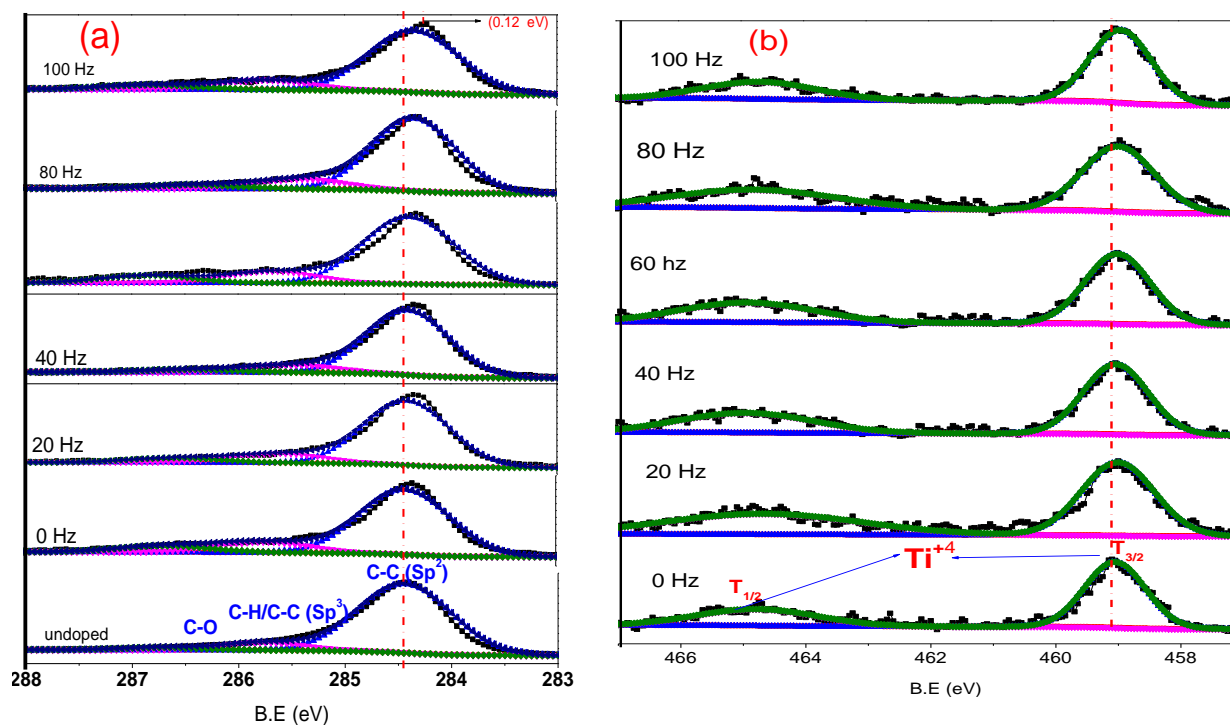


Fig 6.15 (a) XPS spectra of graphene powder and deposited TiO₂ nanoparticles at different powder vibration frequencies (a Shift in the C 1s core levels position and the shift of this position upon TiO₂ deposition. (b) Ti 2p core level spectra [Process pressure = 6 Pa, Time=60 min, powder vibration frequency = [0 to 100 Hz] RF power= 40 W]

Fig 6.16 (a) shows the high-resolution XPS spectra of the O 1s core levels for the decorated graphene with TiO₂ nanoparticles at different powder vibration frequencies. Again the O 1s core level was de-convoluted into three components centered at the binding energy positions of 530.59, 532.09 and 533.54 eV were assigned to Ti-O, C-OH, and C-O bonds respectively. Chemical shifts in the O 1s core level were observed with increasing the powder vibration frequencies. The O 1s core levels were downshifted from 530.59 eV to 530.46 eV when the graphene flakes were decorated with TiO₂ nanoparticles at 100 Hz powder vibration frequencies. This indicates that by the increasing concentration of TiO₂ nanoparticles onto the graphene sheet through powder vibration frequencies, the chemical interaction between the TiO₂ nanoparticles

and graphene increased and variation of the binding energies of the O 1s peak were observed. Due to the surface charge transfer from graphene to TiO₂ reduced the binding energies of the chemical components of the O 1s core level.

Moreover, the OI/Ti is important parameters to evaluate that the deposited TiO₂ nanoparticles are oxygen deficient or not. Measured OI/Ti ratios for the decorated graphene with TiO₂ nanoparticles at different powder vibration frequencies are shown in Fig 6.16 (b). The calculated value of the OI/Ti ratio indicates that, the deposited TiO₂ nanoparticles are under stoichiometric.

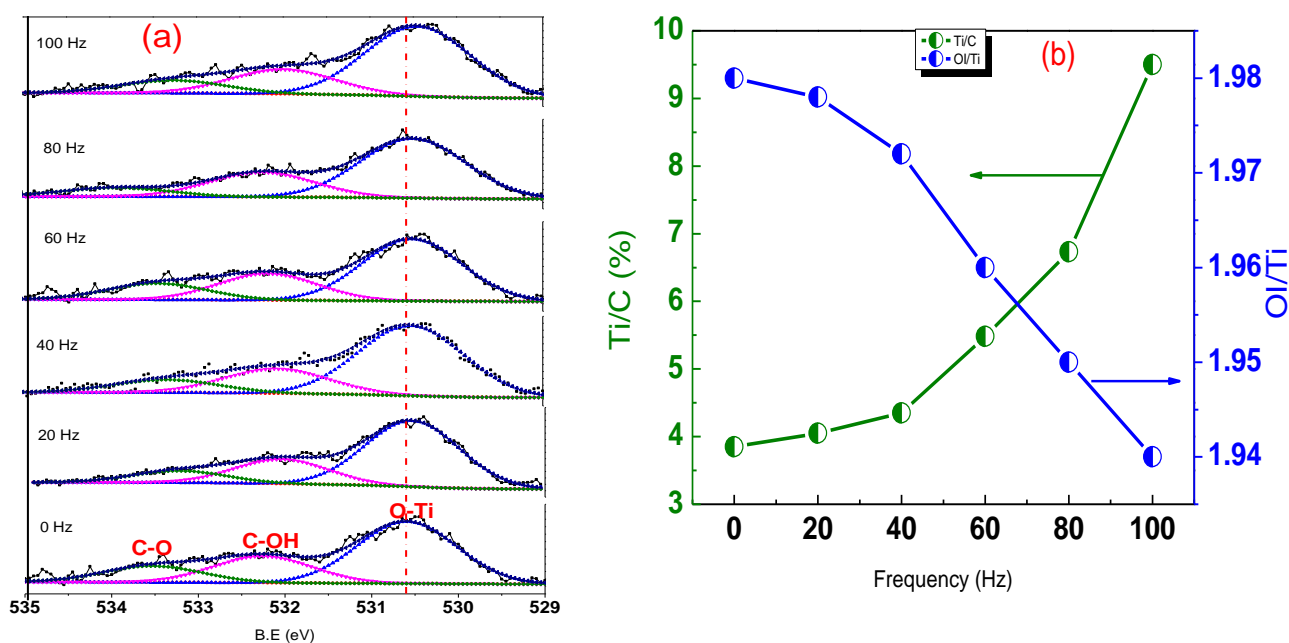


Fig 6. 16(a) O 1s core peak of decorated graphene nanoparticles at different powder vibration frequencies

(b) variations of Ti /C and OI/Ti atomic ratio as a with TiO₂ function at different powder vibration frequencies

Fig 6.15 (a) demonstrates that by the variation of the powder vibration frequencies more TiO₂ nanoparticles were deposited onto graphene sheet compared to the without moving graphene powder. For the without moving graphene powder the obtained Ti/C = 3.86 at. % and reached to Ti/C = 9.46 at. % when the graphene powder vibrated at 100 Hz. It is explained already in

chapter 5 , that by the variation of the powder vibration more sputtered particles are line of sight to the graphene flakes compared to the without moving graphene powder.

6.5.2 XRD analysis undoped graphene and TiO₂ doped graphene deposited at different powder vibration frequencies.

Fig 6.17 (a) depicts the XRD pattern of the undoped graphene and decorated graphene with TiO₂ nanoparticles at different powder vibration frequencies. The FWHM and position of the (002) of graphene were drastically changed by the deposition of TiO₂ nanoparticles at different powder vibration frequencies. Low intensity and broad peak of (002) peak suggest that graphene consists of very few layers of graphene (3 to 5 layers).

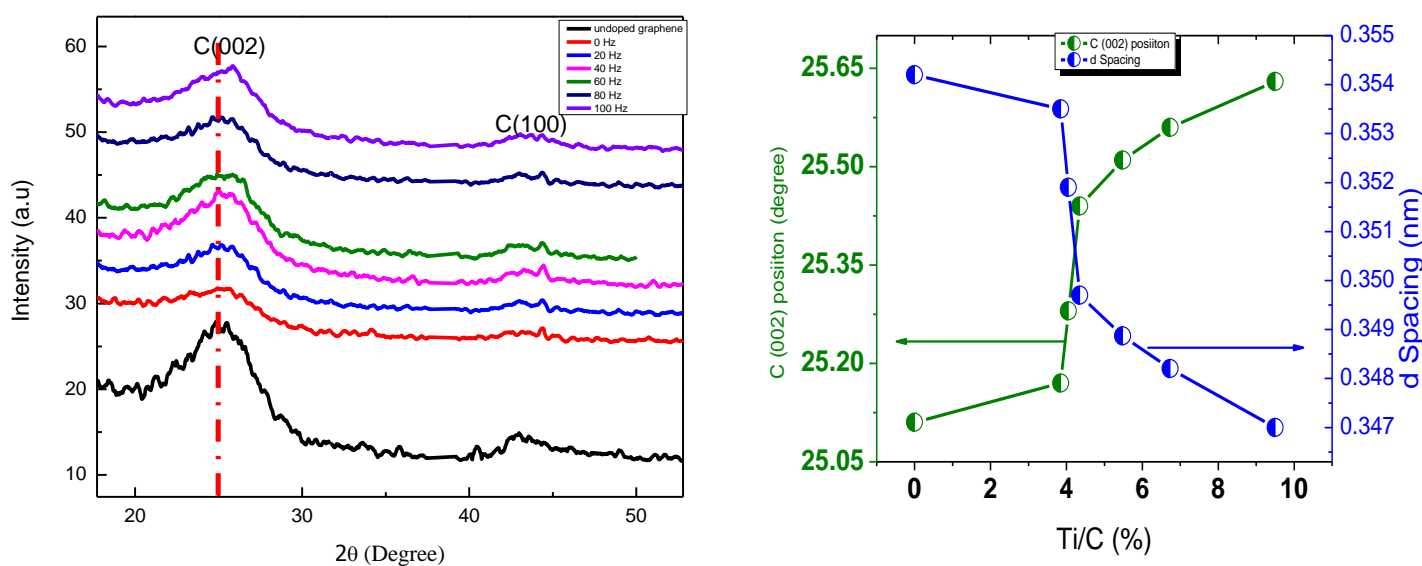


Fig 6. 17 (a) XRD patterns of undoped and TiO₂ doped graphene at different powder vibration frequencies of the (002) and (b) Variation of the 2θ angle position and d-spacing as function of Ti/C at.%

The (002) peak of the graphene shifted to higher 2θ values with deposition of TiO₂ nanoparticles at different powder vibration frequencies. This suggests that by interaction of graphene with TiO₂ nanoparticles the d-spacing of the graphene were reduced. The evaluated d-spacing as a function of the Ti/C (sp²) obtained by the variation of the powder vibration are presented in Fig

6.17 (b). The d-spacing decreased from 0.354 to 0.347 nm with obtained (Ti/C sp²= 9.45 at. %) onto graphene powder at 100 Hz powder vibration frequency. This demonstrates that the lattice of the graphene is contracted with the interaction of the TiO₂ nanoparticles. Additionally, with variation of the TiO₂ concentration onto graphene powder the FWHM of the graphene became wider. The FWHM of graphene and deposited TiO₂ nanoparticles onto graphene powder at different powder vibration frequencies as a function of Ti/C (sp²) is displayed in Fig 6.18.

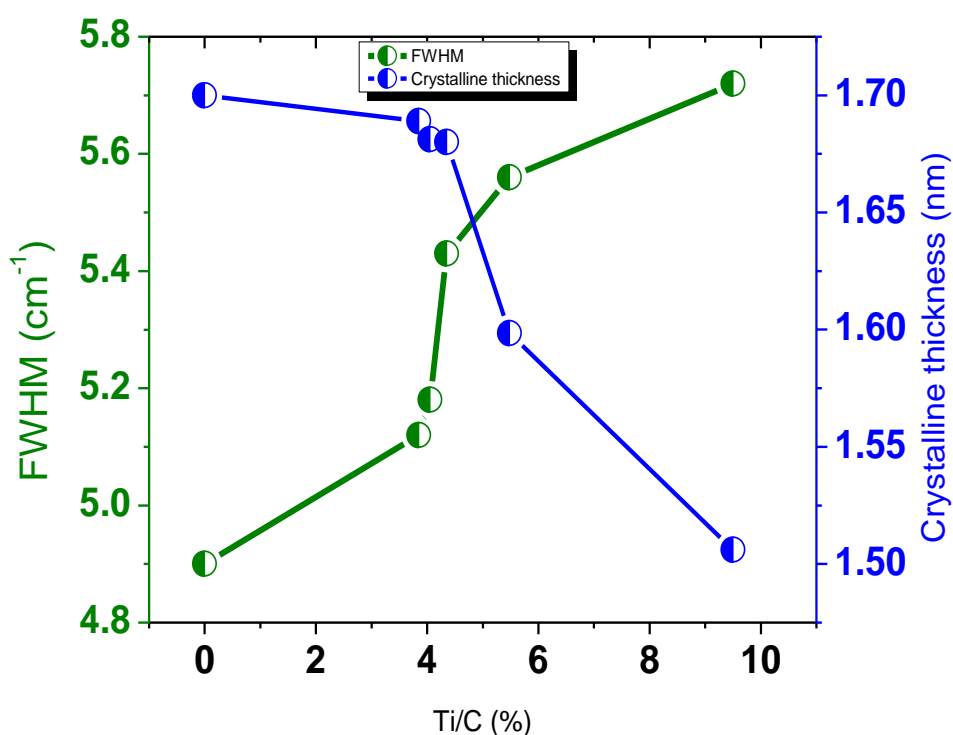


Fig 6. 18 Variation in the FWHM of the (002) peak and crystallite thickness as function of Ti/C at.%

This indicates the planes of the graphene were distorted with deposition of the TiO₂ nanoparticles. The distortion increased with increasing the TiO₂ concentration to the graphene plane. The crystalline thickness of the undecorated graphene and decorated graphene was calculated by Scherer equation and found that the crystalline thickness decreased from 1.7 to 1.5 nm with introduction of the TiO₂ nanoparticles in a ratio Ti/C sp² =9.45 at. % the results are

presented in Fig 6.17. The reduction of the crystalline thickness as a function of Ti/C suggests that with the interaction of the graphene with TiO₂ nanoparticles the stacking order is reduced or may be due to the shrinking of planes graphene with the interaction of TiO₂ nanoparticles.

6.5.3 Raman analysis undoped graphene and TiO₂ doped graphene deposited at different powder vibration frequencies

The Raman spectra of the undecorated graphene and decorated graphene at different powder vibration frequencies are illustrated in Fig 6.19 (a). Four characteristic bands of the graphene attributed to D, G 2D and D+G peaks were observed in all the Raman spectra. For the decorated graphene with TiO₂ nanoparticles four addition bands were also observed in the Raman spectra. The main and strongest mode of the anatase phase centered at 151 cm⁻¹, which attributed to the stretching vibration mode of *Ti-O* bonds. The other three low intensity modes centered at positions 393 cm⁻¹, 513 cm⁻¹ and 632 cm⁻¹, which correspond to the B_{1g}, A_{1g} and E_{1g} modes.

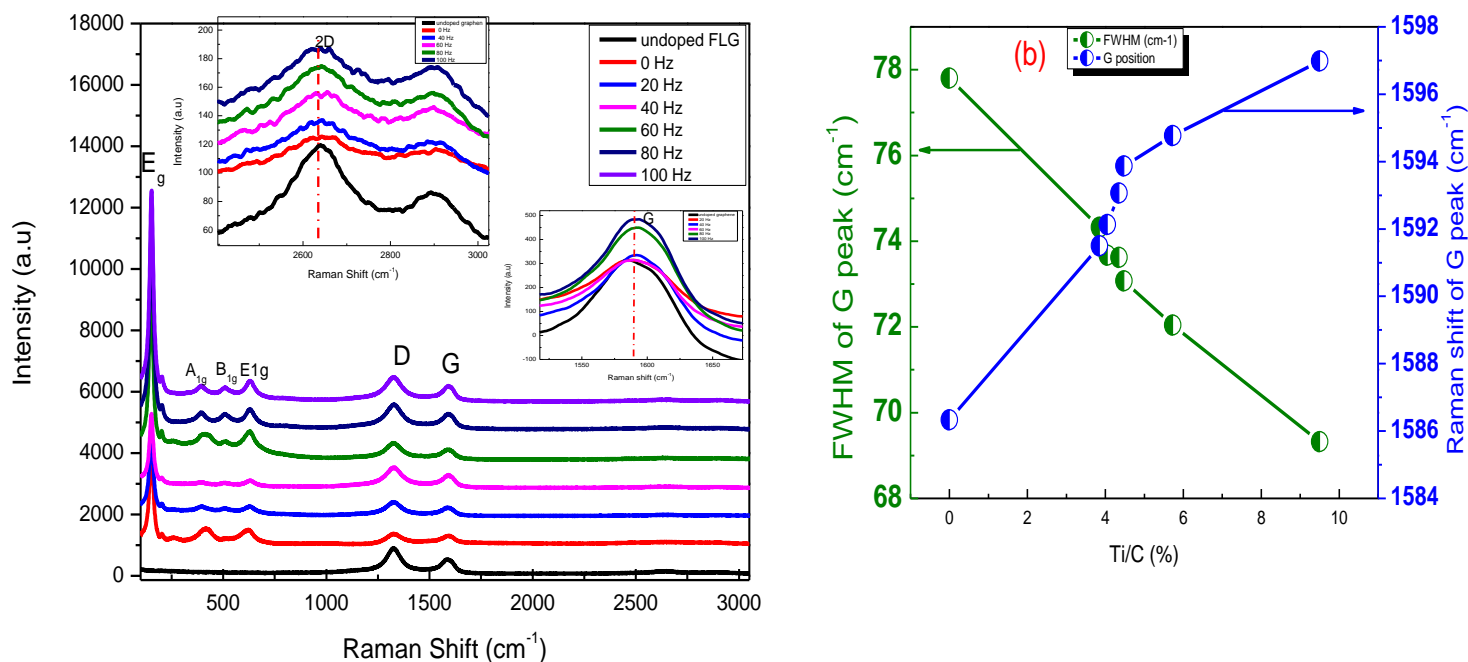


Fig 6. 19 (a) Raman spectra of undoped graphene and

(b) positions of the G and FWHM (G) as a function TiO₂

doped graphene at different powder vibration frequencies of Ti/C at. %

By the deposition of TiO₂ nanoparticles onto graphene sheet at different powder vibration frequencies strongly affected the FWHM, position and intensities of graphene bands. The G and 2D position of graphene is shifted to higher wavenumbers by 4 and 3 cm⁻¹ with deposition of TiO₂ nanoparticles onto graphene powder without moving graphene powder (0 Hz). G and 2D bands were further shifted to higher wavenumbers by increasing the TiO₂ concentrations onto graphene with a variation of powder vibration frequencies. The maximum upshift in G and 2D are 10.65 cm⁻¹ and 9.12 cm⁻¹ observed when the TiO₂ nanoparticles were deposited in a ratio of Ti/C sp²=9.45 at. % at 100 Hz powder vibration frequency and the results are presented in Fig 6.18 (a) (enlarged view). It is well established that doping of graphene changed the position of the G and 2D bands explained by Das et al [311]. Compressive strain and tensile strain has also changed the position of the graphene bands. Our XRD results show that by the deposition of the TiO₂ nanoparticle onto graphene sheet compressive strain is developed in the lattice of graphene. But in the case of compressive strain, the shift in the 2D band is greater than of shift in G band. Casiraghi et al. also reported that the shift in G and 2D bands toward higher frequencies is caused by the compressive strain, if the shift in the 2D band is larger than the shift in G band [312]. But in case of doping of graphene the shift in 2D band is not bigger than that of shift in the G bands. Addition to this, in case of doping the FWHM of the G peak also becomes narrower with the increasing the dopant concentration explained by Namphung Peimyoo et al [312]. In our case the G and 2D bands of the graphene were shifted to higher wavenumbers upon deposition of the TiO₂ nanoparticles and also the FWHM of the G peak became narrower as shown in Fig 6.19 (b), which suggests that the doping phenomena is dominated over the compressive strain. Therefore, the shift in the G and 2D toward the higher wavenumber is caused by p doping graphene with deposition of the TiO₂ nanoparticles. The degree of disorderness and defects

introduced in the structure of graphene with the deposition of TiO₂ nanoparticles were evaluated by using the I_D/I_G ratio. It is shown in Fig 6.20 (a) that by the deposition of TiO₂ nanoparticles at different powder vibration frequencies the intensity of defects peak (D) enhanced. This indicates that the structural defects increased with increasing interaction of graphene with TiO₂ nanoparticles. The I_D/I_G ratio for the decorated graphene with TiO₂ nanoparticles as a function of Ti/C (sp²) are presented in Fig 6.19. The I_D/I_G ratio increased from 1.66 and reached a value of 1.76 with deposition of TiO₂ nanoparticles at 100 Hz powder vibration frequency with a ratio of Ti/C sp²=9.45 at. %.

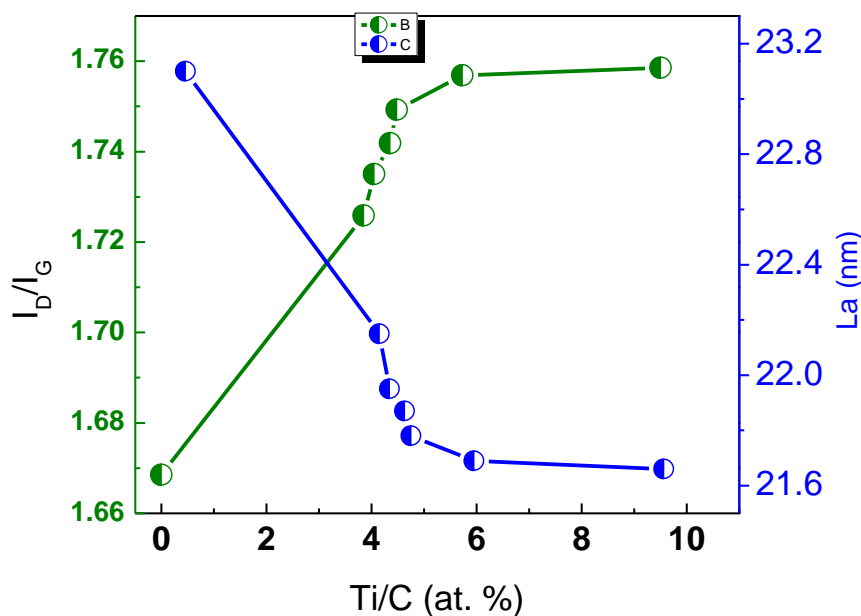


Fig 6. 20 Variation of G and D ratios I_D/I_G and in plane crystallites size (La) plotted against the Ti/C.at (%)

Moreover, the in-plane crystal size La was measured for the undecorated graphene and decorated graphene at different powder vibration frequencies by using equation [1]. The in-plane crystallite size as a function of Ti/C (sp²) is shown in Fig 6.20. It shows that the in plane crystallite sizes decreased from the 23.1 nm to 21.6 nm, when the TiO₂ nanoparticles were introduced in a ratio of Ti/C sp²=9.45 at. %. The more probable reason of the reduction of crystallite size could be

sp² domain breaking or shrinking of the sp² domain size with deposition of the TiO₂ nanoparticles.

6.6 Concluding Remarks

In this chapter of thesis, the interaction of the graphene with TiO₂ nanoparticles were studied in detailed. Three deposition parameters were used to decorate the graphene powder with small and dispersed nanoparticles. The structural analysis of the decorated graphene with TiO₂ nanoparticles were investigated by XRD and Raman. The XPS analysis was used to study the chemical state and composition of the decorated graphene with TiO₂ nanoparticles. The particle nature of the deposited TiO₂ was confirmed by TEM examination. The following conclusions can be driven,

A. Structural analysis of the decorated graphene with TiO₂ nanoparticles (XRD)

- ❖ The lattice of graphene was distorted with decoration of the TiO₂ nanoparticles
- ❖ The spacing between the layers of graphene decreased by interaction of TiO₂ nanoparticles
- ❖ No diffraction peaks of TiO₂ were observed in the XRD patterns.
- ❖ The crystallite thickness of graphene flakes decreased with deposition of the TiO₂ nanoparticles
- ❖ The G and 2D bands of graphene were shifted to higher wavenumber with increasing TiO₂ concentration onto graphene sheet confirming the p doped graphene with TiO₂ nanoparticles.
- ❖ The structural defects and disorders increased by increasing the TiO₂ concentration to the plane graphene.
- ❖ The FWHM of G peak decreased linearly with increasing the doping concentrations in term of Ti/C sp² atomic ratio.

- ❖ The in-plane crystallite size (L_a) of graphene decreased upon the deposition of TiO₂ nanoparticles

B. From the XPS analysis:

- ❖ The C 1s core level of the graphene were shifted to the lower binding energies values upon the deposition of the TiO₂ nanoparticles and downshift of the C 1s core level increased with rising of TiO₂ amount. The downshift of the C 1s core level indicates a charge transfer from graphene to TiO₂ nanoparticles due to the larger work function of TiO₂ relatively to that of graphene.
- ❖ Ti/C at. % ratio increased by increasing the powder vibration frequencies.
- ❖ Similar downshift in the Ti 2p and O 1s core level like C 1s core level were also observed upon raising the TiO₂ concentration.

The interaction of the graphene sheets with TiO₂ nanoparticles were presented in this chapter. The exploration of decorated graphene sheets with M and MO nanostructures applications will be presented in next chapter#7.

Chapter # 7

Exploration of decorated graphene with metal and metal oxide nanostructures applications

7.1 Introduction

The main goal of this chapter is to study enhancement properties of the graphene with deposition of M and MO nanoparticles. It is already discussed that graphene have numerous properties and display some other novel properties, when the graphene surface is modified with M and MO nanostructures, such as with addition of the foreign atoms which is a promising approach to modify the electronic structures, catalytic activity and magnetic behavior. In this chapter, three different kinds of applications were studied for the decorated graphene sheets with TiO₂, Mg and Nb₂O₅ nanoparticles. The ferromagnetic behavior of the graphene and modified graphene with MO nanoparticles (Fe₃O₄, ZnFe₂O₄, CoFe₂O₄, and Co) already has been reported [³¹³,³¹⁴]. The ferromagnetic behavior of graphene decorated with the Nb₂O₅ nanoparticles is not reported till now. The TiO₂ and graphene composite was extensively studied for the improvement of the photocatalytic activity. The photocatalytic activity of the decoration graphene with TiO₂ nanoparticles by RF sputtering technique is not reported in literature. The well dispersed Mg nanoparticles onto graphene shows good catalytic activity towards the hydrogen storage. It is reported that when the small Mg nanoparticles dispersed onto graphene sheet, the hydrogen storage capacity was enhanced at low temperature. Well dispersed Mg nanoparticles were deposited onto graphene sheets by RF sputtering. The hydrogen sorption test was carried out for the decorated graphene with Mg nanoparticles.

7.2 Magnetic properties of undecorated graphene and decorated graphene with Nb₂O₅ nanoparticles

The magnetic property was measured using vibrating sample magnetometer with PPMS (Dyna Cool) with collaboration of Department of Physics, Federal University of Rio Grande do Norte, Natal, RN, Brazil. The samples were analyzed by Prof M. A. Correa. The following deposition parameters were varied during the deposition. The graphene powders were decorated with Nb₂O₅ nanoparticles at different times of deposition (8 to 32 min). The Nb₂O₅ nanoparticles were deposited onto graphene surface without moving powder. The RF power and process pressure values were kept constant at 6 Pa and 40 W respectively. Moreover, with the decoration of Nb₂O₅ nanoparticles on the graphene sheet the defects were pronounced, which has been proved above from Raman and XRD studies. Now we have to proceed to study the magnetic properties of the undoped graphene and Nb₂O₅ decorated graphene. The ferromagnetic behavior was observed in our samples due to defect induced in graphene by the deposition of Nb₂O₅ nanoparticles. Fig 7.1 (a) illustrates the magnetic hysteresis (M-H) loops of the undecorated graphene and decorated graphene with Nb₂O₅ nanoparticles, which suggest that graphene composite with Nb₂O₅ nanoparticles demonstrated the ferromagnetic property at low temperature range. The ferromagnetic behavior with hysteretic curves are displayed for the all the analyzed samples as a function of Nb/C (sp²) atomic ratio (%) at high external magnetic field range for low temperature 5 K. The ferromagnetic behavior of the undoped graphene powder is probably due to the structural defects. This is confirmed from Raman spectroscopy which shows that ratio of I_D/I_G is greater than 1^[315]. Pisani et al is also described that the graphene shows ferromagnetic behavior due to structural defects ^[232]. It is well proved that structural defects play the main role in the ferromagnetism. It was observed that the saturation magnetization (M_s)

values at 5 K for the undoped graphene and 0.49, 0.62 and 0.75 at. % Nb doped graphene are 0.12, 0.38, 0.22 and 0.18 emu/g, respectively. For the undoped graphene flakes very low magnetic moment was observed. Similar results are also reported in the literature [316]. However, the ferromagnetic behavior of graphene increased from 0.12 emu/g to reach 0.38 emu/g, when a small amount of Nb₂O₅ nanoparticles were deposited onto graphene with a ratio Nb/C sp² = 0.67 at. %. On the other hand, the magnetic moment values decreased, when the Nb₂O₅ nanoparticles were deposited onto graphene in a ratio between Nb/C sp² between 1.05 and 1.31 at. (%). These phenomena can be explained by the fact that magnetic behaviors of the nanoparticles are strongly dependent on the shape, imperfection and size [317]. The magnetic property size dependence was described by two hitherto established phenomena.

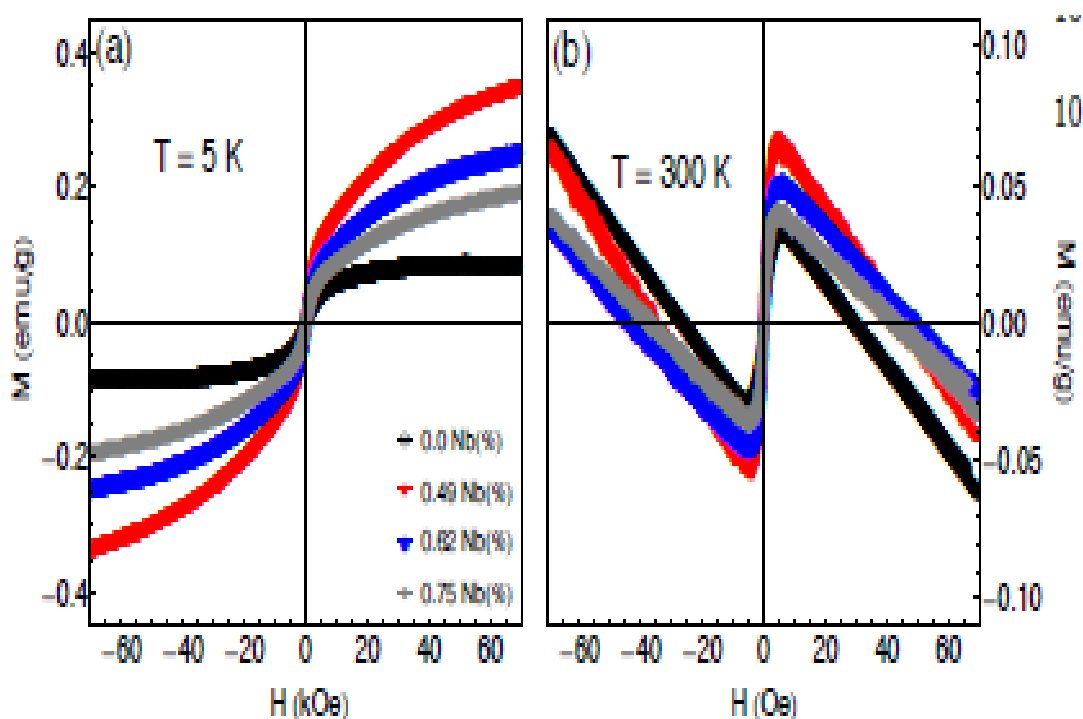


Fig 7. 1 (a, b) M-H curves for undoped graphene and with various Nb doping concentration measured at (a) 5 K and (b) 300 K

Firstly, the decorated nanoparticles on the surface of graphene can undergo coalescence to form 2D planer structure similar to a sheet when the particles size is very small, the size of nanoparticles would be in the range of 1 to 3 nm^[318]. In this context, the magnetic behavior and anisotropy was reported to originate from electronic delocalization and symmetry breaking. ^[319]. Second, when graphene was decorated with large size nanoparticles and these particles made aggregation on the graphene sheet, the particles onto graphene sheet made 3D mass structure and in this case the magnetization values depend on the surface to volume ratio^[233]. In our case, from the TEM images it can be seen (Fig 4.7 in chapter # 4) that the size of deposited Nb₂O₅ nanoparticles onto graphene sheet is larger than that of described in first case and these nanoparticles is made 3D mass structure onto graphene sheet, then magnetic anisotropy generates perpendicular to the surface plane of particles. Consequently the behavior of our deposited Nb₂O₅ nanoparticles onto graphene sheet resembles the second type of behavior. The rapid increase in magnetic moment after deposition of Nb₂O₅ nanoparticles onto graphene in a ratio Nb/C sp² = 0.67 at. %, can suggest that more nanoparticles linearly coupled with applied magnetic field increasing the magnetization behavior. However, the decoration of graphene with Nb₂O₅ nanoparticles in a high Nb/C sp² ratio values between 1.05 and 1.31 at. (%), the random dipole coupling between nanoparticles was observed due to the agglomerated and concentrated nanoparticles. Even in well dispersed Nb₂O₅ nanoparticles in a ratio Nb/C sp² = 1.31 at. % demagnetizations effects were observed from the coupling of the random dipole. To address this point, as reported in the literature, the hysteresis width for the non-interacting single domains only depends on the internal structure of the particles ^[320]. This case is comparable to our deposited Nb₂O₅ nanoparticles onto graphene sheet. The isotropic interaction between Nb₂O₅ nanoparticles, such as in concentrated or agglomerated nanoparticles on the graphene surface,

cause a reduction in coercivity by decreasing the barrier for the magnetization reversal [³²¹]. Fig 7.1 (b) depicts the M-H curve as a function of the Nb₂O_{5-x} concentration at 300 K. The diamagnetism behavior was observed in long range of magnetic field for undecorated graphene and decorated graphene with different Nb₂O_{5-x} concentrations at 300 K. Again the undecorated graphene flakes illustrate the low diamagnetism behavior at high temperature with respect to the decorated graphene with Nb₂O₅ nanoparticles. The high diamagnetism value was observed for the decorated graphene with Nb₂O₅ nanoparticles in a ratio Nb/C sp² = 0.67 at. %. It was observed that the saturation magnetization (M_s) values at 300 K for undecorated graphene and decorated graphene with Nb₂O₅ nanoparticles in ratio of Nb/C sp² = 0.67, 1.05 and 1.31 at. (%) were 0.03, 0.06, 0.05 and 0.04 emu/g respectively. The diamagnetic behavior of the decorated graphene with high Nb/C sp² ratio decreased. The reduction of the diamagnetic behavior will be explained latter.

Furthermore magnetization measurements were carried out in magnetic field range -70 <K Oe < +70 for temperature in the range 5 ≤ T < 300 K irrespective of Nb concentrations shown in Fig. 7.2. The magnetic hysteresis (M-H) curve at a temperature range 5 ≤ T < 300 K for undecorated graphene and decorated graphene with Nb/C sp² atomic ratio in the range {0.62 - 1.31} indicates the two different regions of magnetism. The diamagnetism behavior was observed for the undecorated graphene and decorated graphene with Nb₂O₅ nanoparticles at high temperature range, from 50 to 300 K, while for low temperature noticeable ferromagnetism appeared at temperature range between 5 and 10 K. We obtained a good convergence with our experimental data for the temperature approximately > 50 K which correspond to the region where the ferromagnetism behavior occurred. The diamagnetic contribution emerged for samples at temperature range 50 K < T < 300 K. It is clear, that at high temperature thermal disordering

counteracts the magnetic field. This phenomenon can be explained as follow, it is discussed in the above text that energy of magnetic particles is proportional to the particles size, volume and number of the magnetic molecules in a single magnetic domain under an external field. The thermal fluctuation reduces the total magnetic moment of the applied external field, when the energy of the magnetic particles becomes comparable to the thermal energy [³²²].

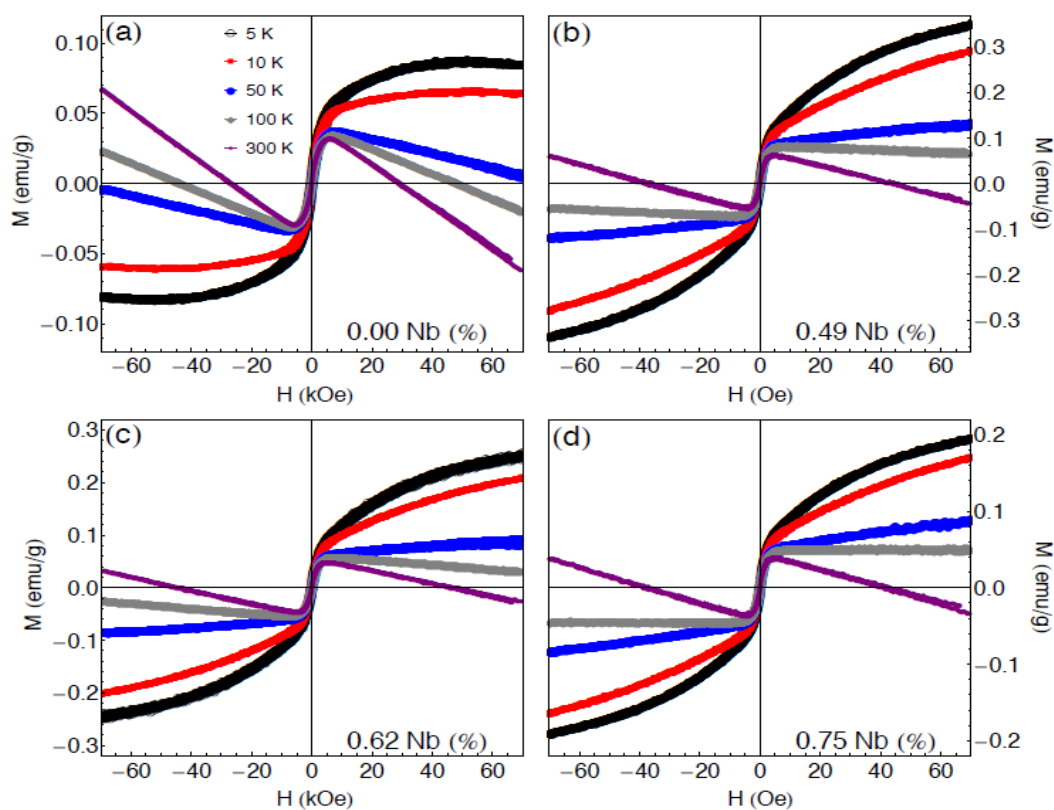


Fig 7. 2 Magnetization curves as a function of the applied temperature $5 \leq T < 300 \text{K}$ for each sample, for all Nb (%) concentration. (a) Magnetization curves for undoped graphene flakes (b) for doped graphene with 0.49 Nb (%) concentration. (c) For doped graphene with 0.62 Nb (%) concentrations. (d) For doped graphene with 0.75 Nb (%) concentrations.

Fig 7.3 depicts the maximum magnetization as a function of the temperature and the coercive field as a function of the Nb concentration. In the first case in Fig. 7.3 (a), a decrease of the magnetic moment with the increase of the temperature is noticed, irrespective of Nb

concentration. At the same time as already discussed, the high magnetic moment was observed for the decorated graphene with Nb_2O_5 nanoparticles with an atomic ratio Nb/C $sp^2 = 0.67$ in the temperature range between 5 and 10 K. On the other hand, the undoped graphene flakes show the lowest magnetic moment. The two distinctive behaviors regarding the coercive field were noticed in the range of temperature between $5 \leq T < 300\text{K}$. Considering low temperature values, high values of the coercive field was reached. This feature can be connected with the decrease in the diamagnetic response for this range of temperature. As a consequence, the ferromagnetic signal prevails and the coercive field increases. On the other side, at high temperature a competition between diamagnetic and ferromagnetic occurs to respond to the external magnetic field excitation leading to the decrease in the coercive field.

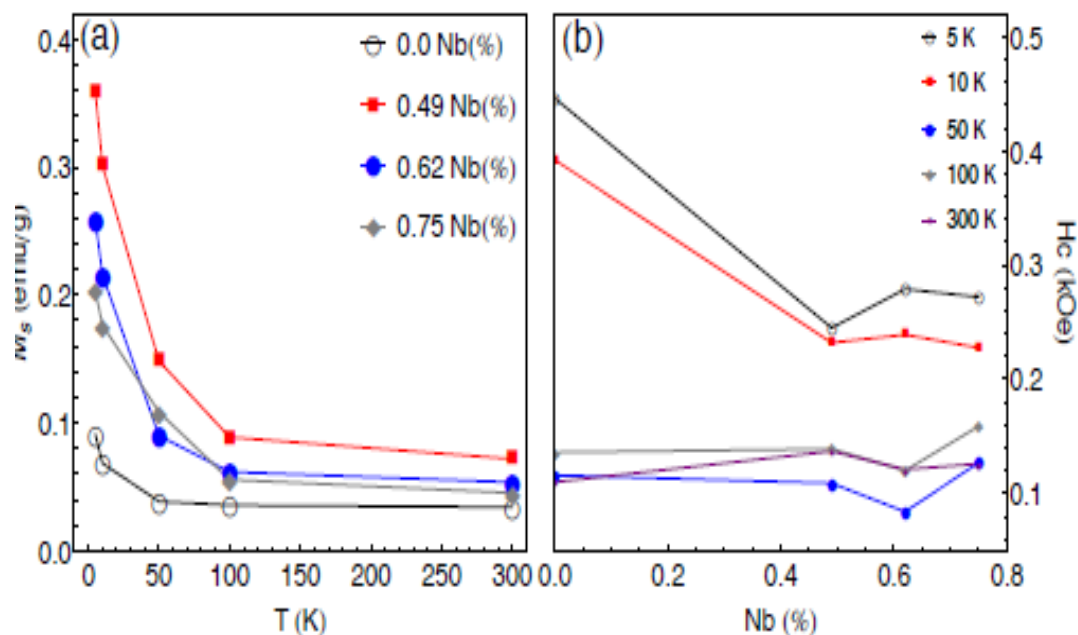


Fig 7. 3 (a) Coercive field as a function of temperature for different Nb (%) concentrations. (b) Coercive field as a function of Nb concentration for different temperatures.

7.3 Photo catalytic activity of the TiO₂ and graphene composite.

The photocatalytic application of undecorated graphene and decorated graphene with TiO₂ nanoparticles were demonstrated in this section. The following process parameters [working pressure = 6 Pa, Time=40 min, Frequency = 20 Hz RF power= 80 W] were used to deposit the TiO₂ nanoparticles onto graphene powder. The photocatalytic activity study of the undecorated graphene and decorated graphene with TiO₂ nanoparticles with an atomic ratio (Ti/C sp²= 13.37 at. %) was carried out by using the methylene red (MR) dye degradation as a model reaction under the UV and visible light. The absorbance peak of the MR decreased with increasing the reaction time under the ultraviolet and visible (UV-vis) radiation as shown in Fig 7.4

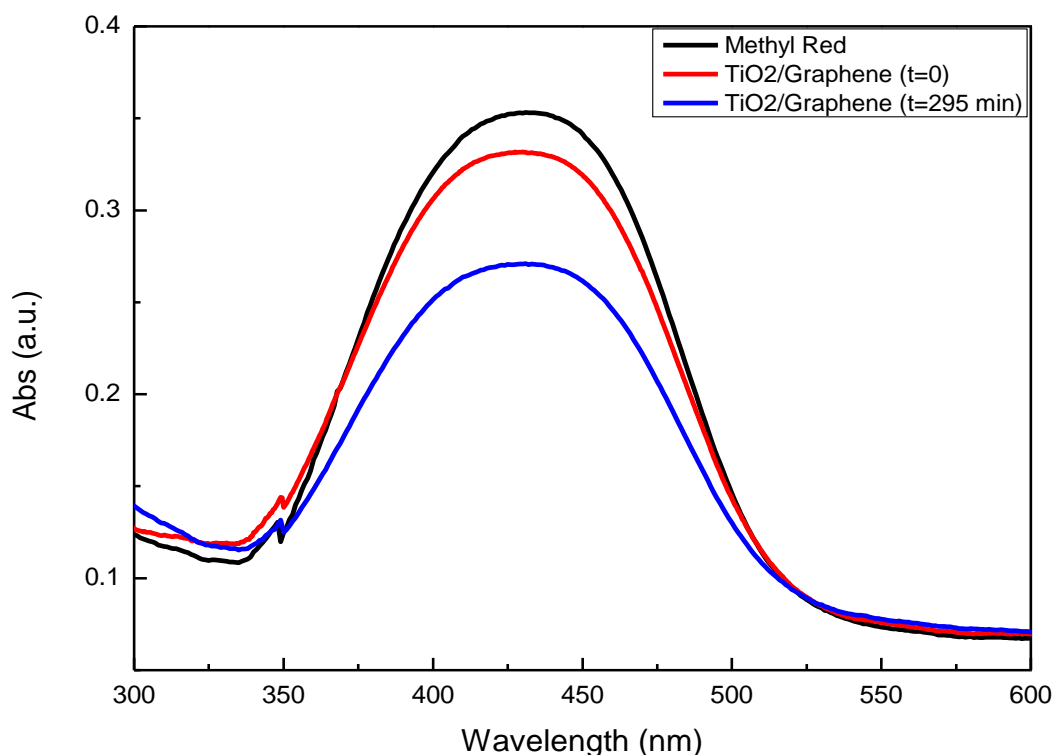


Fig 7.4 . UV-vis spectra of decorated graphene with TiO₂ nanoparticles

The decorated graphene with TiO₂ nanoparticles samples were analyzed by changing the C/C_0 with variation of the absorbance (A/A_0), where A_0 and C_0 is the initial absorbance and

concentration of MR respectively. Fig. 7.5 (b) presents the photo catalytic activity of the undecorated graphene and decorated graphene with TiO₂ nanoparticles. It was observed that the methylene red degraded slightly in the presence of the graphene powder. However, the degradation of MR was enhanced in the presence of graphene-TiO₂ catalyst. The dye was decomposed by about 30% of the initial dye upon the (Uv-vis) irradiation. From the TEM image shown in Fig (6.1) in chapter 6, the deposited TiO₂ nanoparticles onto graphene sheet were well

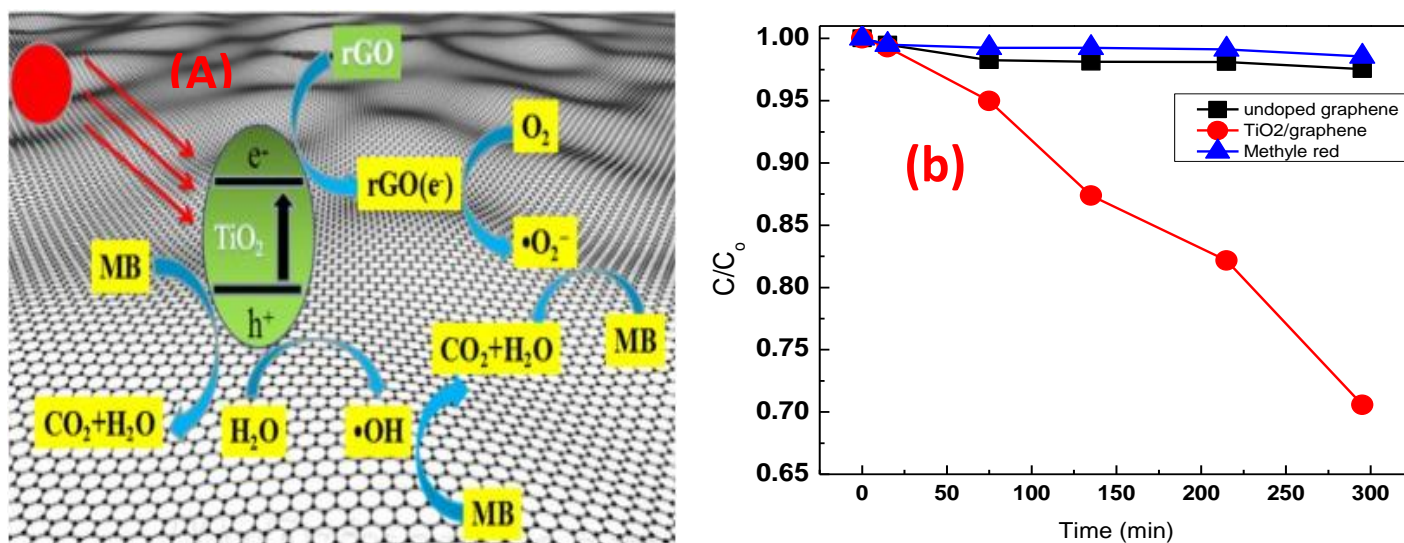


Fig 7.5 (a) Schematic presentations of the decomposition of the dye upon the radiation of light (b) photocatalytic activity of decorated graphene with TiO₂ nanoparticles

The enhancement of the photocatalytic activity of decorated graphene with TiO₂ nanoparticles can be explained as follows, it is reported that, three factors are important for the photocatalytic process, that is, the charge separation and transportation, absorption of light and the adsorption of the pollutant molecules and the scheme is presented in Fig 7.5 (b) [323]. Upon the irradiation of light onto the decorated graphene with TiO₂ nanoparticles, the valence band electrons of TiO₂ were excited to the conduction band and the photogenerated electron and hole could easily transfer to the nearby MB and these photogenerated electrons and holes take part in the redox reaction. As a result the methylene blue decomposed, more methylene blue would transfer

toward the interface from the solution, when the adsorption stability was broken and subsequently methylene red decomposed into CO_2 and H_2O through a series of redox reactions.

It is also reported that the formation of the charge transfer complex between the interface of the TiO_2 and graphene would be expected to facilitate the photocatalytic activity under the Uv-Vis light [³²⁴, ³²⁵]. The interface charge transfer mechanism can facilitate excitation of electrons from graphene to conduction band of the TiO_2 upon the irradiation of the light; as a result the electron hole pairs were not recombined and well separated from each other, leading to enhance the photocatalytic activity through reduced pair recombination. Furthermore our XPS results demonstrate that, the deposited TiO_2 was under stoichiometric, which means that the deposited TiO_2 nanoparticles were oxygen deficient. It is well assumed that such oxygen vacancies in the TiO_2 nanoparticle can to enhance the photocatalytic activity of the TiO_2 and graphene composite. Because the oxygen vacancy in the TiO_{2-x} generate some localized state within the band gap of the TiO_2 , which is ranging from 0.75 to 1.18 eV below the conduction band and leading the photoresponse to the light irradiation [³²⁶].

7.4 Hydrogen sorption capacity of the decorated graphene with Mg nanoparticles

In this study, well dispersed Mg nanoparticles were deposited onto graphene sheets at 80 Hz powder vibration frequency. The other deposition parameters like [working pressure = 6 Pa, deposition time=40 min, RF power= 40 W] were kept constant. The deposited Mg nanoparticles onto graphene sheet were used for hydrogen storage application. In this composite, graphene serves as a supporting material for the decorated materials due to the high surface area. Hydrogen absorption and desorption characteristics of the decorated graphene with Mg nanoparticles were measured using a Sieverts PCT-Pro instrument at 2 bar and 8 bar pressure as shown in Fig 7.6. The hydrogen absorption and desorption were tested using two different

temperatures 330 °C and 360 °C. The hydrogen adsorption of the decorated graphene with Mg nanoparticles was reached a capacity of 3 wt. % within 80 min. Upon dehydrogenation 1.9 wt. % were released at same temperature within 100 min.

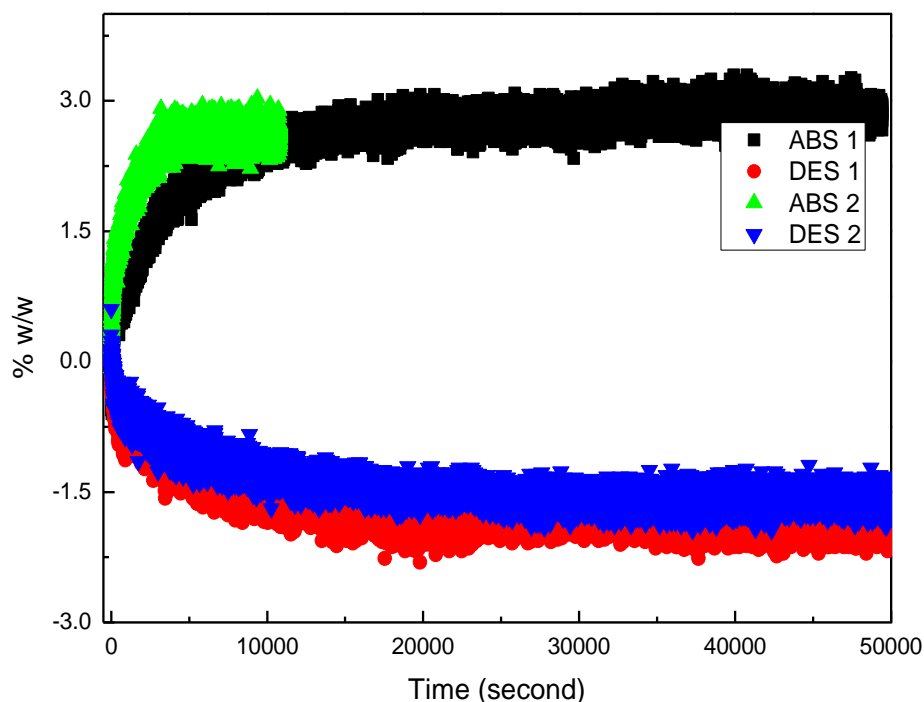


Fig 7.6 Hydrogenation and dehydrogenation of the decorated graphene with Mg nanoparticle at 330° and 360°

It was confirmed from the TEM micrographs that the deposited Mg nanoparticles were uniformly distributed onto graphene sheets, these Mg nanoparticles hydrogenated at 330 °C and 360°C and these particles saturated within 30 min, while these nanoparticles released the hydrogen and became dehydrogenated at the same temperatures. For the undecorated graphene the hydrogen absorption was measured at the 330° and a minimal value of (0.2 -0.5 %) of hydrogen was absorbed at 330 °C. The graphene is not absorbing the hydrogen at this temperature; this absorption could be due to some contaminations during the preparing sample for the absorption. This is the negligible contribution of the graphene in the Mg/graphene composites. It shows that only the decorated Mg nanoparticles absorbed the hydrogen. In our

case H₂ up taking capacity of Mg nanoparticle is high, because all the available Mg nanoparticles on the Mg nanoparticles absorbed the hydrogen to form MgH₂ onto graphene sheets. This point can be explained as follows, from the XPS analysis the calculated weight percentage of the Mg nanoparticles on the graphene surface was 45 %. The total weight of the measured samples was 13 mg. The graphene surface contained only 4 to 5 mg of Mg nanoparticles. Due to the low amount of Mg nanoparticles onto graphene sheet the hydrogen absorption capacity was only 3% in graphene/Mg composite. The hydrogen absorption and desorption of the decorated Mg nanoparticles are presented in Fig 7.7. It was observed that the hydrogen absorption storage capacity for only the Mg nanoparticles was 6.6 wt. %. The similar results is also reported by Eun seon cho et al, they synthesized very small Mg nanoparticles onto graphene sheets and used the composite for the hydrogen absorption. They found that hydrogen storage capacity for Mg nanoparticles was 6.5 wt. % and 0.105 kg H₂ per liter in the total composite at 200 °C and 250 °C at 15 bars.

However, for the surface absorption of the hydrogen onto Mg surface to be accomplished fast kinetic required weak chemical bonding and low diffusion resistance. This is well established behavior between the high storage capacities and fast kinetics. To achieve this kind of fast kinetics' large surface area of the Mg nanostructures sample would be prepared to support separation of gaseous hydrogen and also reduce the diffusion length resistance. Because the charge and discharge of the cycle one of the complex phenomenon, which involves molecular dissociation, diffusion, and chemical bonding. However, it is generally observed phenomenon that, hydrogenation process is controlled by molecular hydrogen dissociation at the Mg surface and hydrogen diffusion into the Mg bulk. Also it is well established that hydrogen molecules can be diffused onto the Mg nanoparticle and the hydrogen molecules must dissociated and form the

metal hydride. But, the molecular hydrogen is so stable and high energy is required to break the H-H bonding at normal temperature. However, with interaction of the molecular hydrogen by metal surface the metal surface weakens the H-H bonding and lowers the barrier of the effective dissociation. Consequently, at the surface of the Mg nanoparticles reflect the aspect of the metal-H interaction. Addition to this the particle size of the deposited Mg nanoparticles was 8 - 12 nm. It has been reported that hydrogen uptake capacity is strongly dependent on the size of Mg nanoparticles. Moreover, by optimization of the Mg nanoparticles size, contents and distribution is essential to improve the hydrogen absorption in graphene.

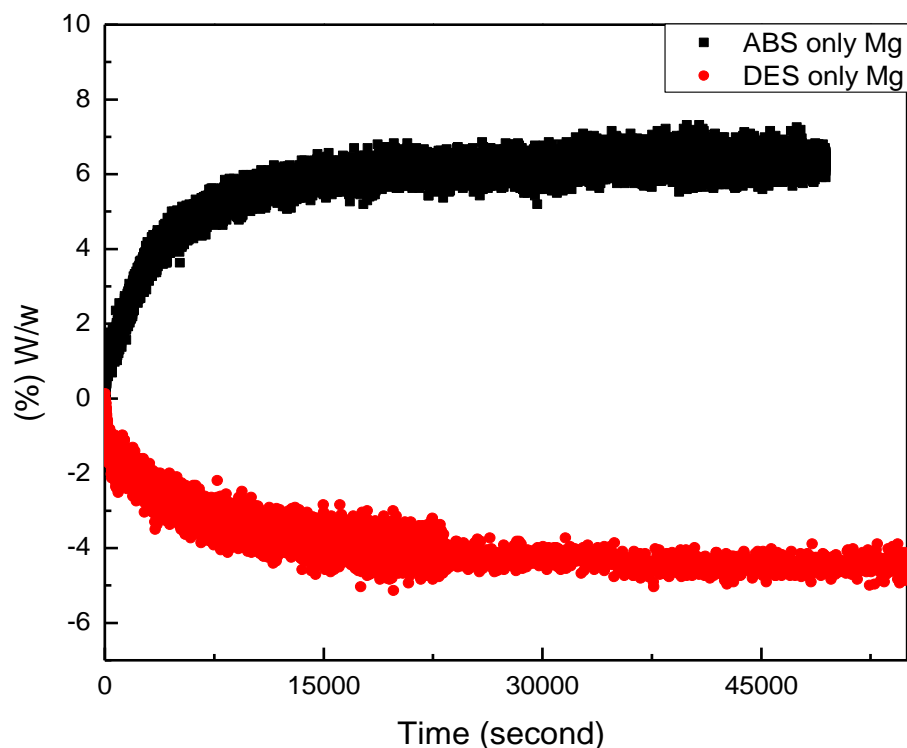


Fig 7.7 Hydrogenation and dehydrogenation of the Mg nanoparticle at 330°

Moreover it should also be noted that the absorption and desorption temperature is still relatively high, which obstructs the practical applications of Mg-based hydrogen storage materials. Therefore, strategies to modify the thermodynamics of Mg-based materials to reduce absorption and desorption energy barrier are clearly to be important topics for further research.

7.5 Conclusions

In this chapter the application potential of the decorated graphene sheets with Nb₂O₅, TiO₂ and Mg nanoparticles was studied. It was found that with decoration of graphene with these metal and metal oxide nanostructures improve the properties of the composite. A ferromagnetic behavior was observed with decoration of graphene sheets with Nb₂O₅ nanoparticles. It was found that, the ferromagnetic property was enhanced with the deposition of the Nb₂O₅ nanoparticles. The photocatalytic activity was studied for the decorated graphene sheet with TiO₂ nanoparticles. It was observed that the decorated graphene sheets with TiO₂ nanoparticles showed reasonably catalytic activity. The hydrogen absorption and desorption was studied for the well dispersed Mg nanoparticles onto graphene sheets. It was found that the decorated Mg nanoparticles absorbed hydrogen. The hydrogen storage capacity for the decorated graphene with Mg nanoparticles was 3 wt. % in whole composite. However the hydrogen storage capacity of the decorated Mg nanoparticles only was 6.6 wt. %.

Concluding remarks and prospective

This thesis was dedicated to decorate graphene sheets with metal and metal oxide nanostructures by RF sputtering technique. Two main objectives were focused in this thesis. 1) To decorate graphene sheets uniformly with metal and metal oxide nanostructure without agglomeration. 2) To explore different kinds of application of decorated graphene sheets with metal and metal oxide nanostructures. In order to achieve the mentioned objectives, we designed and carried out the following research activities and driven the following conclusions.

In the first step, we presented the experimental study results about Nb₂O₅ deposition onto graphite nanoplatelets (GNPs) by the variation of the deposition process parameters. To optimize the deposition parameters, four deposition process parameters (RF power, process pressure, and powder vibration frequency and deposition time) were varied to deposit the Nb₂O₅ layers onto GNPs. The structural, chemical and electronic properties of the decorated GNPs with Nb₂O₅ layers were studied. It was found that with deposition of Nb₂O₅ layers onto GNPs, tensile strain was developed into the planes of the GNPs. The induced tensile strain in and between the planes of GNPs increased with raising the amount of the Nb₂O₅ concentration. The structural defects and disorderness were enhanced with deposition of Nb₂O₅ layers onto GNPs by increasing RF power and at low process pressure values. The structural defects, disorderness and tensile strain in the GNPs were confirmed by the X-ray diffraction and Raman spectroscopy analysis. TEM images shows that GNPs decorated with around 5 to 10 nm uniform layer of Nb₂O₅ at 100 W on their surface were successfully fabricated. From the XPS analysis it was confirmed that, by increasing Nb₂O₅ layer thickness on the GNPs surface with rising RF power values binding energy downshift in C 1s peak suggests a p-type doping of GNPs due to charge transfer at the

Concluding Remarks and prospective

interface as a consequence of the higher work function difference between the Nb₂O₅ (4.70 eV) and GNPs (4.33 eV).

In the second step, the interface between the graphene sheets and Nb₂O₅ nanoparticles were studied. To achieve dispersion of Nb₂O₅ nanoparticles obtained onto graphene sheets three different process parameters were varied. The influence of the Nb₂O₅ concentration on the structural, chemical, morphological and magnetic properties of graphene was discussed. It was established that the structural defects were pronounced with increasing amounts of the Nb₂O₅ concentration. XPS measurement on graphene/Nb₂O₅ suggests p-type doping of graphene due to charge transfer at the interface as a consequence of the high work function of Nb₂O₅. The strong p-doping effect was also confirmed by Raman analysis where the positions of the G and 2D peaks of graphene gradually upshifted upon increasing the Nb₂O₅ concentration. The uniform distribution of decorated Nb₂O₅ nanoparticles onto graphene was confirmed from TEM analysis. The ferromagnetic behavior was observed for the undecorated graphene and decorated graphene with Nb₂O₅ nanoparticles. The ferromagnetic behavior of graphene was enhanced with decoration of the Nb₂O₅ nanoparticles.

In the third step, the effect of the Mg concentration on the structural, chemical and morphological properties of the graphene was described. Well dispersed Mg nanoparticles were decorated onto graphene sheets. The structural properties of the decorated graphene with Mg nanoparticles were studied by Raman and XRD techniques. It was found that from the XRD results, different sizes of the crystalline Mg nanoparticles were obtained onto graphene sheets with variation of the process parameters. The plane of graphene sheets were more distorted with increasing amount of Mg nanoparticles onto graphene sheets. Raman spectra indicated that G and 2D bands of the graphene were shifted to higher wavenumber with deposition of Mg

Concluding Remarks and prospective

nanoparticles. The upshifted in G and 2D bands increased with raising amounts of Mg nanoparticles onto graphene sheets, suggesting that graphene was p doped with interaction Mg nanoparticles. The in-plane crystallite size of the graphene was reduced with deposition of the Mg nanoparticles. The well dispersed and small size of Mg nanoparticles in the range of (8-12 nm) onto graphene sheets was decorated by using a high powder vibration frequency. No agglomeration of the sputtered particles was observed with high powder vibration frequency. This observation was confirmed by TEM micrographs. XPS analysis revealed that the decorated Mg nanoparticles onto graphene were oxidized due to exposure to the atmosphere. The well dispersed decorated Mg nanoparticles onto graphene sheets were studied for the hydrogen absorption and desorption at two different temperatures 330 °C and 360 °C at 2 and 8 bars pressure. The hydrogen up taking capacity for the decorated graphene sheets with Mg nanoparticles was 3 wt. % in whole composite. However, the up taking hydrogen storage capacity of the only Mg nanoparticles was 6.6 wt. %.

In the last step, the interaction of the graphene sheets with TiO₂ nanoparticles was studied. The comprehensive characterization techniques (XRD, Raman, XPS, TEM and photocatalytic activity) were used to study the interaction of the TiO₂ nanoparticles with graphene. The influence of the TiO₂ concentration on the structural, chemical, morphological and photocatalytic activity of the graphene sheets were discussed. The XRD results indicated that the lattice of the graphene sheets was distorted with increasing amount of the TiO₂ concentration. The particle nature of the deposited TiO₂ was confirmed by TEM examination and also the TEM analysis shows that TiO₂ nanoparticles were uniformly distributed onto graphene sheets. The Raman analysis showed that the G and 2D bands of graphene were shifted to higher wavenumber with increasing TiO₂ concentration onto graphene sheet confirming the p doped graphene with TiO₂

Concluding Remarks and prospective

nanoparticles. The FWHM of G peak decreased linearly with increasing the doping concentrations in terms of Ti/C sp^2 atomic ratio. The XPS analysis further confirmed the p doping of graphene upon the deposition of the TiO₂ nanoparticles. The binding energy downshift the C 1s core level of was observed after charge transfer from graphene to TiO₂ nanoparticles due to the larger work function of TiO₂ relatively to that of graphene. The well dispersed nanoparticles onto graphene were used for the photocatalytic application. It was observed that decorated graphene sheets with TiO₂ nanoparticles shows reasonably catalytic activity.

This thesis provides results of a study of the interaction effects of the graphene sheets with Nb₂O₅, Mg and TiO₂ nanoparticles deposited by RF sputtering technique. The obtained results suggest new itineraries for the improvement of the properties of decorated graphene sheets with such materials. In this thesis, we discussed the structural, chemical and electronic properties of decorated graphene sheets with low quantity of Nb₂O₅ nanoparticles since the interfacial properties modification was the aim of the study. The deposition of thick nanoparticles would prevent such study by XPS analysis for example. However, from the point of view of specific applications using the photocatalytic activity or as gas sensing, decoration of graphene sheets with high quantity of Nb₂O₅ nanoparticles will be more useful. The range of the deposition parameters such as (RF power values, powder vibration frequencies) should be further extended to get very uniform decoration of the Nb₂O₅ nanoparticles onto graphene sheets. The decorated samples would be further tested to see the magnetic behavior of the uniform decorated graphene sheets.

It is discussed that the Magnesium is one of the ideal applicant for active hydrogen storage due to its high gravimetric hydrogen capabilities and affordability. Moreover it was observed that the absorption and desorption of decorated graphene sheets with Mg nanoparticle are still relatively

Concluding Remarks and prospective

high temperature processes and of slow release/uptake kinetics, which limits the practical applications of Mg-based hydrogen storage materials. Therefore, strategies to modify the thermodynamics of Mg-based materials to reduce absorption and desorption energy barrier are clearly to be important topics for further research. For hydrogen absorption and desorption capacity evaluation, more samples of the decorated graphene sheets with Mg nanoparticles will be prepared. Specially to get the size of Mg nanoparticles within the range of 2 to 5 nm onto graphene sheets high RF power values would be applied to the Mg target with high powder vibration frequency. To increase the hydrogen up taking capacity and also increase the kinetics, a low quantity of the Nb_2O_5 or Ni or other transition metal will be decorated with Mg nanoparticles onto graphene sheets.

The detailed structure, chemical and electronic properties of the decorated graphene sheets with TiO_2 nanoparticle were presented. It was also noted that decorated graphene sheet with TiO_2 nanoparticles shows reasonable photocatalytic property. The deposition parameters will be varied to get uniform decoration of the graphene sheets with TiO_2 nanoparticles to improve the photocatalytic property. Furthermore it was observed that oxygen vacancies formation was clearly confirmed from the XPS analysis. Therefore, some other spectroscopic techniques (photoluminescence spectroscopy and X-ray absorption fine structure (XAFS)) would be employed to study the interaction of the graphene sheets with TiO_2 nanoparticles.

References

- 167 Parent, B., Shneider, M. N. & Macheret, S. O. Sheath governing equations in computational weakly-ionized plasmadynamics. *Journal of Computational Physics* **232**, 234-251 (2013).
- 168 Chapman, B. N. *Glow discharge processes*. (Wiley, 1980).
- 169 Amin, G. *ZnO and CuO nanostructures: low temperature growth, characterization, their optoelectronic and sensing applications*, Linköping University Electronic Press, (2012).
- 170 Geng, Y., Wang, S. J. & Kim, J.-K. Preparation of graphite nanoplatelets and graphene sheets. *Journal of colloid and interface science* **336**, 592-598 (2009).
- 171 Vinayan, B. & Ramaprabhu, S. Facile synthesis of SnO₂ nanoparticles dispersed nitrogen doped graphene anode material for ultrahigh capacity lithium ion battery applications. *Journal of Materials Chemistry A* **1**, 3865-3871 (2013).
- 172 Tai, J., Hu, J., Chen, Z. & Lu, H. Two-step synthesis of boron and nitrogen co-doped graphene as a synergistically enhanced catalyst for the oxygen reduction reaction. *RSC Advances* **4**, 61437-61443 (2014).
- 173 Al-Harhi, S. H. *et al.* Unusual surface and edge morphologies, sp² to sp³ hybridized transformation and electronic damage after Ar⁺ ion irradiation of few-layer graphene surfaces. *Nanoscale research letters* **7**, 466 (2012).
- 174 Gao, A., Zoethout, E., Sturm, J., Lee, C. & Bijkerk, F. Extreme ultraviolet radiation induced defects in single-layer graphene. *arXiv preprint arXiv:1401.2352* (2014).
- 175 Blume, R. *et al.* The influence of intercalated oxygen on the properties of graphene on polycrystalline Cu under various environmental conditions. *Physical Chemistry Chemical Physics* **16**, 25989-26003 (2014).
- 176 Chin, M. L. *et al.* Planar metal–insulator–metal diodes based on the Nb/Nb₂O₅/X material system. *Journal of Vacuum Science & Technology B, Nanotechnology and Microelectronics: Materials, Processing, Measurement, and Phenomena* **31**, 051204 (2013).
- 177 Ma, Q. & Rosenberg, R. A. in *10th Workshop on RF Superconductivity*.
- 178 Ma, T., Isobe, S., Wang, Y., Hashimoto, N. & Ohnuki, S. Catalytic Effect of Nb₂O₅ in MgH₂-Nb₂O₅ Ball-Milled Composites. *Catalysts* **2**, 344-351 (2012).

References

- 179 Li, M. *et al.* Solar-microbial hybrid device based on oxygen-deficient niobium pentoxide anodes for sustainable hydrogen production. *Chemical Science* **6**, 6799-6805 (2015).
- 180 Luciu, I., Bartali, R. & Laidani, N. Influence of hydrogen addition to an Ar plasma on the structural properties of TiO₂-x thin films deposited by RF sputtering. *Journal of Physics D: Applied Physics* **45**, 345302 (2012).
- 181 Safeen, K., Micheli, V., Bartali, R., Gottardi, G. & Laidani, N. Low temperature growth study of nano-crystalline TiO₂ thin films deposited by RF sputtering. *Journal of Physics D: Applied Physics* **48**, 295201 (2015).
- 182 Li, J. *et al.* Porous graphitized carbon for adsorptive removal of benzene and the electrothermal regeneration. *Environmental science & technology* **46**, 12648-12654 (2012).
- 183 Bhowmik, R. Ferromagnetism in lead graphite-pencils and magnetic composite with CoFe₂O₄ particles. *Composites Part B: Engineering* **43**, 503-509 (2012).
- 184 Meng, X. *et al.* Stable p-and n-type doping of few-layer graphene/graphite. *Carbon* **57**, 507-514 (2013).
- 185 Zak, A. K., Majid, W. A., Abrishami, M. E. & Yousefi, R. X-ray analysis of ZnO nanoparticles by Williamson-Hall and size-strain plot methods. *Solid State Sciences* **13**, 251-256 (2011).
- 186 Cullity, B. *Element of X-ray Diffraction*, Addison-Wesley Reading. *MA Google Scholar* (1978).
- 187 Zhang, B. *et al.* Characterization of the effects of 3-MeV proton irradiation on fine-grained isotropic nuclear graphite. *Carbon* **77**, 311-318 (2014).
- 188 Asthana, A. *et al.* Investigations on the structural disordering of neutron-irradiated highly oriented pyrolytic graphite by X-ray diffraction and electron microscopy. *Journal of applied crystallography* **38**, 361-367 (2005).
- 189 Shibaev, A., Yusin, S., Maksimovskii, E., Ukhina, A. & Bannov, A. Chemical treatment of graphite nanoplatelets and their use in supercapacitors. *Russian Journal of Applied Chemistry* **89**, 739-745 (2016).
- 190 Nikiel, L. & Jagodzinski, P. W. Raman spectroscopic characterization of graphites: A re-evaluation of spectra/structure correlation. *Carbon* **31**, 1313-1317 (1993).

References

- 191 Jawhari, T., Roid, A. & Casado, J. Raman spectroscopic characterization of some commercially available carbon black materials. *Carbon* **33**, 1561-1565 (1995).
- 192 Jorio, A., Saito, R., Dresselhaus, G. & Dresselhaus, M. S. The sp² Nanocarbons: Prototypes for Nanoscience and Nanotechnology. *Raman Spectroscopy in Graphene Related Systems*, 1-15 (2011).
- 193 Matz, D. L., Sojoudi, H., Graham, S. & Pemberton, J. E. Signature vibrational bands for defects in CVD single-layer graphene by surface-enhanced Raman spectroscopy. *The journal of physical chemistry letters* **6**, 964-969 (2015).
- 194 Pimenta, M. *et al.* Studying disorder in graphite-based systems by Raman spectroscopy. *Physical Chemistry Chemical Physics* **9**, 1276-1290 (2007).
- 195 Yan, J., Zhang, Y., Kim, P. & Pinczuk, A. Electric field effect tuning of electron-phonon coupling in graphene. *Physical review letters* **98**, 166802 (2007).
- 196 Zafar, Z. *et al.* Evolution of Raman spectra in nitrogen doped graphene. *Carbon* **61**, 57-62 (2013).
- 197 Kim, J., Kwak, C. H., Jung, W., Huh, Y. S. & Kim, B. H. Variation in the c-axis conductivity of multi-layer graphene due to H₂ exposure. *Physical Chemistry Chemical Physics* **18**, 15514-15518 (2016).
- 198 Jung, N. *et al.* Charge transfer chemical doping of few layer graphenes: charge distribution and band gap formation. *Nano letters* **9**, 4133-4137 (2009).
- 199 Yu, T. *et al.* Raman mapping investigation of graphene on transparent flexible substrate: the strain effect. *The Journal of Physical Chemistry C* **112**, 12602-12605 (2008).
- 200 Ni, Z. H. *et al.* Uniaxial strain on graphene: Raman spectroscopy study and band-gap opening. *ACS nano* **2**, 2301-2305 (2008).
- 201 Ferrari, A. C. & Robertson, J. Raman spectroscopy of amorphous, nanostructured, diamond-like carbon, and nanodiamond. *Philosophical Transactions of the Royal Society of London A: Mathematical, Physical and Engineering Sciences* **362**, 2477-2512 (2004).
- 202 Nemanich, R. & Solin, S. First- and second-order Raman scattering from finite-size crystals of graphite. *Physical Review B* **20**, 392 (1979).
- 203 Wilhelm, H., Lelaurain, M., McRae, E. & Humbert, B. Raman spectroscopic studies on well-defined carbonaceous materials of strong two-dimensional character. *Journal of applied physics* **84**, 6552-6558 (1998).

References

- 204 Cheng, M. *et al.* Restoration of graphene from graphene oxide by defect repair. *Carbon* **50**, 2581-2587 (2012).
- 205 Mallet-Ladeira, P. *et al.* A Raman study to obtain crystallite size of carbon materials: A better alternative to the Tuinstra–Koenig law. *Carbon* **80**, 629-639 (2014).
- 206 Jorio, A., Achete, C. A., Ferreira, E. H. M., Cançado, L. G. & Capaz, R. B. *Measuring disorder in graphene with Raman spectroscopy*. (INTECH Open Access Publisher Rijeka, Croatia, 2011).
- 207 Childres, I., Jauregui, L. A., Park, W., Cao, H. & Chen, Y. P. Raman spectroscopy of graphene and related materials. *New developments in photon and materials research*, 1-20 (2013).
- 208 Ferreira, E. M. *et al.* Evolution of the Raman spectra from single-, few-, and many-layer graphene with increasing disorder. *Physical Review B* **82**, 125429 (2010).
- 209 Ristein, J., Stief, R., Ley, L. & Beyer, W. A comparative analysis of a-C: H by infrared spectroscopy and mass selected thermal effusion. *Journal of applied physics* **84**, 3836-3847 (1998).
- 210 Ferrari, A. C. Raman spectroscopy of graphene and graphite: disorder, electron–phonon coupling, doping and nonadiabatic effects. *Solid state communications* **143**, 47-57 (2007).
- 211 Childres, I., Jauregui, L. A. & Chen, Y. P. Raman spectra and electron-phonon coupling in disordered graphene with gate-tunable doping. *Journal of applied physics* **116**, 233101 (2014).
- 212 Dresselhaus, M. S. & Kalish, R. *Ion implantation in diamond, graphite and related materials*. Vol. 22 (Springer Science & Business Media, 2013).
- 213 Ferrari, A. C. & Basko, D. M. Raman spectroscopy as a versatile tool for studying the properties of graphene. *Nature nanotechnology* **8**, 235-246 (2013).
- 214 Keller, J. & Simmons, R. Sputtering process model of deposition rate. *IBM Journal of Research and Development* **23**, 24-32 (1979).
- 215 Depla, D., Mahieu, S. & De Gryse, R. in *Reactive Sputter Deposition* 153-197 (Springer, 2008).
- 216 Gras-Marti, A. & Valles-Abarca, J. Slowing down and thermalization of sputtered particle fluxes: Energy distributions. *Journal of applied physics* **54**, 1071-1075 (1983).

References

- 217 Drüsedau, T. P. Investigation of the throw distance of sputtered atoms under consideration of gas rarefaction. *Surface and Coatings Technology* **174**, 470-474 (2003).
- 218 Wang, H., Robinson, J. T., Diankov, G. & Dai, H. Nanocrystal growth on graphene with various degrees of oxidation. *Journal of the American Chemical Society* **132**, 3270-3271 (2010).
- 219 Weibin, Z. *et al.* The investigation of NbO₂ and Nb₂O₅ electronic structure by XPS, UPS and first principles methods. *Surface and Interface Analysis* **45**, 1206-1210 (2013).
- 220 Chen, P., Huang, F. & Yun, S. Characterization of the condensed carbon in detonation soot. *Carbon* **41**, 2093-2099 (2003).
- 221 Li, J., Vaisman, L., Marom, G. & Kim, J.-K. Br treated graphite nanoplatelets for improved electrical conductivity of polymer composites. *Carbon* **45**, 744-750 (2007).
- 222 Yasmin, A. & Daniel, I. M. Mechanical and thermal properties of graphite platelet/epoxy composites. *Polymer* **45**, 8211-8219 (2004).
- 223 Ramirez, C., Figueiredo, F. M., Miranzo, P., Poza, P. & Osendi, M. I. Graphene nanoplatelet/silicon nitride composites with high electrical conductivity. *Carbon* **50**, 3607-3615 (2012).
- 224 Ahmad, S. R., Young, R. J. & Kinloch, I. A. Raman spectra and mechanical properties of graphene/polypropylene nanocomposites. *International Journal of Chemical Engineering and Applications* **6**, 1 (2015).
- 225 Anagnostopoulos, G. *et al.* Stress transfer mechanisms at the submicron level for graphene/polymer systems. *ACS applied materials & interfaces* **7**, 4216-4223 (2015).
- 226 Na, S. R. *et al.* Selective mechanical transfer of graphene from seed copper foil using rate effects. *ACS nano* **9**, 1325-1335 (2015).
- 227 Mohiuddin, T. *et al.* Uniaxial strain in graphene by Raman spectroscopy: G peak splitting, Grüneisen parameters, and sample orientation. *Physical Review B* **79**, 205433 (2009).
- 228 Hong, S. *et al.* Competition between electron doping and short-range scattering in hydrogenated bilayer graphene on hexagonal boron nitride. *RSC Advances* **5**, 103276-103279 (2015).
- 229 Apostolov, A., Apostolova, I. & Wesselinowa, J. p-or n-Doping Effects on the Phonon Spectrum of Single-and Bi-Layer Graphene. *Bulg. J. Phys* **40**, 307-324 (2013).

References

- 230 Chen, H.-Y. *et al.* in *Electron Devices Meeting (IEDM), 2012 IEEE International*. 20.25. 21-20.25. 24 (IEEE).
- 231 Anasori, B., Beidaghi, M. & Gogotsi, Y. Graphene–transition metal oxide hybrid materials. *Materials Today* **17**, 253-254 (2014).
- 232 Pisani, L., Montanari, B. & Harrison, N. A defective graphene phase predicted to be a room temperature ferromagnetic semiconductor. *New Journal of Physics* **10**, 033002 (2008).
- 233 Karim, M. R. *et al.* Electrical conductivity and ferromagnetism in a reduced graphene–metal oxide hybrid. *Advanced Functional Materials* **23**, 323-332 (2013).
- 234 Ma, J., Alfe, D., Michaelides, A. & Wang, E. Stone-Wales defects in graphene and other planar s p 2-bonded materials. *Physical Review B* **80**, 033407 (2009).
- 235 Sofo, J. O., Chaudhari, A. S. & Barber, G. D. Graphane: A two-dimensional hydrocarbon. *Physical Review B* **75**, 153401 (2007).
- 236 Romero, R., Ramos-Barrado, J., Martin, F. & Leinen, D. Nb₂O₅ thin films obtained by chemical spray pyrolysis. *Surface and interface analysis* **36**, 888-891 (2004).
- 237 Escamilla, R. & Huerta, L. X-ray photoelectron spectroscopy studies of non-stoichiometric superconducting NbB_{2+x}. *Superconductor Science and Technology* **19**, 623 (2006).
- 238 Bang, S. *et al.* Photocurrent detection of chemically tuned hierarchical ZnO nanostructures grown on seed layers formed by atomic layer deposition. *Nanoscale research letters* **7**, 290 (2012).
- 239 Wang, J., Manga, K. K., Bao, Q. & Loh, K. P. High-yield synthesis of few-layer graphene flakes through electrochemical expansion of graphite in propylene carbonate electrolyte. *Journal of the American Chemical Society* **133**, 8888-8891 (2011).
- 240 Patterson, A. The Scherrer formula for X-ray particle size determination. *Physical review* **56**, 978 (1939).
- 241 Hafiz, S. M. *et al.* A practical carbon dioxide gas sensor using room-temperature hydrogen plasma reduced graphene oxide. *Sensors and Actuators B: Chemical* **193**, 692-700 (2014).

References

- 242 Del Corro, E., Taravillo, M. & Baonza, V. G. Nonlinear strain effects in double-resonance Raman bands of graphite, graphene, and related materials. *Physical Review B* **85**, 033407 (2012).
- 243 Dong, X. *et al.* Doping single-layer graphene with aromatic molecules. *Small* **5**, 1422-1426 (2009).
- 244 Luan, P. T., Zhang, S., Yang, W., Kang, M. & Jung, H. Efficient p-type doping in graphene via monolayer manganese-oxide nanoparticles decoration. *Journal of the Korean Physical Society* **67**, 700-705 (2015).
- 245 Onyszko, M., Urbas, K., Aleksandrak, M. & Mijowska, E. Reduced graphene oxide and inorganic nanoparticles composites—synthesis and characterization. *Polish Journal of Chemical Technology* **17**, 95-103 (2015).
- 246 Alwarappan, S., Erdem, A., Liu, C. & Li, C.-Z. Probing the electrochemical properties of graphene nanosheets for biosensing applications. *The Journal of Physical Chemistry C* **113**, 8853-8857 (2009).
- 247 Tuinstra, F. & Koenig, J. L. Raman spectrum of graphite. *The Journal of Chemical Physics* **53**, 1126-1130 (1970).
- 248 Sugiura, C., Kitamura, M. & Muramatsu, S. Niobium LIII and LII X-ray absorption-edge spectra of Nb₂O₅ and NH₄NbF₆. *Journal of Physics and Chemistry of Solids* **49**, 1095-1099 (1988).
- 249 Ni, Z. H. *et al.* Tunable stress and controlled thickness modification in graphene by annealing. *ACS nano* **2**, 1033-1039 (2008).
- 250 Basko, D., Piscanec, S. & Ferrari, A. Electron-electron interactions and doping dependence of the two-phonon Raman intensity in graphene. *Physical Review B* **80**, 165413 (2009).
- 251 Rao, G., Freitag, M., Chiu, H.-Y., Sundaram, R. S. & Avouris, P. Raman and photocurrent imaging of electrical stress-induced p-n junctions in graphene. *Acs Nano* **5**, 5848-5854 (2011).
- 252 Xu, H., Xie, L., Zhang, H. & Zhang, J. Effect of graphene Fermi level on the Raman scattering intensity of molecules on graphene. *Acs Nano* **5**, 5338-5344 (2011).
- 253 Lee, J., Novoselov, K. S. & Shin, H. S. Interaction between metal and graphene: dependence on the layer number of graphene. *Acs Nano* **5**, 608-612 (2010).

References

- 254 Min, Y. *et al.* Enhanced chemical interaction between TiO₂ and graphene oxide for photocatalytic decolorization of methylene blue. *Chemical engineering journal* **193**, 203-210 (2012).
- 255 Wu, Z.-S. *et al.* Graphene/metal oxide composite electrode materials for energy storage. *Nano Energy* **1**, 107-131 (2012).
- 256 Aguey-Zinsou, K.-F. & Ares-Fernández, J.-R. Synthesis of colloidal magnesium: a near room temperature store for hydrogen. *Chemistry of Materials* **20**, 376-378 (2007).
- 257 Giangregorio, M. *et al.* Insights into the effects of metal nanostructuring and oxidation on the work function and charge transfer of metal/graphene hybrids. *Nanoscale* **7**, 12868-12877 (2015).
- 258 Lide, D. R. Electron work function of the elements. *CRC handbook of chemistry and physics* **88** (2008).
- 259 Choi, E. H., Lim, J. Y., Kang, S. O. & Uhm, H. S. Measurement of work function at MgO crystal surface by the γ -focused ion beam system. *Japanese journal of applied physics* **41**, L1006 (2002).
- 260 Sygellou, L., Paterakis, G., Galiotis, C. & Tasis, D. Work Function Tuning of Reduced Graphene Oxide Thin Films. *The Journal of Physical Chemistry C* **120**, 281-290 (2015).
- 261 Yao, H., Li, Y. & Wee, A. An XPS investigation of the oxidation/corrosion of melt-spun Mg. *Applied Surface Science* **158**, 112-119 (2000).
- 262 Manin, M. *et al.* Deposition of MgO thin film by liquid pulsed injection MOCVD. *Surface and Coatings Technology* **200**, 1424-1429 (2005).
- 263 Luo, Y., Wang, X., Guo, W. & Rohwerder, M. Growth behavior of initial product layer formed on Mg alloy surface induced by polyaniline. *Journal of The Electrochemical Society* **162**, C294-C301 (2015).
- 264 Unocic, K. A. *et al.* Transmission electron microscopy study of aqueous film formation and evolution on magnesium alloys. *Journal of The Electrochemical Society* **161**, C302-C311 (2014).
- 265 Santamaria, M., Di Quarto, F., Zanna, S. & Marcus, P. Initial surface film on magnesium metal: a characterization by X-ray photoelectron spectroscopy (XPS) and photocurrent spectroscopy (PCS). *Electrochimica Acta* **53**, 1314-1324 (2007).

References

- 266 Chakrabarti, A. *et al.* Conversion of carbon dioxide to few-layer graphene. *Journal of Materials Chemistry* **21**, 9491-9493 (2011).
- 267 Makridis, S. *et al.* Polymer-stable magnesium nanocomposites prepared by laser ablation for efficient hydrogen storage. *International Journal of Hydrogen Energy* **38**, 11530-11535 (2013).
- 268 Monshi, A., Foroughi, M. R. & Monshi, M. R. Modified Scherrer equation to estimate more accurately nano-crystallite size using XRD. *World Journal of Nano Science and Engineering* **2**, 154 (2012).
- 269 Huang, M., Yan, H., Heinz, T. F. & Hone, J. Probing strain-induced electronic structure change in graphene by Raman spectroscopy. *Nano letters* **10**, 4074-4079 (2010).
- 270 Li, X. *et al.* Simultaneous nitrogen doping and reduction of graphene oxide. *Journal of the American Chemical Society* **131**, 15939-15944 (2009).
- 271 Ardizzone, S., Bianchi, C., Fadoni, M. & Vercelli, B. Magnesium salts and oxide: an XPS overview. *Applied Surface Science* **119**, 253-259 (1997).
- 272 Sterrer, M., Fischbach, E., Risse, T. & Freund, H.-J. Geometric characterization of a singly charged oxygen vacancy on a single-crystalline MgO (001) film by electron paramagnetic resonance spectroscopy. *Physical review letters* **94**, 186101 (2005).
- 273 Fournier, V., Marcus, P. & Olejford, I. Oxidation of magnesium. *Surface and interface analysis* **34**, 494-497 (2002).
- 274 Lu, H.-L., Ding, S.-J. & Zhang, D. W. Investigation of Thermal Stability of Atomic-Layer-Deposited MgO Thin Films on Si (100) Using X-Ray Photoelectron Spectroscopy. *Electrochemical and Solid-State Letters* **13**, G25-G28 (2010).
- 275 Kim, E., Lee, W.-G. & Jung, J. Agglomeration effects of thin metal catalyst on graphene film synthesized by chemical vapor deposition. *Electronic Materials Letters* **7**, 261 (2011).
- 276 Miyoshi, M. *et al.* Study on transfer-free graphene synthesis process utilizing spontaneous agglomeration of catalytic Ni and Co metals. *Materials Research Express* **2**, 015602 (2015).
- 277 Gadipelli, S. & Guo, Z. X. Graphene-based materials: synthesis and gas sorption, storage and separation. *Progress in Materials Science* **69**, 1-60 (2015).

References

- 278 Bieletzki, M. *et al.* Topography and work function measurements of thin MgO (001) films on Ag (001) by nc-AFM and KPFM. *Physical Chemistry Chemical Physics* **12**, 3203-3209 (2010).
- 279 Yeo, Y.-C., King, T.-J. & Hu, C. Metal-dielectric band alignment and its implications for metal gate complementary metal-oxide-semiconductor technology. *Journal of Applied Physics* **92**, 7266-7271 (2002).
- 280 Ren, Y. *et al.* Controlling the electrical transport properties of graphene by in situ metal deposition. *Applied Physics Letters* **97**, 053107 (2010).
- 281 Song, S. M., Park, J. K., Sul, O. J. & Cho, B. J. Determination of work function of graphene under a metal electrode and its role in contact resistance. *Nano letters* **12**, 3887-3892 (2012).
- 282 Sheng, Z.-H. *et al.* Catalyst-free synthesis of nitrogen-doped graphene via thermal annealing graphite oxide with melamine and its excellent electrocatalysis. *ACS nano* **5**, 4350-4358 (2011).
- 283 Iqbal, M., Singh, A. K., Iqbal, M. & Eom, J. Raman fingerprint of doping due to metal adsorbates on graphene. *Journal of Physics: Condensed Matter* **24**, 335301 (2012).
- 284 Lin, Y.-C. *et al.* Graphene annealing: how clean can it be? *Nano letters* **12**, 414-419 (2011).
- 285 Ullah, K., Ali, A., Ye, S., Zhu, L. & Oh, W.-C. Microwave-Assisted Synthesis of Pt-Graphene/TiO₂ Nanocomposites and Their Efficiency in Assisting Hydrogen Evolution from Water in the Presence of Sacrificial Agents. *Science of Advanced Materials* **7**, 606-614 (2015).
- 286 Qiu, B., Xing, M. & Zhang, J. Mesoporous TiO₂ nanocrystals grown in situ on graphene aerogels for high photocatalysis and lithium-ion batteries. *Journal of the American Chemical Society* **136**, 5852-5855 (2014).
- 287 Joucken, F. *et al.* Charge transfer and electronic doping in nitrogen-doped graphene. *Scientific reports* **5**, 14564-14564 (2014).
- 288 Geng, H.-Z. *et al.* Doping and de-doping of carbon nanotube transparent conducting films by dispersant and chemical treatment. *Journal of Materials Chemistry* **18**, 1261-1266 (2008).

References

- 289 Yu, S. *et al.* Graphene quantum dots to enhance the photocatalytic hydrogen evolution efficiency of anatase TiO₂ with exposed {001} facet. *Physical Chemistry Chemical Physics* **18**, 20338-20344 (2016).
- 290 Zhang, H. *et al.* A facile one-step synthesis of TiO₂/graphene composites for photodegradation of methyl orange. *Nano Research* **4**, 274-283 (2011).
- 291 Chandramohan, S. *et al.* Chemically modified multilayer graphene with metal interlayer as an efficient current spreading electrode for InGaN/GaN blue light-emitting diodes. *Journal of Physics D: Applied Physics* **45**, 145101 (2012).
- 292 Luciu, I. *RF plasma synthesis and characterization of thin films for transparent conductors*, University of Trento, (2012).
- 293 Andonovic, B., Grozdanov, A., Paunović, P. & Dimitrov, A. T. X-ray diffraction analysis on layers in graphene samples obtained by electrolysis in molten salts: a new perspective. *Micro & Nano Letters* **10**, 683-685 (2015).
- 294 Kong, L. *et al.* Electromagnetic wave absorption properties of reduced graphene oxide modified by maghemite colloidal nanoparticle clusters. *The Journal of Physical Chemistry C* **117**, 19701-19711 (2013).
- 295 Ohsaka, T., Izumi, F. & Fujiki, Y. Raman spectrum of anatase, TiO₂. *Journal of Raman spectroscopy* **7**, 321-324 (1978).
- 296 Tang, H., Prasad, K., Sanjines, R., Schmid, P. & Levy, F. Electrical and optical properties of TiO₂ anatase thin films. *Journal of Applied Physics* **75**, 2042-2047 (1994).
- 297 Beams, R., Cañado, L. G. & Novotny, L. Raman characterization of defects and dopants in graphene. *Journal of Physics: Condensed Matter* **27**, 083002 (2015).
- 298 Kim, S. *et al.* Characterization of chemical doping of graphene by in-situ Raman spectroscopy. *Applied Physics Letters* **108**, 203111 (2016).
- 299 Casiraghi, C. *Raman spectroscopy of graphene*. (RSC Publishing: Cambridge, 2012).
- 300 Naumenko, D., Snitka, V., Snopok, B., Arpiainen, S. & Lipsanen, H. Graphene-enhanced Raman imaging of TiO₂ nanoparticles. *Nanotechnology* **23**, 465703 (2012).
- 301 Cancado, L. *et al.* General equation for the determination of the crystallite size L_a of nanographite by Raman spectroscopy. *Applied Physics Letters* **88**, 163106 (2006).
- 302 Răileanu, M. *et al.* Sol-gel doped TiO₂ nanomaterials: a comparative study. *Journal of sol-gel science and technology* **51**, 315-329 (2009).

References

- 303 Schierbaum, K. *et al.* The interaction of Pt with TiO₂ (110) surfaces: a comparative XPS, UPS, ISS, and ESD study. *Surface science* **345**, 261-273 (1996).
- 304 Rossella, F. *et al.* TiO₂ thin films for spintronics application: a Raman study. *Journal of Raman spectroscopy* **41**, 558-565 (2010).
- 305 Jin, Z., Yao, J., Kittrell, C. & Tour, J. M. Large-scale growth and characterizations of nitrogen-doped monolayer graphene sheets. *Acs Nano* **5**, 4112-4117 (2011).
- 306 Mali, K. S., Greenwood, J., Adisoejoso, J., Phillipson, R. & De Feyter, S. Nanostructuring graphene for controlled and reproducible functionalization. *Nanoscale* **7**, 1566-1585 (2015).
- 307 Pisana, S. *et al.* Breakdown of the adiabatic Born–Oppenheimer approximation in graphene. *Nature materials* **6**, 198-201 (2007).
- 308 Sanders, S. *et al.* Engineering high charge transfer n-doping of graphene electrodes and its application to organic electronics. *Nanoscale* **7**, 13135-13142 (2015).
- 309 Jia, Y. *et al.* Characterization and activity of N doped TiO₂ supported VPO catalysts for NO oxidation. *Atmospheric Pollution Research* **6**, 184-190 (2015).
- 310 Cai, Y. & Feng, Y. P. Review on charge transfer and chemical activity of TiO₂: Mechanism and applications. *Progress in Surface Science* **91**, 183-202 (2016).
- 311 Das, A., Chakraborty, B. & Sood, A. Raman spectroscopy of graphene on different substrates and influence of defects. *Bulletin of Materials Science* **31**, 579-584 (2008).
- 312 Casiraghi, C. Doping dependence of the Raman peaks intensity of graphene close to the Dirac point. *Physical Review B* **80**, 233407 (2009).
- 313 Cong, H. P., He, J. J., Lu, Y. & Yu, S. H. Water-Soluble Magnetic-Functionalized Reduced Graphene Oxide Sheets: In situ Synthesis and Magnetic Resonance Imaging Applications. *Small* **6**, 169-173 (2010).
- 314 Zhu, G. *et al.* Flexible Magnetic Nanoparticles–Reduced Graphene Oxide Composite Membranes Formed by Self-Assembly in Solution. *ChemPhysChem* **11**, 2432-2437 (2010).
- 315 Robinson, J. A. *et al.* Epitaxial graphene materials integration: effects of dielectric overlayers on structural and electronic properties. *Acs Nano* **4**, 2667-2672 (2010).

References

- 316 Matte, H. R., Subrahmanyam, K. & Rao, C. Novel magnetic properties of graphene: presence of both ferromagnetic and antiferromagnetic features and other aspects. *The Journal of Physical Chemistry C* **113**, 9982-9985 (2009).
- 317 Park, T.-J., Papaefthymiou, G. C., Viescas, A. J., Moodenbaugh, A. R. & Wong, S. S. Size-dependent magnetic properties of single-crystalline multiferroic BiFeO₃ nanoparticles. *Nano letters* **7**, 766-772 (2007).
- 318 Wu, S.-H. & Chen, D.-H. Synthesis and characterization of nickel nanoparticles by hydrazine reduction in ethylene glycol. *Journal of Colloid and Interface Science* **259**, 282-286 (2003).
- 319 Chappert, C., Le Dang, K., Beauvillain, P., Hurdequint, H. & Renard, D. Ferromagnetic resonance studies of very thin cobalt films on a gold substrate. *Physical Review B* **34**, 3192 (1986).
- 320 Gross, A. F., Diehl, M. R., Beverly, K. C., Richman, E. K. & Tolbert, S. H. Controlling magnetic coupling between cobalt nanoparticles through nanoscale confinement in hexagonal mesoporous silica. *The Journal of Physical Chemistry B* **107**, 5475-5482 (2003).
- 321 Wu, W., He, Q., Chen, H., Tang, J. & Nie, L. Sonochemical synthesis, structure and magnetic properties of air-stable Fe₃O₄/Au nanoparticles. *Nanotechnology* **18**, 145609 (2007).
- 322 Chen, D.-H. & He, X.-R. Synthesis of nickel ferrite nanoparticles by sol-gel method. *Materials Research Bulletin* **36**, 1369-1377 (2001).
- 323 Yang, Y., Xu, L., Wang, H., Wang, W. & Zhang, L. TiO₂/graphene porous composite and its photocatalytic degradation of methylene blue. *Materials & Design* **108**, 632-639 (2016).
- 324 Park, Y. *et al.* Fullerol–Titania Charge-Transfer-Mediated Photocatalysis Working under Visible Light. *Chemistry–A European Journal* **15**, 10843-10850 (2009).
- 325 Seo, Y. S., Lee, C., Lee, K. H. & Yoon, K. B. 1: 1 and 2: 1 Charge-Transfer Complexes between Aromatic Hydrocarbons and Dry Titanium Dioxide. *Angewandte Chemie International Edition* **44**, 910-913 (2005).

References

- 326 Emeline, A. V., Kuznetsov, V. N., Rybchuk, V. K. & Serpone, N. Visible-light-active titania photocatalysts: the case of N-doped s—properties and some fundamental issues. *International Journal of Photoenergy* **2008** (2007).